
The study of renal function and toxicity using zebrafish (*Danio rerio*) larvae as a vertebrate model

Inauguraldissertation

zur

Erlangung der Würde eines Doktors der Philosophie
vorgelegt der
Philosophisch-Naturwissenschaftlichen Fakultät
der Universität Basel

von

JAN STEPHAN BOLTEN

BASEL 2023



Dieses Werk ist unter dem Vertrag "Creative Commons Namensnennung - Nicht kommerziell - Keine Bearbeitungen 4.0" lizenziert. Die vollständige Lizenz kann unter <https://creativecommons.org/licenses/by-nc-nd/4.0/> eingesehen werden.

Originaldokument gespeichert auf dem Dokumentenserver der Universität Basel
edoc.unibas.ch

Genehmigt von der Philosophisch-Naturwissenschaftlichen Fakultät

Auf Antrag von

Prof. Dr. Jörg Huwyler (Erstbetreuer)

Prof. Dr. Alex Odermatt (Zweitbetreuer)

Prof. Dr. Andrea Huwiler (Externe Expertin)

Basel, 28. März 2023

Prof. Dr. Marcel Mayor

Dekan

To my Family
who always supports me

TABLE OF CONTENTS

	Page
1 Introduction	3
1.1 Kidney anatomy and function	3
1.2 Nephrotoxicity	9
1.2.1 Glomerular-related nephrotoxicity	9
1.2.2 Tubular-related nephrotoxicity	10
1.2.3 Interstitium-related nephrotoxicity	14
1.3 Using test models to study kidney function and nephrotoxicity	15
1.3.1 <i>In vitro</i> models	15
1.3.2 <i>Ex vivo</i> models	19
1.3.3 <i>In vivo</i> models	21
1.4 Zebrafish larvae as a vertebrate model	22
1.4.1 Zebrafish larvae as a vertebrate model for nanomedicines	22
1.4.2 Zebrafish larvae as a vertebrate model for renal function and nephrotoxicity	23
2 Aim	25
3 Results	27
3.1 Part I: The study of renal function	27
3.2 Part II: X-ray-based microtomography studies	43
3.2.1 Publication 1	43
3.2.2 Publication 2	63
3.3 Part III: Mechanism of toxicity	91
3.3.1 Publication 1	91
3.3.2 Publication 2	107
3.4 Part IV: Application of the zebrafish model	121
3.4.1 Publication 1	121
3.4.2 Publication 2	133
3.4.3 Publication 3	145
3.4.4 Publication 4	157
4 Discussion & Outlook	167
4.1 The use of zebrafish larvae as a vertebrate model to study renal function	168

TABLE OF CONTENTS

4.2	X-ray-based microtomography	172
4.3	Mechanistic toxicity studies	176
4.4	Application of zebrafish for pharmacokinetic studies of nanoparticles . . .	178
4.5	Future perspectives of the zebrafish model	181
5	Conclusion	185
	Bibliography	187
	Abbreviations	199
	Acknowledgment	201

SUMMARY

Zebrafish (*Danio rerio*) is a powerful model in biomedical and pharmaceutical sciences. The zebrafish model was introduced to toxicological sciences in 1960, followed by its use in biomedical sciences to investigate vertebrate gene functions. As a consequence of many research projects in this field, the study of human genetic diseases became instantly feasible. Consequently, zebrafish have been intensively used in developmental biology and associated disciplines. Due to the simple administration of medicines and the high number of offspring, zebrafish larvae became widely more popular in pharmacological studies in the following years. In the past decade, zebrafish larvae were further established as a vertebrate model in the field of pharmacokinetics and nanomedicines. In this PhD thesis, zebrafish larvae were investigated as an early-stage *in vivo* vertebrate model to study renal function, toxicity, and were applied in drug-targeting projects using nanomedicines.

The first part focused on the characterization of the renal function of three-to four-day-old zebrafish larvae. Non-renal elimination processes were additionally described. Moreover, injection techniques, imaging parameters, and post-image processing scripts were established to serve as a toolbox for follow-up projects.

The second part analyzed the impact of gentamicin (a nephrotoxin) on the morphology of the pronephros of zebrafish larvae. Imaging methodologies such as fluorescent-based laser scanning microscopy and X-ray-based microtomography were applied. A profound comparison study of specimens acquired with different laboratory X-ray-based microto-

TABLE OF CONTENTS

mography devices and a radiation facility was done to promote the use of X-ray-based microtomography for broader biomedical applications.

In the third part, the toxicity of nephrotoxins on mitochondria in renal epithelial cells of proximal tubules was assessed using the zebrafish larva model. Findings were compared with other teleost models such as isolated renal tubules of killifish (*Fundulus heteroclitus*).

In view of the usefulness and high predictability of the zebrafish model, it was applied to study the pharmacokinetics of novel nanoparticles in the fourth part. Various *in vivo* pharmacokinetic parameters such as drug release, transfection of mRNA/pDNA plasmids, macrophage clearance, and the characterization of novel drug carriers that were manipulated with ultrasound were assessed in multiple collaborative projects.

Altogether, the presented zebrafish model showed to be a reliable *in vivo* vertebrate model to assess renal function, toxicity, and pharmacokinetics of nanoparticles. The application of the presented model will hopefully encourage others to reduce animal experiments in preliminary studies by fostering the use of zebrafish larvae.

INTRODUCTION

1.1 Kidney anatomy and function

The renal-urological system consists of a urethra, a urinary bladder, two ureters, and two bean-shaped kidneys [1]. In humans, the kidneys lie in the retroperitoneum and are situated in the posterior part of the left and right abdomen. Depending on the body surface area, age, and sex, the kidney comprises approximately 0.51% to 1.08% of the body weight [1]. It is anatomically separated into the renal cortex (outside layer) and the renal medulla (inside layer) and is strongly supplied with blood, especially the renal cortex [2]. The kidney receives 25% of the cardiac output [1], and in a healthy adult, 1 to 1.2 liter of blood passes through the renal blood vessels every minute.

The purpose of the renal-urological system is the filtration and detoxification of the blood, thereby regulating salt concentration and maintaining acid-base homeostasis and pH regulation [3]. In healthy adults, the kidney produces up to 1 to 2 liters of urine every day from 180 liters of glomerular ultrafiltrate [3]. The filtration of the blood

occurs in the nephrons, the functional units of the kidney. Figure 1.1 shows a schematic overview of the mammalian kidney anatomy.

Approximately 1.2 million nephrons are located in the renal cortex and medulla of the kidney [4]. The nephron is composed of a renal corpus and a renal tubule. The renal corpus consists of a vast network of capillaries forming the glomerulus in the Bowman's capsule. Within the glomerulus, several cell types are present. The contractile mesangial cells are situated between glomerular capillary loops and form a supporting framework that maintains the structural integrity of the glomerular tuft [5]. This, together with the glomerular basement membrane, creates wall tension in the glomerular capillaries, allowing for the change in its geometry that results from mesangial contraction or relaxation [5]. As a summarizing unit, the glomerular filtration barrier (GFB) forms a size-dependent penetration layer for effective blood filtration. This consists of a visceral cell layer formed by podocytes, the glomerular (fenestrated) endothelial cells, and the glomerular basement membrane [6]. The glomerular endothelial cells have a luminal endothelial surface layer called glycocalyx, a negatively charged network of proteoglycans, glycoproteins, and glycolipids [7]. These components maintain a charge-selective barrier [7]. The podocytes form specialized cell-to-cell junctions called slit diaphragms, enabling the size-dependent passage of the plasma filtrate [8]. The GFB allows filtration selectivity based on molecular weight, hydrodynamic size, hydrophilicity, and the charge of molecules [6]. It is freely permeable to water, salt, and other hydrophilic low-molecular-weight substances. The molecular weight cut-off of glomerular filtration is 70 kDa, which correlates to albumin [9].

1.1. KIDNEY ANATOMY AND FUNCTION

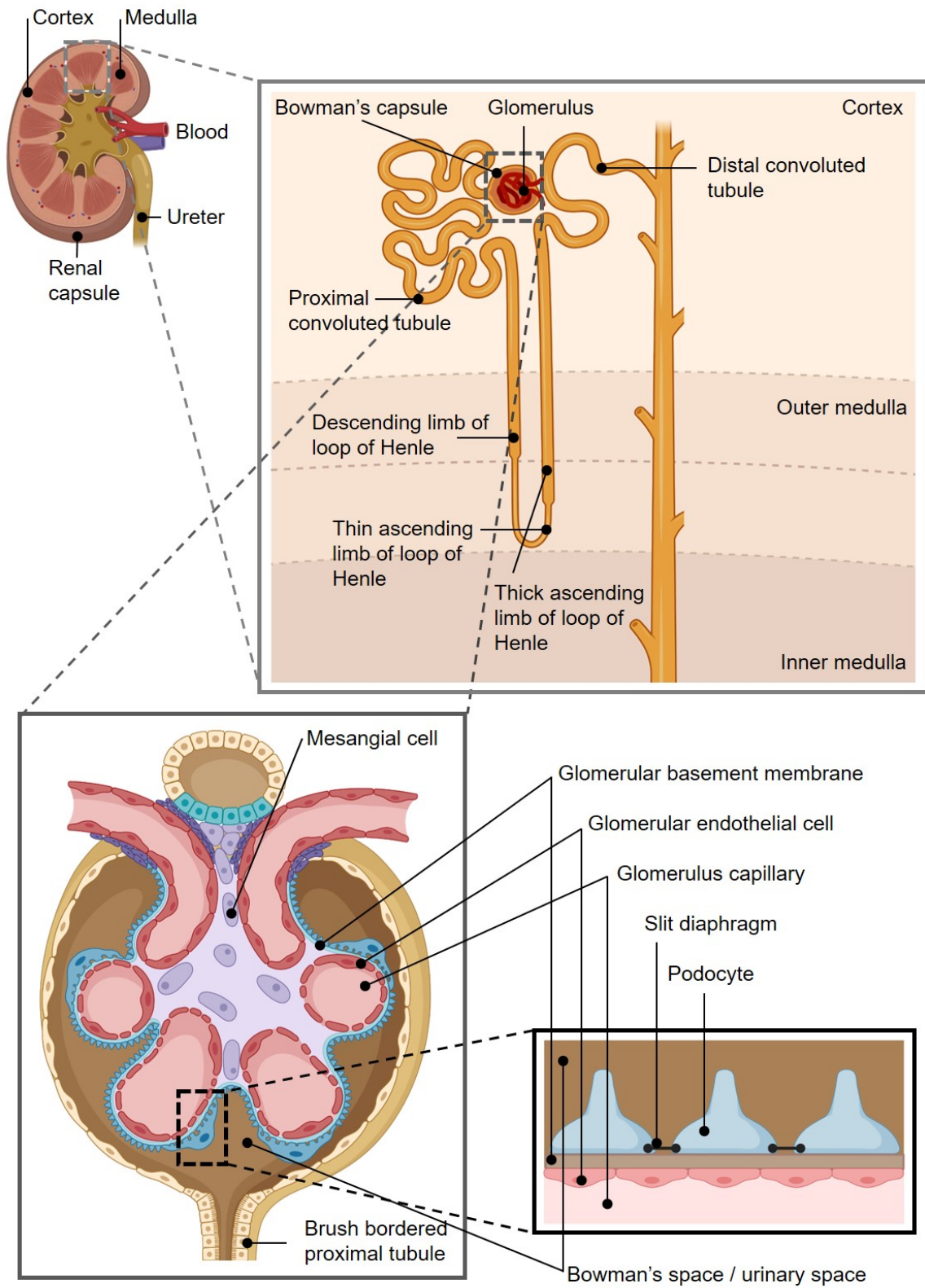


Figure 1.1: Schematic overview of the mammalian kidney anatomy (adapted from [8]).

Blood pressure is the driving force for blood filtration through the GFB into the interior of the Bowman's capsule, which is called the Bowman's or urinary space. From there, the ultrafiltrate is processed into the renal tubular system. This system consists of a proximal convoluted tubule, a proximal straight tubule, a distal straight tubule, a distal convoluted tubule, and the collecting duct. Between the proximal and the distal tubular section, there is a descending and ascending limb called the loop of Henle.

The principal function of the renal tubular system is the recovery of almost 70% of the water, electrolytes, and the active secretion of metabolites and xenobiotics [10]. Motile cilia within the renal tubules facilitate fluid propulsion [11].

First, the ultrafiltrate passes through the proximal convoluted tubules (PCT). Here, essential (filtrated) electrolytes and proteins have to be rescued and xenobiotics excreted. Therefore, the renal epithelial cells of the PCT are equipped with various active and passive tubular excretion and reabsorption transporters. These transporters are either expressed on the apical (urine) or basolateral (blood) side. For salt recovery, the Na^+/K^+ -ATPase and the H^+ -ATPase are directly coupled to ATP hydrolysis and actively exchange NaCl and potassium [10]. In this way, the electrochemical gradient within renal epithelial cells of the PCT is maintained. Various Na^+ -dependent countertransporters and cotransporters benefit from the energy of this gradient, favoring the movement of luminal Na^+ into the cells. For example, owing to the movement of H^+ into the luminal space, HCO_3^- can be reclaimed; this is collectively referred to as renal acidification [10]. Furthermore, glucose is reabsorbed via sodium-independent GLUT or sodium-glucose cotransporter 2 (SGLT2; SLC5A2), which are expressed on the apical side [10]. Other ions and molecules, such as phosphate, citrate, and amino acids, are recovered and exchanged. It should be noted that proximal tubular protein reabsorption is mediated by two receptors, megalin and cubulin. These transporters are located in the brush border of the PCT [12]. They rescue various filtered ligands, medicines, vitamins, and hormones

through an endocytotic reabsorption process [12].

Active blood detoxification from metabolites and xenobiotics is done with the help of energy-dependent transporters belonging to the ATP-binding cassette (ABC) family and solute carriers (SLC). These transporters are not only present in renal epithelial cells but are also expressed in various tissues such as the liver, the intestines, and the brain. They are probably the most important transporters for the absorption, distribution, and excretion of medicines and toxic compounds [13]. For renal drug detoxification, the most relevant transporters within the ABC transporter family are the multidrug resistance protein 1 (MDR1/p-glycoprotein, ABCB1), multidrug resistance-associated protein 2/4 (MRP2/4, ABCC2/4) and the breast cancer resistance protein BCRP (ABCG2) [13]. Moreover, organic cationic and carnitine transporters 1-2 (OCTN1/2, SCL22A4/5) and multidrug and toxin extrusion proteins (MATE1/2, SLC47A1/2) are also present [14]. These are all located on the apical side of the proximal renal epithelial cells [13]. The organic anion transporters 1-3 (OAT1-3, SLC22A66-8) and organic cationic transporter 2 (OCT2, SLC22A2) are on the basolateral side, enabling active reabsorption from the blood into the renal epithelial cells [13]. In Chapter 3.1, a detailed list of examples of (fluorescent) substrates and (non-fluorescent) inhibitors is provided [15].

Compared to the proximal convoluted tubule, with its heavily brushed border, the proximal straight tubule contains fewer microvilli and contributes to the active secretion of xenobiotics and acid-base homeostasis [10].

After essential nutrients and salts are reabsorbed and xenobiotics excreted, water needs to be rescued. Accordingly, a counter-current multiplication system allows the reabsorption of large quantities of filtered water [16]. In this system, the Henle loop encompasses a descending and an ascending limb. Compared to the ascending limb, the thin descending limb of the Henle loop is permeable to water and impermeable to so-

lutes [16]. The thick ascending limb creates a concentration gradient in the medulla of the kidney through a Na^+/K^+ -ATPase, which actively pumps sodium out of the cell [16]. This increases the osmolality of the interstitial fluid from the cortex towards the medulla from 400 to 1200 mOsm/kg [16]. As a result of osmotic forces and the functional expression of aquaporin-1 channels in the descending limb, water is reabsorbed from the ultrafiltrate [16, 17]. In the ascending limb, sodium, potassium, calcium, and magnesium are reabsorbed through transcellular processes [16]. These processes also have an important role in the acid-base homeostasis and ammonia cycle [16].

The following distal tubular section is responsible for the reabsorption of NaCl, magnesium, and calcium [18]. NaCl is rescued by a Na-Cl cotransporter in the apical membrane. A Na^+/K^+ -ATPase subsequently pumps the reabsorbed sodium into the bloodstream. Similarly, the chloride is rescued by a chloride channel located in the basolateral membrane [18]. Magnesium and calcium are transported by defined unilateral transporters [18].

The collecting duct is the last segment of the nephron. Aldosterone and vasopressin (antidiuretic hormones) regulate water and electrolyte balance. Importantly, the collecting duct accounts for only 4 to 5% of the kidney's reabsorption of sodium and 5% of water [19].

Finally, the ultrafiltrate is reduced to one to two liters of urine out of the 180 liters present at the beginning in the PCT. The nephrons reabsorb approximately 178.5 liters of the starting filtrate in a healthy adult every day.

1.2 Nephrotoxicity

Any disturbances of the different physiological mechanisms described in the previous section influence blood pressure, acid-base homeostasis, and electrolyte concentration in the blood. In severe cases, these disturbances can lead to renal impairment and kidney failure. These are usually observed in patients under treatment for diabetes, hypertension, or heart disease, or in patients with genetic predispositions [20]. Drug-induced nephrotoxicity and infection-related renal damage are the most commonly observed causes of renal failure in clinical practice [21, 22].

Drug-induced nephrotoxicity accounts for 20% (66% in older adults) of all episodes that lead to acute kidney failure in hospitals [23]. Treatments involving multiple drugs and intoxications lead to a higher risk of kidney damage. In particular, older patients with comorbidities and complex drug therapies are more susceptible to developing kidney insults [23]. Although toxicity may be reversible, it is often associated with high treatment costs, hospitalization, mental stress and requires a long recovery [23].

Examples and mechanistic insights into how certain drugs can damage the kidneys are described in the following chapter.

1.2.1 Glomerular-related nephrotoxicity

Nephrotoxicity in the kidneys has been observed on the glomerular, tubular, and interstitial levels [24]. The following Table 1.1 lists drugs that cause renal toxicities.

Glomerular-related damage has been seen for medicines that damage the podocytes, the endothelial cells of the glomerulus filtration barrier, and the GBM [24]. Two common drug-induced diseases in the Bowman's capsule are minimal change disease (MCD) and focal segmental glomerulosclerosis (FSGS). MCD is a disease that directly affects the podocytes. The damaged podocytes connect differently to the GBM and therefore lose

their ability to filter the blood [24]. MCD is often characterized in clinics by nephrotic syndrome, including proteinuria, edema, hyperlipidemia, and hypoalbuminemia [25]. Examples of drugs that induce MCD include, amongst others, non-steroidal anti-inflammatory drugs (NSAIDs), lithium, and pamidronate [24].

Similar clinical damage is observed in patients with FSGS, where direct injury to the podocytes is described [26]. However, FSGS is more severe than MCD and can lead to chronic kidney injury [27]. Drugs known to induce FSGS include, for instance, anabolic steroids, lithium, and sirolimus [24].

Direct cell damage to the endothelial cells of the GFB causes a cell injury termed thrombotic microangiopathy [24]. Typically, this disease is associated with the formation of blood clots within the capillaries of the kidney. This results in a reduction in blood flow and organ damage [24]. Clinical manifestations of thrombotic microangiopathy are thrombocytopenia, hypertension, proteinuria, and anemia [24]. Associated drugs include, for instance, gemcitabine, cyclosporine, and clopidogrel [24].

Injury mediated by a strong immune response is described as glomerulonephritis and membranous glomerulopathy. These diseases are usually seen in patients after chronic treatments and are associated with inflammation of the glomeruli caused by autoantibodies [24, 28]. Examples are NSAIDs, captopril, and antibiotics such as ampicillin and penicillin [24].

1.2.2 Tubular-related nephrotoxicity

Renal tubular epithelial cell damage is the most clinical presentation of drug-induced toxicity of the kidney [46]. Nephrotoxins can induce cellular damage that causes cellular degeneration and sloughing from the proximal tubular basement membranes, summarized as acute tubular necrosis [46]. Injuries to the epithelial cells of the kidney tubules lead to direct tubular damage but can also cause a reduction in the glomerular filtration

rate. This has been observed in patients administered aminoglycosides such as gentamicin. Thus, tubular epithelial cell damage leads to an obstruction of the tubular lumen and impairs the glomerular filtration ratio owing to a back leakage of the ultrafiltrate [47].

Tubular damage can lead to morphological changes in renal organs accompanied by necrosis. Of note, analyzing morphological aberrations and investigating mechanisms of toxicity is an essential approach in toxicology. Renal morphological abnormalities are usually studied using renal biopsies from patients. These aberrations of the PCT and glomerulus are seen on two-dimensional histology slides. For instance, gentamicin (aminoglycoside) causes tubular vacuolization, glomerular hypertrophy, and congestion [48]. Atrophic proximal tubules have also been observed in cyclosporin-treated patients and cadmium chloride-intoxicated humans [49, 50].

There are several reasons why proximal tubules are generally vulnerable to various xenobiotics. Mechanistic studies investigating renal toxicity highlight multiple transport processes that enable an accumulation of the drug within renal epithelial cells. Notably, the accumulation of chemicals in these cells is mediated by physiologically relevant transport systems. Examples are OCT/OAT transport and megalin/cubilin-mediated endocytotic reabsorption [12, 14, 51]. Further, functional excretion transporters of the ABC family, including MATE (located on the apical side), play a role in renal toxicity. The pharmacokinetics of substances can be disturbed by, for example, drug-induced downregulations of transporter systems, individuals genetic polymorphisms of the expression of these transporters, and competitive inhibition by drugs [14]. This results in a higher concentration of medicines in the plasma and renal epithelial cell, and favors renal toxicity.

More in-depth mechanistic studies have revealed that mitochondria are often the target organelles of nephrotoxins, causing, among other things, ATP depletion [52]. This im-

pairs the active tubular excretion processes [52]. Mitochondrial damage is well-known for nephrotoxic drugs such as tenofovir, aminoglycosides, cisplatin, and amphotericin B [23]. Impaired mitochondrial function leads, in addition to ATP depletion, to oxidative stress, mitochondrial superoxide formation, and impairment of the mitochondrial membrane potential [48]. Consequently, DNA synthesis is affected, and proinflammatory pathways are activated, leading to tubular injury [53]. Besides mitochondria, certain aminoglycosides also accumulate within lysosomes. This results in the inhibition of the lysosomal enzyme, myelin body formation, and causing lysosomal damage [53].

Another form of renal injury is crystal nephropathy, which is caused by the deposition and precipitation of drugs in, usually, the distal tubules [35]. Crystallization occurs when substances are insoluble in human urine, often caused by transient supersaturation of the urine based on changes in the pH [54]. Fast intravenous administration of drugs such as acyclovir is likely to form crystals [35]. The formation of crystals can cause renal tubular injury owing to the obstruction of urinary flow and interstitial reactions [35]. Examples include antivirals such as acyclovir, indinavir, and antibacterial agents such as ampicillin, ciprofloxacin, and sulfonamides [35].

Table 1.1: List of commonly known medicines that induce nephropathies (adapted from [24])

Mechanisms of Nephrotoxicity	Therapeutic class/Drugs	References
<i>Glomerular-related</i>		
Minimal change disease	NSAIDs, lithium, pamidronate, vaccinations	[23, 28–30]
Focal segmental glomerulosclerosis	Anabolic steroids, heroin, vaccinations, interferons, lithium, pamidronate, sirolimus	[28, 29, 31–33]
Membranous nephropathy	NSAIDs, penicillamine, bucillamine, captopril	[28, 30]
Thrombotic microangiopathy	Gemcitabine, tyrosine kinase inhibitors, cyclosporine, clopidogrel, ticlopidine, quinine, oxymorphone	[23, 28, 30]
Glomerulonephritis	NSAIDs, interferon-alpha, procainamide, ampicillin, penicillin, lithium, pamidronate	[23, 28, 29]
<i>Tubular cell toxicity</i>		
Tubular cell toxicity	Aminoglycosides, amphotericin B, pentamidine, adefovir, cidofovir, tenofovir, cisplatin, iodinated contrast agents	[23, 28, 34]
Crystal nephropathy	Acyclovir, indinavir, foscavir, sulfonamides, ampicillin, ciprofloxacin, methotrexate, ascorbic acid	[23, 28, 35–41]
<i>Interstitial disease</i>		
Acute interstitial nephritis	Sulfonamides, penicillin, cephalosporins, fluoroquinolones, rifampicin, vancomycin, acyclovir, indinavir, NSAIDs, allopurinol, loop diuretics, ranitidine, phenytoin, proton pump inhibitors, checkpoint inhibitors (ipilimumab, nivolumab, pembrolizumab)	[23, 28, 29, 42–45]
Chronic interstitial nephritis	Aspirin, acetaminophen, NSAIDs, cisplatin, lithium, Chinese herbal medicines containing aristocholic acid, cyclosporine, tacrolimus	[23, 28]

1.2.3 Interstitium-related nephrotoxicity

Nephrotoxicity is also observed in the interstitium. The interstitium is the space between the kidney tubules, which consists of fibroblasts and immune cells [24]. Interstitial diseases are usually immune-mediated. Inflammation accompanied by the infiltration of lymphocytes and mononuclear cells within the interstitial space causes acute and, although less likely, chronic interstitial nephritis (AIN/CIN) [24]. Drugs inducing AIN/CIN include sulfonamides, acyclovir, NSAIDs, and proton pump inhibitors [24]. Moreover, infections and autoimmune diseases are common causes of AIN [43]. The clinical appearance of AIN is diverse, but hypersensitivity reactions, allergic responses, and eosinophilia are often seen [24]. The gold standard for confirming AIN is a visual inspection of a renal biopsy [24].

1.3 Using test models to study kidney function and nephrotoxicity

Drug-induced nephrotoxicity can be highly diverse and is a clinical challenge. Drug therapies that affect kidney function must be monitored, replaced, or even stopped, thus limiting the clinical use of certain medicines. Biological test models have been extensively used in the last few decades to verify drug safety and predict undesirable side effects as early as possible in drug development. Various reliable biological test systems have been developed to investigate the renal function and nephrotoxin-induced impairment. In the preclinical phases, there are established *in vitro* (tissue culture), *ex vivo* (organ-isolated tissues from animals), and *in vivo* (living organism) models available. In later-stage clinical trials, biomarkers indicative of nephrotoxicity and others can be collected in the blood and urine of patients and animals to determine organ-specific abnormalities. The following chapters introduce these test models in more detail.

1.3.1 *In vitro* models

There are many kidney-derived cell lines available for cellular *in vitro* nephrotoxicity prediction. These cells allow for toxicological high-throughput screening of different medicines. Noteworthy here is the fact that cells used for *in vitro* screenings are usually cultivated in two dimensions and cannot model an entire organ. Novel approaches use three-dimensional cell culture models that can form spheroids [55], but these are not yet fully established and are not elucidated in detail here.

In vitro experimentation relies on immortal and primary cell types. Primary cells are directly isolated from human or animal tissue. They are, therefore, more expensive, display interdonor variability, are prone to dedifferentiation, lose certain transporter expressions, and cannot be kept in cell culture [55, 56]. Therefore, immortal cell lines

are preferred because they can be kept in a culture and are cheap [56]. Oncogenes (such as E6/E7 or SV40 large T antigen) or telomerase (TERT1) have been incorporated, enabling immortality [57–59]. Table 1.2 presents a list of frequently used cell types and their origin.

1.3. USING TEST MODELS TO STUDY KIDNEY FUNCTION AND NEPHROTOXICITY

Table 1.2: Established cell types to study renal function and nephrotoxicity (adapted from [56])

Cells	Tissue	Species	Tight junctions	Polarization	Transport activity
LLC-RK1 [60, 61]	Proximal tubule epithelia	Rabbit	Yes	Yes	Weak, partially reserved
LLC-PK1 [62, 63]	Proximal tubule epithelia	Pig	Yes	Yes	Partially reserved
VERO [64, 65]	Kidney fibroblast	Monkey	No	No	Different from renal tubular cells
OK [66, 67]	Proximal tubule epithelia	Opossum	Yes	Yes	Partially reserved
MDCK [68, 69]	Distal tubule epithelia	Dog	Yes	Yes	Partially reserved
PCL [70]	Glomerular podocyte	Mouse	No	No	Different from renal tubular cells
HK-2 [57, 66, 71]	Proximal tubule epithelia	Human	Weak	Yes	Partially reserved
hRPTEC [72]	Proximal tubule epithelia	Human	Yes	Yes	Partially reserved
hRPTEC/TERT1 [73]	Proximal tubule epithelia	Human	Yes	Yes	Partially reserved
HEK293 [74]	Human embryonic kidney cells	Human	No	Yes	Partially reserved

Preserving transport and metabolic function in immortal cell lines is challenging. Immortal cell lines keep their basic physiological functional characteristics if the proteins are transduced. TERT1-immortalized renal proximal tubule cells possess the properties closest to proximal tubular cells, such as microvilli, endocytic activity, functional ABC/SLC drug transporters, and tight junctions [55, 75]. HK-2, an immortalized proximal tubule epithelial cell line from a normal adult human kidney, was established to study proximal tubular cell physiology and pathophysiology [57]. Extracted proximal tubular cells become immortal using human papillomavirus E6/E7 genes [57], with functional characteristics such as Na⁺-dependent/phlorizin-sensitive sugar transport and glucose reuptake remaining [57, 76], but the expression and function of drug transporters are limited. No mRNA expression of the SLC22 transporter family (OAT1/3, OCT2), MRP2, and BCRP has been detected [71]. However, the mRNA expression of efflux transporters, such as ABCB1 and several members of the MRP (ABCC) family, has been detected [71]. Furthermore, human embryonic kidney cells (HEK293) represent one of the most used host cells of all human-derived cell lines [74]. These cells are used in toxicology and the production of recombinant therapeutic proteins and vaccines but are less applied in renal physiology [74]. In toxicology, HEK293 is established for the evaluation of several toxic endpoints. This model helps to investigate the drug's effects on cell viability and membrane integrity and to identify toxicity pathways to predict *in vivo* outcomes [74, 77]. To overcome the missing functional drug transporter, ABC/SLC-specific transport DNA plasmid can be transfected into HEK293T cells. This allows for studying a specific drug transport function [78, 79].

Since cells are arranged in a two-dimensional array, functional experiments must be done using a two-compartment system. Cells are cultivated on a permeable transwell format coated with an extracellular matrix [55]. This enables the study of transport from one side to the other. Owing to its simplicity, environmental causes to which kid-

ney tubules are exposed in an *in vivo* setting are lost. For instance, fluid flow across the surface and cell-to-cell signals from other adjacent cell types are missing [55]. As observed in *in vivo* settings, the entire glomerular function cannot be imitated correctly by using a two-dimensional cell format [80]. Additionally, the context of all renal tubular parts interacting in reabsorption and excretion has to be neglected. An example is folic acid, an essential vitamin mainly reabsorbed in distal tubules, but small portions are reported to be rescued in proximal tubules via SLC transporters [81]. To implement more *in vivo* relevant test models that benefit from three-dimensional culture systems with more than one renal cell line present, *ex vivo* models have been established [55].

1.3.2 *Ex vivo* models

More complex (three-dimensional) test models are available to study renal physiology and nephrotoxicity and encompass non-animal and animal tissue methods.

Novel non-animal tissue methods are still experimental, and intensive research is being done to implement them [55, 56]. Examples are specialized kidney cells that can form spheroids, engineered renal tissue arrays, and kidneys on a chip using microfluidic devices [55]. Animal tissues are used for *ex vivo* models such as isolated renal tubules of animals. The use of laboratory animal tissues raises ethical questions, but it is the most common and established model so far [55, 80].

Therefore, the following paragraphs focus on isolated renal tubules of animals.

Ex vivo models are considered to bridge the gap between *in vitro* and *in vivo* models. Besides cutting tissues into slices, investigating their morphological changes, or using them for two-compartment models, there are more reliable strategies for studying processes in the entire organ [80]. For instance, perfusion of isolated organs is established. There are (machine-based) perfusion and non-perfusion strategies available. Perfusion

models imitate continuous *in vivo* similar blood flow and hemodynamics [80]. Isolated perfused kidneys have been established, but only a handful of studies are described [80]. *Ex vivo* models allow for the analysis of, for instance, biliary and renal excretion via ABC/SLC transport systems [82–84]. The drawbacks of these models include complex laboratory skills, low throughput, and tubules are only viable for three to four hours [80].

In terms of handling, a non-perfused renal *ex vivo* model was established around 1995 by Dr. David Miller and Prof. Dr. Gert Fricker at the Mount Desert Island Biological Laboratory (MDIBL) in Maine, United States (US). They used isolated renal tubules from killifish (*Fundulus heteroclitus*) from the vicinity of Maine. The renal tubules of killifish contain almost exclusively proximal tubules but no distal segments [85]. Upon extraction, proximal tubules form a fluid-filled compartment with sealed ends that allows for studying the renal excretion of specific fluorescent ABC/SLC substrates from the incubation media into the luminal compartment. As a result of their impressive work done between 1995 and 2008, Dr. David Miller and Prof. Dr. Gert Fricker could verify functional ABC/SLC transport systems present in the extracted renal tubules of killifish [15, 86]. A detailed list of verified transporter and fluorescent substrates used is provided in Part 3.1 [15].

Furthermore, isolated proximal tubules of killifish allow for the study of transporter regulation and signaling [87, 88]. The effect of toxic compounds on the ABC transporter has been investigated, and the impact on the signaling cascade described [89, 90]. Extracted renal tubules could be used in studies for up to 24 hours in a proper teleost buffer but are usually used within six hours after the extraction.

1.3.3 *In vivo* models

Ex vivo models are reliable, and kidney-specific studies in the entire organ are possible. Nevertheless, in preclinical research, animal experiments using vertebrates such as rabbits, rats, and mice are often required to extrapolate and confirm findings from *in vitro/ex vivo* models. Experiments with animals allow for the study of the effect of an administered drug on the entire organism. Not only can the impact of a medicine on a single organ be studied, but other organs can also be co-investigated. Therefore, *in vivo* experimentation is more complex but needed to extrapolate findings to humans.

The advantages of using animals include collecting more human-relevant data, all side effects in an organism can be assessed, and long-term effects (> 3 days) can be studied. On the other hand, experiments in individuals/animals cause higher experimental variability, are expensive, strict rules and regulations set by law must be respected, and ethical questions about using animals in laboratory settings must be considered. There are many reported experiments using animals to investigate changes in kidney parameters in the urine and blood (biomarkers) as well as the histological examination of kidney biopsies after intoxication [91–94].

Nevertheless, mechanistic studies are challenging to perform in living animals owing to their complexity. Translational *in vivo* models that can bridge the gap between *in vitro/ex vivo* models and animals/human beings are beneficial. Thus, *in vivo* vertebrate models may be used for screening studies and can therefore foster the reduction, replacement, and refinement of animal experiments (3R principles).

1.4 Zebrafish larvae as a vertebrate model

In biomedical sciences, the use of two- to five-day-old zebrafish larvae as a vertebrate model for *in vivo* studies has become popular over the last decade. Zebrafish (*Danio rerio*) are tropical freshwater teleosts originating in the Ganges River (India) and northern India [95]. Zebrafish development is a fast process whereby embryogenesis lasts only two days [96]. From the second day, a functional bloodstream with an intact heart and circulating erythrocytes is visible in the transparent zebrafish.

Since the genome of the zebrafish has been fully sequenced and is easy to manipulate, they are widely used in genetic and vertebrate development studies [97]. In most countries, zebrafish larvae do not count as animals up to 120 hours post-fertilization [98]. This is justified because zebrafish are not considered to experience pain within this development time frame [99]. Therefore, zebrafish larvae have emerged in broader applications as excellent models for studying inflammation, pharmacology, toxicology, and organ diseases [100–102]. For pharmacological and toxicological studies, the incubation of zebrafish larvae in drug solutions or intravenous injection into the bloodstream enables a defined administration. Research, such as determining LD₅₀ values, behavioral studies, or organ-specific toxicity, can be done [103–105]. The generation of mutants, transgenic lines expressing fluorescent proteins in specific cell types, and the targeted knockdown of genes allow for the broad application of zebrafish [97].

1.4.1 Zebrafish larvae as a vertebrate model for nanomedicines

Using zebrafish larvae to extrapolate mechanistic studies from *in vitro* to *in vivo* has recently been shown in our research group to be possible for nanomedicines [106]. Zebrafish larvae were established as a screening model to evaluate the circulation behavior of intravenously injected lipid-based nanomedicine formulations [98]. Furthermore, the interactions of lipid nanoparticles with macrophages and mammalian liver sinu-

soidal endothelial cells (stabilin-2) can be studied [107, 108]. Comparative experiments with rodents verified similar pharmacokinetic characteristics of the nanomedicine formulations used. Zebrafish larvae, as an early-stage *in vivo* model, help to predict the performance of nanomedicines in higher animals by the pre-selection of promising nanomedicine formulations and thus facilitate the formulation and development process [98].

1.4.2 Zebrafish larvae as a vertebrate model for renal function and nephrotoxicity

Since zebrafish are aquatic organisms, kidney function in the early development stages is considered to be present to maintain osmoregulation. Genetic screenings have detected the expression of various genes in renal epithelial cells that are similar to human beings and have similarities in kidney anatomy [109, 110] (Figure 1.2)

The question arises if and how zebrafish larvae can be used as a translational *in vivo* vertebrate model to study renal function and the mechanism of nephrotoxicity.

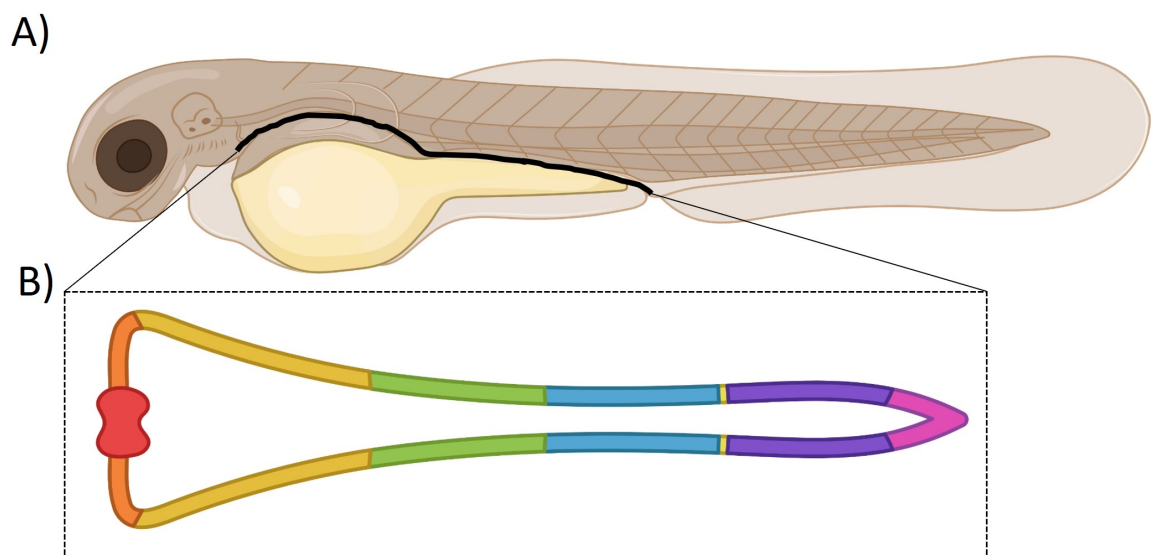


Figure 1.2: **(A)** Schematic image of a 3-day-old zebrafish larvae. The black line indicates the pronephros from a lateral point of view. **(B)** The pronephros from a ventral point of view. Depicted are the glomerulus (red), the neck (orange), the proximal convoluted tubule (yellow), the proximal straight tubule (green), the early distal tubule (blue), the late distal tubule (violet), and the cloaca (purple) (adapted from [15, 109]).

AIM

The aim of the present thesis was to establish zebrafish larvae as an early-stage *in vitro/in vivo* bridging model that can reduce, refine, and replace certain animal experiments with a focus on renal function and medicine-induced nephrotoxicity. Furthermore, zebrafish can be applied to extended studies assessing the *in vivo* pharmacokinetics of nanoparticles. To this end, the following four work packages (**Part I-IV**) were defined.

(I) The study of the renal function of zebrafish larvae

- (i) Key renal functions were verified to establish zebrafish larvae as an *in vivo* model.
- (ii) The results and the zebrafish model were compared to the killifish model.

(II) Nephrotoxins-induced morphological changes

The impact of gentamicin, a model nephrotoxin, on the morphology of the renal organ was analyzed. Methodologies such as fluorescent-based laser scanning microscopy and X-ray-based computer tomography in micrometer size were applied.

The results were extrapolated to kidney biopsies of gentamicin-treated mice to confirm the predictability of the zebrafish model.

(III) Mechanistic studies of nephrotoxin-induced kidney damage

Mechanistic insights into the toxicity of nephrotoxins using the zebrafish model and isolated renal tubules of killifish.

(IV) *In vivo* assessment of novel drug carriers in zebrafish larvae

In view of the usefulness and high predictability of the zebrafish model, it was applied to study the pharmacokinetics of novel nanoparticles.

3.1 Part I: The study of renal function

Zebrafish (*Danio rerio*) larva as an *in vivo* vertebrate model to study renal function

Jan Stephan Bolten, Anna Pratsinis, Claudio Luca Alter, Gert Fricker, Jörg Huwyler

Am J Physiol Renal Physiol. 2022 Mar 1;322(3):F280-F294.

doi: 10.1152/ajprenal.00375.2021.

Personal contribution:

My contribution to this research article includes the planning, design, and execution of scientific experiments and analysis. I established imaging and experimental protocols.

Thus, I created all figures and tables and wrote the manuscript.

RESEARCH ARTICLE

Zebrafish (*Danio rerio*) larva as an in vivo vertebrate model to study renal function

Jan Stephan Bolten,¹ Anna Pratsinis,¹ Claudio Luca Alter,¹ Gert Fricker,^{2,3} and Jörg Huwyl^{1,3}

¹Department of Pharmaceutical Sciences, University of Basel, Basel, Switzerland; ²Institute of Pharmacy and Molecular Biotechnology, University of Heidelberg, Heidelberg, Germany; and ³Mount Desert Island Biological Laboratory, Salsbury Cove, Bar Harbor Maine

Abstract

There is an increasing interest in using zebrafish (*Danio rerio*) larva as a vertebrate screening model to study drug disposition. As the pronephric kidney of zebrafish larvae shares high similarity with the anatomy of nephrons in higher vertebrates including humans, we explored in this study whether 3- to 4-day-old zebrafish larvae have a fully functional pronephron. Intravenous injection of fluorescent polyethylene glycol and dextran derivatives of different molecular weight revealed a cutoff of 4.4–7.6 nm in hydrodynamic diameter for passive glomerular filtration, which is in agreement with corresponding values in rodents and humans. Distal tubular reabsorption of a FITC-folate conjugate, covalently modified with PEG₂₀₀₀, via folate receptor 1 was shown. Transport experiments of fluorescent substrates were assessed in the presence and absence of specific inhibitors in the blood systems. Thereby, functional expression in the proximal tubule of organic anion transporter oat (slc22) multidrug resistance-associated protein mrp1 (abcc1), mrp2 (abcc2), mrp4 (abcc4), and zebrafish larva p-glycoprotein analog abcb4 was shown. In addition, nonrenal clearance of fluorescent substrates and plasma protein binding characteristics were assessed in vivo. The results of transporter experiments were confirmed by extrapolation to ex vivo experiments in killifish (*Fundulus heteroclitus*) proximal kidney tubules. We conclude that the zebrafish larva has a fully functional pronephron at 96 h postfertilization and is therefore an attractive translational vertebrate screening model to bridge the gap between cell culture-based test systems and pharmacokinetic experiments in higher vertebrates.

NEW & NOTEWORTHY The study of renal function remains a challenge. In vitro cell-based assays are approved to study, e.g., ABC/SLC-mediated drug transport but do not cover other renal functions such as glomerular filtration. Here, in vivo studies combined with in vitro assays are needed, which are time consuming and expensive. In view of these limitations, our proof-of-concept study demonstrates that the zebrafish larva is a translational in vivo test model that allows for mechanistic investigations to study renal function.

drug transporter; glomerular filtration; kidney tubule; renal function; zebrafish

INTRODUCTION

The kidney is an important excretory organ. The functional unit of the human kidney is the nephron, where blood enters the glomerulus and is passively filtered. The ultrafiltrate is processed within the proximal convoluted tubule (PCT). Here, small molecules such as salts, water, glucose, citrate, and amino acids are exchanged or recovered to sustain homeostasis. Besides this, epithelial cells of the PCT are equipped with energy-dependent transporters, enabling the active secretion of xenobiotics into the tubular lumen. These drug transporters belong to the superfamilies of ATP-binding cassette (ABC) transporters and solute carriers (SLC), which are either apically or basolaterally expressed (1). Examples include organic anion transporters OAT1–3 (SLC22A66–8) for basolaterally expressed transporters and multidrug resistance gene

MDR1/P-glycoprotein (ABCB1), multidrug resistance protein MRP2/4 (ABCC2/4), and breast cancer resistance protein BCRP (ABCG2) for apically expressed transporters (2). Further downstream within the tubules, Na⁺ and K⁺ are processed and vitamins such as folate (FA) are reabsorbed by endocytotic receptor-mediated transport processes (3, 4).

Aquatic animals such as teleosts have highly conserved kidney structures, which are homologous to human. This is not surprising since 70% of protein coding genes of zebrafish have a related counterpart in humans (5). With respect to kidney transporters, ABC-like transporters are phylogenetically conserved in teleosts and higher vertebrates (2). For example, mRNA expression of human homolog renal secretion and reabsorption transporters abcc1, abcc2, and FA receptor 1 (folr1) between 24 and 120 h postfertilization (hpf) was



Correspondence: J. Huwyl (joerg.huwyl@unibas.ch).
 Submitted 12 October 2021 / Revised 7 January 2022 / Accepted 7 January 2022



detected in various organs of zebrafish larvae (ZFL), including proximal tubule parts (3, 6–8). Furthermore, *abcb4* mRNA expression (a homolog of the human MDR1-like transporter) has been previously described (9). This transporter is involved in the secretion of lipophilic and uncharged xenobiotics. Na^+/K^+ -ATPase is highly expressed in proximal tubules of zebrafish (*Danio rerio*) and other teleosts, e.g., killifish (*Fundulus heteroclitus*) (2, 10).

The *in vivo* study of renal function remains a challenge. Such studies are time consuming and expensive and often rely on *in vivo* experimentation with higher vertebrates. They are often combined with *in vitro* or *ex vivo* transporter assays to provide mechanistic insights at a cellular level. The latter models are reliable and provide a high throughput, but a translation to the *in vivo* situation remains cumbersome (11). In view of these limitations, there is a high unmet need for cost-effective *in vivo* test systems, which should provide a decent throughput and can be used to bridge the gap between *in vitro* cell-based assays and *in vivo* animal experiments in higher vertebrates, including humans. To this end, freshly isolated proximal tubules from killifish can be surgically extracted. They form fully functional sealed tubules when placed in culture media (12, 13). By incubating them with a fluorescent transporter substrate in the presence or absence of specific inhibitors, luminal-directed transport of the fluorescent substrate can be visualized *ex vivo* by confocal microscopy.

Since this *ex vivo* model does not respect all relevant kidney functions and aspects of a living organism, *in vivo* vertebrate models are desired. ZFL can be used for this purpose. They are transparent, undergo fast embryogenesis in that they already hatch by 3 days postfertilization (dpf), are easy to handle, and are therefore frequently used for toxicological, pharmacological, and developmental studies (14). Recent studies have demonstrated that ZFL between 2 and 4 dpf can be used to study the systemic circulation and extravasation of intravenously administered drug formulations (15, 16). These results could be extrapolated to higher vertebrates (i.e., rodents) and establish ZFL as a promising screening model for nanomedicines (17).

Therefore, the aim of this work was to implement ZFL as a translational *in vivo* vertebrate screening model to study renal function. In contrast to the established *ex vivo* killifish model mentioned above, the zebrafish model is expected to cover not only proximal tubular secretion but also glomerular filtration and distal tubular reuptake. These processes were studied in this work using fluorescent model compounds including polymers of different molecular weight and substrates of specific transporters in combination with their corresponding inhibitors. Fluorescent test compound distribution within the pronephros and blood system was assessed by confocal microscopy in living ZFL, using recombinant zebrafish lines expressing the fluorescent proteins enhanced green fluorescent protein (eGFP) or mCherry in the endothelium or glomerulus/proximal tubular cells. Finally, tubular secretion of fluorescent substrates was evaluated *ex vivo* in killifish to compare our results to a well-established tubular secretion model.

MATERIALS AND METHODS

Materials

Sulforhodamine 101 (Sulfo101) was purchased from Chemodex (St. Gallen, Switzerland), 8-(2-[fluoresceinyl]aminoethylthio)adenosine-3',5'-cyclic monophosphate (8-fluocAMP) was purchased from Biolog Life Science (Bremen, Germany), a fluorescent cyclosporine A derivative [*N*-ε-(4-nitrobenzofurazan-7-yl)-D-Lys⁸]cyclosporine A (NBD-Csa) was synthesized as previously described (18), FA-polyethylene glycol PEG-2kDa-FITC was purchased from Biochempeg (Watertown, MA), and NHS-PEG₅-Mal and NHS-PEG₄₀-Mal were obtained from NOF (Tokyo, Japan). SAMSAs fluorescein and NHS-TRITC were purchased from Thermo Fisher Scientific (Waltham, MA). Agarose, probenecid, erythromycin, verapamil hydrochloride, *p*-aminohippuric acid, MK-571 sodium salt hydrate, zosuquidar hydrochloride, saquinavir, indinavir sulfate salt hydrate, folic acid, fluorescein sodium salt (Fluo), FITC-dextran (40, 70, or 150 kDa), 1-phenyl-2-thiourea (PTU), and ethyl-3-aminobenzoate methanesulfonate (MS-222, tricaine) were purchased from Sigma-Aldrich (Buchs, Switzerland).

Ethical Approval

All animal experiments were carried out in accordance with local animal welfare regulations.

Log_{D7.4} Prediction

The log_{D7.4} of test compounds was predicted using the Partitioning PlugIn of Marvin Sketch 20.19.0 software (ChemAxon Europe, Budapest, Hungary).

Fluorescent Labeling of PEG₅ and PEG₄₀

Coupling of SAMSAs fluorescein was performed according to the manufacturer's instructions. In brief, SAMSAs fluorescein was incubated in 100 mM NaOH for 10 min before being added to NHS-PEG₅ or NHS-PEG₄₀-Mal at a two- to threefold excess in 100 mM NaPi, 150 mM NaCl, and 5 mM EDTA (pH 7.2). The SAMSAs fluorescein PEG mixtures were left to react overnight at room temperature, before purification by gel filtration (Sephadex G50 fine), as previously described (19). Collected fractions were pooled and concentrated using 3-kDa cutoff Amicon filter device (Merck Millipore, Burlington, MA).

Fluorescence Correlation Spectroscopy

The hydrodynamic diameter (D_H) of fluorescent-labeled polymers [i.e., FITC-dextran (40, 70, or 150 kDa) and FITC-PEG (5 and 40 kDa)] was determined by fluorescence correlation spectroscopy. An Olympus IX73 inverted microscope (Olympus, Tokyo, Japan) using an immersion Super Apochromat objective (1.2 numerical aperture, ×60, UplanSApo, Olympus) was used to perform the measurements. Emitted photons were filtered with a bandpass filter (512 nm) before detection with a single-photon avalanche diode (SPCM CD3516H, Excelitas). The free dye Atto 488 carboxylic acid ($D = 400 \mu\text{m}^2/\text{s}^2$ at 298 K, Thermo Fisher Scientific) was dissolved at a concentration of 10

nM in double distilled water and used to calibrate the confocal volume of the excitation channel at 481 nm. Intensity fluctuations were recorded over 60 s. The experimental autocorrelation curves of the calibration dye Atto 488 and the fluorophore coupled samples were fitted with a one-component triplet state model, as previously described (20). Data were processed using PicoQuant Software (Berlin, Germany).

Intravenous Injections and Imaging of ZFL

Animal experiments and husbandry were carried out in accordance with Swiss animal welfare regulations. Regarding the terminology of zebrafish, we followed the life stage definitions established by Kimmel et al. (21), who defined >72 hpf old zebrafish as “larvae.” Eggs from adult zebrafish (Table 1) were collected from different parents at 0.5–1 hpf and kept at 28°C in zebrafish culture media (25).

The number of larvae in a 25-mL dish did not exceed 100. The formation of pigment cells was suppressed by adding 30 µg/mL PTU to the media. Then, 72 and 96 hpf hatched ZFL were embedded in 0.3% agar containing PTU and tricaine (0.01%). Experiments were carried out at room temperature. Randomly chosen larvae were injected with a calibrated volume of 1–2 nL of 0.1–2 mM stock solutions of test compounds into the cardinal vein (CV) above the heart. Embryos were obtained from the mating of six male and six female adult zebrafish and were randomly assigned to the treatment groups. Water-soluble substances were dissolved in PBS. Lipophilic substances such as NBD-CsA, erythromycin, and probenecid were administered in an up to 15% (vol/vol) DMSO-PBS solution by injection of 2×1 nL with a delay of 30 s between injections. FA-PEG₂₀₀₀-FITC was dissolved in Tris buffer (pH 9.3). Chemically reactive compounds (i.e., Sulfo101) were incubated for 2.5 h in FCS (BioConcept Amimed, Allschwil, Switzerland) to neutralize reactive moieties followed by a short centrifugation before injection. For intravenous injections, a micromanipulator (Wagner Instrumentenbau, Schöffengrund, Germany), a pneumatic Pico Pump PV830 (World Precision Instruments, Sarasota, FL), and a Leica SAPO microscope (Leica, Wetzlar, Germany) were used. Tail regions were imaged 0.5–9 h postinjection (hpi) using an Olympus FV3000 confocal laser scanning microscope equipped with a $\times 20$ UPlabSApo (numerical aperture of 0.75) objective and a $\times 30$ UPlabSApo (numerical aperture of 1.05) objective. Confocal images were acquired using a sequential line scan, excitation wavelengths of 488 and 561 nm (argon laser), and emission wavelengths of 500–540 and 570–620 nm, respectively. Of note, no signal cross talk was detected between the different channels.

To reduce intraexperimental variability, comparative experiments were performed during the same day by the same operator and using the same stage. Droplet size consistency (sample volume) was permanently checked using a reticle mounted on the eyepiece of a Leica SAPO binocular to ensure that the same volume of compound was injected throughout the course of the experiment. Reproducibility was verified by repeating series of experiments on at least three different days. For each condition of each series of experiments at least five zebrafish larvae were used ($n = 5$). For the preparation of figures and the corresponding quantitative analysis, data from one representative series of experiments were used.

Signal Intensity Quantification and Postprocessing of Images

Obtained confocal microscopy images were analyzed and edited using OMERO software 5.4.10 (<https://www.openmicroscopy.org/omero/>) as an image processing program. Quantitative signal intensities in distinct organs were evaluated using Fiji software 2.1.0/1.53c (<https://imagej.net/software/fiji/>) and were done as follows: for drug transport experiments (i.e., tubular secretion and endocytosis), zebrafish lines were used, which express a fluorescent marker (i.e., kdrl:eGFP or kdrl:mCherry or wt1b:eGFP) in vascular endothelia or renal epithelia. This allowed for a localization of fluorescent-labeled compounds within a defined three-dimensional anatomic structure such as the dorsal artery (DA) or kidney tubule. Signals were quantified by measuring mean signal intensities within this selected region of interest. Untreated controls and all corresponding treatment groups were analyzed using the same laser and microscopy settings, which allowed for a direct comparison of treatment groups. Alternatively (Figs. 2 and 7), regions of interest were selected based on bright-field microscopy images. Analysis of the DA was used to quantify signals of circulating fluorophores within the blood compartment. Quantification of signal intensities was based on maximum intensity projections. Signal intensities are presented as fold changes normalized to the mean of the (experimental) control.

Killifish and Tissue Preparation

Killifish (*F. heteroclitus*) proximal kidney tubules were isolated and prepared as previously described (12). In brief, killifish were purchased from local fishermen in the vicinity of Mount Desert Island, ME and maintained at the Mount Desert Biological Laboratory in tanks with natural flowing, aerated sea water. Since no sex-related differences were observed, extracted tubules from at least six randomly

Table 1. Transgenic zebrafish lines with the corresponding promoter coupled to either eGFP or mCherry indicating which organ is fluorescently marked

Transgenic Line	Characteristics	Reference	Source
AB/Tübingen	Wild-type		Prof. Dr. Affolter, Basel, Switzerland
Tg(wt1b:eGFP)	Glomerulus and proximal convoluted tubule GFP marker	(22)	Prof. Dr. Schiffer, Erlangen, Germany
Tg(kdrl:eGFP)	Endothelium GFP marker	(23)	Prof. Dr. Affolter, Basel, Switzerland
Tg(kdrl:mcherry-CAAX)	Endothelium mCherry marker	(24)	Prof. Dr. Affolter, Basel, Switzerland

Shown is an overview of the transgenic lines. eGFP, enhanced green fluorescent protein.

3.1. PART I: THE STUDY OF RENAL FUNCTION

chosen killifish were incubated in enriched marine teleost buffer (140 mM NaCl, 2.5 mM KCl, 1.5 mM CaCl₂, 1 mM MgCl₂, and 20 mM Tris) containing 1 μM of the indicated fluorescent substrate in the presence or absence of a 10- to 20-fold excess of a nonfluorescent inhibitor. Incubations were carried out at 8°C. Tubular accumulation of fluorescence signals was monitored using an Olympus FV1000 inverted confocal laser scanning microscope (×20, PlanFluo Dry, numerical aperture 0.5). Signal intensities were quantified using image capture and analysis software (NIH Image 1.61, <https://imagej.nih.gov/>).

Statistical Analysis

Statistical analysis was performed with GraphPad Prism v. 8.0.2 (GraphPad Software, San Diego, CA) using unpaired two-tailed *t* test analysis for direct comparisons. Where appropriate, individual data points are presented as dot plots next to the average and SD for the group.

RESULTS

The pronephros of ZFL consists of two nephrons that are combined at the larva's midline just ventral to the dorsal aorta (26). For a better anatomic visualization of the pronephros, genetically modified tg(wt1b:eGFP) ZFL, expressing eGFP in epithelial cells of the PCT and glomerulus, were used. In Fig. 1A, a confocal image of this triangle-shaped

organ can be seen in a lateral and ventral projection. Figure 1B shows a schematic representation of three distinct sections of the ZFL pronephros indicating the three main kidney processes, passive glomerular filtration, active proximal tubular excretion, and active distal tubular reabsorption. Examples of the transport proteins of interest are provided, and their expression at defined membrane domains (basolateral or luminal) of epithelial cells is shown. Thus, the used fluorescent model compounds including polymers of different molecular weight and substrates of specific transporters in combination with their corresponding inhibitors are illustrated.

In a first step, glomerular filtration was investigated. This includes the evaluation of the presence of an adequate barrier to sieve molecules based on their physicochemical properties (e.g., size), whether a molecular weight cutoff can be established, and how this relates to values obtained from literature for higher vertebrates. The glomerular filtration molecular weight cutoff in the 96-hpf wild-type ZFL was determined using fluorescent dextran and PEG conjugates. FITC-DX was commercially available; larger molecular weight PEG was instead coupled to SAMSA fluorescein in house. The *D_H* and purity of these polymers were measured using fluorescence correlation spectroscopy. We obtained a diffusion coefficient of 125 and 48 μm²/s for FITC-PEG₅ and FITC-PEG₄₀ samples, respectively. This corresponds to a *D_H* of 3.7 and 9.7 nm (Fig. 2A). For FITC-DX₄₀ and FITC-DX₇₀, diffusion coeffi-

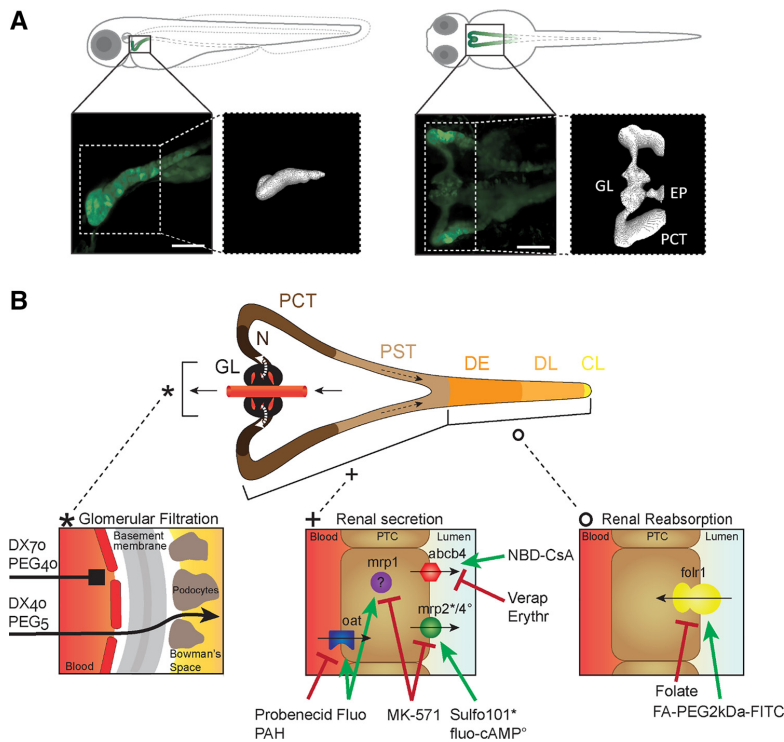
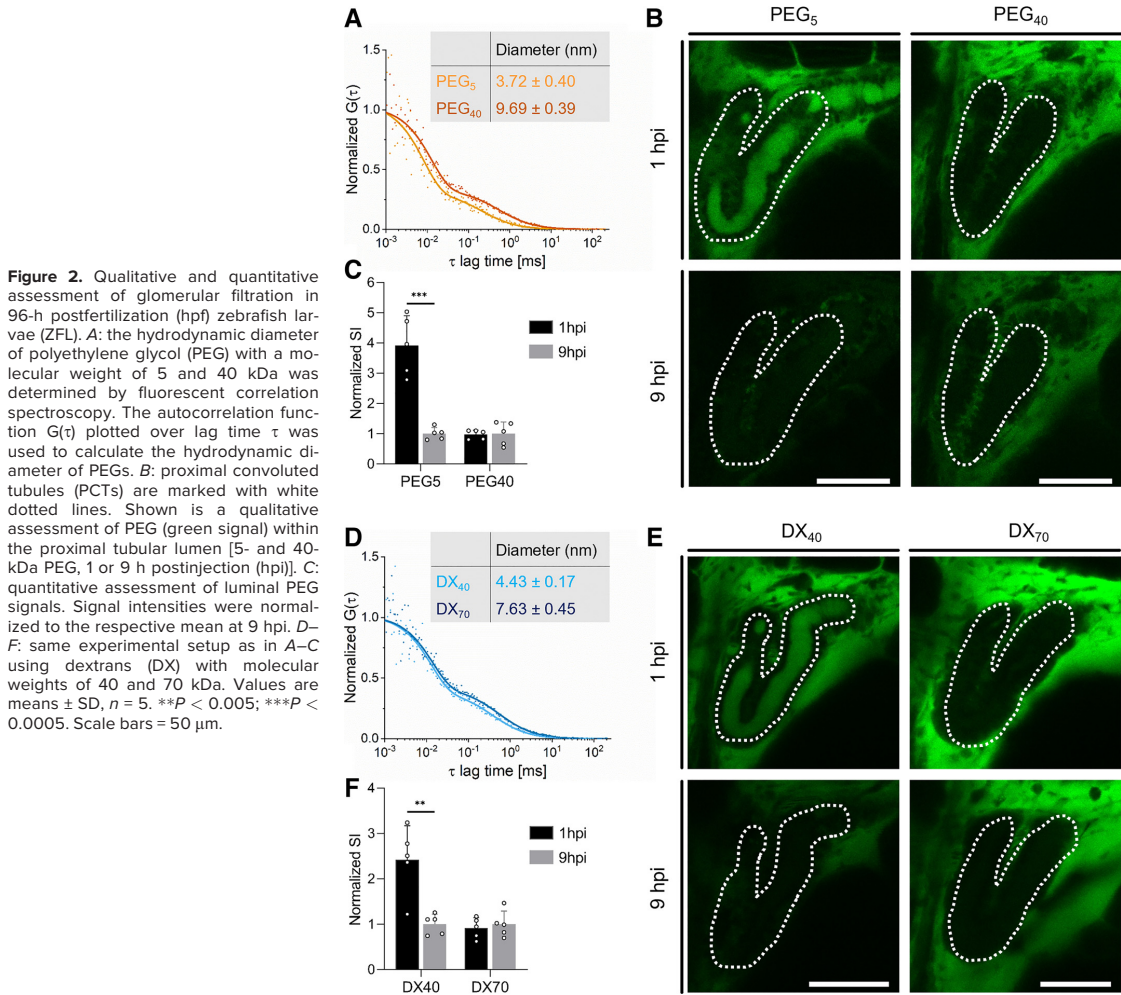


Figure 1. Anatomic localization of the pronephros in a 72-h postfertilization (hpf) zebrafish larva (ZFL) and schematic representation of its functional units. **A:** lateral and ventral projection of a 72-hpf tg(wt1b:eGFP) ZFL expressing enhanced green fluorescent protein (eGFP) mainly in the proximal convoluted tubule (PCT) and glomerulus (GL). A faint signal was also present in the exocrine pancreas (EP). A three-dimensional projection of the pronephros is shown. Scale bars = 50 μm. **B:** the pronephros consists of two nephrons with a fused GL, neck (N), PCT, proximal straight tubule (PST), distal early (DE), late distal (DL), and collecting duct and cloaca (CL). Renal function encompasses glomerular filtration (*left*), renal secretion (*middle*), and renal reabsorption (*right*). Transporters are listed together with their substrates (green label) and inhibitors (red label) used in this study. abcb4, zebrafish homolog of human MDR1; DX, dextran; Erythr, erythromycin; FA, folate; Flu, fluorescein sodium salt; folr1, folate receptor 1; mrp, multidrug resistance-associated protein; NBD-CsA, NBD-labeled cyclosporin A; oat, organic anion transporter; PAH, *p*-aminohippurate; PEG, polyethylene glycol; PTC, proximal tubule cell; Sulfo101, sulforhodamine 101; Verap, verapamil hydrochloride.



clients of $D = 105$ and $61 \mu\text{m}^2/\text{s}$ translate to a $D_H = 4.4$ and 7.6 nm, respectively (Fig. 2D). Their glomerular filtration *in vivo*, assessed by detection of cleared substances in the lumen of the PCT, was determined at 1 and 9 hpi by confocal microscopy. A representative confocal image of the pronephros is shown in Fig. 2, B and E. For quantitative analysis, the luminal signals were each normalized to 9 hpi and are shown in Fig. 2, C and F. Qualitative as well as quantitative analysis revealed the accumulation of small-molecular weight PEG and dextran within the proximal tubular lumen, being indicative of glomerular filtration, whereas high-molecular weight polymers were not filtered. The cutoff of glomerular filtration in ZFL corresponds to a D_H of the polymers between 4.4 nm and 7.6 nm. The D_H for 40-kDa PEG is significantly higher than

similar 40-kDa dextran polymers, indicating that not the molecular weight but the D_H determines the cutoff of glomerular filtration.

Next, distal tubular reuptake of FA by the folr1 homolog transporter was investigated using a fluorescent labeled derivative of FA, i.e., FA-PEG₂₀₀₀-FITC (Fig. 3A). The purity and D_H of the fluorescent polymer were characterized using fluorescence correlation spectroscopy. The D_H of the FA-PEG₂₀₀₀-FITC conjugate was 1.08 ± 0.57 nm. The filtered fluorescent FA-PEG polymer appeared in the lumen of the distal tubule 5 min after injection of a high concentration (1 nL of a 2 mM solution). These high concentrations were necessary to allow for detection in the patent luminal space of the distal tubule. To assess FA-mediated tubular reabsorption, a 100-fold molar excess of native FA as a specific inhibitor was

3.1. PART I: THE STUDY OF RENAL FUNCTION

KIDNEY FUNCTION IN ZEBRAFISH LARVAE

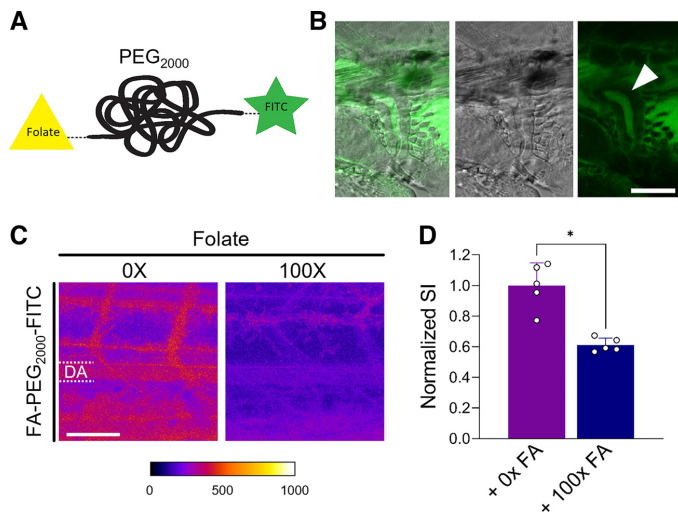


Figure 3. Reabsorption of folate (FA) in the distal tubule. **A:** FA receptor 1 (*folr1*)-mediated distal tubular reabsorption was studied using a FA conjugate covalently modified with polyethylene glycol (PEG; molecular weight: 2,000 Da) and the fluorescent dye FITC. **B:** accumulation of in the lumen of the distal tubule 5 min postinjection of a 72-hpf zebrafish larva (ZFL). Scale bar = 30 μ m. **C:** confocal microscopy image of the tail region of a 72-hpf ZFL 1 h after intravenous injection of a fluorescent-labeled FA-PEG₂₀₀₀-FITC derivative in the presence and absence of a 100-fold excess of native FA (100 \times FA). **D:** quantitative evaluation of the dorsal artery (DA) in C. Signal intensities (SI) were normalized to the mean of the control (no inhibitor, 0 \times FA). Values are means \pm SD; $n = 5$. * $P < 0.0001$. Scale bar = 50 μ m.

preinjected 10 min before administration of 1 nL of 0.1 mM FA-PEG₂₀₀₀-FITC. Intensity within the DA was assessed 1 hpi to evaluate the extent of reabsorption from the tubular lumen back into the bloodstream. A representative confocal image is shown in Fig. 3C, left, demonstrating higher signal intensities (red > blue) in the DA compared with FA-preinjected ZFL. This is indicative of continuous tubular reuptake of FA-PEG₂₀₀₀-FITC in ZFL. This reuptake is reduced by a factor of 2 in the presence of an excess of native FA, which indicates competitive tubular reabsorption via *folr1* (Fig. 3D, right).

Proximal tubular secretion was investigated based on specific clearance of fluorescent labeled transporter substrates from the bloodstream. The transport substrate/inhibitor pairs selected for this study were selected based on a comprehensive review of the existing literature. Table 2 thus shows information on the ABC- and SLC-transporter specificity of fluorescent substrates and nonfluorescent inhibitors in different teleost species and their tissue-specific expression patterns. The specificity of fluorescent substrates and nonfluorescent inhibitor is shown in Table 2.

To evaluate tubular secretion, 72–80 hpf *tg(kdrl:eGFP/mCherry-CAAX)* ZFL were preinjected and incubated with a specific inhibitor (e.g., 10 min except for 1 h for verapamil) followed by the injection of a fluorescently labeled substrate. One hour postinjection, the tail region was imaged and signal intensity within the DA was compared with ZFL that were not preinjected with the corresponding inhibitor. Starting with apically located transporters, the functionality of *mrp2* (*abcc2*) was assessed using Sulfo101 (or Texas red) as a fluorescent substrate and MK-571 as an inhibitor. Inhibitor concentration-dependent inhibition of *mrp2* by MK-571 resulted in reduced renal secretion and thus enhanced retention in the bloodstream (Fig. 4A). Quantitative analysis of the fluorescent signal within the DA revealed a three- to fourfold increase in plasma concentrations compared with control (i.e., absence of MK-

571). Of note, in these experiments, an increase in Sulfo101 secretion was associated with the appearance of a fluorescent signal in the yolk next to the cloaca. This could be indicative of local reabsorption of excreted Sulfo101. As expected, inhibitors of the basolaterally expressed SLC *oat* (*slc22*), i.e., probenecid and *p*-aminohippurate, did not interfere with transport of the *mrp2* substrate Sulfo101 (Fig. 4B). Likewise, transport of the *mrp4* (*abcc4*) substrate fluo-cAMP was inhibited by MK-571 but not by probenecid and *p*-aminohippurate, leading to an up to 5.5-fold increase in plasma concentrations (Fig. 4C). Transport of Fluo, a substrate of both ABC transporter *mrp1* and SLC *oat* (*slc22*), was sensitive to inhibition by MK-571, probenecid, and *p*-aminohippurate (Fig. 4D). NBD-CsA, a substrate of the P-glycoprotein analog *abcb4* in ZFL, showed a statistically significant sensitivity toward typical inhibitors of human P-glycoprotein (ABCBI), namely, verapamil and erythromycin (Fig. 4E).

Analysis of the ZFL vasculature after injection of fluorescent labeled substrates of proximal tubule transporters revealed in some instances a punctuated staining pattern at the level of the dorsal CV (Figs. 4A and 5, A and B). Experiments in a transgenic fish line expressing mCherry in endothelial cells [*tg(kdrl:mCherry-CAAX)*] revealed colocalization of NBD-CsA with endothelial cells 1 hpi (Fig. 5A). Such signals were not observed in ZFL preinjected with dextran sulfate, a stabilin scavenger receptor inhibitor (Fig. 5B) (15). The same was also observed for Sulfo101 but not for fluo-cAMP. Quantitative analysis of signal intensity ratios between the CV and DA revealed a 1.5- to 2.5-fold increased accumulation at the level of the CV of Sulfo101 and NBD-CsA (Fig. 5C). By preinjecting ZFL with dextran sulfate, signal intensities led to a balanced CV-to-DA ratio of 1. Besides this, dextran sulfate had no effect on more hydrophilic compounds such as fluo-cAMP. These findings suggest inhibition of an endocytotic process in nonprofessional phagocytotic endothelial cells expressing the dextran sulfate-sensitive

Table 2. Overview of organ specific drug transporters in different teleost species

Transporter	Species	Organ	Substrate	Inhibitor	References
MDR1-like (ABCB1-like)	Killifish (<i>Fundulus heteroclitus</i>)	Isolated renal proximal tubules	NBD-CsA	Rapamycin ¹ , octreotide ² , vermicin ³ , PSC-833 ⁴ , SIP ⁴ , FTY ⁴ , CsA ⁵ , CsG ⁵ , verapamil ⁵ , vinblastine ⁵ , DNP ⁵ , KCN ⁵ , Quin ⁵	(27) ¹ , (28) ² , (12, 18) ³ , (29) ⁴ , (18) ⁵
	Dogfish (<i>Squalus acanthias</i>)	Isolated brain capillaries	NBD-rapamycin BODIPY-ivermectin BODIPY-verapamil	Rapamycin, CsA, verapamil, FK506, PSC-833	(27)
	Rainbow trout (<i>Oncorhynchus mykiss</i>)	Isolated brain capillaries	NBD-CsA	PSC-833, SIP	(12)
	Killifish (<i>F. heteroclitus</i>)	Isolated renal proximal tubules	Fluorescein (FL)	Octreotide, verapamil, CsA, PSC-833, LTC4	(28)
OAT1:3-like (SLC226-8-like)	Dogfish (<i>S. acanthias</i>) Killifish (<i>F. heteroclitus</i>)	Isolated choroid plexus Isolated renal proximal tubules	FL-MTX	PSC-833, CsA	(30)
MRP2-like (ABCC2-like)	Killifish (<i>F. heteroclitus</i>)	Isolated renal proximal tubules	Fluorescein (FL)	PSC-833 CsA, PSC-833	(30)
	Zebrafish (<i>Danio rerio</i>) Killifish (<i>F. heteroclitus</i>)	Isolated renal proximal tubules	Fluorescein (FL)	PSC-833 CsA ^{1,2} , VO ₂ ¹ , vinblastine ¹ , reversin 205 ² , MK-571 ^{1,2}	(30)
	Killifish (<i>F. heteroclitus</i>)	Isolated renal proximal tubules	Fluorescein (FL)	Reversin 205, verapamil, CsA, MK-571	(32)
	Dogfish (<i>S. acanthias</i>)	Isolated brain capillaries	FL-MTX	Reversin 205	(32)
	Killifish (<i>F. heteroclitus</i>)	Isolated brain capillaries	FL-MTX	PAH ^{1,2,3,4,5} , probenecid ^{1,4} , CdCl ₂ ³ , HgCl ₂ ³	(12) ¹ , (18) ² , (33) ³ , (34) ⁴ , (29) ⁵ , (35) ⁶
	Killifish (<i>F. heteroclitus</i>)	Isolated choroid plexus	FL-MTX	(2,4-D), probenecid LTC4 ^{1,2} , octreotide ¹ , vermicin ² , CdCl ₂ ^{4,6} HgCl ₂ ^{4,6} , PAH ⁵ , probenecid ⁵ , MTX ⁵ , folate ⁵ , BSP ⁵ , BCG ⁵ , CsA ⁵ , verapamil ⁵ , TEA ⁵ MK-571 ⁶ , ET-1 ⁶ , PTH ⁶ , PTHrP ⁶ , SNP ⁶ , PMA ⁶ , gentamicin ⁶ , amikacin ⁶ , diazepam ⁶ , 8-BrcGMP ⁶ , RP-8-BrcGMP ⁶	(36)
	Dogfish (<i>S. acanthias</i>)	Isolated brain capillaries	FL-MTX	LTC4	(30)
	Killifish (<i>F. heteroclitus</i>)	Isolated brain capillaries	FL-MTX	LTC4	(30)
	Dogfish (<i>S. acanthias</i>)	Isolated choroid plexus	FL-MTX	Probenecid, folate, MTX, taurocholate, PAH, ES, digoxin, LTC4, MK-571	(30)
	Killifish (<i>F. heteroclitus</i>)	Isolated renal proximal tubules	Sulfior01 (Texas red)	ES, digoxin, LTC4, MK-571 verapamil ¹ , LTC4 ²	(40) ¹ , (34) ²
	Killifish (<i>F. heteroclitus</i>)	Isolated renal proximal tubules	Sulfior01 (Texas red)	LTC4	(30)
	Dogfish (<i>S. acanthias</i>)	Isolated renal proximal tubules	Sulfior01 (Texas red)	ES, digoxin, TC, MTX, MK-571	(41)
	Killifish (<i>F. heteroclitus</i>)	Isolated renal proximal tubules	Sulfior01 (Texas red)	ET-1, big ET-1, PMA, forskolin, RP-cAMP	(42)
MRP-like	Zebrafish (<i>Danio rerio</i>)	Zebrafish 24 hpf ionocytes	BCECF-AM	PSC-833, CsA, MK-571	(43)
MRP4-like (ABCC4-like)	Killifish (<i>F. heteroclitus</i>)	Isolated renal proximal tubules	Fluo-cAMP	MK-571, LTC4, AZT, cAMP, adefovir (PMEA), 8-bromo-cGMP	(13)
BCRP2-like (ABCG2-like)	Killifish (<i>F. heteroclitus</i>)	Isolated renal proximal tubules	Mitoxantrone	KOH43, FTC	(44)
Abcb4 (ABCB1-like)	Zebrafish (<i>D. rerio</i>)	Zebrafish embryo 48 hpf	Rhodamine B	CsA, PSC-833, vinblastine, verapamil, phenanthrene, tonalide, vincristine, doxorubicin, galaxolide	(9)
	Zebrafish 24 hpf ionocytes ⁷ / 48 hpf embryo ¹		Calcein-AM	CsA ^{1,2} , PSC-833 ^{1,2} , vinblastine ²	(9) ¹ , (43) ²
	Zebrafish 24 hpf ionocytes		DiOC6(3)	CsA, PSC-833, MK-571, verapamil	(43)

Shown are the used fluorescent model substrates and their corresponding inhibitors. (2,4-D), 2,4-dichlorophenoxyacetic acid; AZT, azidothymidine; BCECF-AM, 2',7'-bis(2-carboxyethyl)-5-(and 6)-carboxyfluorescein-AM; BCG, bromocresol green; BSP, bromosulfophthalein; DiOC6(3), 3,3'-dihexyloxacarbocyanine iodide; DNP, 2,4-dinitrophenol; ES, estrone sulfate; ET-1, endothelin-1; FTC, funitremorgin; FTY, FTY720 is a prodrug of FTY720P; MTX, methotrexate; PAH, *p*-aminophenylurea; PMA, phorbol-12-myristate-13-acetate; PTH, parathyroid hormone; PTHrP, resnPTHrP [sea bream (*Sparus aurata*)] recombinant parathyroid hormone-related protein; quin, quinine; RP-8-BrcGMP, inactive isoform of 8-BrcGMP; RP-cAMP, cAMP analog that does not activate PKA; SIP, sphingosine-1-phosphate; SNP, sodium nitroprusside; TC, taurocholate; TEA, tetraethylammonium; VO₂, vanadate.

3.1. PART I: THE STUDY OF RENAL FUNCTION

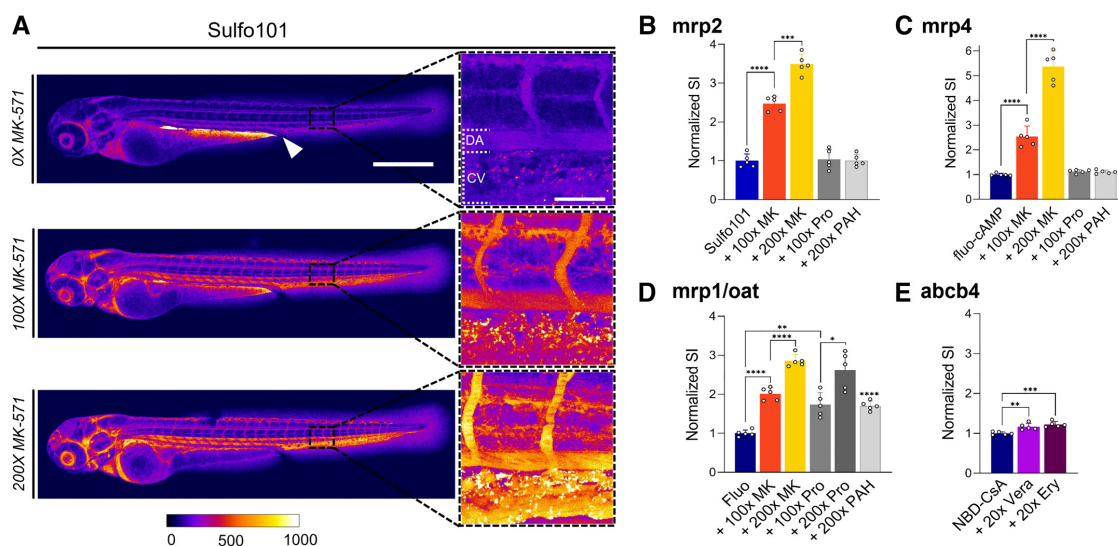


Figure 4. Proximal tubular secretion of fluorescent labeled substrates of drug transporters. **A:** confocal microscopy analysis of 72-h post fertilization (hpf) zebrafish larvae (ZFL) at 1 h postinjection (hpi) of sulforhodamine 101 (Sulfo101) in the presence of increasing concentrations of the multidrug resistance-associated protein (mrp) inhibitor MK-571 (MK). The white arrow shows the gastrointestinal tract and cloaca. Scale bar = 500 μ m. Magnified sections of the tail region vasculature are shown. Increasing signal intensity is shown from blue to red to white. Scale bar = 50 μ m. **B–E:** quantitative analysis compared with control (no inhibitor) of 72 hpf ZFL injected with the indicated transporter substrate (blue bar) and a x-fold excess of inhibitor. The signal was quantified within the dorsal artery (DA). The inhibitors used were as follows: probenecid (Pro), *p*-aminohippurate (PAH), verapamil (Vera), and erythromycin (Ery). Values are means \pm SD; $n = 5$. * $P < 0.05$; ** $P < 0.005$; *** $P < 0.0005$; **** $P < 0.0001$. CV, cardinal vein; Fluo, fluorescein; NBD-CsA, NBD-cyclosporine A.

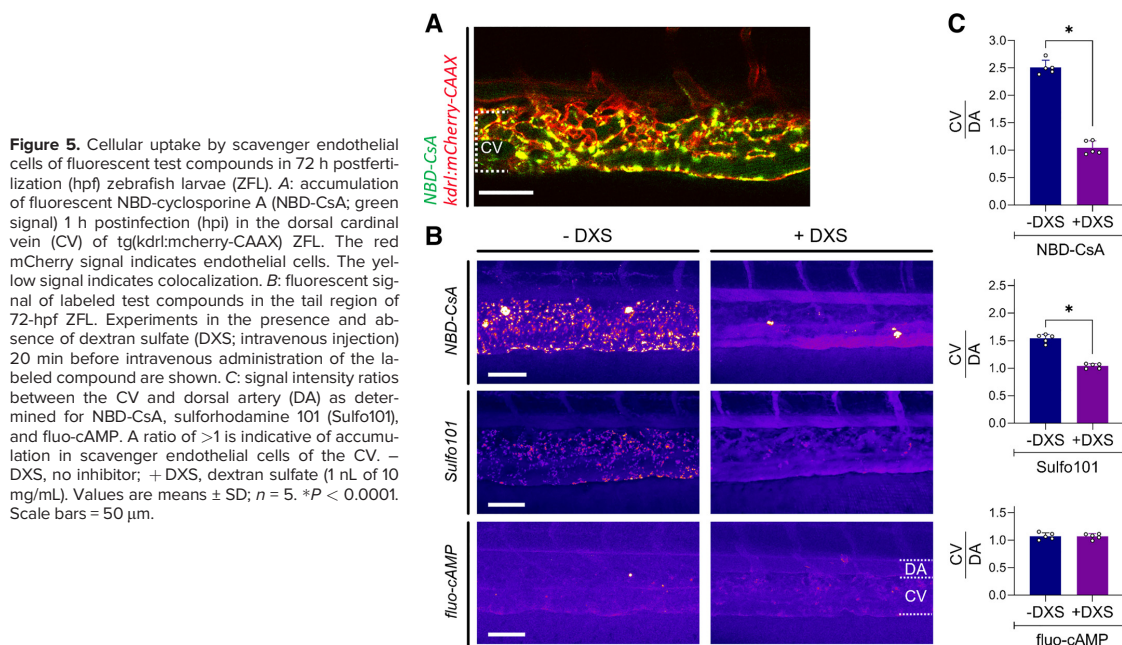
scavenger receptor stabilin-1/2. It is tempting to speculate that protein binding precedes stabilin receptor-mediated endocytosis since stabilin-1/2 is known to mediate blood clearance of macromolecules (15).

To verify the hypothesis that endocytosis of protein-bound fluorescent small molecules gives rise to the observed punctuated staining patterns in ZFL, a chemically reactive fluorescent dye (TRITC-NHS), used as amine-reactive cross-linker for protein labeling, was intravenously injected. Indeed, a punctuated staining pattern within, for example, the PCT was observed (Fig. 6A). Qualitative and quantitative (Fig. 6B) evaluation of these signals revealed a threefold reduction of intensity when TRITC-NHS was hydrolyzed before injection. In a next step, the pronephros region was photobleached and the signal evolution was monitored over time. Signals reappeared after photobleaching being indicative of resequestration of fluorescent-labeled species. After photobleaching, signals reached a new maximum within 7.5 h, pointing to a very long half-life and thus persistence in the circulation of the labeled species.

We found that indirect assessment of renal clearance of fluorescent substrates based on their disappearance from the central blood compartment is more reliable than a measurement of their appearance within the PCT. Although direct transporter-mediated luminal secretion into the PCT of hydrophilic test compounds such as fluo-cAMP and fluorescein ($\log D_{7.4} < 0.25$) could be visualized based on their appearance within the PCT, their lipophilic counterparts (i.e., Sulfo101 and NBD-CsA, $\log D_{7.4} > 0.25$) could not be

detected within the PCT but did accumulate within tubular epithelial cells (Fig. 6C). In these experiments, ZFL had to be analyzed within 10 min of 1 nL of 2 mM working solution due to rapid disappearance of fluorescent signals (Fig. 6D).

To allow for a direct assessment of proximal tubular secretion based on the appearance of fluorescent signals within the tubular lumen, isolated proximal tubules of killifish (*F. heteroclitus*) were used as a renal tubular transport model (Fig. 7). In contrast to the pronephros of the living ZFL, these isolated tubules are not patent but sealed due to partial collapse during the isolation procedure. Secreted fluorescent substrates could indeed be detected in the tubular lumen and excretion inhibited using corresponding transport inhibitors. Figure 7 shows a qualitative assessment by confocal fluorescence microscopy of accumulated transporter substrates (1 μ M) within the proximal tubular lumen in the presence and absence of a 10- to 20-fold excess of the correlating transport inhibitor. Image analysis allowed for a statistical assessment of specific transporter inhibition. The remaining activity in the presence of inhibitor for the ABC transporters was $65 \pm 7\%$ for mrp2 (abcc2) (substrate: Sulfo 101, inhibitor: MK571), $55 \pm 8\%$ for mrp4 (abcc4) (substrate: fluo-cAMP, inhibitor: MK571), $45 \pm 8\%$ for mdr1 (abcb1) (substrate: NBD-CsA, inhibitor: verapamil), and $60 \pm 9\%$ for bcrp (abcg2) (substrate: mitoxantrone, inhibitor: KO-143). For the SLC transporter oat (slc22), excretion of fluorescein was reduced to $72 \pm 12\%$ in the presence of *p*-aminohippurate and to $11 \pm 15\%$ in the presence of MK-571.



All values are presented as means \pm SD, $n = 12$ and showed a level of significance of $P < 0.05$ compared with control (no inhibitor).

DISCUSSION

Anatomic structures of the developing pronephros in teleosts show high similarity to corresponding structures in mammals, including humans (12, 45). This notion is supported by the observation that, for example, transcription factors responsible for patterning the developing kidney in zebrafish are evolutionary conserved in mammals (2, 45, 46). With respect to renal functionality, the question arises if ZFL can be used as a vertebrate screening model to study renal processing of pharmaceuticals. It was therefore the aim of this study to evaluate to which degree the ZFL pronephros functionality reflects the situation in higher vertebrates, including humans.

To control chemical exposure within ZFL, all test compounds were injected intravenously into the duct of Cuvier, resulting in a bioavailability of 100%. By this approach, potential interference by intestinal metabolism can be as well excluded. Of note, alternative clearance mechanisms via the liver are not considered to take place since liver associated xenobiotic metabolism is not operational by 5 dpf (47, 48). Injection volumes in these experiments were 1–2 nL, which corresponds to an estimated 2% of the total blood volume of a 72-hpf ZFL. Injected solutions did contain a maximum of 15% DMSO. This procedure was well tolerated by the ZFL as demonstrated by monitoring of heart beat and viability during the duration of control experiments (i.e., injection

of DMSO-PBS followed by 2-h monitoring). There were no statistically significant changes in heart beat ($n = 16$ ZFL) and no apparent signs of toxicity.

Of note, blood concentrations of circulating fluorophores were measured within the DA. Signals in the CV are indicative of cellular uptake by nonprofessional phagocytic cells. This process is mediated by endothelial scavenger receptors (e.g., stabilin-1/2), as shown in Fig. 5.

In the first series of experiments, we could confirm functionality of the ZFL glomerulus at 96 hpf by the determination of a D_H threshold for glomerular filtration in the range of 4.4–7.6 nm. This is in line with studies in rats (49, 50) that demonstrated that the majority of macromolecules are retained within the glomerulus by small pores of a radius 4–5 nm or negatively charged slit diaphragms of radius 6 nm. Thus, the passage of proteins such as, for example, albumin (human serum albumin: 69 kDa, 7- to 10-nm diameter) (51) is restricted across these pores (52). The contribution of the glomerular basement membrane and its morphology toward glomerular filtration has been previously discussed (53, 54).

Although ZFL, before reaching 96 hpf, are reported to have size-dependent glomerular filtration (55), there are reports indicating that slit diaphragm formation is not yet completed at this development stage (52). Therefore, we used in this study 96-hpf ZFL. We assume that at this stage podocyte foot processes, endothelial cell fenestrations, and slit diaphragms are mature and fully functional and therefore justify the present use of ZFL as an in vivo vertebrate model to study renal function (24, 35).

Our experiments were carried out using fluorescent labeled PEG or dextran of different molecular weight, whose

3.1. PART I: THE STUDY OF RENAL FUNCTION

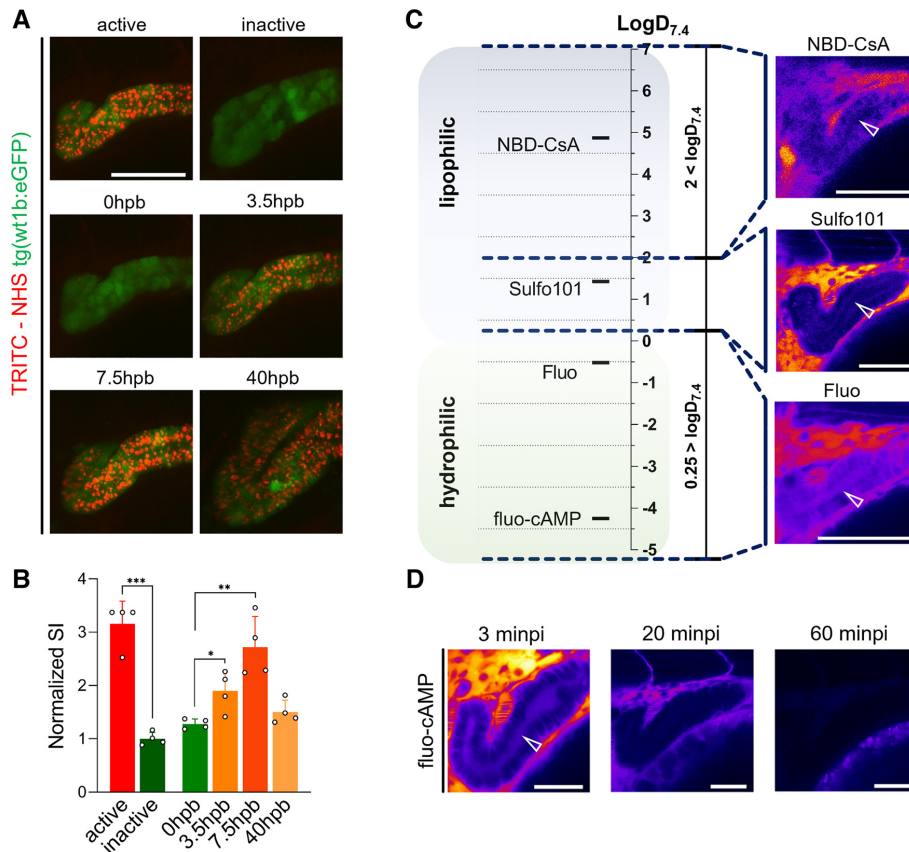


Figure 6. Endocytosis of protein-bound TRITC-NHS in the proximal convoluted tubule (PCT) and luminal secretion of hydro- and lipophilic fluorescent substrates. *A*: top: “active” indicates the PCT signal of a chemical reactive fluorescent compound (TRITC-NHS) 3 h postinjection (hpi); “inactive” indicates TRITC-NHS injected after inactivation by hydrolysis. *A*, middle and bottom: photobleaching of the PCT after injection of active TRITC-NHS and shown after 3.5, 7.5, and 40 h postbleaching (hpb). The green signal indicates 80-h postfertilization (hpf) *tg(wt1b:eGFP)* ZFL. Scale bar = 50 μ m. *B*: quantitative assessment of TRITC-associated signals within the PCT (green) shown in *A*. Normalized SI is the PCT signal intensity compared with inactive TRITC-NHS. *C*: fluorescent substrates of proximal tubular drug transporters were categorized by lipophilicity ($\log D_{7.4} < 0.25$ and $\log D_{7.4} > 2$). Representative lateral projections of 72 hpf ZFL are shown to provide an alignment of hydrophilic/lipophilic classifications and the corresponding tubular signals. The white arrow indicates the tubular lumen. Scale bars = 50 μ m. *D*: time-dependent depletion of the fluo-cAMP signal in the lumen of the PCT. Minpi, minutes postinjection. Scale bars = 30 μ m. Values are means \pm SD; $n = 4$. * $P < 0.02$; ** $P < 0.002$; *** $P < 0.0001$.

purity and hydrodynamic radii were determined by fluorescence correlation spectroscopy. Dextran and PEG are frequently used as pharmaceutical excipients (56). Covalently bound, PEG sterically stabilizes macromolecules and drug-containing particles (56). In the systemic circulation, PEG increases the half-life of these molecules. A few studies have been done describing characteristics of renal clearance based on PEG length (57). Here, our study revealed that rather the D_H of PEG and dextran polymers determines renal filtration properties instead of molecular weights, i.e., 40-kDa PEG is not filtrated, whereas 40-kDa dextran is rapidly cleared. In ZFL, these results confirm previous reports on size-selective glomerular filtration in 72-hpf ZFL (55, 58) and 96-hpf ZFL [e.g., 10- vs. 500-kDa dextran polymer (59)], albeit we are the first who determined a clear cutoff value.

Distal tubular reabsorption was assessed based on receptor-mediated transport of FA/vitamin B₉ via folr1 (ZLF analog of the human FOLR1 receptor) (3). FOLR1 is expressed on the apical side of PCT cells (60) and facilitates transcytosis (61). However, folr1 is also conserved in a wide range of vertebrates. Recently, homolog mRNA expression of human FOLR1 was detected in zebrafish throughout embryogenesis in distal tubules and showed high structural homology of the FA-binding site with vertebrates and humans. In particular, FA-binding site 1, consisting of five amino acids, is conserved in cows, mice, and rats (3). In our study, we used a fluorescently labeled FA-PEG polymer with an experimentally determined D_H of 1.1 nm, which is in alignment with literature reports of similar PEG polymers (62). The fluorescently labeled FA analog was retained in the ZFL circulation but was

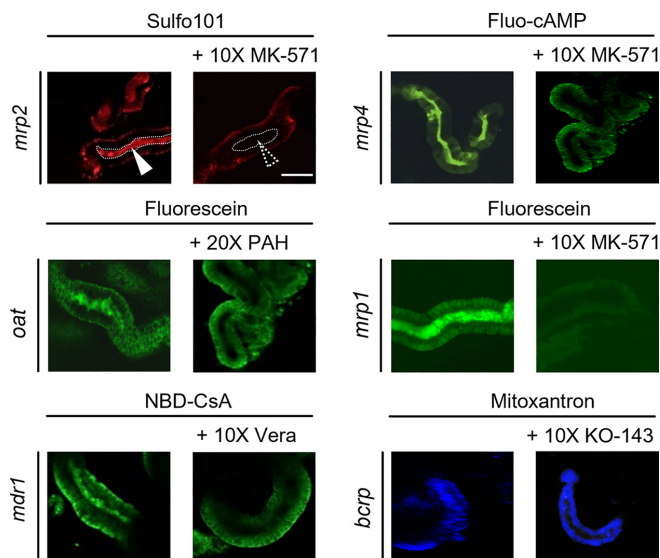


Figure 7. Excretion of fluorescent model substrates in isolated killifish proximal tubules in the presence or absence of specific inhibitors. Freshly isolated proximal tubules were incubated with fluorescent transporter substrates and analyzed by confocal microscopy. Renal secreted substrates were detected in the lumen of isolated proximal tubules. *Left:* no inhibitor. *Right:* incubations in the presence of fold excess of the indicated inhibitor. Signals within the luminal space (white arrows and dotted area) indicate tubular excretion of the transported substrate. Scale bar = 50 μm .

rapidly renal excreted in presence of an excess of nonlabeled FA. Our inhibition experiments thus demonstrate specific and receptor-mediated distal tubular reuptake of FA by a FA receptor-mediated process. It should be noted that the tubular system in the living ZFL is patent, i.e., urine is rapidly expelled to the surrounding media by the continuous action of cilia lining the inner surface of the tubules (63). It should be noted that FA-PEG2000-FITC is present in the distal tubular lumen but hardly visible in the surrounding tubular epithelial cells. We have observed a similar phenomenon earlier in a transendothelial transport study using a fluorescent-labeled IgG monoclonal antibody directed against the rodent transferrin receptor (64). In these experiments, transcellular receptor-mediated transport (i.e., transcytosis) was demonstrated to be a highly efficient and fast process resulting in very low steady-state concentrations of the transported IgG within endothelial cells.

Transporter-mediated proximal tubular excretion of fluorescent labeled xenobiotics was studied based on their appearance within the PCT or, alternatively, their disappearance from the central blood compartment. Criteria for the selection of the used fluorescent substrates and nonfluorescent inhibitors as well as information on their selectivity and use by other authors are shown in Table 2. The studied ABC transporters include *abcb4*, *mrp1* (*abcc1*), *mrp2* (*abcc2*), and *mrp4* (*abcc4*). mRNA expression levels in ZFL determined between 24 and 120 hpf point to homolog expression of these transporters in teleosts and mammals, including humans, in various organs and proximal tubules (6–8). The *abcb4* transporter has been described as a homolog of human p-glycoprotein/MDR1 (9). In this study, we could demonstrate that these transporters are fully functional in ZFL at 72 hpf and mediate active secretion into the PCT of their respective substrates. SLC [i.e., *oat* (*slc22*)] transport functionality was

confirmed using negatively charged Fluo as a substrate (34, 65). In addition, we could show in this study that fluorescein was transported by an *mrp* transporter. This finding suggests functional expression of *mrp1* in zebrafish since, first, fluorescein is a substrate of human MRP1 (ABCC1) (66) and, second, *mrp1* expression in zebrafish has been previously demonstrated by genetic analysis (7). Specificity of transport was demonstrated in these experiments using combinations of fluorescent transporter substrates and their respective inhibitors. Again, the appearance of fluorescent signals within the tubular lumen was a less reliable measure compared with disappearance of transporter substrates from the central blood compartment, recorded based on fluorescent signals present in the DA. This underlines that the pronephros of ZFL is an open fluid compartment and that clearance of drugs is a rapid process. The higher luminal accumulation of hydrophilic substances can be explained by the fact that hydrophilic compounds experience both saturable active as well as dose-linear passive (glomerular filtration) clearance, whereas most lipophilic compounds are only transported actively (4). Furthermore, some lipophilic compounds, such as NBD-CsA, did not reveal any luminal signals but showed an association with renal epithelial cells instead. Consequently, hydrophilic compounds are cleared faster and show higher transient signals in the tubular lumen.

Although the human homolog p-glycoprotein/MDR1 (ABCB1) gene is absent in ZFL, active secretion of lipophilic, uncharged, or moderately basic substrates in ZFL can be compensated by an *abcb4* transporter (2, 9, 67). Furthermore, and to the best of our knowledge, the results of our study suggest, for the first time, functional expression of *mrp1* (*abcc1*) in teleosts, i.e., zebrafish and killifish.

We cannot exclude that expression of drug transporters outside of the pronephros may have an impact on the

3.1. PART I: THE STUDY OF RENAL FUNCTION

indirect measurements of fluorescent substrates within the blood compartment. This can potentially lead to the accumulation of fluorescent signals in specific organs and tissues such as the brain or developing liver. However, we have not observed such effects (e.g., Fig. 4). This can be explained by the fact that drug transporters studied in the present work have a protective function preventing cellular accumulation. Of note, stabilin-mediated endocytosis by endothelia of the CV leads to a punctuated staining pattern. This latter observation has prompted us to study elimination of circulating compounds by pathways others than renal excretion in greater detail.

When comparing tail images from our transporter experiments, a punctuated staining pattern after injection of NBD-CSA and Sulfo101 was observed within the CV. Experiments with 72-hpf tg(kdrl:mCherry-CAAX) ZFL expressing mCherry in endothelial cells revealed a colocalization of fluorescent signals. This observation is indicative of cellular uptake of fluorescent molecules by scavenger endothelial cells located in the CV. Such endothelial cells with a scavenging function can be found in various organs in teleost fish, sharks, and lampreys (68). In mammals, they predominantly line the liver sinusoids. In a previous study (15), we could demonstrate stabilin-2-dependent scavenging of lipid nanoparticles in the CV region of ZFL. In this as well as the present study, stabilin-2-mediated clearance could be selectively blocked by preinjection of dextran sulfate. Dextran sulfate is an inhibitor of stabilin-2 and related scavenger receptors. Since stabilin-2 mediates cellular uptake of negatively charged macromolecules or nanoparticles by a clathrin-coated pit pathway (69), it is reasonable to assume that in our experiments not the free fluorescent small molecule was recognized but a protein-associated conjugate thereof. Indeed, cyclosporine analogs are characterized by a very high protein binding of >98% (70). Sulfo101 or Texas red is used as an astrocyte-specific marker (71). Its hydrolysis product is a water-soluble sulfonic acid derivative, which shows reduced adsorption to proteins. This is in line with the observation that preincubation of Sulfo101 in serum or buffer reduces the appearance of the punctuated staining pattern in zebrafish. These experiments suggest that protein adducts accumulate within endothelial cells of the CV by a stabilin-mediated endocytotic process.

Of interest, chemically reactive TRITC-NHS (amine-reactivity via *N*-hydroxysuccinimide) showed an additional punctuated staining of the PCT. This finding is in line with previous reports of PCT endocytosis of smaller 10-kDa dextran-FITC conjugates (72, 73) or endocytosis and lysosomal processing of a red fluorescent protein consisting of the monomeric vitamin D-binding protein (1/2vdp-mCherry) (74). Again, the punctuated staining pattern was only visible using the chemically reactive fluorescent marker but not when using its hydrolyzed counterpart. This and photobleaching experiments suggest that long circulating protein adducts were present in the circulation up to 40 h post-bleaching, leading to continuous endocytosis and cellular accumulation at the level of the PCT. It remains to be elucidated by which mechanism the protein adducts are reabsorbed from the tubular lumen.

To confirm the conservation of transport functions in an additional teleost species, freshly isolated and sealed tubuli

of killifish (*F. heteroclitus*) were used as a complementary *in vivo* transport model (12). These tubuli are characterized by collapsed and thus sealed ends. Therefore, accumulation of transporter substrates within a closed tubular lumen can be monitored (18, 34). Indeed, using the same representative inhibitors and fluorescent substrate pairs, our results in ZFL could be confirmed. This supports that tubular transporters are highly conserved in teleosts.

Perspectives and Significance

The ZFL is an attractive *in vivo* vertebrate model that is extensively used, for instance, in toxicological, pharmacological, and nanomedicine research (16, 58). Our study revealed that ZFL at 96 hpf have a fully functional pronephros. Glomerular filtration is characterized by a cutoff similar to that of higher vertebrates. Small-molecule substrates of ABC and SLC transporters are actively secreted at the level of the proximal tubule. Receptor-mediated endocytosis by the FA receptor could be demonstrated for the distal tubule. The here-proposed protocol uses intravenous injections (allowing for a precise dosing and defined exposure of the ZFL) in combination with fluorescent reference compounds to study renal function in 3- to 4-dpf larvae. If transport experiments are carried out using calibrated amounts of transport substrates dose-dependent kinetic effects can be monitored. During such experiments, additional information can be obtained with respect to the tolerability, circulation behavior, extravasation, cellular interaction, and tissue accumulation of test compounds *in vivo*. The ZFL model provides a higher throughput compared with alternative screening models in vertebrates. It can therefore be considered to be a cost-effective and attractive translational tool to bridge the gap between cell culture-based test systems and pharmacokinetic experiments in higher vertebrates such as rodents. We propose that this model can be used as a screening model to identify interactions of unknown test compounds with renal transport based on their interactions with coinjected fluorescent markers.

ACKNOWLEDGMENTS

We thank the Swiss foundation "Stiftung zur Förderung des pharmazeutischen Nachwuchses in Basel" for the generous support of the present project. The authors thank Dr. Kai Schleicher from the Imaging Core facility of the Biocenter (University of Basel) for support with confocal microscopy and image analysis. Prof. Dr. Hermann Haller (Hannover Medical School), Prof. Dr. Mario Schiffer (University of Erlangen), Prof. Dr. Markus Affolter, Dr. Heinz Georg Belting, and Kathrin Gundel (University of Basel) are acknowledged for providing support for zebrafish experiments. Furthermore, we thank Prof. Dr. Iain Drummond (MDIBL) and Prof. Dr. Alex Odermatt (University of Basel) for the fruitful scientific exchange and discussions. Killifish images were acquired using equipment of the Light Microscopy Facility at the MDIBL, which is supported by Mainz INBRE Grant GM103423 from the National Institute of General Medical Sciences, National Institutes of Health. In addition, we thank the Salisbury Cove Research Foundation and the Ulric Dahlgren Fund for support of this work. Some illustrations were created with Biorender.com (BZ232EFA4).

GRANTS

J.S.B. was supported by the Stiftung zur Förderung des pharmazeutischen Nachwuchses in Basel. J.S.B., G.F., and J.H. were supported by Maine INBRE Grant GM103423, Salisbury Cove Research Foundation, and Ulric Dahlgren Fund.

DISCLOSURES

No conflicts of interest, financial or otherwise, are declared by the authors.

AUTHOR CONTRIBUTIONS

J.S.B., A.P., C.L.A., and J.H. conceived and designed research; J.S.B., A.P., C.L.A., G.F., and J.H. performed experiments; J.S.B., A.P., C.L.A., and J.H. analyzed data; J.S.B., A.P., C.L.A., G.F., and J.H. interpreted results of experiments; J.S.B., C.L.A., and G.F. prepared figures; J.S.B., C.L.A., and J.H. drafted manuscript; J.S.B., A.P., C.L.A., G.F., and J.H. edited and revised manuscript; J.S.B., A.P., C.L.A., G.F., and J.H. approved final version of manuscript.

REFERENCES

- Lechner C, Mönning U, Reichel A, Fricker G. Potential and limits of kidney cells for evaluation of renal excretion. *Pharmaceuticals (Basel)* 14: 908, 2021. doi:10.3390/ph14090908.
- Luckenbach T, Fischer S, Sturm A. Current advances on ABC drug transporters in fish. *Comp Biochem Physiol C Toxicol Pharmacol* 165: 28–52, 2014. doi:10.1016/j.cbpc.2014.05.002.
- Jones RN, Erhard SA, Malham MR, Gen AY, Sullivan K, Olsen KW, Dale RM. Expression and characterization of the zebrafish orthologue of the human FOLR1 gene during embryogenesis. *Gene Expr Patterns* 25-26: 159–166, 2017. doi:10.1016/j.gep.2017.08.002.
- Kenakin TC. Chapter 8 – pharmacokinetics II: distribution and multiple dosing. In: *Pharmacology in Drug Discovery*, edited by Kenakin TP. Academic Press, 2012, p. 155–183. doi:10.1016/C2009-0-63928-3.
- Howe K, Clark MD, Torroja CF, Torrance J, Berthelot C, Muffato M, et al. The zebrafish reference genome sequence and its relationship to the human genome. *Nature* 496: 498–503, 2013 [Erratum in *Nature* 505: 248, 2014]. doi:10.1038/nature12111.
- Long Y, Li Q, Zhong S, Wang Y, Cui Z. Molecular characterization and functions of zebrafish ABCC2 in cellular efflux of heavy metals. *Comp Biochem Physiol C Toxicol Pharmacol* 153: 381–391, 2011. doi:10.1016/j.cbpc.2011.01.002.
- Long Y, Li Q, Cui Z. Molecular analysis and heavy metal detoxification of ABCC1/MRP1 in zebrafish. *Mol Biol Rep* 38: 1703–1711, 2011. doi:10.1007/s11033-010-0283-z.
- Lu X, Long Y, Lin L, Sun R, Zhong S, Cui Z. Characterization of zebrafish Abcc4 as an efflux transporter of organochlorine pesticides. *PLoS One* 9: e111664, 2014. doi:10.1371/journal.pone.0111664.
- Fischer S, Klüver N, Burkhardt-Medicke K, Pietsch M, Schmidt A-M, Wellner P, Schirmer K, Luckenbach T. Abcb4 acts as multixenobiotic transporter and active barrier against chemical uptake in zebrafish (*Danio rerio*) embryos. *BMC Biol* 11: 69, 2013. doi:10.1186/1741-7007-11-69.
- Cosentino CC, Roman BL, Drummond IA, Hukriede NA. Intravenous microinjections of zebrafish larvae to study acute kidney injury. *J Vis Exp*: e2079, 2010. doi:10.3791/2079.
- Feng B, Varma MV, Costales C, Zhang H, Tremaine L. In vitro and in vivo approaches to characterize transporter-mediated disposition in drug discovery. *Expert Opin Drug Discov* 9: 873–890, 2014. doi:10.1517/17460441.2014.922540.
- Fricker G, Gutmann H, Droulle A, Drewe J, Miller DS. Epithelial transport of anthelmintic ivermectin in a novel model of isolated proximal kidney tubules. *Pharm Res* 16: 1570–1575, 1999. doi:10.1023/A:1018956621376.
- Reichel V, Masereeuw R, van den Heuvel JJMW, Miller DS, Fricker G. Transport of a fluorescent cAMP analog in teleost proximal tubules. *Am J Physiol Regul Integr Comp Physiol* 293: R2382–R2389, 2007. doi:10.1152/ajpregu.00029.2007.
- Lele Z, Krone PH. The zebrafish as a model system in developmental, toxicological and transgenic research. *Biotechnol Adv* 14: 57–72, 1996. doi:10.1016/0734-9750(96)00004-3.
- Campbell F, Bos FL, Sieber S, Arias-Alpizar G, Koch BE, Huwyler J, Kros A, Bussmann J. Directing nanoparticle biodistribution through evasion and exploitation of Stab2-dependent nanoparticle uptake. *ACS Nano* 12: 2138–2150, 2018. doi:10.1021/acsnano.7b06995.
- Sieber S, Grossen P, Detampel P, Siegfried S, Witzigmann D, Huwyler J. Zebrafish as an early stage screening tool to study the systemic circulation of nanoparticle drug delivery systems in vivo. *J Control Release* 264: 180–191, 2017. doi:10.1016/j.jconrel.2017.08.023.
- Sieber S, Grossen P, Bussmann J, Campbell F, Kros A, Witzigmann D, Huwyler J. Zebrafish as a preclinical in vivo screening model for nanomedicines. *Adv Drug Deliv Rev* 151–152: 152–168, 2019. doi:10.1016/j.addr.2019.01.001.
- Schramm U, Fricker G, Wenger R, Miller DS. P-glycoprotein-mediated secretion of a fluorescent cyclosporin analogue by teleost renal proximal tubules. *Am J Physiol Renal Physiol* 268: F46–F52, 1995. doi:10.1152/ajprenal.1995.268.1.F46.
- Pratsinis A, Uhl P, Bolten JS, Hauswirth P, Schenk SH, Urban S, Mier W, Witzigmann D, Huwyler J. Virus-derived peptides for hepatic enzyme delivery. *Mol Pharm* 18: 2004–2014, 2021. doi:10.1021/acs.molpharmaceut.0c01222.
- Okuno D, Iino R, Noji H. F1-ATPase: fundamental properties and structure. In: *Encyclopedia of Biophysics*, edited by Roberts GCK. Berlin: Springer, p. 717–725.
- Kimmel CB, Ballard WW, Kimmel SR, Ullmann B, Schilling TF. Stages of embryonic development of the zebrafish. *Dev Dyn* 203: 253–310, 1995. doi:10.1002/aja.1002030302.
- Perner B, Englert C, Bollig F. The Wilms tumor genes wt1a and wt1b control different steps during formation of the zebrafish pronephros. *Dev Biol* 309: 87–96, 2007. doi:10.1016/j.ydbio.2007.06.022.
- Jin S-W, Beis D, Mitchell T, Chen J-N, Stainier DYR. Cellular and molecular analyses of vascular tube and lumen formation in zebrafish. *Development* 132: 5199–5209, 2005. doi:10.1242/dev.02087.
- Hogan BM, Hoppers R, Witte M, Heloterä H, Alitalo K, Duckers HJ, Schulte-Merker S. Vegf/Flt4 signalling is suppressed by Dll4 in developing zebrafish intersegmental arteries. *Development* 136: 4001–4009, 2009. doi:10.1242/dev.039990.
- Sieber S, Siegrist S, Schwarz S, Porta F, Schenk SH, Huwyler J. Immobilization of enzymes on PLGA sub-micrometer particles by crosslinked layer-by-layer deposition. *Macromol Biosci* 17: 1700015, 2017. doi:10.1002/mabi.201700015.
- Drummond IA, Davidson AJ. Chapter 9 – zebrafish kidney development. In: *Methods in Cell Biology*, edited by Detrich HW, Westerfield M, Zon LI. Academic Press, 2010, p. 233–260. doi:10.1016/B978-0-12-384892-5.00009-8.
- Miller DS, Fricker G, Drewe J. p-Glycoprotein-mediated transport of a fluorescent rapamycin derivative in renal proximal tubule. *J Pharmacol Exp Ther* 282: 440–444, 1997.
- Gutmann H, Miller DS, Droulle A, Drewe J, Fahr A, Fricker G. P-glycoprotein- and mrp2-mediated octreotide transport in renal proximal tubule. *Br J Pharmacol* 129: 251–256, 2000. doi:10.1038/sj.bjp.0703003.
- Miller DS. Sphingolipid signaling reduces basal P-glycoprotein activity in renal proximal tubule. *J Pharmacol Exp Ther* 348: 459–464, 2014. doi:10.1124/jpet.113.210641.
- Miller DS, Graeff C, Droulle L, Fricker S, Fricker G. Xenobiotic efflux pumps in isolated fish brain capillaries. *Am J Physiol Regul Integr Comp Physiol* 282: R191–R198, 2002. doi:10.1152/ajpregu.00305.2001.
- Sturm A, Ziemann C, Hirsch-Ernst KI, Segner H. Expression and functional activity of P-glycoprotein in cultured hepatocytes from *Oncorhynchus mykiss*. *Am J Physiol Regul Integr Comp Physiol* 281: R1119–R1126, 2001. doi:10.1152/ajpregu.2001.281.4.R1119.
- Zaja R, Klobučar RS, Smital T. Detection and functional characterization of Pgp1 (ABCB1) and MRP3 (ABCC3) efflux transporters in the PLHC-1 fish hepatoma cell line. *Aquat Toxicol* 81: 365–376, 2007. doi:10.1016/j.aquatox.2006.12.015.

3.1. PART I: THE STUDY OF RENAL FUNCTION

33. Terlouw SA, Graeff C, Smeets PHE, Fricker G, Russel FGM, Masereeuw R, Miller DS. Short- and long-term influences of heavy metals on anionic drug efflux from renal proximal tubule. *J Pharmacol Exp Ther* 301: 578–585, 2002. doi:10.1124/jpet.301.2.578.
34. Masereeuw R, Russel FG, Miller DS. Multiple pathways of organic anion secretion in renal proximal tubule revealed by confocal microscopy. *Am J Physiol Renal Physiol* 271: F1173–F1182, 1996. doi:10.1152/ajprenal.1996.271.6.F1173.
35. Notenboom S, Miller DS, Kuik LH, Smits P, Russel FGM, Masereeuw R. Short-term exposure of renal proximal tubules to gentamicin increases long-term multidrug resistance protein 2 (Abcc2) transport function and reduces nephrotoxicant sensitivity. *J Pharmacol Exp Ther* 315: 912–920, 2005. doi:10.1124/jpet.105.089094.
36. Villalobos ARA, Miller DS, Renfro JL. Transepithelial organic anion transport by shark choroid plexus. *Am J Physiol Regul Integr Comp Physiol* 282: R1308–R1316, 2002. doi:10.1152/ajpregu.00677.2001.
37. Wever KE, Masereeuw R, Miller DS, Hang XM, Flik G. Endothelin and calciotropic hormones share regulatory pathways in multidrug resistance protein 2-mediated transport. *Am J Physiol Renal Physiol* 292: F38–F46, 2007. doi:10.1152/ajprenal.00479.2005.
38. Notenboom S, Miller DS, Smits P, Russel FGM, Masereeuw R. Involvement of guanylyl cyclase and cGMP in the regulation of Mrp2-mediated transport in the proximal tubule. *Am J Physiol Renal Physiol* 287: F33–F38, 2004. doi:10.1152/ajprenal.00443.2003.
39. Baehr CH, Fricker G, Miller DS. Fluorescein-methotrexate transport in dogfish shark (*Squalus acanthias*) choroid plexus. *Am J Physiol Regul Integr Comp Physiol* 291: R464–R472, 2006. doi:10.1152/ajpregu.00814.2005.
40. Zaremba A, Miller DS, Fricker G. Zinc chloride rapidly stimulates efflux transporters in renal proximal tubules of killifish (*Fundulus heteroclitus*). *Toxicol Appl Pharmacol* 334: 88–99, 2017. doi:10.1016/j.taap.2017.09.001.
41. Reichel V, Miller DS, Fricker G. Texas red transport across rat and dogfish shark (*Squalus acanthias*) choroid plexus. *Am J Physiol Regul Integr Comp Physiol* 295: R1311–R1319, 2008. doi:10.1152/ajpregu.90373.2008.
42. Miller DS, Masereeuw R, Karnaky KJ. Regulation of MRP2-mediated transport in shark rectal salt gland tubules. *Am J Physiol Regul Integr Comp Physiol* 282: R774–R781, 2002. doi:10.1152/ajpregu.00333.2001.
43. Gordon WE, Espinoza JA, Leerberg DM, Yelon D, Hamdoun A. Xenobiotic transporter activity in zebrafish embryo ionocytes. *Aquat Toxicol Amst Toxicol* 212: 88–97, 2019. doi:10.1016/j.aquatox.2019.04.013.
44. Mahringer A, Bernd A, Miller DS, Fricker G. Aryl hydrocarbon receptor ligands increase ABC transporter activity and protein expression in killifish (*Fundulus heteroclitus*) renal proximal tubules. *Biol Chem* 400: 1335–1345, 2019. doi:10.1515/hsz-2018-0425.
45. Wingert RA, Davidson AJ. The zebrafish pronephros: a model to study nephron segmentation. *Kidney Int* 73: 1120–1127, 2008. doi:10.1038/ki.2008.37.
46. Naylor RW, Qubisi SS, Davidson AJ. Zebrafish pronephros development. In: *Kidney Development and Disease*, edited by Miller RK. Cham: Springer International Publishing, 2017, p. 27–53. doi:10.1007/978-3-319-51436-9_2.
47. Chu J, Sadler KC. A new school in liver development: lessons from zebrafish. *Hepatology* 50: 1656–1663, 2009. doi:10.1002/hep.23157.
48. Howarth DL, Passeri M, Sadler KC. Drinks like a fish: Using zebrafish to understand alcoholic liver disease. *Alcohol Clin Exp Res* 35: 826–829, 2011. doi:10.1111/j.1530-0277.2010.01407.x.
49. Soo Choi H, Liu W, Misra P, Tanaka E, Zimmer JP, Itty Ipe B, Bawendi MG, Frangioni JV. Renal clearance of quantum dots. *Nat Biotechnol* 25: 1165–1170, 2007. doi:10.1038/nbt1340.
50. Tencer J, Frick IM, Oquist BW, Alm P, Rippe B. Size-selectivity of the glomerular barrier to high molecular weight proteins: upper size limitations of shunt pathways. *Kidney Int* 53: 709–715, 1998. doi:10.1046/j.1523-1755.1998.00797.x.
51. Rashid H, Muzammil S, Tayyab S. Comparison of bilirubin binding and other molecular properties of tile serum albumin of several mammalian species. *Biochem Mol Biol Int* 44: 165–173, 1998. doi:10.1080/15216549800201182.
52. Kramer-Zucker AG, Wiessner S, Jensen AM, Drummond IA. Organization of the pronephric filtration apparatus in zebrafish requires nephrin, podocin and the FERM domain protein Mosaic eyes. *Dev Biol* 285: 316–329, 2005. doi:10.1016/j.ydbio.2005.06.038.
53. Schlöndorff D, Wyatt CM, Campbell KN. Revisiting the determinants of the glomerular filtration barrier: what goes round must come round. *Kidney Int* 92: 533–536, 2017. doi:10.1016/j.kint.2017.06.003.
54. Lawrence MG, Altenburg MK, Sanford R, Willett JD, Bleasdale B, Ballou B, Wilder J, Li F, Miner JH, Berg UB, Smithies O. Permeation of macromolecules into the renal glomerular basement membrane and capture by the tubules. *Proc Natl Acad Sci USA* 114: 2958–2963, 2017. doi:10.1073/pnas.1616457114.
55. Hentschel DM, Mengel M, Boehme L, Liebsch F, Albertin C, Bonventre JV, Haller H, Schiffer M. Rapid screening of glomerular slit diaphragm integrity in larval zebrafish. *Am J Physiol Renal Physiol* 293: F1746–F1750, 2007. doi:10.1152/ajprenal.00009.2007.
56. D'souza AA, Shegokar R. Polyethylene glycol (PEG): a versatile polymer for pharmaceutical applications. *Expert Opin Drug Deliv* 13: 1257–1275, 2016. doi:10.1080/17425247.2016.1182485.
57. Zeuzem S, Welsch C, Herrmann E. Pharmacokinetics of peginterferons. *Semin Liver Dis* 23 Suppl 1: 23–28, 2003. doi:10.1055/s-2003-41631.
58. Wu T-S, Yang J-J, Yu F-Y, Liu B-H. Evaluation of nephrotoxic effects of mycotoxins, citrinin and patulin, on zebrafish (*Danio rerio*) embryos. *Food Chem Toxicol* 50: 4398–4404, 2012. doi:10.1016/j.fct.2012.07.040.
59. Kotb AM, Müller T, Xie J, Anand-Apte B, Endlich K, Endlich N. Simultaneous assessment of glomerular filtration and barrier function in live zebrafish. *Am J Physiol Renal Physiol* 307: F1427–F1434, 2014 [Erratum in *Am J Physiol Renal Physiol* 314: F142, 2018]. doi:10.1152/ajprenal.00029.2014.
60. Kamen BA, Smith AK. A review of folate receptor alpha cycling and 5-methyltetrahydrofolate accumulation with an emphasis on cell models in vitro. *Adv Drug Deliv Rev* 56: 1085–1097, 2004. doi:10.1016/j.addr.2004.01.002.
61. Samodelov SL, Gai Z, Kullak-Ublick GA, Visentin M. Renal reabsorption of folates: pharmacological and toxicological snapshots. *Nutrients* 11: 2353, 2019. doi:10.3390/nu1102353.
62. Dong X, Al-Jumaily A, Escobar IC. Investigation of the use of a bio-derived solvent for non-solvent-induced phase separation (NIPS) fabrication of polysulfone membranes. *Membranes* 8: 23, 2018. doi:10.3390/membranes8020023.
63. Kramer-Zucker AG, Olale F, Haycraft CJ, Yoder BK, Schier AF, Drummond IA. Cilia-driven fluid flow in the zebrafish pronephros, brain and Kupffer's vesicle is required for normal organogenesis. *Development* 132: 1907–1921, 2005. doi:10.1242/dev.01772.
64. Cerletti A, Drewe J, Fricker G, Eberle A, Huwyler J. Endocytosis and transcytosis of an immunoliposome-based brain drug delivery system. *J Drug Target* 8: 435–447, 2000. doi:10.3109/10611860008997919.
65. Pritchard JB, Miller DS. Mechanisms mediating renal secretion of organic anions and cations. *Physiol Rev* 73: 765–796, 1993. doi:10.1152/physrev.1993.73.4.765.
66. Saengkhae C, Loetchutinat C, Garnier-Suillerot A. Kinetic analysis of fluorescein and dihydrofluorescein effluxes in tumour cells expressing the multidrug resistance protein, MRP1. *Biochem Pharmacol* 65: 969–977, 2003. doi:10.1016/S0006-2952(02)01662-3.
67. Gordon WE, Espinoza JA, Leerberg DM, Yelon D, Hamdoun A. Xenobiotic transporter activity in zebrafish embryo ionocytes. *Aquat Toxicol* 212: 88–97, 2019. doi:10.1016/j.aquatox.2019.04.013.
68. Seternes T, Sørensen K, Smedsrød B. Scavenger endothelial cells of vertebrates: A nonperipheral leukocyte system for high-capacity elimination of waste macromolecules. *Proc Natl Acad Sci USA* 99: 7594–7597, 2002. doi:10.1073/pnas.102173299.
69. Weigel PH. Discovery of the liver hyaluronan receptor for endocytosis (HARE) and its progressive emergence as the multi-ligand scavenger receptor stabilin-2. *Biomolecules* 9: 454, 2019. doi:10.3390/biom9090454.

70. **Yang H, Elmquist WF.** The binding of cyclosporin A to human plasma: an in vitro microdialysis study. *Pharm Res* 13: 622–627, 1996. doi:10.1023/a:1016066609489.
71. **Hill RA, Grutzendler J.** In vivo imaging of oligodendrocytes with sulforhodamine 101. *Nat Methods* 11: 1081–1082, 2014. doi:10.1038/nmeth.3140.
72. **Anzenberger U, Bit-Avragim N, Rohr S, Rudolph F, Dehmel B, Willnow TE, Abdellilah-Seyfried S.** Elucidation of megalin/LRP2-dependent endocytic transport processes in the larval zebrafish pronephros. *J Cell Sci* 119: 2127–2137, 2006. doi:10.1242/jcs.02954.
73. **Hayashi Y, Takamiya M, Jensen PB, Ojea-Jiménez I, Claude H, Antony C, Kjaer-Sorensen K, Grabher C, Boesen T, Gilliland D, Oxvig C, Strähle U, Weiss C.** Differential nanoparticle sequestration by macrophages and scavenger endothelial cells visualized in vivo in real-time and at ultrastructural resolution. *ACS Nano* 14: 1665–1681, 2020. doi:10.1021/acsnano.9b07233.
74. **Chen Z, Luciani A, Mateos JM, Barmettler G, Giles RH, Neuhauss SCF, Devuyst O.** Transgenic zebrafish modeling low-molecular-weight proteinuria and lysosomal storage diseases. *Kidney Int* 97: 1150–1163, 2020. doi:10.1016/j.kint.2019.11.016.

3.2 Part II: X-ray-based microtomography studies

3.2.1 Publication 1

Zebrafish (*Danio rerio*) larvae as a predictive model to study gentamicin-induced structural alterations of the kidney

Jan Stephan Bolten, Christine Tanner, Griffin Rodgers, Georg Schulz, Soledad Levano, Timm Weitkamp, Samuel Waldner, Ramya Deepthi Puligilla, Daniel Bodmer, Bert Müller, Jörg Huwyler

PLOS ONE 18(4): e0284562

doi: 10.1371/journal.pone.0284562

Personal contribution:

My contribution to this research article includes the planning, design, and execution of scientific experiments and analysis. I co-performed X-ray microtomography experiments at the synchrotron facility in Soleil and was involved in the post-processing quantification. Furthermore, I created all figures and tables and wrote the first draft.

RESEARCH ARTICLE

Zebrafish (*Danio rerio*) larvae as a predictive model to study gentamicin-induced structural alterations of the kidney

Jan Stephan Bolten¹, Christine Tanner², Griffin Rodgers², Georg Schulz², Soledad Levano³, Timm Weitkamp⁴, Samuel Waldner¹, Ramya Deepthi Puligilla¹, Daniel Bodmer³, Bert Müller², Jörg Huwyler¹*

1 Division of Pharmaceutical Technology, Department of Pharmaceutical Sciences, University of Basel, Basel, Switzerland, **2** Biomaterial Science Center, University of Basel, Basel, Switzerland, **3** Department of Biomedicine, University Hospital Basel, Basel, Switzerland, **4** Synchrotron SOLEIL, Saint-Aubin, France

* joerg.huwyler@unibas.ch



OPEN ACCESS

Citation: Bolten JS, Tanner C, Rodgers G, Schulz G, Levano S, Weitkamp T, et al. (2023) Zebrafish (*Danio rerio*) larvae as a predictive model to study gentamicin-induced structural alterations of the kidney. PLoS ONE 18(4): e0284562. <https://doi.org/10.1371/journal.pone.0284562>

Editor: Domokos Máthé, Semmelweis University, HUNGARY

Received: January 13, 2023

Accepted: April 3, 2023

Published: April 20, 2023

Copyright: © 2023 Bolten et al. This is an open access article distributed under the terms of the [Creative Commons Attribution License](https://creativecommons.org/licenses/by/4.0/), which permits unrestricted use, distribution, and reproduction in any medium, provided the original author and source are credited.

Data Availability Statement: [Supporting information](#), including representative tomography data, is available in a public Zenodo data repository (<https://doi.org/10.5281/zenodo.7006260>).

Funding: This project was supported by a grant (SCAHT-GL 21-09) from the Swiss Centre for Applied Human Toxicology – SCAHT - for R.P. (<https://www.scaht.org/en/>). Equipment used for this study (ANATOMIX) is an Equipment of Excellence (EQUIPEX) funded by the Investments for the Future program of the French National

Abstract

Nephrotoxicity is an important drug safety aspect to be assessed during drug discovery and development. To study renal toxicity, *in vitro* cell-based assays are often used. Unfortunately, translating the results of such cell assays to vertebrates including human remains challenging. Therefore, we aim to evaluate whether zebrafish larvae (ZFL) could serve as a vertebrate screening model to detect gentamicin-induced changes of kidney glomeruli and proximal tubules. To validate the model, we compared the results of ZFL with those obtained from kidney biopsies of gentamicin-treated mice. We used transgenic zebrafish lines expressing enhanced green fluorescent proteins in the glomerulus to visualize glomerular damage. Synchrotron radiation-based computed tomography (SR μ CT) is a label-free approach providing three-dimensional representations of renal structures with micrometre resolution. Clinically used gentamicin concentrations induce nephrotoxicity and affect glomerular and proximal tubular morphology. Findings were confirmed in mice and ZFL. There was a strong correlation between fluorescent signals in ZFL, SR μ CT-derived descriptors of glomerular and proximal tubular morphology and the histological analysis of mouse kidney biopsies. A combination of SR μ CT and confocal microscopy provides unprecedented insights into anatomical structures of the zebrafish kidney. Based on our findings, we suggest to use ZFL as a predictive vertebrate screening model to study drug-induced nephrotoxicity and to bridge the gap between cell culture-based test systems and experiments in mammals.

Introduction

The kidney is an essential excreting organ. Renal function comprises glomerular filtration, tubular excretion, and tubular reabsorption. Thereby, certain xenobiotics accumulate within the kidney and may cause nephrotoxicity at the vascular, glomerular, or tubular level. Examples of such nephrotoxic compounds include aminoglycosides, heavy metals, and antiviral

Research Agency (ANR), project NanoimagesX, grant no. ANR-11-EQPX-0031. The funders had no role in study design, data collection and analysis, decision to publish, or preparation of the manuscript.

Competing interests: The authors have declared that no competing interests exist.

Abbreviations: Dpf, days post-fertilization; eGFP, enhanced green fluorescent protein; FITC, Fluorescein isothiocyanate; H&E, hematoxylin and eosin; hpf, hours post-fertilization; hpi, hours post-injection; PAS, periodic acid-Schiff stain; PCT, proximal convoluted tubule; PST, proximal straight tubule; PTC, proximal tubule cell; PTU, 1-phenyl-2-thiourea; SI, Signal intensity; SR μ CT, synchrotron radiation-based computed tomography; Tg, transgenic; ZFL, zebrafish larva(e); μ CT, micro computed tomography.

agents [1]. In clinical settings, therapies with potentially nephrotoxic drugs need to be monitored, and doses have to be adjusted in the case of renal impairment. For instance, nephrotoxic side effects are common in patients treated with the antibiotic drug gentamicin. In 50% of patients, signs of nephrotoxicity can be detected after 14 days of drug therapy [2, 3]. Gentamicin-induced nephrotoxicity is thus clinically relevant and was described as a class effect of aminoglycosides leading to acute kidney injury [4]. The toxic effect is associated with receptor-mediated accumulation in renal epithelial cells by megalin/ cubulin [5, 6].

The problem of potential nephrotoxic side effects of drugs should be addressed during the early phases of preclinical development. Usually, *in vitro* cell-based assays are standard methods for safety and toxicity assessments [7]. They are cost-effective and provide mechanistic insights. However, *in vitro* assays do not cover certain renal functions, such as glomerular filtration [7, 8]. Therefore, findings must be confirmed in living organisms, which is a demanding task. Here, various challenges have to be addressed. Animal experiments are time-consuming, involve substantial costs and rely on *in vivo* experimentation with higher and more complex vertebrates, such as rats and mice. There is an urgent and unmet need to reduce, replace, and refine animal models (as described in the 3R principles) and establish animal-reducing (screening) *in vivo* test systems.

Previously we demonstrated that zebrafish larvae (ZFL) between two and four days post-fertilization (dpf) can be used as a predictive vertebrate *in vivo* screening model for nanomedicine [9]. ZFL are transparent, have a short generation time, and have the regulatory status of cell culture models up to 120 hours' post-fertilization (hpf). They are widely used in developmental biology, toxicology, and pharmacology [10, 11] including nephrotoxicology [12, 13]. Intravenous (*i.v.*) administration of fluorescent substances allows for studying the pharmacokinetics and tissue distribution of test compounds [8, 14]. Semiquantitative assessment of systemic circulation and extravasation of intravenously injected drug formulations [14, 15] allows for extrapolation to higher vertebrates including rodents.

Previously, we could demonstrate that 3-to-4-day-old ZFL has fully developed renal functions [8]. The teleost pronephron shares high similarities with the function and anatomy of the vertebrate kidney [16, 17]. Indeed, ZFL were used to study aspects of nephrotoxicity on cellular and glomerular levels [12, 18, 19].

Nevertheless, it is still unclear how nephrotoxins affect excreting organs of the ZFL, especially with respect to the morphology of the pronephron. Therefore, the present study aimed to clarify whether ZFL can be used as a model for the morphological characterization of kidneys exposed to toxic drugs and for the extrapolation of such results to higher vertebrates.

For this study, gentamicin sulphate, a well-established nephrotoxic antibiotic drug, was chosen as a model compound to induce acute toxicity in proximal tubules [20]. Several studies in ZFL have demonstrated functional impairment of glomerular filtration upon gentamicin treatment [19, 21]. These results correlate with clinical findings [22]. We, therefore, treated ZFL with nephrotoxic concentrations of gentamicin and used a transgenic zebrafish reporter line that expresses enhanced green fluorescent protein (eGFP) in the glomerulus/proximal convoluted tubule cells [23]. Glomerular impairment was visualized by confocal microscopy. SR μ CT [24–27] was used for three-dimensional visualization of ZFL and mouse kidney biopsies and the semiquantitative evaluation of morphological changes. By SR μ CT, a label-free visualization of anatomical structure can be achieved [24], in our case, at 0.65 μ m pixel size. A scheme of workflow and methods is provided in Fig 1. To our knowledge, SR μ CT was not used previously to assess renal damage. We, therefore, used drug-treated zebrafish larvae and animals to visualize and quantify structural alterations of the kidney after exposure to the nephrotoxin gentamicin.

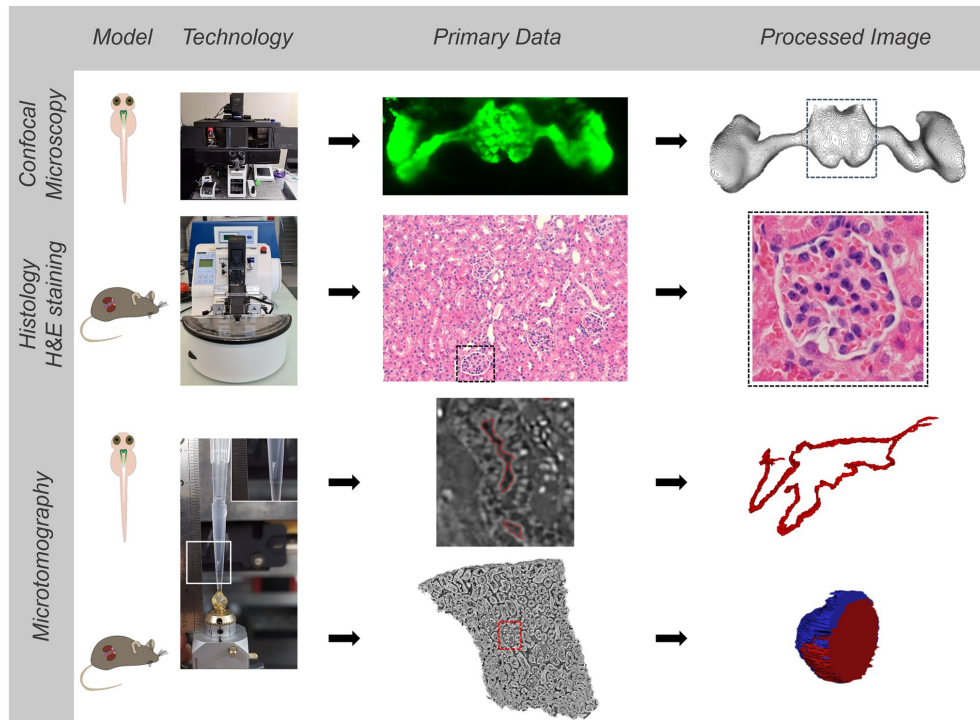


Fig 1. Analytical technologies, workflow, and outcome. Summary of employed imaging strategies to study toxic effects using zebrafish pronephros and mouse kidney biopsies. Methods include confocal laser scanning microscopy, synchrotron radiation-based computed tomography (SR μ CT), and semiquantitative image analysis of H&E/PAS stained histology slides.

<https://doi.org/10.1371/journal.pone.0284562.g001>

Materials and methods

Animals

Five- to six-week-old C57BL/6J mice were purchased from Janvier Laboratories (France). The animals were housed in pathogen-free conditions at the animal facility of the Department of Biomedicine of the University Hospital Basel. All methods used on the animals were chosen to minimize pain. In addition, animals were monitored daily during gentamicin treatment using a score sheet. Zebrafish husbandry and intravenous injections were done as described [8]. Animal and zebrafish experiments were carried out in accordance with Swiss animal welfare regulations. They were approved by regulatory authorities of the Canton Basel Stadt (License 2755_29404 for mice/ 1027H, 1014HE2, 1014G for zebrafish studies).

Materials

Gentamicin sulfate (725 g/mol) was purchased from Biowest (Nuaille, France). Agarose, 1-phenyl-2-thiourea (PTU) and ethyl-3-aminobenzoate methanesulfonate (MS-222, tricaine) were purchased from Sigma-Aldrich (Buchs, Switzerland). The transgenic (Tg) wt1b:eGFP

ZFL line expressing enhanced green fluorescent protein (eGFP) in the glomerulus and parts of the PCT were kindly provided by Prof. Dr. Schiffer from the University of Erlangen in Germany [23].

Intravenous injections and imaging of zebrafish larvae

Regarding terminology, we follow the life stage definitions established by Kimmel et al. [28], which defines >72 hpf old zebrafish as "larvae". In brief, eggs from adult zebrafish were collected from different parents 0.5–1 hpf and kept at a temperature of 28°C in zebrafish culture media [29].

The number of larvae in a 25-mL dish did not exceed 100. The formation of pigment cells was suppressed by adding 30 µg/ml 1-phenyl-2-thiourea (PTU) to the media. 72 and 96 hpf hatched ZFL were embedded in 0.3% agar containing PTU and tricaine (0.01%). Experiments were carried out at room temperature. Randomly chosen larvae were injected with a calibrated volume of 1 nL of 14.4, 21 and 42 mM stock solutions of gentamicin sulfate into the cardinal vein (CV) above the heart. Injected sample volume was verified by calibration measurements using a reticle mounted on a Leica SAPO binocular eyepiece. For intravenous injections, a micromanipulator (Wagner Instrumentenbau, Schöffengrund, Germany), a pneumatic Pico Pump PV830 (World Precision Instruments, Sarasota, FL, US), and a Leica SAPO microscope (Leica, Wetzlar, Germany) were applied. Larvae were immobilized in agar and laid on their back for imaging. The kidney region was imaged 24 hours post-injection (hpi) using an Olympus FV3000 inverted confocal laser scanning microscope (Olympus Ltd., Tokyo Japan) equipped with a 30X UPIanSApo (numerical aperture of 1.05) objective. Confocal images were acquired using a sequential line scan, an excitation wavelength of 488 nm (argon laser) and emission wavelengths of 500 to 540 nm.

Signal intensity quantification and post-processing of images

Confocal microscopy images were analyzed and edited using the open-source OMERO software (version 5.4.10, <https://www.openmicroscopy.org/omero/>) as an image-processing program. Signal intensities (SI) in distinct organs were quantified using the open-source Fiji image analysis software (version 2.1.0/1.53c, <https://imagej.net/software/fiji/>) as described [8]. Controls and corresponding treatment groups were analyzed during the same experiment and using the same laser and microscopy settings. A self-written Fiji script allowed for the automatic quantification of SI based on maximum intensity projections using a selected threshold. SI are presented as fold-change normalized to the mean of the PBS-treated control. Tubular dilatation was scored semi-quantitatively by a blinded observer who evaluated PAS-stained sections of nine microscopy images of three control and three treated mice. At least 20 PCT were examined at 40x magnification.

Sample processing for microtomography experiments

ZFL were processed for microtomography experiments as described [24]. In brief, ZFL were euthanized with tricaine methanesulfonate and fixed for one hour in 4% paraformaldehyde (PFA). Fixed specimens were dehydrated using ethanol at increasing concentrations (25%, 50%, 70%, and ≥99.8%) for 15 min each under gentle agitation and stored at a temperature of 4°C. Larvae fixed in ethanol were transferred into plastic pipette tips filled with ethanol shortly before imaging and mounted on a sample holder for imaging.

Kidney tissue samples were obtained from mice treated intraperitoneally with gentamicin at 150–170 mg/kg body weight daily for ten days. The saline-treated animals were used as control animals. After 14 days, mice were euthanized by intraperitoneal injection of 150 mg/kg

pentobarbital, perfused transcardially with phosphate-buffered saline (PBS), and the kidneys were isolated. For histology examination, the right kidney was cut in half, fixed in 4% ice-cold PFA for 40 hours, washed with PBS, and transferred to 70% ethanol. For microtomography measurements, the left kidney was immediately put on dry ice after extraction, followed by -80°C freezing. Needle biopsies were prepared by punching small cylindrical samples from frozen tissue using a G18 injection needle. They were immediately transferred to ice-cold 4% PFA for half an hour. Biopsies were washed three times with ethanol, stored in $>99\%$ ethanol, and then mounted on a microtomography sample holder.

Histology of mice kidney biopsies

Kidneys were paraffinized using a tissue processor and a tissue embedding station (TPC15, Medite Medical GmbH, Burgdorf, Germany). In brief, $3\ \mu\text{m}$ paraffin tissue slices were prepared using a Thermo Scientific rotary microtome (Waltham, MA, US) and mounted on thin glass slides (Menzel, Braunschweig, Germany). Histological slices were stained with hematoxylin and eosin (H&E) or periodic acid-Schiff stain (PAS) performed by a Gemini AS automated stainer (Eprexia, Portsmouth, NH, US). Stained slices were imaged using a laser microscope (Olympus Ltd., Tokyo, Japan) equipped with a 40X UPIanSApo (numerical aperture of 1.05) objective. To quantify the glomerular area, samples were blinded to limit the biased interpretation of treatment and were analyzed by up to three operators. Thirty glomeruli per mouse were visually examined. The ratio between the mean glomerulus area and the mean glomerulus area occupied by cells was determined based on manual segmentation using a Wacom Intuos pen tablet (Wacom, Kazo, Japan) and Fiji software for quantification.

Synchrotron radiation-based microtomography analysis

Synchrotron radiation-based computed tomography (SR μ CT) was performed at the ANATOMIX beamline of Synchrotron SOLEIL (Saint-Aubin, France) [30]. The undulator X-ray source was set to a magnetic gap of 8.3 mm. A $10\ \mu\text{m}$ Au filter was implemented to obtain a filtered white beam with a mean photon energy of around 17 keV. The detector was placed 50 mm downstream of the sample to allow for propagation-based phase contrast. Projections were recorded with an effective pixel size of $0.65\ \mu\text{m}$. The detector consisted of a $20\ \mu\text{m}$ LuAG scintillator coupled via a $10\times$ objective to a scientific CMOS camera (Hamamatsu Orca Flash 4.0 V2, 2048×2048 pixels, $6.5\ \mu\text{m}$ physical pixel size) [31]. An exposure time of 50 ms was selected, providing an average detector signal of approximately 30,000 analog-digital units (ADU) in the flat field. For tomographic imaging, 4,000 projections were recorded over 180° in flyscan mode. Each height step covered a cylindrical volume with 1.3 mm diameter and 1.3 mm height and required a scan time of approximately 3.5 minutes. Depending on alignment, one or two height steps were needed to image the whole zebrafish larva.

Tomographic reconstruction was performed using the software pipeline and computational resources available at the ANATOMIX beamline, which uses the PyHST2 software (ESRF, Grenoble, France) for the filtered backprojection step. Prior to reconstruction, projections were phase-retrieved using Paganin's filter [32] with a kernel length of $15\ \mu\text{m}$ [33]. A double flat-field correction was applied to suppress ring artefacts [33].

Three-dimensional rendering and segmentation

The lumen of proximal tubules of ZFL and glomeruli of mouse biopsies were manually segmented using Amira software (Version 6.2.0, ThermoFisher, Massachusetts, US). The segmented volume was subsequently analyzed in Matlab (release R2020a, The MathWorks Inc., Natick, US). Tubules of treated ZFL were compared by extracting their centerlines via medial

axis transformation. The medial axis consists of all points which have more than one closest point on the object's boundary. It was extracted with the Matlab function "bwskel". The tubules were aligned based on the manually identified turning point (TP) and the geodesic distance along the centerline. The geodesic distance was determined by reducing the three-dimensional centerline coordinates to one dimension via the Isomap mapping software provided by van der Maaten et al. [34]. The length, as well as spatially-resolved diameters, cross-section areas, and SI of the areas, were calculated for each centerline and summarized.

Statistical analysis

Statistical analysis was performed with GraphPad Prism Version 8.0.2 (GraphPad Software, San Diego, CA) using one-way analysis of variance (ANOVA) followed by Dunnett's multi-comparison tests or unpaired two-tailed t-test analysis for direct comparisons. Where appropriate, individual data points are presented as dot plots next to the group's average and standard deviation (SD). The number of individual ZFL and mice is indicated as (n). The statistical significance of the difference against the control population was evaluated at the 0.05 and 0.001 probability level and marked by asterisks. Data are shown as a box-and-whisker plot indicating the datasets' minimum, maximum, median, first quartile, and third quartile.

Results

The zebrafish larvae's kidney formation is illustrated in Fig 2A. The pronephros consist of two renal tubules that are glomerular fused ventral to the dorsal aorta at the larvae's midline [16]. The pronephros can be divided into three functional units (Fig 2A). First, the blood is filtered within the glomerulus (GL). The filtrate is collected within the proximal tubules (PT) and drained through the distal tubules (DT) to the cloaca. The anatomy and morphology of the upper renal system of the ZFL can be visualized using transgenic lines expressing eGFP in the glomerulus and parts of the PT, e.g. Tg(wt1b:eGFP). Confocal laser scanning microscopy allows for the three-dimensional imaging of the glomerulus, marked in Fig 2B by a white dotted quadrant. A confocal laser scanning microscope was used for dorsal imaging. This allows for the quantitative determination of SI and three-dimensional volume calculations of the glomerulus. Results show a steady monotonic decrease in SI of eGFP in the transgenic lines as the concentrations of the injected gentamicin are increased (Fig 2C). The intensity decrease is statistically significant at the 0.001 level for the tested gentamicin concentrations. The volume of the glomerulus, calculated based on thresholding the eGFP signal, is not significantly changed for injected concentrations up to 1 nL of 21 mM gentamicin. However, for the highest injected concentration (1 nL of 42 mM), we observed a statistically significant decrease at the 0.05 level of the glomerulus volume.

In Tg(wt1b:eGFP) ZFL, eGFP expression is limited to the glomerulus and the proximal tubules. To analyze the tubular system more completely, we used SR μ CT with voxels of $(0.65 \mu\text{m})^3$ (Fig 3). As observed, fixation of the samples with PFA was necessary to avoid the formation of gas bubbles in aqueous buffers upon X-ray irradiation. Fig 3A shows two stacked tomograms of control and treated ZFL (1 nL of 42 mM gentamicin injected, 24 h incubation). Applying Paganin's filter, body surfaces and inner organs can be visually inspected after 3D surface rendering. Gentamicin-treated ZFL shows malformations, i.e. a pronounced body curvature. A prominent feature is the enlarged pericardial sac, indicative of cardiac edema caused by acute kidney injury (Fig 3B).

Virtual slices of the processed data through sagittal (XZ), traverse (YZ) and coronal (XY) planes allow for the manual localization of the renal tubules. Representative images are shown in Fig 4. The latter has a weak SI and is easily identifiable. Renal epithelial cells have diverse SI,

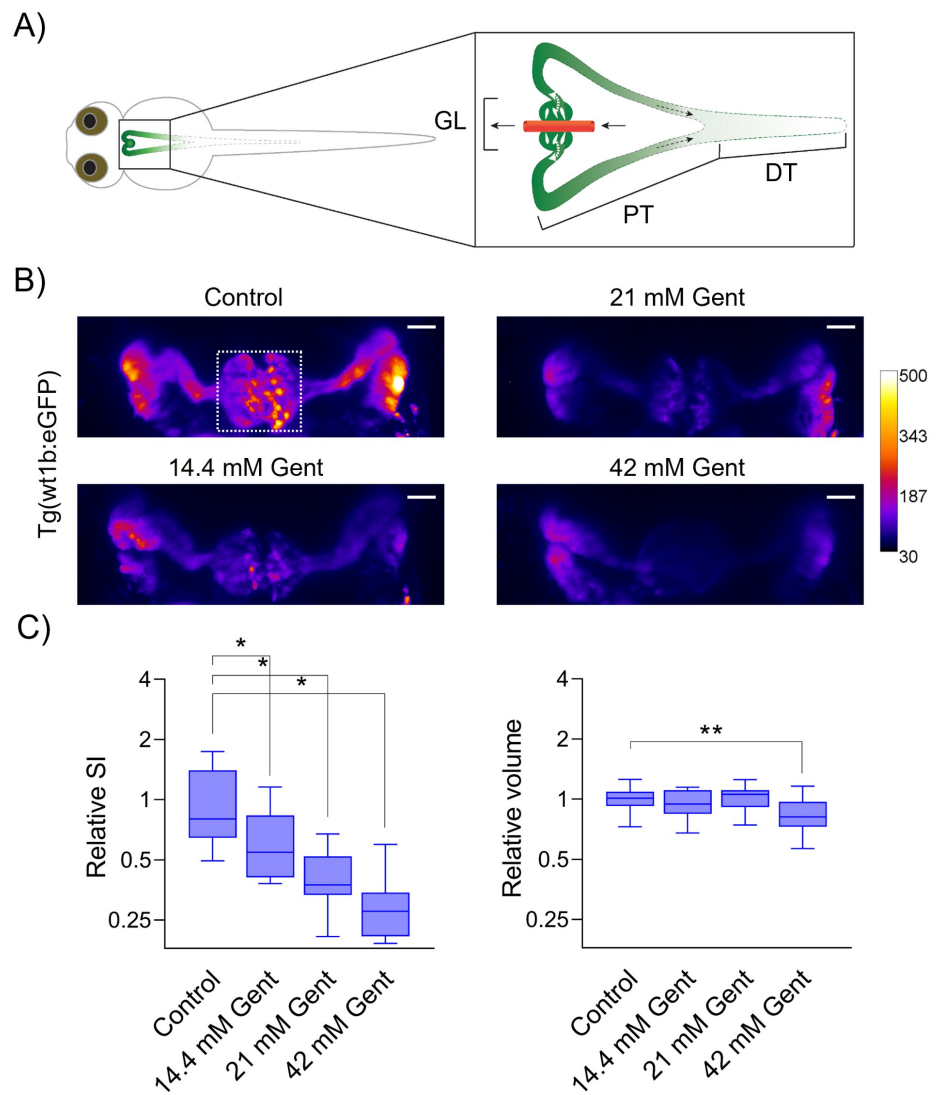


Fig 2. Gentamicin-induced damage to the pronephros in 96 hpf *Tg(wt1b:eGFP)* ZFL. (A) Schematic representation of renal pronephros in 96 hpf ZFL. GL: glomerulus, PT: proximal convoluted and straight tubule, DT: distal early and late tubule. Pronephros are fused together at the midline above the yolk and heart. Transgenic expression of eGFP leads to a fluorescent signal (green) in the glomerulus and upper parts of the tubules. (B) 72 hpf *Tg(wt1b:eGFP)* ZFL were injected with 1 nL of 14.4 mM to 42 mM gentamicin. Representative images of maximum projections. The color-coded heat map indicates SI, e.g. white correlates to high SI values and black to weak SI. Scale bar: 25 μ m. Gent: gentamicin. (C) Relative SI and relative volume of the glomerulus (panel B, white dotted rectangle) as compared to normalized control is shown using a box-and-whisker plot, $n \geq 10$ ZFL. * $p < 0.001$, ** $p < 0.05$.

<https://doi.org/10.1371/journal.pone.0284562.g002>

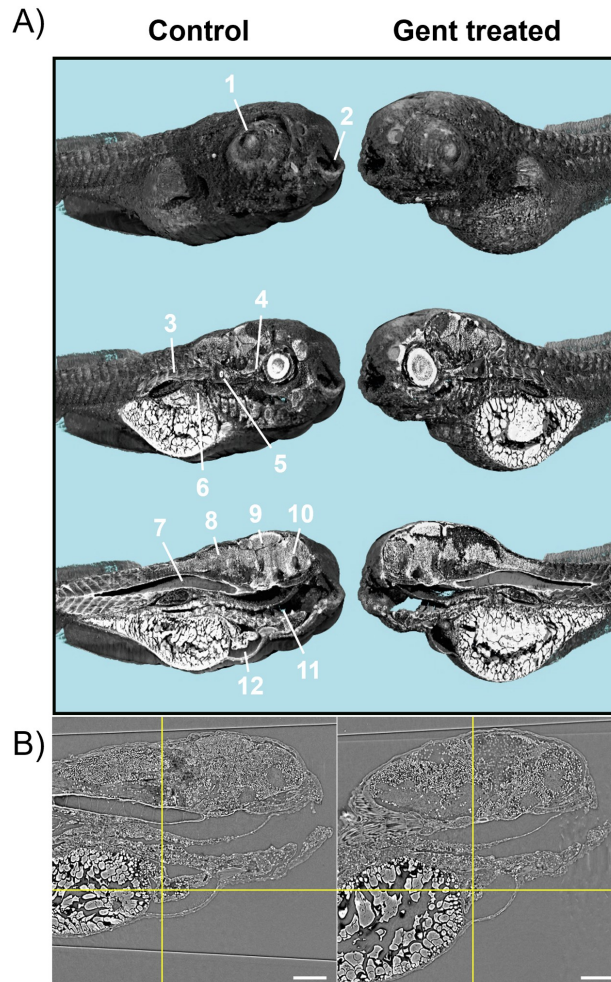


Fig 3. Synchrotron radiation-based computed tomography (SR μ CT) of control and gentamicin-treated ZFL. (A) 3D renderings of 96 hpf ZFL at 24 hpi of 1 nL of control buffer (left panels) or 1 nL of 42 mM gentamicin (right panels) with sagittal cuts. Pixel size: 0.65 μ m. Anatomical structures: 1 = eye lens, 2 = mouth, 3 = muscle tissues, 4 = optical nerve, 5 = otoliths, 6 = liver, 7 = notochord, 8 = hindbrain, 9 = midbrain, 10 = frontbrain, 11 = intestine, 12 = heart. (B) Representative virtual slices through the heart chambers (yellow reticle) of control (left) and 1 nL of 42 mM gentamicin (right) treated ZFL. Scale bar: 100 μ m.

<https://doi.org/10.1371/journal.pone.0284562.g003>

such as cell nuclei (white), cell membranes (dark grey) and cytosols (black). Comparing renal tubules of the gentamicin treated with control ZFL, a clear enlargement of the tubular lumina in the PT region was observed.

To quantify aberrations in the morphology of proximal tubules of gentamicin-treated ZFL, renal tubules were manually segmented in two dimensions (XY and YZ), and diameters along

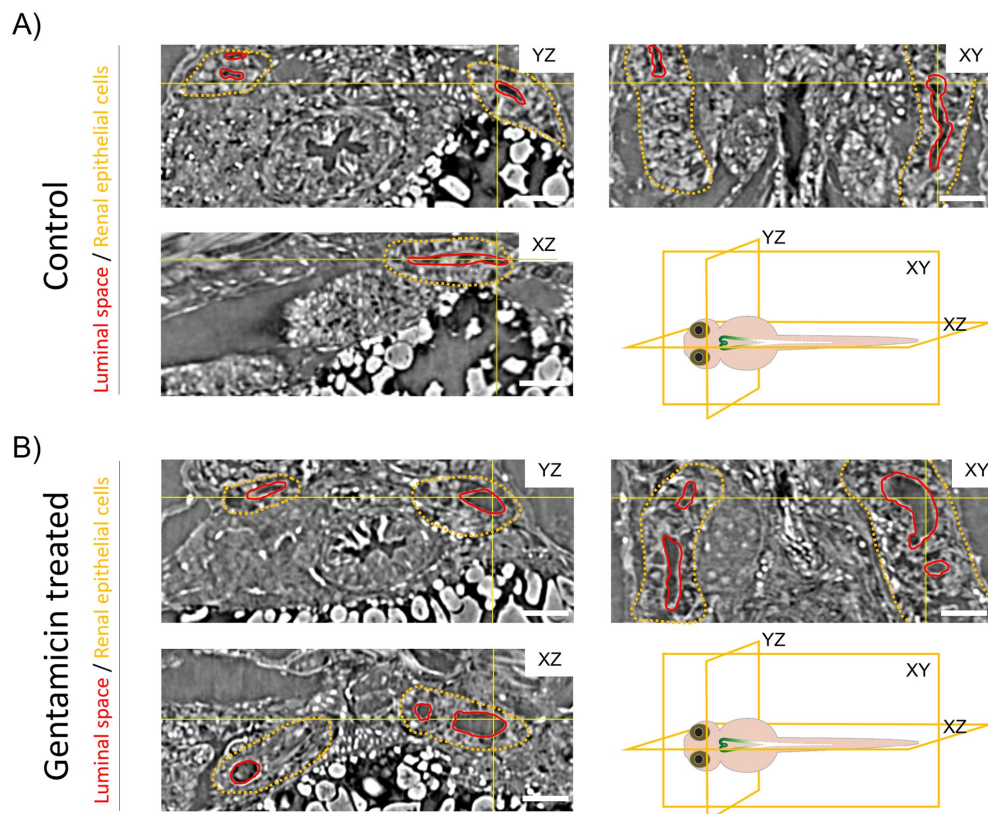


Fig 4. Microtomography-based visualization of the ZFL pronephros. (A) Orthogonal sections from the 4 dpf ZFL through the microtomography volume of PBS (control) and treated with 1 nL of 42 mM gentamicin (24 hour incubation). Yellow lines show the position of the virtual slices, which intersect at the reticle point located in the luminal space. Luminal space is outlined in red, renal epithelial cells are in yellow. Schematic illustrations indicate the cutting planes. Scale bar: 100 μm .

<https://doi.org/10.1371/journal.pone.0284562.g004>

the centerline were determined. A representative 3D rendering of control and treated renal tubules is shown in Fig 5. Confirming observations from the virtual slices in Fig 4, the shape and thickness of the volume of control and treated tubules differ in both a lateral (Fig 5A) and ventral (Fig 5B) view. Based on a three-dimensional segmentation and evaluation, the thickness of renal lumina (Fig 5C) can be represented using a color-coded map. Red indicates enlarged diameters of the luminal space (6 μm), which was observed in gentamicin-treated animals only. Analysis of eight treated and four control ZFL showed no difference in the length of the segmented tubules (Fig 5D) but a statistically significant 1.75-fold increase in diameter (Fig 5E and S1 Fig). Differences in the entire volume are not statistically significant (Fig 5F).

To quantify the extent of tubular damage in distinct tubule sections, the segmented proximal tubule was manually divided into PCT and proximal straight tubules (PST), as shown in Fig 6A. Furthermore, the centerline along the tubules was projected onto a coordinate system

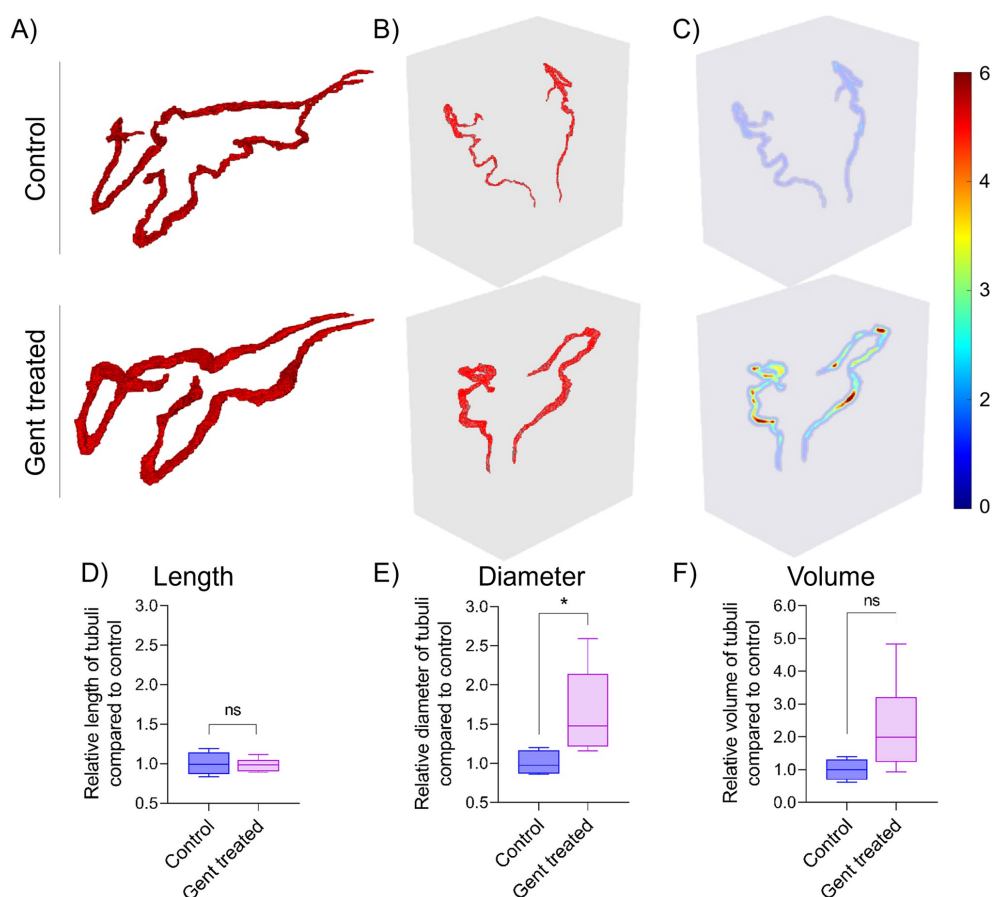


Fig 5. SR μ CT-based reconstruction and quantification of ZFL proximal tubules. Rendered proximal renal tubules of control and gentamicin-treated ZFL (1 nL of 42 mM gentamicin, analysis 24 hpi) are shown in (A) lateral and (B) ventral projection. (C) Color-coded heat map, with values at the centerline corresponding to the diameter of the luminal area (blue: 0 μ m; dark red: 6 μ m) of tubules shown in B. (D, E, F) Semiquantitative analysis of length, diameter, and volume of treated ZFL tubules (n = 8) in terms of fold change as compared to the mean of control ZFL tubules (n = 4). Box plots are shown. *p < 0.05. ns: p > 0.05.

<https://doi.org/10.1371/journal.pone.0284562.g005>

(Fig 6B). The turning point (TP) was defined as zero. The distance between TP and the glomerulus (neck) is approximately 100 μ m essentially in the x-direction, whereas the last segmentable lumen of the nephros is located around 300 μ m with an overall orientation in the y-direction. The area along the center line was plotted for control and gentamicin-treated ZFL. Semiquantitative analysis of distinct regions (-75 μ m to 175 μ m) reveals a significant increase in the tubular lumen of gentamicin ZFL in the PCT but not in the PST.

In a next step, extracted mouse kidneys were subjected to histology and SR μ CT analyses (Fig 7). In contrast to ZFL, the mouse kidney cortex contains a multitude of nephrons (i.e. glomeruli and renal tubules). Histological examination of periodic acid-Schiff (PAS) stained

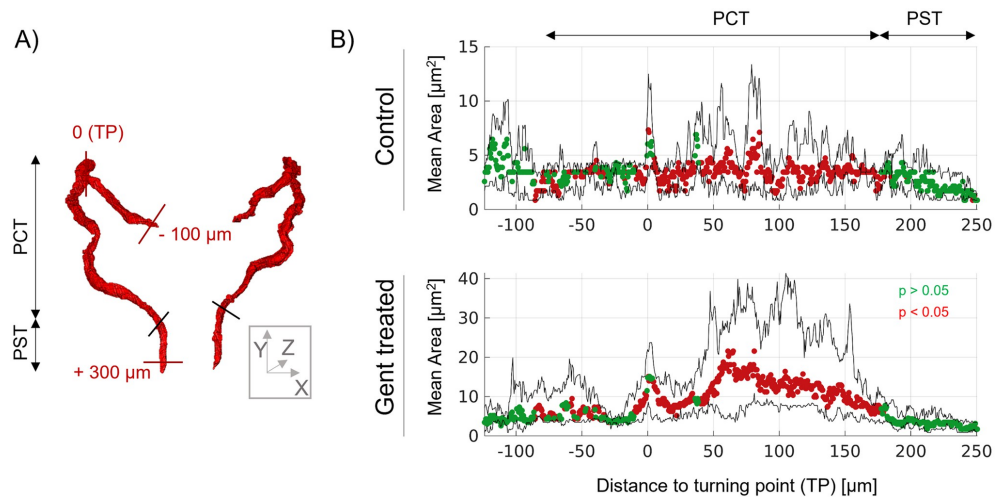


Fig 6. Localization of gentamicin-induced tubular damage. (A) Rendered renal tubules are divided into PCT and PST. Distances to the turning point (TP, defined as zero) are indicated in the direction of the glomerulus (negative values) and towards the cloaca (positive values). (B) The plot of tubule cross-section area against distance from TP. Gentamicin treatment: 1 nL of 42 mM gentamicin, analysis 24 hpi injection. Symbols: mean cross-sectional area, color coded with respect to significant differences between control ($n = 4$) and gentamicin ($n = 8$) treated ZFL. Green symbols: $p > 0.05$. Red symbols: $p < 0.05$.

<https://doi.org/10.1371/journal.pone.0284562.g006>

3 μm -thin tissue sections reveals distinct differences between control and treated animals. Compared to the control, gentamicin-treated kidney biopsies show enlarged PCT lumina, whereas DT are unaffected. More detailed studies focusing on glomeruli are depicted in Fig 7B. Hematoxylin and eosin (H&E) stained kidney sections reveal a homogenous arrangement of mesangial cells (Me) and their Nuclei (Nu) in control animals. The basal membrane (BM) is visible and present, and the Bowman's space (BS) is narrow and uncolored.

In comparison, kidney sections from gentamicin-treated mice show a heterogeneous pattern (Fig 7C right panel). It has an enlarged BS, and the BM is hardly present. Further, cellular waste and debris are located within the glomerular space.

For semiquantitative analysis, histology images of 30 glomeruli of three mice from each treatment group were compared (Fig 7B) and further evaluated. 75% of analyzed PCT of gentamicin-treated mice showed tubular dilatation compared to 13% of the control group (Fig 7C, left panel). The ratio of the glomerulus area divided by the cellular area of the same glomerulus shows a significant 1.2-fold increase ($p < 0.01$) in the gentamicin group (Fig 7C, right panel). The mean glomerular area of the control group was $(3\,337 \pm 322) \mu\text{m}^2$, and the corresponding area of the gentamicin group was $(3\,524 \pm 295) \mu\text{m}^2$ (ns). The mean cellular area of the control group was $(2\,866 \pm 321) \mu\text{m}^2$ vs $(2\,565 \pm 226) \mu\text{m}^2$ (ns) of the gentamicin group. The morphological changes observed using SR μ CT to obtain 3D representations of glomeruli are similar to 2D analysis, but the volumes are statistically significant ($p < 0.01$). Two representative, segmented glomeruli are shown colored in red (Bowman's space) and green (mesangial cells of the glomerulus). Next, the quantitative analysis of five glomeruli from three control and three treated mice was performed (Fig 7E). Gentamicin leads to a 1.4-fold increase in the ratio of the glomerular to cellular volume. Thus, using this alternative imaging method, we could

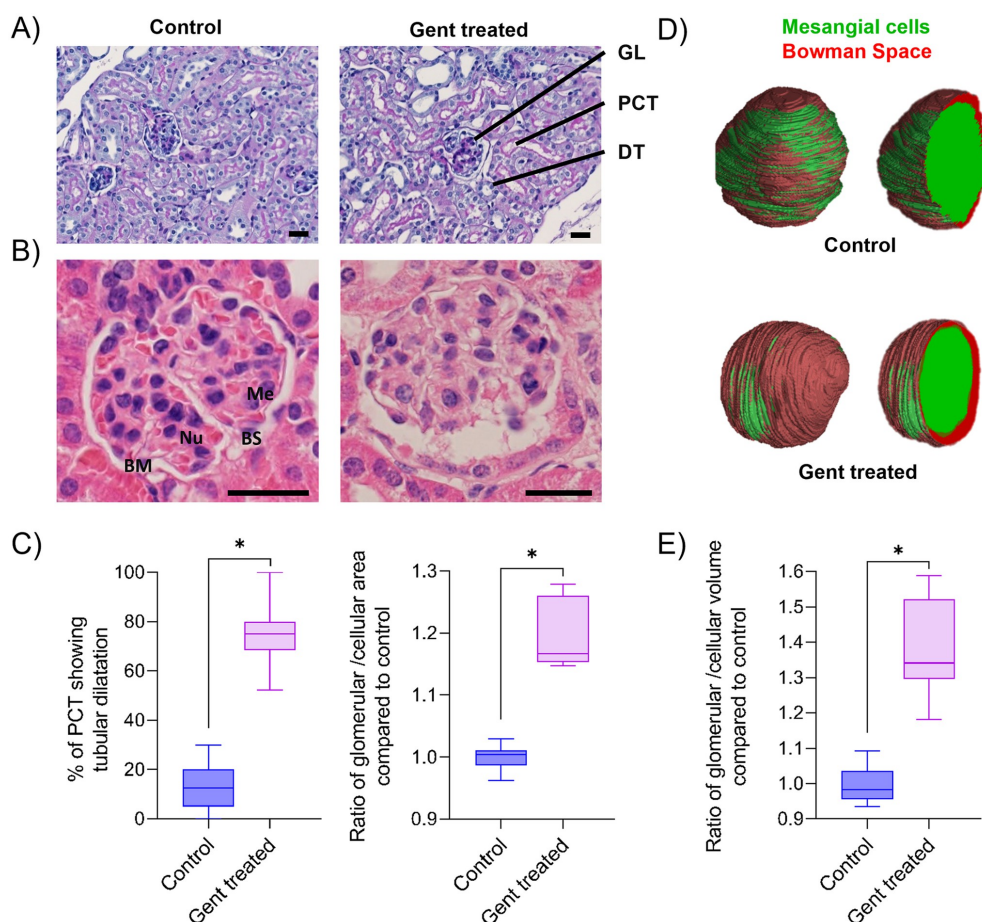


Fig 7. 2D and 3D assessment of kidney damage in gentamicin-treated mice. (A) Representative PAS-stained histology slices (3 μm) from a kidney biopsy of a control and a gentamicin-treated mouse. Gentamicin treatment: daily i.p. injections for ten days of 150 mg gentamicin. Glomerulus = GL, proximal convoluted tubules = PCT, distal tubules = DT. (B) Representative images of an H&E stained 3 μm histological slice of a glomerulus of control and a gentamicin-treated mouse. Mesangial cells = Me, Nuclei = Nu, basal membrane = BM, basal space = BS. (C) Semiquantitative analysis of % of PCT showing tubular dilatation and the ratio of glomerular to cellular area normalized to the mean of the control. 180 PCT of three mice (control or treated) and 30 glomeruli of six mice (control or treated) were analyzed, respectively. (D) SR μ CT analysis and visualization of a representative 3D rendered glomerulus of a control and a gentamicin-treated mouse. Mesangial cells are labelled in green, and Bowman's space in red. (E) SR μ CT-based analysis of the ratio of glomerular to cellular volume as compared to the mean of the control. Box plots are shown of five manually segmented glomeruli of three mice each. * $p < 0.01$. Scale bar: 25 μm .

<https://doi.org/10.1371/journal.pone.0284562.g007>

demonstrate that the glomerular volume is significantly ($p < 0.01$) elevated in the gentamicin-treated group ($81\,083\ \mu\text{m}^3 \pm 19\,479\ \mu\text{m}^3$ vs $25\,379\ \mu\text{m}^3 \pm 7\,756\ \mu\text{m}^3$). In contrast, the cellular volume is not significantly ($p = 0.09$) reduced compared to the control group ($121\,265\ \mu\text{m}^3 \pm 15\,682\ \mu\text{m}^3$ vs $131\,994\ \mu\text{m}^3 \pm 22\,455\ \mu\text{m}^3$).

Discussion

Xenobiotics such as the aminoglycoside antibiotic gentamicin accumulate within renal tissue during their elimination and cause nephrotoxicity. We used in the present study ZFL as a vertebrate model to assess the impact of gentamicin on kidney morphology. Findings were compared to results from SR μ CT of kidney biopsies of gentamicin-treated mice. We could demonstrate that extrapolation of findings in ZFL to rodents is possible thus confirming similarity of anatomical and functional structures of the developing pronephros of ZFL and corresponding structures in mammals, including humans [16, 35].

Zebrafish larvae offer the possibility to inject a defined dose into the bloodstream using an appropriate injection platform. Hereby, an initial concentration is known, and blood concentration follows a kinetic profile as done with other *in vivo* (vertebrate) studies. Bathing zebrafish larvae in a toxin solution is an easier approach but lacks information about initial blood concentrations. Therefore, we believe that *i.v.* injection of nephrotoxins into zebrafish larvae is the better and more vertebrate-relevant approach for nephrotoxicity studies. This approach was also confirmed in other literature reports using zebrafish larvae in nephrology [12, 36].

The concentration used for zebrafish studies in this study was chosen based on clinical relevant plasma concentrations in the range of 2 to 20 μ M gentamicin, daily doses for seven to ten days [37, 38]. For serious bacterial infections, a longer course of therapy might be necessary. With respect to zebrafish, the model drug was intravenously injected into the cardinal vein using an injection volume of 1 nL, corresponding to approximately 0.8% of the total blood volume of a 96 hpf ZFL [8]. This was a prerequisite to obtain defined exposure of ZFL towards gentamicin and to avoid potential interference with intestinal metabolism. Trough to peak plasma concentrations reached in our study (single bolus injection) are therefore estimated to cover a range of 12 to 350 μ M gentamicin.

Using a transgenic zebrafish line expressing eGFP in the glomerulus and parts of proximal renal tubules under the *wt1b* promoter [23], mean SI in the glomerulus was assessed 24 hours post gentamicin injection. A concentration-dependent SI decrease indicated a cytotoxic effect interfering with eGFP expression. These findings are in agreement with previous studies using wild-type ZFL at three dpf [21]. Functional assays using FITC-DX 70 kDa showed that gentamicin-induced nephrotoxicity lead to impaired glomerular filtration resulting in an acute kidney injury with loss of cell polarity of proximal tubules [12, 18]. Exposure towards different types of nephrotoxins led to impaired kidney function (e.g., reduced clearance of FITC-dextran) and upregulation of kidney injury marker genes [21]. It should be noted that a decrease in the fluorescent SI of a marker protein is not necessarily indicative of renal damage. We therefore used synchrotron radiation-based microtomography with a pixel size of 0.65 μ m to visualize morphological aberrations of renal tubules. It was thus possible to study unstained organs, including renal tubules and the changes in the morphology of the heart. In contrast to previous studies using a mean photon energy of 10.5 keV [24], the central photon energy used in this study was higher, at around 17 keV. However, this did not offer additional advantages as images were of similar quality. It is tempting to speculate that recent laboratory-based tomography instruments providing phase-contrast capabilities, liquid metal X-ray source technology, and X-ray detector optics may provide a spatial and density resolution comparable to the present study [25]. This will provide opportunities for a broader applicability of the presented tomography-based approach, although at the expense of longer acquisition times.

The toxic effect of gentamicin caused impairment of larval development in general, leading to body curvature and cardiac edema [18], in addition to renal impairment. This finding is similar to previous studies using the same transgenic line to assess drug-induced kidney malformation and other toxicants [39, 40]. The pronephric kidney of the ZFL is located caudal of

the head and above the yolk. The glomerulus is located above the heart. The microtomography cross sections easily reveal the pronephros since it is a pair-wise organ with a low x-ray absorbing fluid-filled luminal space surrounded by a high x-ray absorbing cell layer.

In contrast, the segmentation of PCT tubules with a diameter of two to 30 pixels from the surrounding tissue was a challenge. We had to rely on manual segmentation, since automated procedures using dedicated software tools were not applicable. Consequently, we focused on determining volumetric parameters (e.g., tubule diameter, length, area, and volume). This approach allows for a label-free microtomography imaging of organ-specific morphological aberrations caused by nephrotoxin in ZFL. Thus, in contrast to previous studies, no density-based labelling strategies using density-rich elements such as zinc, iron and copper [41] were employed.

This study used SR μ CT analysis to visualize and analyze the pronephros of ZFL. Glomeruli were not segmented, since mesangial cells are densely packed within Bowman's capsule. Therefore, no separation of cell layers was possible. In mice, renal tubules were analyzed using 2D tissue sections. This was sufficient to allow for rapid and precise evaluation of tubular toxicity.

There is a strong correlation between findings in the ZFL and rodents. In agreement with ZFL findings, histology sections of H&A/PAS-stained mouse renal biopsies revealed gentamicin-induced damage of glomeruli and an increase of the lumen of proximal tubules. This correlated with findings in the rat [42–44] and was corroborated by three-dimensional reconstruction of murine glomeruli based on SR μ CT analysis. It is noteworthy that 3D image reconstruction allowed for a visualization of the whole glomerulus, which is superior to the analysis of histology sections due to the asymmetric distribution of collapsed apoptotic cells and capillaries within the damaged glomerulus [45]. Functional studies in gentamicin-treated mice confirms renal impairment by elevated kidney function biomarkers, such as serum creatinine, blood urea nitrogen and urea together with increased cytokine levels, such as interleukin-6 and tumor necrosis factor-alpha (TNF- α) [46, 47].

Conclusion and outlook

ZFL is a useful *in vivo* vertebrate screening model that is frequently used in pharmacological, toxicological and nanomedicine research [9, 21]. The study using gentamicin as a model nephrotoxin reveals a similarity between morphological aberrations in ZFL and rodent kidney. Glomerular and proximal tubular damage can be visualized by confocal microscopy using the Tg(wt1b:eGFP) fish line that expresses GFP in the glomerulus and parts of the PCT. Alternatively, label-free SR μ CT-based tissue analysis can be employed. We, therefore, propose ZFL as a translational model to assist in the extrapolation from cell-culture-based test systems to mammals. The approach is cost-effective, in agreement with 3R principles of animal welfare, and could therefore be of interest for identifying potential nephrotoxins in drug discovery.

Supporting information

S1 Fig. 3D reconstruction and quantification of four control and eight gentamicin-treated ZFL pronephros.

(DOCX)

S1 Graphical abstract.

(TIF)

S1 Text.

(TXT)

Acknowledgments

The authors thank Dr Kai Schleicher from the Imaging Core facility of the Biocenter (University of Basel) for support with confocal microscopy and image analysis. We thank Prof. Dr. Mario Schiffer (University of Erlangen, Germany) for providing the Tg(wt1b:eGFP) zebrafish line. Prof. Dr Markus Affolter and Dr Heinz Georg Belting (University of Basel) are acknowledged for providing support for zebrafish experiments. Further, we thank Prof. Dr Alex Odermatt (University of Basel) for the scientific exchange and discussions. Dr. Christian M. Schlepütz is acknowledged for support with preliminary μ CT experiments at the TOMCAT beamline of the Swiss Light Source at the Paul Scherrer Institute in Switzerland. Dr Diego Calabrese of the Histology Core Facility of the Department of Biomedicine is acknowledged for support with histology preparations. The authors acknowledge the Synchrotron Soleil in Saint-Aubin for providing beamtime (proposal #20211541) and Melissa Osterwalder (University of Basel) for support with pilot experiments.

Author Contributions

Conceptualization: Jan Stephan Bolten, Christine Tanner, Griffin Rodgers, Soledad Levano, Daniel Bodmer, Bert Müller, Jörg Huwyler.

Data curation: Timm Weitkamp, Samuel Waldner.

Formal analysis: Jan Stephan Bolten, Christine Tanner.

Investigation: Jan Stephan Bolten, Griffin Rodgers, Georg Schulz, Soledad Levano, Timm Weitkamp, Ramya Deepthi Puligilla.

Methodology: Jan Stephan Bolten, Christine Tanner, Jörg Huwyler.

Resources: Timm Weitkamp, Bert Müller, Jörg Huwyler.

Supervision: Timm Weitkamp, Daniel Bodmer, Bert Müller, Jörg Huwyler.

Validation: Jörg Huwyler.

Visualization: Jan Stephan Bolten, Christine Tanner, Georg Schulz, Samuel Waldner, Bert Müller, Jörg Huwyler.

Writing – original draft: Jan Stephan Bolten.

Writing – review & editing: Christine Tanner, Griffin Rodgers, Georg Schulz, Soledad Levano, Timm Weitkamp, Samuel Waldner, Ramya Deepthi Puligilla, Daniel Bodmer, Bert Müller, Jörg Huwyler.

References

1. Naughton CA. Drug-Induced Nephrotoxicity. *Am Fam Physician*. 2008; 78: 743–750. PMID: [18819242](https://pubmed.ncbi.nlm.nih.gov/18819242/)
2. Silan C, Uzun O, Comunoğlu NU, Gokçen S, Bedirhan S, Cengiz M. Gentamicin-induced nephrotoxicity in rats ameliorated and healing effects of resveratrol. *Biol Pharm Bull*. 2007; 30: 79–83. <https://doi.org/10.1248/bpb.30.79> PMID: [17202664](https://pubmed.ncbi.nlm.nih.gov/17202664/)
3. Leehey DJ, Braun BI, Tholl DA, Chung LS, Gross CA, Roback JA, et al. Can pharmacokinetic dosing decrease nephrotoxicity associated with aminoglycoside therapy. *J Am Soc Nephrol*. 1993; 4: 81–90. <https://doi.org/10.1681/ASN.V4I181> PMID: [8400072](https://pubmed.ncbi.nlm.nih.gov/8400072/)
4. Watanabe A, Nagai J, Adachi Y, Katsube T, Kitahara Y, Murakami T, et al. Targeted prevention of renal accumulation and toxicity of gentamicin by aminoglycoside binding receptor antagonists. *J Controlled Release*. 2004; 95: 423–433. <https://doi.org/10.1016/j.jconrel.2003.12.005> PMID: [15023454](https://pubmed.ncbi.nlm.nih.gov/15023454/)
5. Sun J, Hulthenby K, Axelsson J, Nordström J, He B, Wernerson A, et al. Proximal Tubular Expression Patterns of Megalin and Cubilin in Proteinuric Nephropathies. *Kidney Int Rep*. 2017; 2: 721–732. <https://doi.org/10.1016/j.ekir.2017.02.012> PMID: [29142988](https://pubmed.ncbi.nlm.nih.gov/29142988/)

6. Hori Y, Aoki N, Kuwahara S, Hosojima M, Kaseda R, Goto S, et al. Megalin Blockade with Cilastatin Suppresses Drug-Induced Nephrotoxicity. *J Am Soc Nephrol*. 2017; 28: 1783–1791. <https://doi.org/10.1681/ASN.2016060606> PMID: 28052987
7. Allen DD, Caviedes R, Cárdenas AM, Shimahara T, Segura-Aguilar J, Caviedes PA. Cell Lines as In Vitro Models for Drug Screening and Toxicity Studies. *Drug Dev Ind Pharm*. 2005; 31: 757–768. <https://doi.org/10.1080/03639040500216246> PMID: 16221610
8. Bolten JS, Pratsinis A, Alter CL, Fricker G, Huwyler J. Zebrafish (*Danio rerio*) larva as an in vivo vertebrate model to study renal function. *Am J Physiol-Ren Physiol*. 2022; 322: F280–F294. <https://doi.org/10.1152/ajprenal.00375.2021> PMID: 35037468
9. Sieber S, Grossen P, Bussmann J, Campbell F, Kros A, Witzigmann D, et al. Zebrafish as a preclinical in vivo screening model for nanomedicines. *Adv Drug Deliv Rev*. 2019; 151–152: 152–168. <https://doi.org/10.1016/j.addr.2019.01.001> PMID: 30615917
10. Bambino K, Chu J. Zebrafish in Toxicology and Environmental Health. *Curr Top Dev Biol*. 2017; 124: 331–367. <https://doi.org/10.1016/bs.ctdb.2016.10.007> PMID: 28335863
11. Ellertsdóttir E, Lenard A, Blum Y, Krudewig A, Herwig L, Affolter M, et al. Vascular morphogenesis in the zebrafish embryo. *Dev Biol*. 2010; 341: 56–65. <https://doi.org/10.1016/j.ydbio.2009.10.035> PMID: 19895803
12. Cosentino CC, Roman BL, Drummond IA, Hukriede NA. Intravenous Microinjections of Zebrafish Larvae to Study Acute Kidney Injury. *JoVE J Vis Exp*. 2010; e2079. <https://doi.org/10.3791/2079> PMID: 20729805
13. McKee RA, Wingert RA. Zebrafish Renal Pathology: Emerging Models of Acute Kidney Injury. *Curr Pathobiol Rep*. 2015; 3: 171–181. <https://doi.org/10.1007/s40139-015-0082-2> PMID: 25973344
14. Sieber S, Grossen P, Detampel P, Siegfried S, Witzigmann D, Huwyler J. Zebrafish as an early stage screening tool to study the systemic circulation of nanoparticulate drug delivery systems in vivo. *J Controlled Release*. 2017; 264: 180–191. <https://doi.org/10.1016/j.jconrel.2017.08.023> PMID: 28851572
15. Campbell F, Bos FL, Sieber S, Arias-Alpizar G, Koch BE, Huwyler J, et al. Directing Nanoparticle Biodistribution through Evasion and Exploitation of Stab2-Dependent Nanoparticle Uptake. *ACS Nano*. 2018; 12: 2138–2150. <https://doi.org/10.1021/acs.nano.7b06995> PMID: 29320626
16. Drummond IA, Davidson AJ. Chapter 9—Zebrafish Kidney Development. In: Detrich HW, Westerfield M, Zon LI, editors. *Methods in Cell Biology*. Academic Press; 2010. pp. 233–260.
17. Drummond I. Making a zebrafish kidney: a tale of two tubes. *Trends Cell Biol*. 2003; 13: 357–365. [https://doi.org/10.1016/S0962-8924\(03\)00124-7](https://doi.org/10.1016/S0962-8924(03)00124-7) PMID: 12837606
18. Hentschel DM, Mengel M, Boehme L, Liebsch F, Albertin C, Bonventre JV, et al. Rapid screening of glomerular slit diaphragm integrity in larval zebrafish. *Am J Physiol-Ren Physiol*. 2007; 293: F1746–F1750. <https://doi.org/10.1152/ajprenal.00009.2007> PMID: 17699558
19. Hentschel DM, Park KM, Cilenti L, Zervos AS, Drummond I, Bonventre JV. Acute renal failure in zebrafish: a novel system to study a complex disease. *Am J Physiol-Ren Physiol*. 2005; 288: F923–F929. <https://doi.org/10.1152/ajprenal.00386.2004> PMID: 15625083
20. Randjelovic P, Veljkovic S, Stojilkovic N, Sokolovic D, Ilic I. Gentamicin nephrotoxicity in animals: Current knowledge and future perspectives. *EXCLI J*. 2017; 16: 388–399. <https://doi.org/10.17179/excli2017-165> PMID: 28507482
21. Bauer B, Liedtke D, Jarzina S, Stammer E, Kreisel K, Lalomia V, et al. Exploration of zebrafish larvae as an alternative whole-animal model for nephrotoxicity testing. *Toxicol Lett*. 2021; 344: 69–81. <https://doi.org/10.1016/j.toxlet.2021.03.005> PMID: 33722575
22. Ali BH. Gentamicin nephrotoxicity in humans and animals: Some recent research. *Gen Pharmacol Vasc Syst*. 1995; 26: 1477–1487. [https://doi.org/10.1016/0306-3623\(95\)00049-6](https://doi.org/10.1016/0306-3623(95)00049-6) PMID: 8690234
23. Perner B, Englert C, Bollig F. The Wilms tumor genes wt1a and wt1b control different steps during formation of the zebrafish pronephros. *Dev Biol*. 2007; 309: 87–96. <https://doi.org/10.1016/j.ydbio.2007.06.022> PMID: 17651719
24. Cörek E, Rodgers G, Siegrist S, Einfalt T, Detampel P, Schlepütz CM, et al. Shedding Light on Metal-Based Nanoparticles in Zebrafish by Computed Tomography with Micrometer Resolution. *Small*. 2020; 16: 2000746. <https://doi.org/10.1002/sml.202000746> PMID: 32567135
25. Migga A, Schulz G, Rodgers G, Osterwalder M, Tanner C, Blank H, et al. Comparative hard x-ray tomography for virtual histology of zebrafish larva, human tooth cementum, and porcine nerve. *J Med Imaging*. 2022; 9: 031507. <https://doi.org/10.1117/1.JMI.9.3.031507> PMID: 35372637
26. Osterwalder M, Bolten JS, Rodgers G, Humbel M, Schulz G, Tanner C, et al. Hard X-ray microtomography of Zebrafish larvae. *International Conference on X-Ray Lasers 2020*. SPIE; 2021. pp. 308–322.
27. Osterwalder M, Bolten JS, Rodgers G, Schulz G, Tanner C, Cörek E, et al. Three-dimensional x-ray microscopy of zebrafish larvae. *Bioinspiration, Biomimetics, and Bioreplication XI*. SPIE; 2021. pp. 65–77.

28. Kimmel CB, Ballard WW, Kimmel SR, Ullmann B, Schilling TF. Stages of embryonic development of the zebrafish. *Dev Dyn*. 1995; 203: 253–310. <https://doi.org/10.1002/aja.1002030302> PMID: 8589427
29. Sieber S, Siegrist S, Schwarz S, Porta F, Schenk SH, Huwyler J. Immobilization of Enzymes on PLGA Sub-Micrometer Particles by Crosslinked Layer-by-Layer Deposition. *Macromol Biosci*. 2017; 17: 1700015. <https://doi.org/10.1002/mabi.201700015> PMID: 28388000
30. Weitkamp T, Scheel M, Giorgetta J, Joyet V, Le Roux V, Cauchon G, et al. The tomography beamline ANATOMIX at Synchrotron SOLEIL. *J Phys Conf Ser*. 2017; 849: 012037. <https://doi.org/10.1088/1742-6596/849/1/012037>
31. Desjardins K, Carcy A, Giorgetta J-L, Menneglier C, Scheel M, Weitkamp T. Design of Indirect X-Ray Detectors for Tomography on the Anatomix Beamline. *Proc Mech EngDesign Synchrotron Radiat Equip Instrum*. 2018;MEDSI2018: 3 pages, 0.999 MB.
32. Paganin D, Mayo SC, Gureyev TE, Miller PR, Wilkins SW. Simultaneous phase and amplitude extraction from a single defocused image of a homogeneous object. *J Microsc*. 2002; 206: 33–40. <https://doi.org/10.1046/j.1365-2818.2002.01010.x> PMID: 12000561
33. Mirone A, Brun E, Guoullart E, Tafforeau P, Kieffer J. The PyHST2 hybrid distributed code for high speed tomographic reconstruction with iterative reconstruction and a priori knowledge capabilities. *Nucl Instrum Methods Phys Res Sect B Beam Interact Mater At*. 2014; 324: 41–48. <https://doi.org/10.1016/j.nimb.2013.09.030>
34. van der Maaten L., Postma E., van den Herik J. Dimensionality Reduction: A Comparative Review. *J Mach Learn Res*. Vol 10 No 66–71 P 13 2009.: 36.
35. Wingert RA, Davidson AJ. The zebrafish pronephros: A model to study nephron segmentation. *Kidney Int*. 2008; 73: 1120–1127. <https://doi.org/10.1038/ki.2008.37> PMID: 18322540
36. Rider SA, Bruton FA, Collins RG, Conway BR, Mullins JJ. The Efficacy of Puromycin and Adriamycin for Induction of Glomerular Failure in Larval Zebrafish Validated by an Assay of Glomerular Permeability Dynamics. *Zebrafish*. 2018; 15: 234–242. <https://doi.org/10.1089/zeb.2017.1527> PMID: 29480793
37. Boyer A, Timsit J-F, Klouche K, Canet E, Phan T, Bohé J, et al. Aminoglycosides in Critically Ill Septic Patients With Acute Kidney Injury Receiving Continuous Renal Replacement Therapy: A Multicenter, Observational Study. *Clin Ther*. 2021; 43: 1116–1124. <https://doi.org/10.1016/j.clinthera.2021.04.011> PMID: 34039478
38. Halstenson CE, Wong MO, Herman CS, Heim-Duthoy KL, Teal MA, Afrime MB, et al. Effect of concomitant administration of piperacillin on the dispositions of isepamicin and gentamicin in patients with end-stage renal disease. *Antimicrob Agents Chemother*. 1992; 36: 1832–1836. <https://doi.org/10.1128/AAC.36.9.1832> PMID: 1416875
39. Peng H-C, Wang Y-H, Wen C-C, Wang W-H, Cheng C-C, Chen Y-H. Nephrotoxicity assessments of acetaminophen during zebrafish embryogenesis. *Comp Biochem Physiol Part C Toxicol Pharmacol*. 2010; 151: 480–486. <https://doi.org/10.1016/j.cbpc.2010.02.004> PMID: 20170747
40. Westhoff JH, Giselbrecht S, Schmidts M, Schindler S, Beales PL, Tönshoff B, et al. Development of an Automated Imaging Pipeline for the Analysis of the Zebrafish Larval Kidney. *PLoS ONE*. 2013; 8: e82137. <https://doi.org/10.1371/journal.pone.0082137> PMID: 24324758
41. Bourassa D, Gleber S-C, Vogt S, Yi H, Will F, Richter H, et al. 3D Imaging of Transition Metals in the Zebrafish Embryo by X-ray Fluorescence Microtomography. *Met Integr Biometal Sci*. 2014; 6: 1648–1655. <https://doi.org/10.1039/c4mt00121d> PMID: 24992831
42. Mahmoud YI. Kiwi fruit (*Actinidia deliciosa*) ameliorates gentamicin-induced nephrotoxicity in albino mice via the activation of Nrf2 and the inhibition of NF- κ B (Kiwi & gentamicin-induced nephrotoxicity). *Biomed Pharmacother*. 2017; 94: 206–218. <https://doi.org/10.1016/j.biopha.2017.07.079> PMID: 28759758
43. Jaikumkao K, Pongchaidecha A, Thongnak L, Wanchai K, Arjinajarn P, Chatsudthipong V, et al. Amelioration of Renal Inflammation, Endoplasmic Reticulum Stress and Apoptosis Underlies the Protective Effect of Low Dosage of Atorvastatin in Gentamicin-Induced Nephrotoxicity. *PLOS ONE*. 2016; 11: e0164528. <https://doi.org/10.1371/journal.pone.0164528> PMID: 27727327
44. Bayomy NA, Elbakary RH, Ibrahim MAA, Abdelaziz EZ. Effect of Lycopene and Rosmarinic Acid on Gentamicin Induced Renal Cortical Oxidative Stress, Apoptosis, and Autophagy in Adult Male Albino Rat. *Anat Rec*. 2017; 300: 1137–1149. <https://doi.org/10.1002/ar.23525> PMID: 27884046
45. Martínez-Salgado C, López-Hernández FJ, López-Novoa JM. Glomerular nephrotoxicity of aminoglycosides. *Toxicol Appl Pharmacol*. 2007; 223: 86–98. <https://doi.org/10.1016/j.taap.2007.05.004> PMID: 17602717

46. Abd-Eldayem AM, Dahpy MA, Badary DM, Alnasser SM, Hareedy MS. Celecoxib has Preventive and Therapeutic Benefits against Nephrotoxicity Caused by Gentamicin in Mice. *Drug Res.* 2022; 259–267. <https://doi.org/10.1055/a-1785-4005> PMID: 35359021
47. Nassan MA, Soliman MM, Aldahrani A, Althobaiti F, Alkhedaide AQ. Ameliorative impacts of Glycyrrhiza glabra root extract against nephrotoxicity induced by gentamicin in mice. *Food Sci Nutr.* 2021; 9: 3405–3413. <https://doi.org/10.1002/fsn3.2183> PMID: 34262702

3.2.2 Publication 2

Comparative hard X-ray tomography for virtual histology of zebrafish larva, human tooth cementum, and porcine nerve

Alexandra Migga, Georg Schulz, Griffin Rodgers, Melissa Osterwalder, Christine Tanner, Holger Blank, Iwan Jerjen, Phil Salmon, William Twengström, Mario Scheel, Timm Weitkamp, Christian M Schlepütz, **Jan S Bolten**, Jörg Huwyler, Gerhard Hotz, Srinivas Madduri, Bert Müller

J Med Imaging (Bellingham). 2022 May;9(3):031507.

doi: 10.1117/1.JMI.9.3.031507.

Personal contribution:

My contribution to this research article includes the preparation of zebrafish larvae for X-ray-based microtomography imaging and assisted microtomography imaging. Further, I reviewed the manuscript.

Comparative hard x-ray tomography for virtual histology of zebrafish larva, human tooth cementum, and porcine nerve

Alexandra Migga,^{a,b} Georg Schulz,^{a,c} Griffin Rodgers^{Ⓞ,a,b},
Melissa Osterwalder,^{a,b} Christine Tanner^{Ⓞ,a,b} Holger Blank,^d
Iwan Jerjen^{Ⓞ,e}, Phil Salmon^{Ⓞ,f}, William Twengström,^g Mario Scheel,^h
Timm Weitkamp^{Ⓞ,h}, Christian M. Schlepütz^{Ⓞ,i}, Jan S. Bolten,^j
Jörg Huwyler^{Ⓞ,j}, Gerhard Hotz,^{k,l} Srinivas Madduri,^{a,m,n}
and Bert Müller^{Ⓞ,a,b,*}

^aUniversity of Basel, Biomaterials Science Center, Department of Biomedical Engineering, Allschwil, Switzerland

^bUniversity of Basel, Biomaterials Science Center, Department of Clinical Research, Basel, Switzerland

^cUniversity of Basel, Core Facility Micro- and Nanotomography, Department of Biomedical Engineering, Allschwil, Switzerland

^dCarl Zeiss Microscopy GmbH, Oberkochen, Germany

^eGloor Instruments AG, Kloten, Switzerland

^fBruker Micro-CT, Kontich, Belgium

^gExciscope AB, Kista, Sweden

^hSynchrotron SOLEIL, Gif-sur-Yvette, France

ⁱPaul Scherrer Institut, Swiss Light Source, Villigen, Switzerland

^jUniversity of Basel, Pharmaceutical Technology, Department of Pharmaceutical Sciences, Basel, Switzerland

^kNatural History Museum of Basel, Anthropological Collection, Basel, Switzerland

^lUniversity of Basel, Integrative Prehistory and Archaeological Science, Basel, Switzerland

^mUniversity of Geneva, Department of Surgery, Geneva, Switzerland

ⁿUniversity Hospital Basel, Department of Plastic, Reconstructive, Aesthetic and Hand Surgery, Basel, Switzerland

Abstract

Purpose: Synchrotron radiation-based tomography yields microanatomical features in human and animal tissues without physical slicing. Recent advances in instrumentation have made laboratory-based phase tomography feasible. We compared the performance of three cutting-edge laboratory systems benchmarked by synchrotron radiation-based tomography for three specimens. As an additional criterion, the user-friendliness of the three microtomography systems was considered.

Approach: The three tomography systems—SkyScan 2214 (Bruker-microCT, Kontich, Belgium), Exciscope prototype (Stockholm, Sweden), and Xradia 620 Versa (Zeiss, Oberkochen, Germany)—were given 36 h to measure three medically relevant specimens, namely, zebrafish larva, archaeological human tooth, and porcine nerve. The obtained datasets were registered to the benchmark synchrotron radiation-based tomography from the same specimens and selected ones to the SkyScan 1275 and phoenix nanotom m[®] laboratory systems to characterize development over the last decade.

Results: Next-generation laboratory-based microtomography almost reached the quality achieved by synchrotron-radiation facilities with respect to spatial and density resolution, as indicated by the visualization of the medically relevant microanatomical features. The SkyScan 2214 system and the Exciscope prototype demonstrated the complementarity of phase information by imaging the eyes of the zebrafish larva. The 3- μ m thin annual layers in the tooth cementum were identified using Xradia 620 Versa.

*Address all correspondence to Bert Müller, bert.mueller@unibas.ch

Migga et al.: Comparative hard x-ray tomography for virtual histology of zebrafish larva...

Conclusions: SkyScan 2214 was the simplest system and was well-suited to visualizing the wealth of anatomical features in the zebrafish larva. Data from the Exciscop prototype with the high photon flux from the liquid metal source showed the spiral nature of the myelin sheaths in the porcine nerve. Xradia 620 Versa, with detector optics as typically installed for synchrotron tomography beamlines, enabled the three-dimensional visualization of the zebrafish larva with comparable quality to the synchrotron data and the annual layers in the tooth cementum.

© The Authors. Published by SPIE under a Creative Commons Attribution 4.0 International License. Distribution or reproduction of this work in whole or in part requires full attribution of the original publication, including its DOI. [DOI: [10.1117/1.JMI.9.3.031507](https://doi.org/10.1117/1.JMI.9.3.031507)]

Keywords: phase-contrast tomography; image registration; x-ray microscopy; phase retrieval; tooth cementum; porcine nerve; zebrafish larvae; spatial and density resolution.

Paper 21289SSR received Nov. 4, 2021; accepted for publication Mar. 8, 2022; published online Mar. 31, 2022.

1 Introduction

Hard x-ray microtomography is a three-dimensional (3D) imaging technique that allows for the quantitative evaluation of microstructures in post mortem tissues.¹ Advanced instrumentation is applied for myriad scientific purposes, including the anatomical analysis of zebrafish larvae,² the characterization of annual layers in cementum of human teeth,³ and the visualization of paraffin-embedded nerves.⁴ Traditionally, the highest density and spatial resolutions have been achievable at synchrotron radiation facilities. However, this unique instrumentation only offers limited beam times based on successful applications or extra payments. Laboratory-based systems have been improved substantially by incorporating improved x-ray sources, phase-contrast capabilities, and x-ray detector optics.⁵ With the increasing number of such systems on the market, a detailed comparison is needed to understand the performance of these next-generation scanners with respect to other available laboratory systems and dedicated microtomography beamlines at synchrotron radiation facilities. To this end, the performances of three cutting-edge laboratory-based tomography systems, employing absorption and phase-contrast modes, were compared for the above-mentioned scientific applications. The common volumes extracted from datasets were three-dimensionally registered to synchrotron radiation-based micro computed tomography from the TOMCAT beamline at the Swiss Light Source (SLS) [Paul Scherrer Institute (PSI), Villigen, Switzerland] or the ANATOMIX beamline at the Synchrotron SOLEIL (Gif-Sur-Yvette, France) and then evaluated with respect to spatial resolution and contrast. In addition, the user-friendliness of the three next-generation scanners was appraised by a single novice.

1.1 Laboratory-Based Phase-Contrast X-Ray Tomography

Conventional x-ray tomography used in medicine relies on absorption contrast, which is very suitable for imaging hard tissues. Soft tissue imaging usually requires appropriate staining. As an alternative, one can take advantage of phase contrast modes to visualize tissues consisting of light elements together with hard tissue components, including teeth, bone, and plaque, because of the linear dependence of the phase shift on the electron density.⁶ For attenuation-contrast x-ray tomography, it is especially demanding, since x-ray attenuation versus atomic number exhibits a power law with an exponent between 3 and 4. As the x-ray beam passes through condensed matter, it exhibits both absorption, and with sufficient beam coherence, a phase shift.⁷ For soft tissues, the linear absorption coefficient is three orders of magnitude lower than the related coefficient for the phase shift.⁸ Thus, for the majority of medically relevant hard x-ray images of tissues in health and disease, phase-contrast methods are preferred.⁸ Several phase tomography approaches have been evaluated for soft tissue imaging.^{6,8-12} Single-distance propagation-based approaches are often the simplest to implement and generally offer the best spatial resolution. Therefore, these systems are frequently used with micro- and nanotomography beamlines at

synchrotron radiation facilities and are implemented in sophisticated laboratory-based microtomography systems.

High-resolution microtomography is more and more often referred to as “virtual histology,” because it extends the anatomical information from conventional histological sections to the third dimension.^{13,14} Virtual histology yields anatomical information without physical slicing. The spatial resolution is roughly equal in the three orthogonal directions—a distinct feature compared to serial sectioning and essential for the anatomical context, e.g., nervous tissue, as well as simple and fast data acquirement for much larger samples.^{5,13} Using nanoholotomography, one can even reach a spatial resolution beyond the optical limits given by the optical means employed to image the histological slices.¹⁵ Such measurements, however, suffer from limited access to synchrotron radiation facilities, since the purchase of beamtime is only common for industrial research, and a research proposal can only be submitted a few times per year, which leads to substantial delays and a focus on a smaller number of priority samples. As an alternative, several research teams use virtual histology based on laboratory-based microtomography systems. The obtained results, however, are generally compromised with respect to data from synchrotron radiation-based systems. The gap between laboratory- and synchrotron radiation-based tomography data, clearly obvious a decade ago,¹⁶ is becoming narrower and narrower (see e.g., see Refs. 17 and 18) with only minor differences in image quality.^{5,13,19} These advances in laboratory-based approaches motivated our team to evaluate cutting-edge instrumentation with the goal to directly compare the tomographic imaging of selected, medically relevant scientific questions related to the cellular anatomy of zebrafish larvae, to the annual layers in human tooth cementum, and to the 3D representation of paraffin-embedded porcine nerves. The acquisition of the necessary radiographs from the three selected specimens, and their reconstruction, was restricted to a period of 36 h per advanced instrument, to guarantee comparability and to have a reasonable timeframe for future experiments. It should be noted that while longer experiments could yield substantially better deliverables, the 36-h period was selected as tradeoff between standard user experience and the manufacturers’ requests. As a benchmark, the three specimens were imaged, prior to measurements with the advanced instrumentation, at the tomography setups of the TOMCAT (SLS, PSI, Villigen, Switzerland) or ANATOMIX (Synchrotron SOLEIL, Gif-sur-Yvette, France) beamlines. To validate progress in imaging the three selected specimens, the laboratory-based systems SkyScan 1275 (Bruker microCT, Kontich, Belgium) and nanotom m (Waygate Technologies, phoenixlx-ray, Wunstorf, Germany) available at the core facility of the University of Basel were included in the comparison. The four to six datasets per specimen were three-dimensionally registered to segment the common volume for a qualitative and quantitative comparison of image quality.

1.2 Zebrafish Larvae—A Versatile Biomedical Research Model

The zebrafish larva is a well-established animal for in vivo biomedical research. This rather basic vertebrate model offers an outstanding balance between relevant physiology and accessibility regarding ethical context, a rapid and effective life-cycle, and husbandry, as well as an attractive similarity to the human genome.²⁰ Therefore, the zebrafish larva finds numerous applications, including studies in pathological conditions such as kidney injury²¹ and treatment such as transplantation,²² to name a few. High-resolution hard x-ray tomography was used to examine the single organ-centered anatomy of zebrafish heart²³ and muscles,²⁴ as well as nanoparticle distribution.²⁵ In a recent study, synchrotron radiation was applied in whole-organism histotomography, thereby enabling the extraction of cellular architectures.²⁶ This study promises a broader understanding of anatomy and corresponding physiology and pathophysiology. Previously, we showed that more than 50% of anatomical features identified by synchrotron radiation-based microcomputed tomography (SR μ CT) can also be identified with standard laboratory-based tomography systems.²⁷ We can, therefore, expect that the cutting-edge laboratory-based systems will provide images comparable to the tomography setups at synchrotron radiation facilities. Such a level of success implies the possibility to easily perform large experimental series of high-resolution imaging fundamental in zebrafish larva-based research activities.

1.3 Tooth Root Cementum—A Lifelong Growing, Mineralized Tissue

Tooth cementum is a mineralized tissue that exists in vertebrate teeth and covers the entire surface of the tooth root, belonging functionally to its anchor, the periodontium. In contrast to bone, this avascular complex is independent of regular remodeling, and thus it expands over a lifetime with location-dependent growth rates.^{28,29} For humans, the homogeneous structure reveals about 3- μ m thin incremental layers, as originally found in optical micrographs of thin tooth slices.³⁰ These incremental layers were recently detected using synchrotron radiation-based microtomography.³ Our team is currently evaluating data for entire teeth collected during a beamtime session at the ANATOMIX beamline in February 2021. The related analysis pipeline is presented in a recent paper.³¹ Incremental layers are seasonally deposited, similar to the well-known layers in a tree trunk. Thus, a pair of layers, consisting of dark and bright structures, represents one year.³² Resulting predictions of the season of death based on these layers³³ indicates tooth cementum as a tissue highly valuable for anthropology³² and forensics.³⁴ Layer thickness is influenced by a number of factors, including hormonal changes in pregnancy and stress events, such as pathologies as well as nutrition, as examined profoundly in recent studies.^{33,35} Nonetheless, cervical acellular extrinsic fiber cementum provides the steadiest growth rate in terms of conserving layer thickness.^{28,29,32} Unfortunately, counting these layers is error-prone and observer-dependent, leading most commonly to an underestimation of age despite high-resolution imaging methods.^{36,37} Further investigation is therefore desired and suggested in archeological samples with corresponding life history.^{32,37} For these unique ancient samples, tomographic imaging should be favored to conventional microscopy, the latter requiring physical slicing.³ In this study, we show to what extent the incremental layers can be detected by means of laboratory-based tomography setups. It can be reasonably assumed that owing to the developments in x-ray source and detector technology for the advanced instrumentation, incremental layers could come to light.

1.4 Nerves—Clinical Application of Hard X-Ray Tomography-Controlled Products

Nerves show slow self-healing and some reinnervation potential after damage up to a minimum twelve months post-injury following a degenerative phase. Surgical treatment might be needed, especially in neuronal endplate involvement, i.e., neurotomy or even grafting in the case of potential tension by end-to-end suturing.³⁸ Still, more than one-quarter of patients do not regain motor function³⁹ without substantial improvement over the last two decades.^{38,39} Additionally, the quantification of nerve damage, which currently relies on conventional histology, assists in understanding the pathomechanisms, diagnostics, and therapy for multiple sclerosis⁴⁰ and vasculitis, including Wegener's polyangiitis.⁴¹ Microtomography with resolution down to the sub-cellular level has been proposed as a tool for nerve imaging and further investigations into nerve regeneration.^{4,42} In contrast to histology, phase-contrast microtomography of myelinated nerves provides visualization and the quantification of the microanatomy of nerves and may lead to profound physiological comprehension.^{43,44} We hypothesize that advanced laboratory instrumentation will lead to substantial improvements in microanatomical feature visibility compared to established laboratory-based tomography systems.^{4,42,45}

1.5 Assessment of User-Friendliness

A satisfying experience with a purchased product strongly depends on a subjective evaluation of usability rather than purely objective criteria such as effectiveness and efficiency.⁴⁶ Assessments of software user-friendliness have thus been well-established since the 1980s through the use of standard questionnaires, including the system usability scale.⁴⁶ Crucial criteria appraised by the analysis of comments on tested systems include easy handling and intuitive design.⁴⁷ Unintuitive systems run the risk of malfunction, leading to reduced overall performance of technology, and may even be hazardous in a medical context.⁴⁸ Therefore, we included the user-friendliness of advanced laboratory systems as a valid purchasing criterion for next-generation systems. We integrated four criteria to appraise novice user experience in cutting-edge setups: (i) intuitive

interface, (ii) structural organization, (iii) efficiency and effectiveness, and (iv) reliability. These areas were scored by a single beginner-level user who participated in the test measurements.

2 Materials and Methods

2.1 Sample Preparation

2.1.1 Preparation of three-day-old paraffin-embedded zebrafish larvae

Three-day-old zebrafish larvae were euthanized using tricaine methanesulfonate containing 0.612-mM trisamino-methane. Subsequently, the larvae were fixated in 4% paraformaldehyde at room temperature before refrigerating the samples at a temperature of 4°C for storage. These fixed larvae were dehydrated in a dilution series of ethanol from 25% via 50% and 70% to above 99.5% in time steps of 15 min. Then, the dehydrated zebrafish larvae were washed twice in xylene, >98%, Carl Roth, Switzerland, and subsequently transferred into liquid paraffin at a temperature of 68°C (Leica Microsystems, Wetzlar, Hesse, Germany). After cooling, metal punches with inner diameters of 2.8 or 3.6 mm were used to cut out the embedded specimens to obtain cylinders for the imaging tasks. For the synchrotron radiation-based experiments, the paraffin cylinders were further manually trimmed to remove excess paraffin.

2.1.2 Selection of archaeological human tooth

The selected premolar tooth from the maxilla of a woman who died at the age of 36 comes from the reference skeleton series Basel-Spitalfriedhof, which is archived at the Natural History Museum Basel, Switzerland.

The skeletons were exhumed in 1988 and 1989 from the cemetery of the former Basel City Hospital. Based on historical sources, it was possible to identify the skeletons of former hospital patients, who died between 1845 and 1868. In addition, further information on social and geographical origin, information on living and working situations, medical histories, etc., are available. This detailed historical information, combined with corresponding skeletons from the 19th century, is unique worldwide and allows, e.g., the reconstruction of biographies taking into account biological and historical sources. Furthermore, these skeletons are used for method verification and the development of future methods.

2.1.3 Preparation of porcine nerves for tomographic imaging

After excision, the peripheral nerves were processed by following a standard histology protocol for formalin fixation and paraffin embedding. Briefly, the nerves were straightened by firmly tugging both ends with surgical forceps, fixed in histology-grade 4% formalin over a period of 24 h, and then dehydrated in ascending ethanol solutions. Subsequently, nerves were transferred to xylene and then perfused in a liquid paraffin-polymer mixture (Leica Paraplast, Muttens, Switzerland).

When liquid paraffin perfusion was completed, the nerves were removed from the histological tissue processor, placed in a metal container, and left for a period of 24 h inside an oven at a temperature of 60°C. This step is important in removing air bubbles trapped inside or around the specimen, as they can potentially cause artifacts during x-ray imaging and compromise automatic data analysis. Subsequently, the specimens were thoroughly washed under flowing liquid paraffin, to remove high-absorbing particles or debris on the sample surface that would affect imaging quality. Finally, the nerves were immersed in paraffin several times while holding on one edge, until a uniform cylindrical specimen was formed and then cooled down to a temperature of 4°C over a period of 15 min.

2.2 Data Acquisition with SkyScan 2214

The samples were mounted on a thin carbon fiber stage for high-resolution nanoCT scanning in the SkyScan 2214 system. It is noteworthy that the SkyScan 2214 setup consists of up to three

3.2. PART II: X-RAY-BASED MICROTOMOGRAPHY STUDIES

Migga et al.: Comparative hard x-ray tomography for virtual histology of zebrafish larva...

cameras that can be easily exchanged by the user. The selected x-ray camera was set in a near position with a source-camera distance of ~ 235 mm (for details, see Tables 1–3). Acceleration voltage was set to 40 kV for imaging the zebrafish larva, 70 kV for imaging the tooth cementum, and 30 kV for the porcine nerve bundle. A 0.5-mm thin aluminum filter was only applied for data acquisition of the human tooth. An LaB₆-type source filament was employed for all scans; depending on the desired spatial resolution and flux, W or LaB₆ cathodes can be implemented. The individual scans were limited to a duration of <11 h. Spot size was about 0.5 μm for zebrafish larva and tooth radiograph recording, and about 1.5 μm for nerve bundle recording. Scan pixel sizes were set to 330, 750, and 800 nm for zebrafish larva, tooth, and nerve bundle, respectively. The total numbers of recorded projections were 3001, 2118, and 2401, for zebrafish larva, tooth, and nerve fiber bundles, respectively. All scans were acquired over 360 deg, and frame averaging was employed. For the zebrafish larva and tooth imaging, two images per projection were averaged, while four images were used per nerve projection. Active ring artifact suppression by random horizontal (compensated) camera movement was done for all scans. Post-scan

Table 1 Scanning parameters used in zebrafish larva microtomography.

	Nanotom m	SkyScan 1275	SkyScan 2214	Exciscope	Xradia 620 Versa	TOMCAT
Source-camera distance (mm)	600	286.0	237.5	280.0	12.6	25,012.0
Source-object distance (mm)	6.5	13.7	8.65	225.0	6.0	25,000.0
Effective voxel size (μm)	1.1	3.7	0.33	1.28	0.33	0.33
Acceleration voltage (kV)	60	15	40	40	50	(12 keV)
Beam current (μA)	310	156	116	1400	90	
Horizontal FOV (pixels)	3072	1944	4032	2048	2048	2560
Number of radiographs	720	720	3001	3600	4801	2000
Rotation steps (deg)	0.5	0.5	0.12	0.1	0.07	0.09
Exposure time (s)	9	2.5	4.7	7	8	0.2
Scan time (h)	2.5	4	10.5	7.25	14	0.15

Table 2 Scanning parameters used in human tooth cementum microtomography.

	SkyScan 2214	Exciscope	Xradia 620 Versa	ANATOMIX
Source-camera distance (mm)	235.2	280.0	128.55	170,050.0
Source-object distance (mm)	10.1	225.0	13.55	170,000.0
Effective voxel size (μm)	0.75	1.28	0.71	0.65
Acceleration voltage (kV)	70	70	80	(33 keV mean)
Beam current (μA)	80	1400	125	
Horizontal FOV (pixels)	4032	2048	2048	11,300
Number of radiographs	2118	3600	2501	9000
Rotation steps (deg)	0.17	0.1	0.14	0.04
Exposure time (s)	7	12	7 to 14	0.1
Scan time (h)	11	12.25	8.5	0.75

Table 3 Scanning parameters used in porcine nerve microtomography.

	SkyScan 1275	SkyScan 2214	Exciscope	Xradia 620 Versa	ANATOMIX
Source-camera distance (mm)	286.0	235.2	280.0	44.35	170,050.0
Source-object distance (mm)	30.2	10.8	225.0	9.35	170,000.0
Effective voxel size (μm)	8.5	0.8	1.28	0.71	0.65
Acceleration voltage (kV)	20	30	40	60	(33-keV mean)
Beam current (μA)	175	150	1400	108	
Horizontal FOV (pixels)	1944	4032	2048	2048	15,000
Number of radiographs	720	2401	3600	3201	9000
Rotation steps (deg)	0.25	0.15	0.1	0.11	0.04
Exposure time (s)	0.65	1.1	10	6.2	0.05
Scan time (h)	2.3	6.0	10.25	7.5	0.5

correction was applied⁴⁹ to minimize thermal movement artifacts. Image reconstruction was performed by a Feldkamp-type cone-beam algorithm,⁵⁰ using Bruker NRecon™ software with GPU acceleration and by applying Gaussian smoothing, ring artifact, and beam hardening corrections. Phase retrieval was also carried out for the acquired data.⁵¹

2.3 Data Acquisition with Exciscope

The three selected samples were imaged at KTH Royal Institute of Technology in Stockholm, Sweden. The setup is based on the MetalJet D2 x-ray source (Excillum AB, Kista, Sweden), the XSight Micron LC 1080 sCMOS X-ray detector (Rigaku Innovative Technologies Europe s.r.o., Czech Republic) and the URS100BCC rotation stage (Newport, California, United States). Both acquisition control and image reconstruction were done using Exciscope software (Exciscope AB, Kista, Sweden). The experimental setup had a source-object distance of 225 mm and a source-detector distance of 280 mm. Effective pixel size was set to 1.28 μm at the scintillator and 1.03 μm at the object, due to geometric magnification. Projections were acquired equian-gularly over a full 360 deg rotation. The reconstruction included phase retrieval with Paganin's method⁵² and tomographic reconstruction using the FDK method.⁵⁰ The scan parameters for the three samples are listed in Tables 1–3.

2.4 Data Acquisition with Xradia 620 Versa

X-ray microscopy measurements were performed on a Zeiss Xradia 620 Versa system (Carl Zeiss X-ray Microscopy, Inc., Dublin, California, United States). Projections of the samples were recorded in a unique two-stage magnification process that included optical magnification. For the zebrafish larva data recording, we employed an acceleration voltage of 50 kV, a beam current of 90 μA , a 20 \times objective, 325-nm effective pixel size, an 8 s exposure time, and 4801 projections. For the human tooth we used an acceleration voltage of 80 kV, a beam current of 125 μA , a 4 \times objective, narrowing of the x-ray bandwidth by the LE4 filter, 710-nm effective pixel size, a rotation angle-dependent exposure time ranging from 7 to 14 s, and 2501 projections. The porcine nerve was imaged with an acceleration voltage of 60 kV, a beam current of 108 μA , a 4 \times objective, 709-nm effective pixel size, an exposure time of 6.2 s, and 3201 projections. The tomography datasets were reconstructed with ZEISS Scout-and-Scan Reconstructor software, using the cone-beam method for the tooth and zebrafish larva data and the OptiRecon method for the nerve data. In addition, the zebrafish larva data were reconstructed with the DeepRecon Pro reconstruction module and post-processed with the PhaseEvolve software module.

2.5 Data Acquisition at the TOMCAT Beamline

Synchrotron radiation-based phase-contrast x-ray microtomography measurements of zebrafish larva were acquired at the TOMCAT beamline X02DA of the SLS.⁵³ The x-ray beam generated by the 2.9 T superbend magnet was monochromatized to 12 keV at a bandwidth of around 2%, using an Ru/C double multilayer monochromator. Projection images of the sample placed about 25 m from the source were converted to visible light by a 20- μm thick $\text{Lu}_3\text{Al}_5\text{O}_{12}:\text{Ce}$ scintillator (Crytur, Turnov, Czech Republic) positioned 12-mm downstream of the sample. The image on the scintillator was magnified 20-fold by a visible-light microscope (Olympus UPLAPO 20 \times objective) and recorded by a pco. Edge 5.5 sCMOS camera (PCO, Germany) with a native pixel size of 6.5 μm , resulting in an effective pixel size of 0.325 μm . During the continuous 180 deg rotation of the sample (parallel beam geometry), 2000 projections with 200-ms exposure time were recorded for the reconstruction, resulting in an angular step of 0.09 deg and a scan time of 400 s. Additionally, 30 dark-field and 50 white-field images were recorded for image correction. Propagation-based phase-contrast projections were calculated from the flat field- and dark field-corrected radiographs, using Paganin's algorithm with the parameters $\delta = 10^{-7}$ and $\beta = 2 \cdot 10^{-9}$.⁵² The absorption- and phase-contrast reconstructions were then computed from the corrected and phase-filtered projections, respectively, with the gridrec reconstruction algorithm.⁵⁴

2.6 Data Acquisition at the ANATOMIX Beamline

Measurements at the Synchrotron SOLEIL, ANATOMIX beamline⁵⁵ were taken with a filtered white beam at a gap of 5.5 mm from the U18 in-vacuum undulator source of the beamline. The beam was filtered with 20- μm thick Au and 100- μm thick Cu films. The resulting beam had an estimated mean photon energy of about 33 keV. The detector consisted of a 20- μm thick $\text{Lu}_3\text{Al}_5\text{O}_{12}:\text{Ce}$ scintillator (Crytur, Turnov, Czech Republic) coupled to a scientific-grade CMOS detector (Hamamatsu Orca Flash 4.0 V2) of 2048 \times 2048 pixels by microscope optics (Mitutoyo 10 \times M PLAN APO, numerical aperture 0.28) and with a magnification of 10, resulting in an effective pixel size of 0.65 μm . As the size of the nerve and the tooth were larger than the field of view, we performed an extended-field acquisition, where we acquired scans at four and three off-center positions, respectively. The neighboring radiographs were stitched together based on maximizing cross-correlation in the overlapping regions. At an electron current of 450 mA in the SOLEIL storage ring, exposure time for each of the 9000 projections per height step/ring taken over a range of 360 deg was 50 and 100 ms, respectively. The scan was taken in continuous on-the-fly mode. With the time required for the acquisition of flat and dark images, and including dead time, the overall scan time for each height step was around 30 and 45 min, respectively. Before the absorption-contrast reconstruction, the projections were filtered with a Gaussian of width $\sigma = 1.25$ pixel and 0.75 pixel, respectively, to increase the contrast-to-noise ratio (CNR).⁵⁶

2.7 Data Acquisition with Nanotom m[®] and SkyScan 1275

Parameters for data acquisition of the three selected specimens, i.e., paraffin-embedded zebrafish larva and porcine nerve, using the established microtomography systems nanotom m[®] and SkyScan 1275 are given in Tables 1 and 3.

2.8 Data Registration

The registration pipeline consisted of several steps. First, we found an approximate position in the SR μ CT datasets corresponding to the volume imaged in the laboratory scanner. The laboratory-based volume was then manually pre-aligned with this SR μ CT image region via ITK-SNAP⁵⁷ (version 3.8.0). The images were then automatically registered with an affine or similarity transformation employing the open-source registration toolbox elastix (version 4.9).^{58,59} In the case of the zebrafish larva and tooth specimens, the foreground region was determined by semi-automatic segmentation via thresholding and morphological operations. Image registration parameters were tuned by checking the progression of the image similarity measure

Table 4 Main registration parameters for the three classes of samples.

	Zebrafish larva	Tooth cementum	Pig nerve bundle
Transformation	Affine	Affine	Similarity
Image similarity measure	Normalized correlation coefficient	Normalized correlation coefficient	Advanced Mattes mutual information
Multi-resolution image pyramid with three levels	16 \times , 8 \times , 4 \times	4 \times , 2 \times , 1 \times	4 \times , 2 \times , 1 \times
Number of iterations	4000	2000 or 3000	3000
Number of sample points	8192	130,000 or 1,950,000	65,536

during registration and by visually inspecting alignment. The original laboratory-based μ CT volumes were transformed to the space of the SR μ CT volumes region using cubic B-spline interpolation, as this preserved image intensities far better than nearest-neighbor and linear interpolation.⁶⁰ Registrations of the zebrafish larva, tooth cementum, and porcine nerve bundle images were performed independently by three of the authors (G.R., M.O., and C.T.). The registration parameters are listed in Table 4.

2.9 Identification of Anatomical Structures

Representative slices of the tomography datasets were compared in anatomy to atlas data. For the paraffin-embedded zebrafish larva, the images were compared to histological slices published in the Zebrafish Lifespan Atlas.⁶¹ Qualitative comparison was done for the zebrafish larva dataset, because the same region is imaged in every dataset.

For the paraffin-embedded porcine nerve, the porcine sciatic nerve model was used.⁶²

3 Results and Discussion

Image quality was initially evaluated by visual assessment, i.e., a microanatomical description, with subsequent calculation of the spatial resolution. The representative cross-sectional virtual histology slices acquired with synchrotron radiation sources showed a wealth of anatomical features, therefore, serving as the gold standard. In Sec. 3.1, we present a comparison of the zebrafish larva and the porcine nerve alongside the results of the currently available inhouse systems nanotom m[®] and SkyScan 1275. Sections 3.2, 3.4, and 3.6 contain the results of the next-generation laboratory systems for the three selected specimens in comparison to the synchrotron radiation-based microtomography data for the same specimens.

3.1 Descriptive Microanatomy of Selected Tomographic Slices

Cross-sectional slices of the paraffin-embedded zebrafish larva head are shown in Fig. 1, top row. The data acquired at the TOMCAT beamline, image on the right, are phase-retrieved and demonstrate true single-cellular and even subcellular resolution. In particular, one can see mesencephalic and ophthalmic nuclei. Individual ocular cell layers that can be distinguished are the ganglion cells, inner plexiform, amacrine cells, the photoreceptor layer, and the retinal pigmented epithelium—apart from the distinction between the bipolar and outer plexiform layers. Mesencephalic nuclei with high electron density are separated from their surroundings; however, corresponding cartilage features around the pharynx remain low in contrast.

The established laboratory-based systems SkyScan 1275 and nanotom m[®] (top row, left and center images of Fig. 1) do not yield sufficiently high spatial resolution or contrast, respectively. It is noteworthy that the nanotom m[®] data barely provide meaningful images of this low-absorbing specimen, since the aluminum layer on the detection unit suppresses photons with energies below 30 keV. Therefore, only the otoliths and the overall shape are visible as shown in a recent study.²⁵

3.2. PART II: X-RAY-BASED MICROTOMOGRAPHY STUDIES

Migga et al.: Comparative hard x-ray tomography for virtual histology of zebrafish larva...

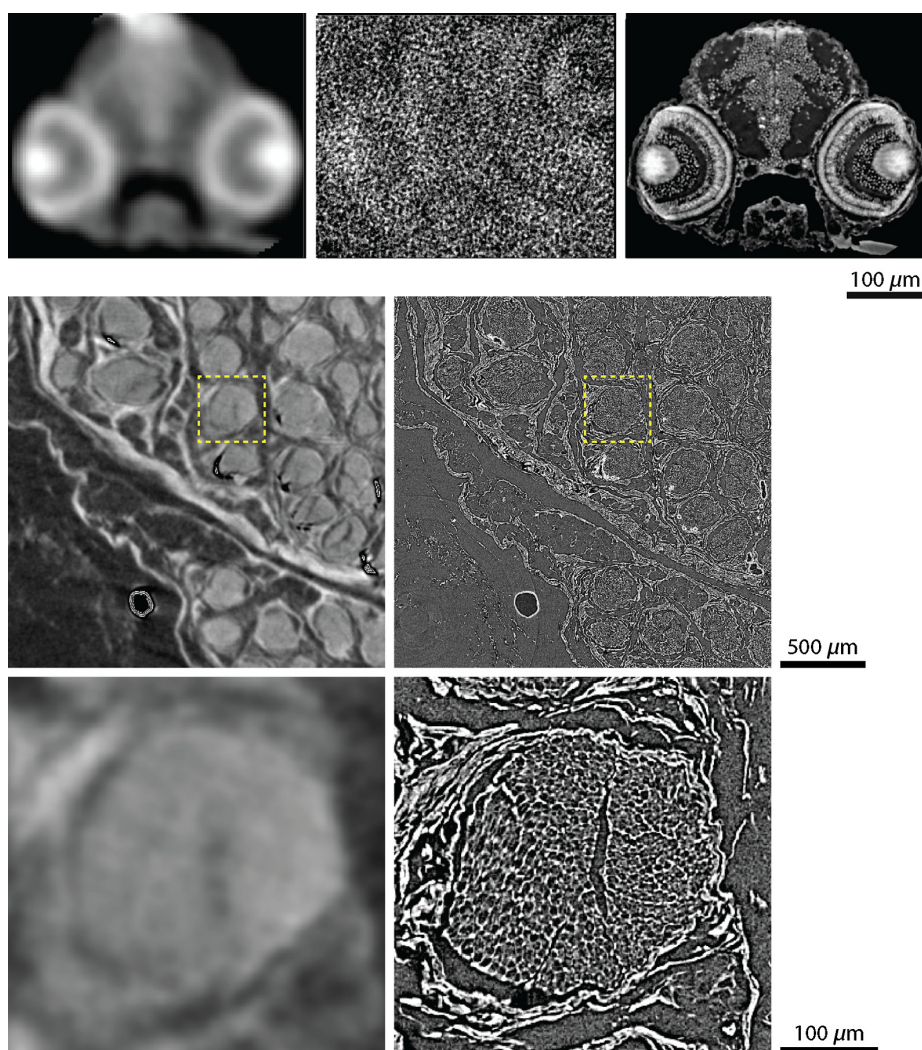


Fig. 1 First row: corresponding virtual slices through the zebrafish larva head by means of the established laboratory-based microtomography systems SkyScan 1275 and nanotom m[®] in comparison with data from the TOMCAT beamline (left to right), which can obviously serve as the gold standard in zebrafish larva imaging. Second row: corresponding cross-sectional slices of unprocessed, paraffin-embedded porcine nerves. Using 5- μ m wide pixels, SkyScan 1275 (left) provides poorer spatial resolution in comparison to the ANATOMIX beamline (right) with 0.65- μ m wide pixels and propagation-based phase contrast, obtaining anatomical features down to the sub-cellular level. The magnified views in the third row, the locations of which are indicated by the yellow-colored dashed lines, show a selected nerve fiber bundle. The image clearly demonstrates the gap between established laboratory-based systems and tomography setups at synchrotron radiation facilities.

The SkyScan 1275 system allows the detection of photons with an energy down to 10 keV, where even the ocular layers can be distinguished. The contrast between the denser nuclear mesencephalic region and its surroundings is satisfactory. Limited spatial resolution, however, prevents true cellular resolution.

The data from ANATOMIX beamline have revealed the characteristic anatomy of the peripheral nerve, which consists of epi-, peri- and endoneurium, as well as primary nerve fiber bundles surrounded by myelin sheaths. The latter is highlighted in the magnified view (Fig. 1, lower right, with location given by the yellow dashed box). The vasa nervorum was invisible due

to a lack of contrast. The absorption-contrast SkyScan 1275 datasets (cp. second row of Fig. 1 left) allowed for visualization of the blood vessels; however, myelin sheaths could not be resolved due to insufficient spatial resolution or contrast.

3.2 Comparing Zebrafish Larva Imaging of Next-Generation Laboratory-Based Scanners with Tomographic Imaging Available at TOMCAT Beamline

3.2.1 Performance of SkyScan 2214

The comparison of the images in the top row of Fig. 1 with the ones in Fig. 2 elucidates the leap in evolution from established microtomography to cutting-edge systems. Even the most affordable among the three systems, namely, SkyScan 2214, allows for the resolution of the individual cells within the zebrafish larva head, as especially recognized in the images with higher magnification provided in the right column (see left part of the top row). The similarity to the gold standard data (right part of the top row) is striking. The eye region with ophthalmic cells were used for estimating spatial resolution, using the Fourier domain.⁶³ Briefly, the logarithm of the squared norm of the Fourier transform was plotted as a function of the squared distance from the origin, then a linear fit allowed for the estimation of the width of a Gaussian point spread function. The instrument at the TOMCAT beamline yielded $1.3 \mu\text{m}$, whereas SkyScan 2214 data produced $1.6 \mu\text{m}$.

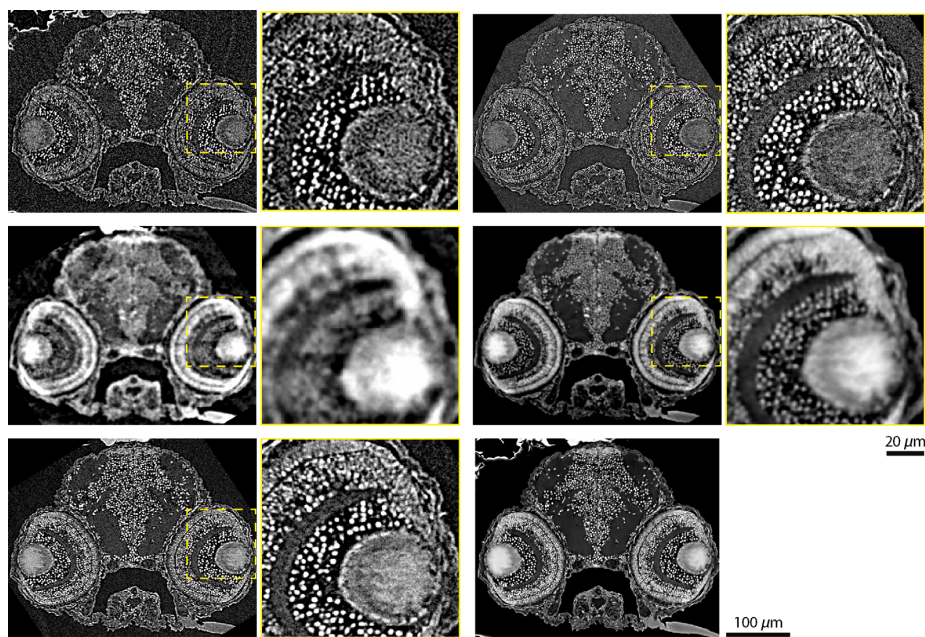


Fig. 2 The tomographic imaging of the zebrafish larva shows comparable results between the synchrotron radiation-based and next-generation laboratory-based instrumentation. First column: corresponding virtual slices through the zebrafish larva head by means of the cutting-edge, laboratory-based microtomography SkyScan 2214 system (top row) in comparison with data acquired at Exciscope (second row) and absorption-contrast tomography images from Xradia 620 Versa (third row). The dashed yellow squares indicate the position of the enlarged views (second column). Third column: corresponding virtual slices through the head of the zebrafish larva recorded at the TOMCAT beamline; the first row shows data reconstructed without phase retrieval, and the second row shows it after Paganin phase retrieval. The dashed yellow squares indicate the position of the enlarged views (fourth column). The image in the third column and third row is obtained from the Xradia 620 Versa instrument using software including the Zeiss PhaseEvolve algorithm.

3.2.2 Performance of Exciscope

The related virtual slices through the zebrafish larva shown in the left part of the second row in Fig. 2 were prepared by including phase retrieval with Paganin's method. Therefore, the TOMCAT beamline data given in the right part of the second row of Fig. 2 exhibit modified contrast with respect to the images in the top row of Fig. 2. In addition, the spatial resolution has been compromised. Cellular resolution was mostly preserved, although several anatomical features of the eye vanished, owing to noise level. This behavior is even more pronounced in the data for Exciscope, most probably because of the less appropriate detector optics. The individual cells can hardly be recognized; hence, the Exciscope system—at least in the configuration used herein—cannot resolve the cells within a paraffin-embedded zebrafish larva. The eye region with the ophthalmic cells (magnified view) was also used for estimating spatial resolution within the phase-retrieved datasets.⁶³ Here, the phase retrieved data from the TOMCAT beamline yielded 1.8 μm and the Exciscope 4.3 μm .

3.2.3 Performance of Xradia 620 Versa

The selected virtual slice through the zebrafish larva obtained with the Xradia 620 Versa system was recorded in the absorption contrast mode (see left part of third row in Fig. 2). Xradia 620 Versa resembles data from the TOMCAT beamline, see top row right part, best, most probably because of the same optical components in both detection systems. Some edge enhancement is visible in these two datasets, e.g., the feature in the lower-right corner. The eye region with the ophthalmic cells used to estimate spatial resolution⁶³ gave rise to a spatial resolution of 1.6 μm , slightly above the value mentioned for the tomography setup at TOMCAT beamline (1.3 μm).

The Xradia 620 Versa setup could only provide reconstructions based on absorption contrast (status March 2021). The manufacturer, however, has stated that a feature for image enhancement using phase contrast will be available soon. In August 2021, the reconstruction module DeepRecon Pro was presented.⁶⁴ In this reconstruction, the image contrast with respect to propagation-based phase-contrast effects was enhanced using the PhaseEvolve module with parameters: fringe width 5.24 and fringe strength 12 (right image in bottom row of Fig. 2). Depending on the chosen parameters, the result is comparable to the single-distance phase-retrieved data set, shown above in the second row of Fig. 2.

3.3 Zebrafish Larva—Full-Specimen Imaging in Pre-Medical Studies

Concerning the detection of anatomical features Xradia 620 Versa showed the highest resolution, i.e., down to single nuclei; the contrast in the provided images was further improved with the software PhaseEvolve. SkyScan 2214 produced a likewise high-quality dataset with a slight increase in noise. Distinction of cells was impossible with Exciscope, but it nonetheless showed satisfactory layer separation within the zebrafish larva eye. It is noteworthy that this was achieved in unstained samples, whereas, previously, staining has been widely used with laboratory instrumentation.²³ A detailed comparison of the three x-ray microscopes was impossible, as at the time of our measurement, i.e., March 2021, the DeepRecon Pro and PhaseEvolve software modules were not available yet in Europe for the Xradia 620 Versa, SkyScan 2214 data measurements had to be repeated, and the Exciscope prototype only provided detector optics with an effective pixel size of 1.3 μm . Following visual inspection, however, advances in table-top μCT systems, in comparison to the established systems in our lab, were evident, leading to an image quality close to that of SR μCT , although at longer scan times.

Recent studies of zebrafish larvae, e.g., their complete histological phenotyping²⁶ and the determination of nanoparticle distribution,²⁵ have relied on SR μCT . Based on the present results with cutting-edge μCT systems, future studies of the zebrafish larva in a laboratory setting are planned. Moreover, with the attractive homology to humans, as underlined by exemplary drug target conservation,⁶⁵ further investigations of pharmacological and phenomics studies with high-resolution imaging of organs and whole zebrafish larva will be led by cellular resolution in an accessible setup for fast-feedback and follow-up imaging. This volumetric imaging provides a 3D context—in contrast to conventional histology serving as an alternative for pharmacological studies. Future

zebrafish larva studies will include imaging the progression of kidney diseases and the renal regeneration with the goal to identify therapeutics that enhance human renal regeneration.²¹

3.4 Comparing the Imaging of Annual Layers in Human Tooth Cementum by Applying Next-Generation Laboratory-Based Scanners and ANATOMIX Beamline Microtomography

Applying mosaic-style acquisition,⁶⁶ the entire human tooth cementum was made visible by means of single-distance phase-contrast tomography. This approach avoided the presence of artifacts known from local scans with true micrometer resolution when objects with centimeter diameters were studied. Thus, local tomography data from the three selected next-generation, laboratory-based tomography systems could be registered to the large dataset from the ANATOMIX beamline. This approach was helpful, since local tomography at pre-defined positions could not be guaranteed. Therefore, the data shown in Figs. 3 and 4 do not cover the same regions of the human tooth, but they have been always registered to the same ANATOMIX dataset. Consequently, the comparability of tomography data from the cutting-edge instrumentation is definitely provided.

3.4.1 Performance of SkyScan 2214

The part of the human tooth shown in the first row of Fig. 3 is a superb choice, because many annual layers can be traced from left to right within data from the ANATOMIX beamline

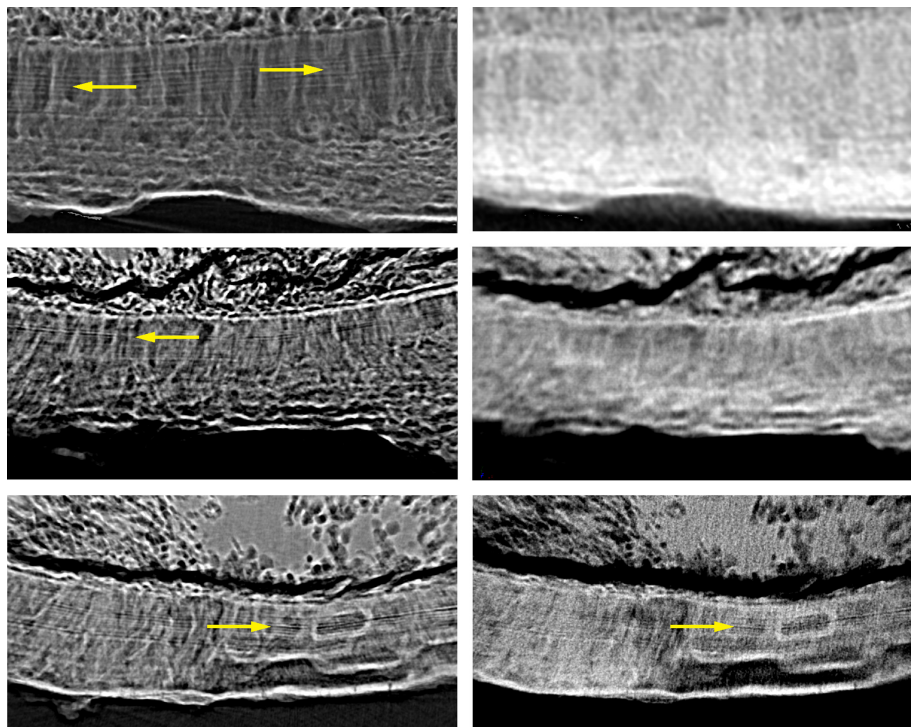


Fig. 3 Selected regions of interest from the human tooth cementum acquired at the ANATOMIX beamline (images in the left column) and registered data from SkyScan 2214 (right image, top row), from Exciscope (right column, middle image), and from Xradia 620 Versa (right column, bottom image). The registered data are represented in a special 3D fashion: 100 slices were rendered using the sum along ray tool from VGStudio MAX to improve the visibility of the incremental layers (see yellow arrows).³¹ Annual layers are visible not only in data acquired at the synchrotron radiation facility, but also in the dataset gathered at the cutting-edge laboratory-based Xradia 620 Versa system. The width of each image equals about 600 μm .

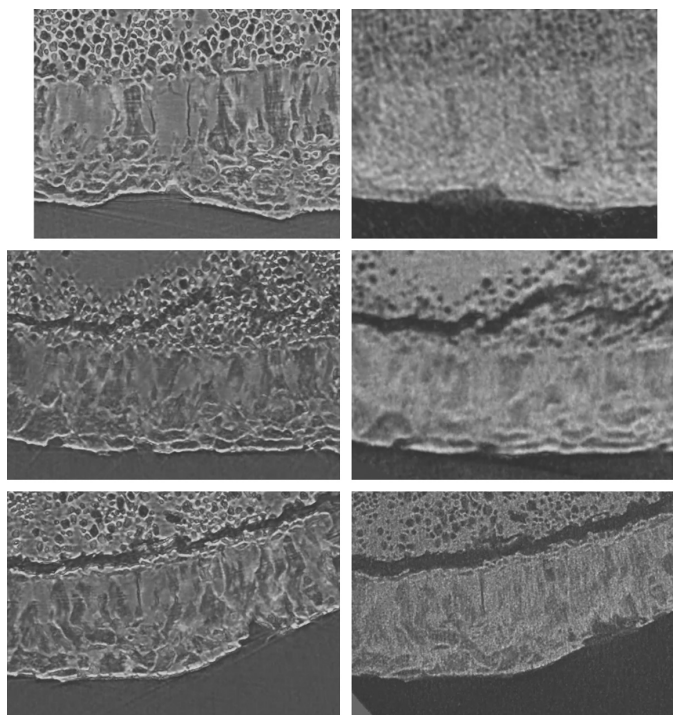


Fig. 4 A still image of [Video 1](#) showing the annual layers are detectable in the movies in the left column and at the one on the bottom in the right column: Scroll-through 160 cross-sectional virtual histology slices, prepared by the software VGStudio MAX, of the human tooth obtained at the ANATOMIX beamline (images in the left column) and corresponding local scans by means of SkyScan 2214 without phase retrieval (right column, top row), of Exciscope with a priori phase retrieval (right column, middle row), and of Xradia 620 Versa without phase retrieval (right column, bottom row). The width of each box equals about $600\ \mu\text{m}$ ([Video 1](#), MP4, 11639 KB [URL: <https://doi.org/10.1117/1.JMI.9.3.031507.1>]).

(see left image). As found previously,³ the $3\text{-}\mu\text{m}$ thin annual layers are much clearer in the low-absorbing parts of the tooth cementum. The SkyScan 2214 setup, however, only shows contrast between the lower and higher x-ray-absorbing regions in the tooth cementum, while the annual layers remain invisible. This observation is also supported by Fig. 4 (first row), when scrolling through the 160 selected virtual slices obtained from the datasets of the two tomography systems.

3.4.2 Performance of Exciscope

The images in Fig. 3, middle row shows a part of the human tooth with the following anatomical features. In the upper part, one finds dentin with a crack of characteristic morphology. In the middle, tooth cementum with the annual layers is found. The lower part in black represents the surrounding air. Whereas the annual layers are easily recognized within the data from the ANATOMIX beamline, indicated by the yellow-colored arrow, Exciscope instrumentation in the configuration used could not resolve these anatomical features with an average thickness of only $3\ \mu\text{m}$. An objective with higher resolution, however, might master this deficiency. These findings are further elucidated by Fig. 4. It is noteworthy that in Fig. 4, middle part explicitly shows that the thin lines, usually termed incremental lines, are actual 3D layers, given by the continuity of the visible lines scrolling through the 160 slices of the synchrotron radiation-based dataset.

3.4.3 Performance of Xradia 620 Versa

The bottom rows in Figs. 3 and 4 demonstrate that annual layers can also be made visible with a laboratory-based system. Although Xradia 620 Versa does not reach the resolution of the synchrotron radiation-based setup, this result is nevertheless promising and could even be further improved by substantially increasing acquisition time. It is noteworthy that the manufacturers had only 36 h to image the three selected samples, and the flux from the laboratory sources is orders of magnitude less than that of the synchrotron radiation facilities.

3.5 Human Tooth Cementum—Requirement for Non-Destructive Imaging Techniques in Unique Samples

To date, incremental layers may only be imaged to a satisfying extent at synchrotron radiation facilities³⁷ or by means of conventional optical microscopy of thin sections.^{32,34,36} A laboratory-based μ CT was suggested by Mani-Caplazi et al.³ based on physically sliced samples and a close source-sample position. In the current study, we showed that advanced laboratory instrumentation generates great potential for facilitating high-resolution incremental layer imaging in a non-destructive manner. Barely identifiable lines in tooth cementum obtained with Xradia 620 Versa were enhanced by an oriented projection of 100 slices.³¹ High-resolution, 3D imaging of human tooth cementum, as evidenced in the SR μ CT or μ CT, provides a sufficient anatomical context to show that the thin lines actually correspond to curved 3D layers,⁶⁷ which we showed in scroll-through Fig. 4, where those lines were continuous.

Our findings demonstrate great potential for laboratory sources in ongoing research into tooth cementum annulation (TCA). This phenomenon has been studied in humans for around four decades³²; however, there is—as of yet—neither a coherent explanation nor a standard protocol for tooth selection, preparation, and layer counting, and yet many advances have been made.^{32,34} Laboratory-based μ CT may benefit region selection applied a priori to SR μ CT³ or conventional microscopy, where samples are cut irreversibly into about 100- μ m thin slices.³⁶ Furthermore, the promising results offered by Xradia 620 Versa indicate that laboratory-based μ CT alone could be used to quantify these layers, e.g., in large-scale studies of archeological samples with recorded history, to standardize age estimation or examine the factors influencing layer growth. This approach might be extended to animal studies.

3.6 Comparing the Three-Dimensional Imaging of the Spiral Organization in a Paraffin-Embedded Porcine Nerve by Applying the Next-Generation Laboratory-Based Scanners and ANATOMIX Beamline Microtomography

Similar to tooth imaging, a paraffin-embedded nerve with a diameter of 6 mm does not fit into the field-of-view of the microtomography setups at the spatial resolution selected. Therefore, mosaic-style acquisition⁶⁶ was also applied for porcine nerve imaging at the ANATOMIX beamline. Again, local tomograms from the cutting-edge laboratory-based instruments were registered to data acquired at the ANATOMIX beamline. Figure 5 shows parts of the registered data comparing the gold standard from the ANATOMIX beamline with the selected cutting-edge laboratory-based systems SkyScan 2214, Exciscope, and Xradia 620 Versa, respectively. In the movies, one clearly recognizes a spiral structure to the nerve fiber bundles, which can be approximated by right-handed or left-handed helices with a pitch of about 830 μ m. To provide an idea to the readers without access to the movies, Fig. 6 shows a sequence of 20 virtual slices indicating this spiral structure. This representation of the data from the ANATOMIX beamline, however, is much less convincing than scrolling through the series of adjacent slices in Fig. 5.

3.6.1 Performance of SkyScan 2214

It is not really surprising that data from the laboratory-based system show much more noise than the ones from the synchrotron radiation facility, as easily explained by the photon statistics.

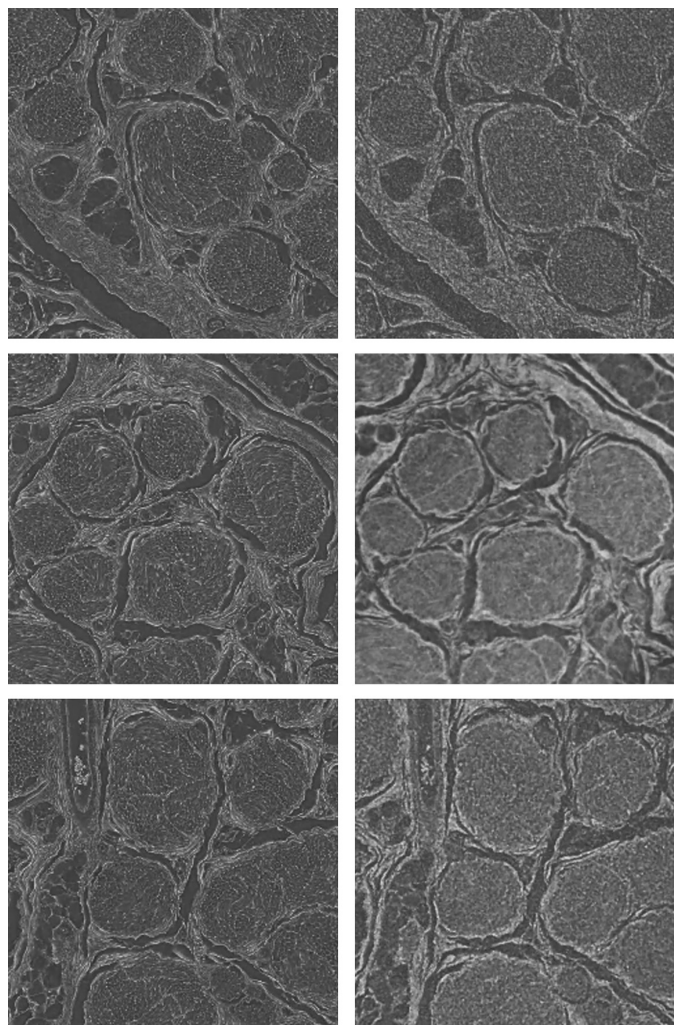


Fig. 5 A still image of [Video 2](#) showing the scroll-through 160 cross-sectional virtual histology slices, prepared by the software VGStudio MAX, of the porcine nerve obtained at the ANATOMIX beamline (left column) and registered local tomography data of SkyScan 2214, Exciscope, and Xradia 620 Versa (right column from top to bottom). The spiral structure of the primary nerve fiber bundles is recognized via rotation during scrolling. The width of each box equals about $780 \mu\text{m}$ ([Video 2](#), MP4, 11503 KB [URL: <https://doi.org/10.1117/1.JMI.9.3.031507.2>]).

The myelin sheaths are slightly more visible in tomography data from the SkyScan 2214 instrument than for the Xradia 620 Versa, as demonstrated by Fig. 5, cp. right column movies at top and bottom.

3.6.2 Performance of Exciscope

Since Exciscope is equipped with a liquid metal source, the photon flux is much higher than for the other two laboratory-based tomography devices. Thus, the density resolution is superior, as seen by the well-preserved myelin sheaths in Fig. 5, second row, right part. This phenomenon is even enhanced by implemented phase retrieval, and consequently, the spiral structure is far more visible. It should be noted that there are right- and left-handed spirals.

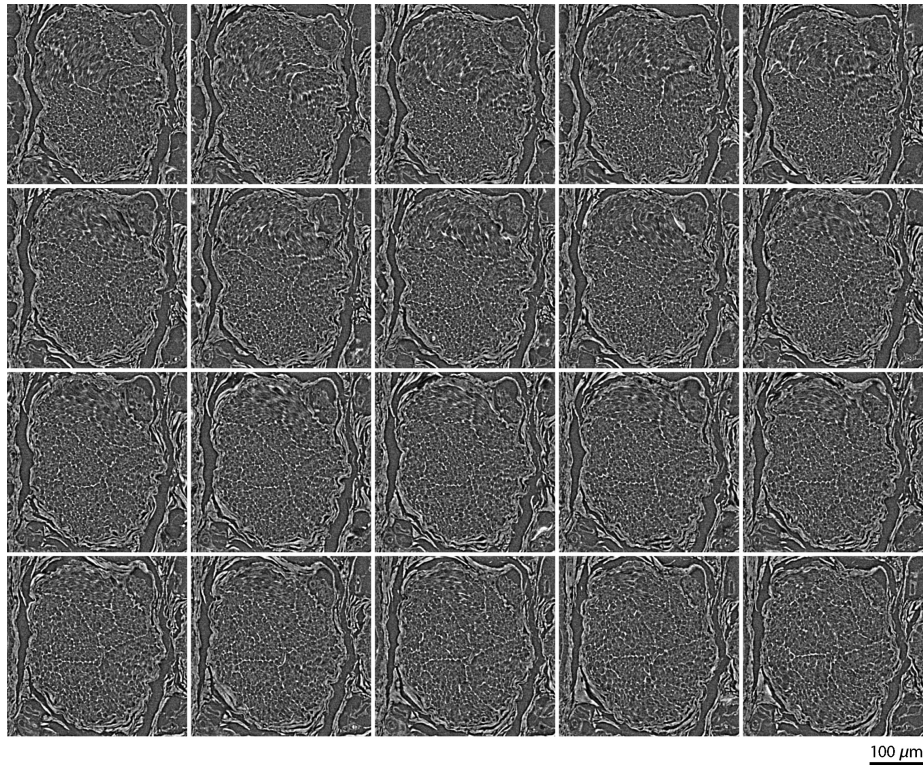


Fig. 6 The sequence of 20 virtual slices from the dataset recorded at the ANATOMIX beamline signifies the spiral structure of the selected nerve fiber bundle (counterclockwise).

3.6.3 Performance of Xradia 620 Versa

Figure 5 (bottom row) clearly demonstrates the substantial improvement of Xradia 620 Versa imaging with respect to the SkyScan 1275 system (cp. Fig. 1). Nevertheless, the myelin sheaths were barely resolved. Regardless, one can detect the spiral structure of the nerve fiber bundles.

3.7 Nerve—Clinical Application

High-density resolution and sub-micrometer spatial resolution are required to quantify changes in axonal bundles and myelin sheaths as the result of nerve injury and regeneration. We showed that the cutting-edge tomography systems SkyScan 2214, Exciscope, and Xradia 620 Versa yield enough spatial and density resolution to enable the visibility of several myelin sheaths and axonal bundles. Therefore, x-ray virtual histology, combined with bioengineering, could facilitate protocols for stepwise de- and re-cellularization, including follow-up laboratory imaging for fast feedback control. Already, laboratory-based μ CT, with or without the combination of conventional histology, can assist in studies of nerve regeneration, including grafting.^{45,68} Furthermore, μ CT could support the urgent diagnostic need of Wegener's polyangiitis,⁶⁹ the gold standard of which is histological examination of tissue biopsy.⁴¹ Moreover, μ CT allows for the further investigation of pathomechanisms of this vasculitis and other neurovascular diseases via the computational extraction of neurovascular networks,⁷⁰ or supporting the 3D prospective mapping of neuron connectivity, to understand the anatomical context.⁷¹ Based on the image quality demonstrated herein, we expect the further integration of advanced μ CT into the study of nerve disease, injury, and regeneration.

In Fig. 5, the spiral shape of nerve bundles is observed as one scrolls through the reconstructed slices. This behavior has been described previously as a chevron pattern in longitudinal histotomographical nerve slices.^{43,44} Whilst the function of this pattern warrants further investigation, one explanation could be a gain in stability, analogous to (steel) wire ropes.⁷²

3.8 Limitations of the Study

The comparative study of next-generation tomography systems for virtual histology has several drawbacks, as already pointed out by manufacturers during data acquisition. The 36-h limit was chosen to create comparable and fair conditions between the laboratory systems as well as to address the real-life lab operation at an imaging platform. Longer scanning times would probably yield improved results considering the reference images from the synchrotron radiation facilities were acquired with a much higher photon flux. The present study did not consider the unequal numbers of photons used for the individual tomograms.

Measurements with the SkyScan 2214 system in March 2021 did not achieve expected data quality; therefore, the measurements were repeated in July 2021, which might have resulted in some bias in terms of direct comparison.

At the time of the measurements (March 2021), the Exciscope system was still in a prototype stage. Therefore, the optics only allowed for data acquisition with an effective pixel size of $1.3 \mu\text{m}$. Simply exchanging a standard optical element would allow for pixel sizes of $0.65 \mu\text{m}$. Since the experiments, Exciscope has designed and built a system with improved specifications. This system has an entirely rebuilt mechanical platform complete with vibration dampening, temperature control, redesigned radiation shielding, electrical control, and safety systems. Furthermore, the system has now a motion system with seven motorized axes, which allows for improved control and automation through the software interface. The vertical object stage is ready to make 280-mm helical CTs with a few microns' resolution. In addition, the rotation stage has a typical error motion of only 0.5 to $0.6 \mu\text{m}$, which together with a high-resolution detector will allow for an isotropic spatial resolution of $1 \mu\text{m}$.

The lack of the PhaseEvolve software for the Xradia 620 Versa system at the stage of data analysis, and the limited pixel size of the Exciscope system, made a direct comparison of the CNR impossible. Together with spatial resolution, CNR is an essential metric in assessing the image quality of acquired tomograms.⁵⁶

Spatial resolution depends not only on the pixel size employed, but also on many other parameters such as the mechanical stability of the entire system and the design of the detection unit. The spatial resolution, we have calculated here, should be treated with care, because the analysis of the power spectrum of reconstructions used^{63,73} is challenging and less straightforward than, for example, the measurement of test patterns. Nonetheless, the quantities derived with the model provided by Mizutani et al.⁶³ are consistent with visual inspection.

3.9 User-Friendliness

The main author, a master's student in medicine, together with the second author, an experienced physicist and an expert in the field, observed the 36-h measurements at the three manufacturers of the cutting-edge, laboratory-based microtomography systems. During the setup of the experiments, the software for the x-ray microscopes was explained in detail. The user-friendliness of the software was compared on the basis of (i) intuitive interface, (ii) structural organization, (iii) efficiency and effectiveness, and (iv) reliability.

Overall, the operation by a novice was best supported by the Xradia 620 Versa software. This interface allowed for a rather simple and intuitive measurement setup. Proceeding through the well-structured software required user input, which was assisted by a compact two-page manual. A live camera showed the sample position within the instrument. Time saving and precise sample centering were based on double-clicking on radiographs at 0 deg and 90 deg rotation angles. A single click allowed for repositioning the sample along the x axis, y axis, and z axis as well as the source and detector along a single axis. Fragile samples were protected from collisions by automatically measuring the sample diameter. Filter and source settings could be comfortably modified via software. A table in the short two-page overview assisted in choosing the best suitable filter, and rapid pre-scanning enabled scouting. Subsequent fine-tune sample centering was performed automatically after manual center identification in the pre-scan data. In addition, "recipes" could be created to facilitate a session for scanning multiple samples. The estimated scanning time was met.

Bruker's software for SkyScan 2214 was also user-friendly. The interface, however, was less self-explanatory. It consisted of one screen combining visualization of the sample using a camera, an immense live-view x-ray window, and the necessary settings. This approach was advantageous for experienced users, but a novice might miss essential adjustments, due to the absence of guidance throughout the preparation steps. Additional settings were hidden in the "options" panel. The sample could be rotated by 360 deg and relocated in the x , y , and z directions, automatically. Translation in the x and y dimensions was simplified by drag-and-drop. Additionally, the detector could be mechanically moved in one dimension. Automatic sample protection was unavailable, but the source and filter could be chosen comfortably via software. The selection of these settings, however, was not guided and linked to the user's prior experience with measurements. Similar to Xradia 620 Versa, rapid pre-scanning allowed for scouting, whilst fine-tune centering was performed manually. Finally, estimated scanning time was generally reliable, although it once underestimated the required scan time.

The user-friendliness of Exciscope could not be assessed, since the prototype was missing a user interface in March 2021, when the measurements took place. The prototype required numerous modifications that precluded operation by a novice user. The reliability of the estimated scan time was satisfactory.

In summary, the software of the Xradia 620 Versa convinced the novice user in terms of ease of use. Bruker's software for SkyScan 2214 offered an almost similarly satisfactory interface, albeit with less simplicity, and user-friendliness could not be assessed for the Exciscope prototype.

The assessment of the usability of the tomography systems was restricted to one novice user, which is a limitation of the present study in consequence of the constraints during the COVID-19 pandemic.

3.10 Laboratory-Based Phase Tomography

The present study belongs to the very few comparative experimental approaches to microtomography^{13,14,16} and should support the purchase of next-generation, laboratory-based systems, especially for the field of medicine. The time is now ripe to combine absorption and phase tomography in a single laboratory-based device and reach an isotropic spatial resolution close to 1 μm , maybe even to 100 nm and below. The gap between the tomography setups at the synchrotron radiation facilities and the established laboratory-based microtomography systems is becoming more and more narrow.

The volumetric evaluation of tissues of human and animal origin is currently mainly done by serial sectioning, staining, and microscopic imaging of individual slices. This approach has its drawbacks, though, such as restricted spatial resolution perpendicular to the slices, and the numerous preparation artifacts. High-resolution hard x-ray tomography can complement histology. Prior to sectioning, the stained and unstained tissues can be made visible in absorption and phase contrast modes, to extract local densities. Histotomography similarly facilitates decision-making in terms of the cutting location and the angle of a probe for further histological examination.⁷⁴ Similarly, laboratory-based phase tomography can support choosing a region of interest prior to valuable beamtimes at synchrotron facilities.

The zebrafish larva is an appropriate example through which to demonstrate complementary information from the absorption and phase contrast modes (see Fig. 2). The combination of 3D data, using a bivariate histogram, can allow for dedicated segmentation tasks.⁷⁵

3.11 Outlook for Virtual Histology

This work demonstrates that the latest laboratory-based systems employing phase and absorption contrast provide scans with the adequate contrast and resolution to differentiate single cells. Previous work has shown that microtomography has excellent correlation with the conventional histology of embedded tissue slices,^{14,24,26,74} and so x-ray microtomography can be referred to as virtual histology. This imaging technique is also compatible with prior MRI-techniques, e.g., diffusion MRI,⁷⁶ or subsequent electron microscopy.⁷⁷ Furthermore, volumetric virtual histology provides a third dimension for histopathological investigation that has typically relied on irreversible, sparse, two-dimensional sectioning. Microtomography does not require stained samples

Migga et al.: Comparative hard x-ray tomography for virtual histology of zebrafish larva...

and avoids slicing them, which results in irreversible destruction of the sample. The conventional approach has further drawbacks, including preparation artifacts such as tears, folds, and non-uniform strains, as well as a requirement for staining.

Laboratory-based systems have the potential to enable the faster availability of virtual histology, as it is currently carried out in synchrotron radiation facilities with limited user access—and most often at a great distance from hospitals. Therefore, further potential benefits of the laboratory-based technique should be explored. While it finds broad application in many research areas, as shown in this study, microtomography could complement future clinical work.

The gold standard for histopathological investigation is conventional histology, based on two-dimensional sectioning, staining, and imaging with optical microscopy. This approach runs the risk of missing important areas or of being time-intensive for the pathologist searching for the region of interest in large samples. Therefore, certain tissues could be examined beforehand, using a laboratory-based system to locate relevant areas and define the best sectioning angle,⁷⁴ and to help removing unreasonable samples early.⁷⁷ This will support that subsequent histology shows the relevant areas under the microscope.

The extent to which virtual histology could support pathology as a diagnostic tool in the future needs to be investigated. Open questions could revolve around the effectiveness of pre-scans using microtomography. Scouting might reduce the overall diagnostic time in larger tissue samples. Nevertheless, a rapid scan followed by slicing needs sufficient spatial resolution and contrast in a reasonable measurement time to indicate a slicing position. The question here arises as to what an appropriate time might be. If one plans first to perform a high-resolution scan of the tissue, subsequent histology might not be necessary because of virtual histology's recently established and validated value for histopathological analysis. However, staining and histology may remain the gold standard in certain cases, e.g., a recent study has shown that Tau proteins in human brains of Alzheimer's disease patients remain undetected in virtual histology.¹³ Still, for many cases, virtual histology could serve as the sole diagnostic tool with scan-times of approximately 10 h per probe. Future studies should determine and validate label-free virtual histology as a reliable diagnostic tool.

4 Conclusions

Due to the advances in instrumentation over the last decade, propagation-based phase-contrast microtomography is no longer reserved for synchrotron radiation facilities. Laboratory x-ray microscopes can provide satisfying (sub-) cellular resolutions to visualize anatomical features with true micrometer resolution. The compared scanners will be further complemented, but they can already provide high-quality datasets of medically relevant hard and soft tissue specimens. These laboratory-based systems not only support beamtime planning by a priori non-destructive isotropic overview scans, but they can also be used in stand-alone imaging. Such imaging can be applied for pre-clinical trials to quantify pathological mechanisms through the versatile zebrafish larva model, the analysis of TCA in mammals, as well as pre-clinical and clinical trials on the regeneration and grafting of nerves.

Disclosure

Phil Salmon is working for Bruker micro-CT, Kontich, Belgium. William Twengström is active at the company Exciscope AB, Kista, Sweden. Holger Blank is employed at Carl Zeiss Microscopy GmbH, Oberkochen, Germany. Iwan Jerjen working at Gloor Instruments AG, Kloten, Switzerland is responsible for the sales and distribution of the Xradia system in Switzerland.

Acknowledgments

We are grateful to the Swiss National Science Foundation for its financial support within the project Micro- and Nanotomography (Grant No. 133802). We acknowledge the Paul Scherrer Institut, Villigen, Switzerland, for the provision of synchrotron radiation beamtime at the TOMCAT beamline X02DA of the SLS, and the Synchrotron SOLEIL for the provision of

synchrotron radiation beamtime at the ANATOMIX beamline within the frame of proposal 20200712. ANATOMIX is an Equipment of Excellence (EQUIPEX) funded by the Investments for the Future program of the French National Research Agency (ANR), project NanoimagesX, grant no. ANR-11-EQPX-0031. We thank Hans Hertz, KTH Stockholm, Sweden, for his kind introduction and support at the Exciscope facility (Stockholm, Sweden). Authors greatly acknowledge the enabling funding support by EUROSTARS (E!10668) and Surgery Foundation of University Hospital Basel to S. Madduri. An earlier version of this paper was published as Proc. SPIE 11840, 1184008 (2021).

References

1. G. Schulz, H. Deyhle, and B. Müller, *Imaging the Human Body: Micro-and Nanostructure of Human Tissues*, Springer (2012).
2. M. Osterwalder et al., “Three-dimensional x-ray microscopy of zebrafish larvae,” *Proc. SPIE* **11586**, 115860J (2021).
3. G. Mani-Caplazi et al., “Imaging of the human tooth cementum ultrastructure of archaeological teeth, using hard x-ray microtomography to determine age-at-death and stress periods,” *Proc. SPIE* **10391**, 103911C (2017).
4. C. Bikis et al., “Three-dimensional and non-destructive characterization of nerves inside conduits using laboratory-based micro computed tomography,” *J. Neurosci. Methods* **294**, 59–66 (2018).
5. M. Töpperwien et al., “Three-dimensional virtual histology of human cerebellum by x-ray phase-contrast tomography,” *Proc. Natl. Acad. Sci. U. S. A.* **115**(27), 6940–6945 (2018).
6. A. Momose, “Recent advances in x-ray phase imaging,” *Jpn. J. Appl. Phys.* **44**(9R), 6355 (2005).
7. D. Paganin, *Coherent X-Ray Optics*, Oxford University Press on Demand (2006).
8. A. Bravin, P. Coan, and P. Suortti, “X-ray phase-contrast imaging: from pre-clinical applications towards clinics,” *Phys. Med. Biol.* **58**(1), R1 (2012).
9. M. Endrizzi, “X-ray phase-contrast imaging,” *Nucl. Instrum. Methods Phys. Res. Sect. A: Accel., Spectrom., Detectors Assoc. Equip.* **878**, 88–98 (2018).
10. A. Khimchenko et al., “Implementation of a double-grating interferometer for phase-contrast computed tomography in a conventional system nanotom[®] m,” *APL Bioeng.* **2**(1), 016106 (2018).
11. S. Lang et al., “Experimental comparison of grating-and propagation-based hard x-ray phase tomography of soft tissue,” *J. Appl. Phys.* **116**(15), 154903 (2014).
12. I. Zanette et al., “Holotomography versus x-ray grating interferometry: a comparative study,” *Appl. Phys. Lett.* **103**(24), 244105 (2013).
13. M. Töpperwien et al., “Correlative x-ray phase-contrast tomography and histology of human brain tissue affected by Alzheimer’s disease,” *NeuroImage* **210**, 116523 (2020).
14. A. Khimchenko et al., “Extending two-dimensional histology into the third dimension through conventional micro computed tomography,” *NeuroImage* **139**, 26–36 (2016).
15. A. Khimchenko et al., “Hard x-ray nanoholotomography: large-scale, label-free, 3D neuro-imaging beyond optical limit,” *Adv. Sci.* **5**(6), 1700694 (2018).
16. S. Drews et al., “Comparative micro computed tomography study of a vertebral body,” *Proc. SPIE* **7078**, 70780C (2008).
17. P. Bidola et al., “Application of sensitive, high-resolution imaging at a commercial lab-based x-ray micro-CT system using propagation-based phase retrieval,” *J. Microsc.* **266**(2), 211–220 (2017).
18. M. Krenkel et al., “Propagation-based phase-contrast tomography for high-resolution lung imaging with laboratory sources,” *AIP Adv.* **6**(3), 035007 (2016).
19. M. Töpperwien et al., “Three-dimensional mouse brain cytoarchitecture revealed by laboratory-based x-ray phase-contrast tomography,” *Sci. Rep.* **7**, 42847 (2017).
20. K. Howe et al., “The zebrafish reference genome sequence and its relationship to the human genome,” *Nature* **496**(7446), 498–503 (2013).
21. K. K. McCampbell and R. A. Wingert, “New tides: using zebrafish to study renal regeneration,” *Transl. Res.* **163**(2), 109–122 (2014).

3.2. PART II: X-RAY-BASED MICROTOMOGRAPHY STUDIES

Migga et al.: Comparative hard x-ray tomography for virtual histology of zebrafish larva...

22. R. M. White et al., "Transparent adult zebrafish as a tool for in vivo transplantation analysis," *Cell Stem Cell* **2**(2), 183–189 (2008).
23. F. Babaei et al., "Contrast-enhanced x-ray micro-computed tomography as a versatile method for anatomical studies of adult zebrafish," *Zebrafish* **13**(4), 310–316 (2016).
24. W. Vågberg et al., "X-ray phase-contrast tomography for high-spatial-resolution zebrafish muscle imaging," *Sci. Rep.* **5**, 16625 (2015).
25. E. Cörek et al., "Shedding light on metal-based nanoparticles in zebrafish by computed tomography with micrometer resolution," *Small* **16**(31), 2000746 (2020).
26. Y. Ding et al., "Computational 3D histological phenotyping of whole zebrafish by x-ray histotomography," *Elife* **8**, e44898 (2019).
27. M. Osterwalder et al., "Hard x-ray microtomography of zebrafish larvae," *Proc. SPIE* **11886**, 1188614 (2021).
28. D. D. Bosshardt and K. A. Selvig, "Dental cementum: the dynamic tissue covering of the root," *Periodontology 2000* **13**(1), 41–75 (1997).
29. T. Yamamoto et al., "Histology of human cementum: its structure, function, and development," *Jpn. Dent. Sci. Rev.* **52**(3), 63–74 (2016).
30. G. Mani-Caplazi et al., "Measuring incremental line width and appearance in the tooth cementum of recent and archaeological human teeth to identify irregularities: first insights using a standardized protocol," *Int. J. Paleopathol.* **27**, 24–37 (2019).
31. C. Tanner et al., "Extended-field synchrotron microtomography for non-destructive analysis of incremental lines in archeological human teeth cementum," *Proc. SPIE* **11840**, 1184019 (2021).
32. S. Naji et al., "Cementochronology, to cut or not to cut?" *Int. J. Paleopathol.* **15**, 113–119 (2016).
33. D. E. Lieberman, "Life history variables preserved in dental cementum microstructure," *Science* **261**(5125), 1162–1164 (1993).
34. T. Colard et al., "Toward the adoption of cementochronology in forensic context," *Int. J. Legal Med.* **132**(4), 1117–1124 (2018).
35. P. Cerrito et al., "Parturitions, menopause and other physiological stressors are recorded in dental cementum microstructure," *Sci. Rep.* **10**, 5381 (2020).
36. B. Bertrand et al., "Age at death estimation by cementochronology: too precise to be true or too precise to be accurate?" *Am. J. Phys. Anthropol.* **169**(3), 464–481 (2019).
37. A. Le Cabec et al., "Nondestructive adult age at death estimation: visualizing cementum annulations in a known age historical human assemblage using synchrotron x-ray microtomography," *Am. J. Phys. Anthropol.* **168**(1), 25–44 (2019).
38. S. K. Lee and S. W. Wolfe, "Peripheral nerve injury and repair," *J. Am. Acad. Orthop. Surg.* **8**(4), 243–252 (2000).
39. D. Pan, S. E. Mackinnon, and M. D. Wood, "Advances in the repair of segmental nerve injuries and trends in reconstruction," *Muscle Nerve* **61**(6), 726–739 (2020).
40. C. Lubetzki et al., "Remyelination in multiple sclerosis: from basic science to clinical translation," *Lancet Neurol.* **19**(8), 678–688 (2020).
41. W. Gross, A. Trabandt, and E. Reinhold-Keller, "Diagnosis and evaluation of vasculitis," *Rheumatology* **39**(3), 245–252 (2000).
42. C. Bikis et al., "Three-dimensional imaging and analysis of entire peripheral nerves after repair and reconstruction," *J. Neurosci. Methods* **295**, 37–44 (2018).
43. M. Töpperwien et al., "Phase-contrast tomography of sciatic nerves: image quality and experimental parameters," *J. Phys.: Conf. Ser.* **849**, 012001 (2017).
44. M. Bartels et al., "Myelinated mouse nerves studied by x-ray phase contrast zoom tomography," *J. Struct. Biol.* **192**(3), 561–568 (2015).
45. T. M. Hopkins et al., "Combining micro-computed tomography with histology to analyze biomedical implants for peripheral nerve repair," *J. Neurosci. Methods* **255**, 122–130 (2015).
46. J. R. Lewis, "The system usability scale: past, present, and future," *Int. J. Hum.-Comput. Interact.* **34**(7), 577–590 (2018).
47. A. A. Kumar et al., "An evaluation of the user-friendliness of Bayesian forecasting programs in a clinical setting," *Br. J. Clin. Pharmacol.* **85**(10), 2436–2441 (2019).

48. J. Gonzalez-Bermejo et al., “Evaluation of the user-friendliness of 11 home mechanical ventilators,” *Eur. Respir. J.* **27**(6), 1236–1243 (2006).
49. P. Salmon, X. Liu, and A. Sasov, “A post-scan method for correcting artefacts of slow geometry changes during micro-tomographic scans,” *J. X-Ray Sci. Technol.* **17**(2), 161–174 (2009).
50. L. A. Feldkamp, L. C. Davis, and J. W. Kress, “Practical cone-beam algorithm,” *J. Opt. Soc. Am. A* **1**(6), 612–619 (1984).
51. D. M. Paganin and T. E. Gureyev, “Phase contrast, phase retrieval and aberration balancing in shift-invariant linear imaging systems,” *Opt. Commun.* **281**(5), 965–981 (2008).
52. D. Paganin et al., “Simultaneous phase and amplitude extraction from a single defocused image of a homogeneous object,” *J. Microsc.* **206**(1), 33–40 (2002).
53. M. Stampanoni et al., “Trends in synchrotron-based tomographic imaging: the SLS experience,” *Proc. SPIE* **6318**, 63180M (2006).
54. F. Marone and M. Stampanoni, “Regriding reconstruction algorithm for real-time tomographic imaging,” *J. Synchrotron Radiat.* **19**(6), 1029–1037 (2012).
55. T. Weitkamp et al., “The tomography beamline ANATOMIX at Synchrotron SOLEIL,” *J. Phys.: Conf. Ser.* **849**, 012037 (2017).
56. G. Rodgers et al., “Optimizing contrast and spatial resolution in hard x-ray tomography of medically relevant tissues,” *Appl. Phys. Lett.* **116**(2), 023702 (2020).
57. P. A. Yushkevich et al., “User-guided 3D active contour segmentation of anatomical structures: significantly improved efficiency and reliability,” *NeuroImage* **31**(3), 1116–1128 (2006).
58. S. Klein et al., “Elastix: a toolbox for intensity-based medical image registration,” *IEEE Trans. Med. Imaging* **29**(1), 196–205 (2009).
59. D. P. Shamonin et al., “Fast parallel image registration on CPU and GPU for diagnostic classification of Alzheimer’s disease,” *Front. Neuroinf.* **7**, 50 (2014).
60. T. M. Lehmann, C. Gonner, and K. Spitzer, “Addendum: B-spline interpolation in medical image processing,” *IEEE Trans. Med. Imaging* **20**(7), 660–665 (2001).
61. K. C. Cheng, “A life-span atlas for the zebrafish,” *Zebrafish* **1**(2), 69–69 (2004).
62. J. C. Burrell et al., “A porcine model of peripheral nerve injury enabling ultra-long regenerative distances: surgical approach, recovery kinetics, and clinical relevance,” *Neurosurgery* **87**(4), 833–846 (2020).
63. R. Mizutani et al., “A method for estimating spatial resolution of real image in the Fourier domain,” *J. Microsc.* **261**(1), 57–66 (2016).
64. M. Andrew et al., “New technologies for x-ray microscopy: phase correction and fully automated deep learning based tomographic reconstruction,” *Proc. SPIE* **11840**, 118400I (2021).
65. R. Santos et al., “A comprehensive map of molecular drug targets,” *Nat. Rev. Drug Discov.* **16**(1), 19–34 (2017).
66. R. Vescovi et al., “TomoSaiC: efficient acquisition and reconstruction of teravoxel tomography data using limited-size synchrotron x-ray beams,” *J. Synchrotron Radiat.* **25**(5), 1478–1489 (2018).
67. E. Newham et al., “A robust, semi-automated approach for counting cementum increments imaged with x-ray computed tomography,” bioRxiv (2021).
68. P. Heimel et al., “Iodine-enhanced micro-CT imaging of soft tissue on the example of peripheral nerve regeneration,” *Contrast Media Mol. Imaging* **2019**, 7483745 (2019).
69. A. P. Diamantopoulos et al., “The fast-track ultrasound clinic for early diagnosis of giant cell arteritis significantly reduces permanent visual impairment: towards a more effective strategy to improve clinical outcome in giant cell arteritis?” *Rheumatology* **55**(1), 66–70 (2016).
70. Y. Cao et al., “Synchrotron radiation micro-tomography for high-resolution neurovascular network morphology investigation,” *J. Synchrotron Radiat.* **26**(3), 607–618 (2019).
71. A. T. Kuan et al., “Dense neuronal reconstruction through x-ray holographic nanotomography,” *Nat. Neurosci.* **23**(12), 1637–1643 (2020).
72. C. Chaplin, “Failure mechanisms in wire ropes,” *Eng. Fail. Anal.* **2**(1), 45–57 (1995).
73. P. Modregger et al., “Spatial resolution in Bragg-magnified x-ray images as determined by Fourier analysis,” *Phys. Status Solidi (a)* **204**(8), 2746–2752 (2007).

3.2. PART II: X-RAY-BASED MICROTOMOGRAPHY STUDIES

Migga et al.: Comparative hard x-ray tomography for virtual histology of zebrafish larva...

74. A. K. Stalder et al., "Combined use of micro computed tomography and histology to evaluate the regenerative capacity of bone grafting materials," *Int. J. Mater. Res.* **105**(7), 679–691 (2014).
75. C. Bikis et al., "Sensitivity comparison of absorption and grating-based phase tomography of paraffin-embedded human brain tissue," *Appl. Phys. Lett.* **114**(8), 083702 (2019).
76. S. Trinkle et al., "Synchrotron x-ray micro-CT as a validation dataset for diffusion MRI in whole mouse brain," *Magn. Reson. Med.* **86**(2), 1067–1076 (2021).
77. A. Morales et al., "Micro-CT scouting for transmission electron microscopy of human tissue specimens," *J. Microsc.* **263**(1), 113–117 (2016).

Alexandra Migga is a master's degree student of medicine at the University of Basel, Switzerland since 2020. She received her BS degree in medicine from the ETH Zürich, Switzerland in 2020, which concluded with a research internship at the Biomaterials Science Center at the University of Basel. There, she has worked in 2021 toward her master's thesis on comparing advances in the visualization of microanatomical features in cutting-edge, laboratory-based microtomography systems employing absorption and phase contrast.

Georg Schulz graduated in theoretical physics at the University Freiburg, Germany, in 2008. Subsequently, he started his PhD project on the multimodal visualization of human brain at the University of Basel, Switzerland. He earned his doctoral degree in physics in 2012. Since 2012, he has been a research associate in the field of high-resolution hard x-ray imaging and has become responsible for the core facility microtomography and nanotomography at the medical faculty of the University Basel, Switzerland.

Griffin Rodgers is a postdoctoral researcher at the Biomaterials Science Center, University of Basel, Switzerland. He studied physics at the University of California, Berkeley and ETH Zurich. In 2021, he received his PhD in physics at the University of Basel with a thesis entitled Hard x-ray microtomography for virtual histology of the brain with cellular resolution. He is currently working on two projects: brain mapping with cellular resolution within the Swiss National Science Foundation-funded project Hierarchical x-ray imaging of the entire human brain and development of novel x-ray optics within the SNI Nano Argovia project 16.01: "ACHROMATIX,"

Melissa Osterwalder is a PhD student at the Biomaterials Science Center of the University of Basel, Switzerland, working on her thesis project entitled Hierarchical X-ray imaging of the entire human brain post mortem. She graduated from her studies in nanoscience at the University of Basel in 2019, where she conducted her master's thesis in the Quantum and Nanoelectronics Group. From 2012 to 2014, she has further studied four semesters of human medicine at the University of Zurich, Switzerland.

Christine Tanner is senior scientist in medical image processing and data analysis. She worked for Siemens AG in Munich, Germany, as a software engineer for 12 years. In 1998, she graduated from the University of Edinburgh, United Kingdom, with a degree in artificial intelligence and mathematics. After a research MSc on radar target classification, she completed her parttime PhD at King's College London, United Kingdom, in 2005 on registration and lesion classification of magnetic resonance breast images. She then was a research fellow and lecturer at University College London, United Kingdom, ETH Zürich, Switzerland, in the field of medical image analysis. In 2020, she joined the Biomaterials Science Center at the University of Basel, Switzerland, for support it in all aspects of quantitative information extraction from images.

Holger Blank graduated in physics in 2007 at the University of Karlsruhe, Germany. He then worked at the Laboratory for Electron Microscopy, Karlsruhe Institute of Technology, Germany, with a main focus on nanoparticle characterization and method development for low-energy scanning transmission electron microscopy. Since 2014 he has a position as application specialist for x-ray microscopy at Carl Zeiss Microscopy GmbH, Oberkochen, Germany.

Iwan Jerjen received his master's degree in physics in 1999 from ETH Lausanne, Switzerland, and his PhD in natural science in 2007 from ETH Zurich, Switzerland. From 2006 to 2008,

he was developing and characterizing superconducting detectors as scientist at European Space Research and Technology Center/European Space Agency, Noordwijk, the Netherlands. From 2008 to 2014, he was responsible for the x-ray microcomputed tomography research at Empa, Dübendorf, Switzerland. Then he worked 3 years as senior assistant at the Institute for Biomedical Engineering of ETH, Zurich, Switzerland, conducting research on differential phase contrast imaging of renal stones at PSI and serving as industrial liaison officer at the TOMCAT beamline of the SLS. Since 2018, he has a position as sales engineer at Gloor Instruments AG, Kloten, Switzerland.

Phil Salmon is currently application scientist at Bruker in Belgium, engaged in development, sales and training for micro-CT imaging systems and software. He received his BSc degree at Southampton University, United Kingdom, two MSc degrees from Plymouth Polytechnic and St Andrews University, Scotland, United Kingdom, and his PhD at Bristol University, United Kingdom. His research career began in radiobiology, then turned to bone biology first at the Royal Veterinary College, London, then AEA Technology, Harwell, United Kingdom.

William Twengström received his PhD in 2018 from KTH Royal Institute of Technology, Stockholm, Sweden. He has researched method and algorithm developments for laboratory-based x-ray phase-contrast tomography as well as the development of biomedical applications. His postdoctoral work was focused on virtual histology of tumor samples. Presently, he is the CEO of Exciscope AB, a company that commercializes the spin-off technologies from KTH to build compact x-ray phase-contrast tomography systems.

Mario Scheel holds a PhD in physics obtained in 2009 from the University of Göttingen. In more than 10 years of work in synchrotron x-ray imaging, he has acquired expertise over a wide range of techniques such as high-energy microtomography, inline phase-contrast imaging, and hard x-ray full-field transmission microscopy (TXM). He is the author of more than 50 peer-reviewed publications. As a scientist at the ANATOMIX tomography beamline at Synchrotron SOLEIL, he is in charge of the TXM nanotomography endstation, which he designed and built. He is also heavily involved in the application of his developments to areas such as materials science and biomedical research.

Timm Weitkamp received a PhD in physics from the University of Hamburg, Germany, in 2002. He has more than 20 years of experience in synchrotron radiation-based x-ray phase-contrast imaging and has authored more than 150 publications. He is the head of the ANATOMIX micro- and nanotomography beamline at Synchrotron SOLEIL, the French national synchrotron light source. His research interests are x-ray optics, imaging and x-ray microscopy, and their applications in various fields of research from advanced materials and systems to biological and medical studies.

Christian Matthias Schlepütz is a beamline scientist at the TOMCAT beamline for tomographic microscopy at the SLS. He received his PhD in experimental physics from the University of Zürich in 2009. After a postdoctoral fellowship at the University of Michigan, he became a beamline scientist in 2011 at Argonne National Laboratory's Advanced Photon Source near Chicago. In 2015, he returned to Switzerland to join the TOMCAT team and since specializes in high-speed time-resolved tomographic measurements.

Jan Stephan Bolten graduated from the University of Basel as a master's degree in pharmacy in 2019 and obtained his federal diploma as a pharmacist in the same year. He is currently working as a PhD student in the research group of Pharmaceutical Technology headed by J. Huwyler at the same University. His research interests focus on zebrafish embryo as an *in vivo* vertebrate model to study aspects of pharmacokinetics, especially renal function and nephrotoxicity

Jörg Huwyler is full professor of pharmaceutical technology at the Department of Pharmaceutical Sciences of the University of Basel, Switzerland. His research interest is in the field of drug delivery and drug targeting using particulate drug carriers. He pioneered the use of zebrafish larvae as a pharmacokinetic screening model.

3.2. PART II: X-RAY-BASED MICROTOMOGRAPHY STUDIES

Migga et al.: Comparative hard x-ray tomography for virtual histology of zebrafish larva...

Gerhard Hotz is curator at the Natural History Museum Basel (Switzerland), where he is responsible for the anthropological collection. In 2003, he completed his PhD at the University of Basel on dietary issues in an alpine skeletal series. Since 2003, he is lecturer at the University of Basel at the Integrative Prehistory and Archaeological Science, where he teaches archaeoanthropology. His main research interests are biographical research on identified skeletons and mummies and the study of living conditions in the 18th and 19th centuries.

Srinivas Madduri directs research in the field of biomaterials and tissue bioengineering at Universities of Basel and Geneva, Switzerland. He completed his masters in biotechnology from Sri Venkateswara University, India. In 2009, he received his PhD from ETH Zurich, Switzerland, in the field of biomedical engineering and neuroregeneration. His past research resulted in more than 50 journal publications and his current research is focused on bio-based biomaterials, therapeutic biotechnology, and nerve tissue bioengineering.

Bert Müller holds the Thomas Straumann Chair for Materials Science in Medicine at the University of Basel, Switzerland and is founding director of the Biomaterials Science Center. He received his master degree in physics from the Dresden University of Technology, Germany; his PhD in experimental physics from the University of Hannover, Germany; and his habilitation in experimental physics from ETH Zurich, Switzerland. His current research interests include high-resolution hard x-ray imaging and physics-based approaches in medicine and dentistry. He is a Fellow of SPIE and named as the 2022 recipient of the SPIE Biophotonics Technology Innovator Award.

3.3 Part III: Mechanism of toxicity

3.3.1 Publication 1

Nephrotoxicity of iopamidol is associated with mitochondrial impairment in human cell and teleost models

Jan Stephan Bolten, Riccardo Vincenzo Mancuso, Noëmi Johanna Roos, Aline Mayr, Ramya Deepthi Puligilla, Lisa Kraus, Alex Odermatt, Gert Fricker, Jörg Huwyler

Toxicology & Applied Pharmacology, Volume 466, 2023, 116493.

doi: 10.1016/j.taap.2023.116493.

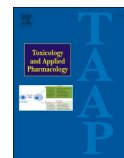
Personal contribution:

My contribution to this research article includes the planning of the project and idea. Thus, I designed the structure and scope of the project and conducted scientific experiments and analyses. I established imaging and experimental protocols. Furthermore, I created all figures and wrote the manuscript.



Contents lists available at ScienceDirect

Toxicology and Applied Pharmacology

journal homepage: www.elsevier.com/locate/taap

Nephrotoxicity of iopamidol is associated with mitochondrial impairment in human cell and teleost models

Jan Stephan Bolten^a, Riccardo Vincenzo Mancuso^{b,c}, Noëmi Johanna Roos^a, Aline Mayr^a, Ramya Deepthi Puligilla^a, Lisa Kraus^d, Alex Odermatt^e, Gert Fricker^{d,f}, Jörg Huwyler^{a,f,*}

^a Department of Pharmaceutical Sciences, Division of Pharmaceutical Technology, University of Basel, 4056, Switzerland

^b Department of Pharmaceutical Sciences, Division of Clinical Pharmacology & Toxicology, University of Basel, 4031, Switzerland

^c Department of Pharmaceutical Sciences, Division of Molecular Pharmacy, University of Basel, 4056, Switzerland

^d Institute of Pharmacy and Molecular Biotechnology, University of Heidelberg, 69120, Germany

^e Department of Pharmaceutical Sciences, Division of Molecular and Systems Toxicology, University of Basel, 4056, Switzerland

^f Mount Desert Island Biological Laboratory, Salsbury Cove, ME 04672, USA

ARTICLE INFO

Editor: Lawrence Lash

Keywords:

Zebrafish
Killifish
Iopamidol
Renal tubular toxicity
Nephrotoxicity
Contrast media

ABSTRACT

Iopamidol is a nonionic, low-osmolar iodinated contrast agent used for angiography. Its clinical use is associated with renal dysfunction. Patients suffering from preexisting kidney disease have an increased risk of renal failure upon iopamidol administration. Studies in animals confirmed renal toxicity, but the involved mechanisms remain unclear.

Therefore, the aim of the present study was to use human embryonic kidney cells (HEK293T) as a general cell model of mitochondrial damage, as well as, zebrafish larvae, and isolated proximal tubules of killifish to investigate factors promoting renal tubular toxicity of iopamidol with a focus on mitochondrial damage.

Results from *in vitro* HEK293T cell-based assays indicate that iopamidol affects mitochondrial function. Treatment with iopamidol induces ATP depletion, reduces the mitochondrial membrane potential, and elevates mitochondrial superoxide and reactive oxygen species accumulation. Similar results were obtained with gentamicin sulfate and cadmium chloride, two well-known model compounds associated with renal tubular toxicity. Confocal microscopy confirms changes in mitochondrial morphology, such as mitochondrial fission. Importantly, these results were confirmed in proximal renal tubular epithelial cells using *ex vivo* and *in vivo* teleost models.

In conclusion, this study provides evidence for iopamidol-induced mitochondrial damage in proximal renal epithelial cells. Teleost models allow studying proximal tubular toxicity with translational relevance for humans.

1. Introduction

Due to the high metabolic activity and excretory function of the kidney, high concentrations of metabolites and xenobiotics can accumulate within its tubular system. This may cause nephrotoxicity, as evident by vascular, glomerular, or tubular damage. Examples of

nephrotoxins inducing renal tubular damage are gentamicin sulfate (an aminoglycoside antibiotic), cadmium chloride (a heavy metal), and iopamidol (a member of the class of iodinated contrast agents) (Naughton, 2008).

Acute adverse reactions to iodinated contrast agents are observed in 1 to 12% of patients, with severe reactions, such as renal failure, from

Abbreviations: AK, Adenylate kinase; CdCl₂, Cadmium chloride; Ctrl, Control; DHR123, Dihydrorhodamine 123; DMEM, Dulbecco's modified eagle medium; eGFP, Enhanced green fluorescent protein; FCCP, Carbonylcyanid-4-(trifluoromethoxy)phenylhydrazone; Gent, Gentamicin sulfate; hpf, Hours post-fertilization; Iopa, Iopamidol; LTDR, Lysotracker Deep Red; MDIBL, Mount Desert Island Biological Laboratory; MMP, Mitochondrial membrane potential; Mrp2, Fish homologue of human multidrug resistance protein 2 (MRP2); MTG, Mitotracker green; O₂^{•-}, Mitochondrial superoxide; PCT, Proximal convoluted tubule; PTC, Proximal tubular cell; Rho123, Rhodamine 123; ROS, Reactive oxygen species; SI, Signal intensity; Sulfo101, Sulforhodamine 101; TMRM, Tetramethylrhodamine methyl ester; ZFL, Zebrafish larva(e).

* Corresponding author at: Pharmaceutical Technology, University of Basel, Department of Pharmaceutical Sciences, Klingelbergstrasse 50, Basel CH-4056, Switzerland.

E-mail address: joerg.huwyler@unibas.ch (J. Huwyler).

<https://doi.org/10.1016/j.taap.2023.116493>

Received 9 February 2023; Received in revised form 23 March 2023; Accepted 24 March 2023

Available online 26 March 2023

0041-008X/© 2023 The Authors. Published by Elsevier Inc. This is an open access article under the CC BY license (<http://creativecommons.org/licenses/by/4.0/>).

0.01 to 3% of total cases (Bush and Swanson, 1991; Gomi et al., 2010; Katayama et al., 1990; Kim et al., 2017). These numbers of acute nephrotoxic events are most pronounced in patients with underlying renal dysfunction (Andreucci et al., 2014). The older ionic contrast agents (high-osmolar) are more nephrotoxic than the newer generation of nonionic (low and isoosmolar) contrast agents, such as iopamidol (Jiang et al., 2019; Wolf et al., 1989). Many studies showed that iopamidol has fewer side effects among contrast agents (Gomi et al., 2010; Wolf et al., 1989), and it is currently used in diagnostics for computer tomography, with over 75 million applications per year (Bottinor et al., 2013).

The uptake of iopamidol into renal epithelial cells occurs through passive diffusion and is favored by its high extracellular diffusion characteristic (Deray, 2006). Since iopamidol is eliminated mainly through glomerular filtration, a high urinary concentration of iopamidol facilitates renal tubular epithelial uptake by diffusion (Deray, 2006). To investigate iopamidol-induced renal impairment, several animal and cell-based studies were carried out. Toxicity studies in animal models, such as rats and rabbits, confirmed iopamidol-induced nephropathy manifested by GFR reduction, reduced blood flow, damage of tubular epithelial cells, and renal tubular cell apoptosis (He et al., 2017; Sugiura et al., 2020). Several biomarkers were found in the urine of treated rats that indicate renal damage, such as increased blood urea nitrogen and plasma creatinine (Sugiura et al., 2020). Damage on the level of proximal tubular epithelial cells was prominent in rats with repeated administration of iopamidol (Niu, 1993). Antioxidants were reported to ameliorate nephrotoxic effects by reducing oxidative stress (Oh et al., 2019). *In vitro* cell-based assays using porcine proximal tubule cells were indicative of impaired mitochondrial membrane potential (Hardiek et al., 2001). It was therefore the aim of the present study to follow up on these preliminary observations and to investigate to which extent mitochondrial damage contributes to the nephrotoxic effects of iopamidol.

Mitochondrial damage caused by toxins is usually studied *in vitro* using fluorescence and luminescence-based assays (Roos et al., 2020). *In vitro* experiments provide mechanistic insights and are cost-effective. However, they do not cover important renal functions, such as flux, gradient- and energy-dependent tubular transport, and glomerular filtration (Allen et al., 2005; Bolten et al., 2022). Confirming findings from *in vitro* assays in living animals is demanding. Various challenges need to be overcome due to the anatomical complexity, species-specific differences, and non-transparency of, e.g., rodents. Furthermore, there is a high and unmet need to reduce, replace, and refine animal experiments (according to the 3R principles) by studying mitochondrial damage in animal-replacing living systems.

Our previous work extensively demonstrated that teleost models can be used in Pharmaceutical Sciences and Toxicology (Bolten et al., 2022; Fricker et al., 1999; Sieber et al., 2019). We studied renal drug transport, the involved signaling cascades, and the effects of toxicants on membrane transporters in isolated renal tubules of killifish (Miller et al., 1997; Oezen et al., 2022; Zaremba et al., 2017). Furthermore, we showed that zebrafish larvae (ZFL) between two to four days old are an ideal *in vivo* vertebrate model for mechanistic and screening studies of nanomedicines (Sieber et al., 2017a, 2019). Recently, we verified that three to four days old ZFL have fully functional pronephros. This allows for using ZFL for physiology and nephrotoxicology studies according to the 3R-principles (reduce, refine and replace animal experiments) (Bolten et al., 2022).

Therefore, we combined *in vitro* cell-based assays with *ex vivo* (killifish) and *in vivo* (ZFL) teleost models to evaluate the mitochondrial damage caused by iopamidol.

We assessed mitochondria-specific parameters, such as ATP content, mitochondrial membrane potential, and the generation of mitochondrial superoxide as well as cellular reactive oxygen species (ROS) in the human embryonic kidney cell line HEK293T. These assays were carried out using fluorescence and luminescence-based standardized assays in

living cells, killifish, and zebrafish models. The killifish models offer an *ex vivo* experimental setup using isolated proximal renal tubules. Finally, in ZFL, the toxic effect of iopamidol was studied in isolated renal epithelial cells (*ex vivo*) and *in vivo*. A schematic representation of the assays, workflow, and experimental setup is provided in Fig. 1.

To our knowledge, this is the first study that applies teleost models to investigate the tubular toxicity of compounds with a focus on mitochondrial impairment. We provide evidence that ZFL can be used as a screening vertebrate model to study renal tubular toxicity.

2. Methods

2.1. Cell culture

Human embryonic kidney cells (HEK293T) were kept at 37 °C with a 5% CO₂ supply in a cell culture incubator. Cells were cultivated in Dulbecco's modified eagle medium (DMEM) high glucose, containing 4.5 g/L D-glucose, 0.584 g/L L-glutamine, and 0.11 g/L sodium pyruvate. The medium was supplemented with 10% (v/v) inactivated fetal calf serum (FCS), penicillin (100 units/mL), and streptomycin (100 µg/mL). Cells were passaged using Trypsin-EDTA (0.25%) solution and harvested at 80% confluency. A Neubauer hemocytometer from BRAND (Merck KGaA, Darmstadt, Germany) was used to count the viable cells. Cells were used between passages 13 and 42.

2.2. Clarification of concentration units used

The mitochondrial damage of iopamidol, gentamicin sulfate, and cadmium chloride (CdCl₂) was tested in different models. Gentamicin sulfate and CdCl₂ were purchased from Sigma-Aldrich (Buchs, Switzerland), and iopamidol (Iopamiro, Bracco, Switzerland) was purchased from a local pharmacy. The concentrations used are of clinical relevance, as argued in the discussion. For easier comparison with existing literature, we kept the concentration units most frequently used in the literature (gentamicin: mM; CdCl₂: µM; iopamidol: (milligram iodine per milliliter (mgI/mL)). Thereby, 6.25, 12.5, 25, and 50 mgI/mL equal 16.4, 32.8, 65.5, and 131 mM of iopamidol.

2.3. Treatment of HEK293T cells

HEK293T cells were treated with different concentrations of gentamicin sulfate (3, 6, 12 mM), iopamidol (6.25, 12.5, 25, 50 mgI/mL), and CdCl₂ (10, 50, 100 µM) for 6 and 24 h. Stock solutions were prepared in 1× phosphate-buffered saline (PBS) and stored at 4 °C (gentamicin sulfate and CdCl₂) or room temperature (iopamidol). The pH was adjusted to physiological conditions. Working solutions were prepared in cell medium, and the same amount of PBS was used in the control treatment.

2.4. Cellular ATP content

To measure the ATP content of treated HEK293T cells, the CellTiter-Glo 2.0 Assay (Promega Madison, WI) was used. Experiments were carried out according to the manufactures instructions. Celltiter-Glo Reagent (50 µL/well) was added to 50 µL of cell medium, followed by incubation on an orbital shaker for 2 min (400 rpm, 24 °C), and the plate was equilibrated at room temperature for another 10 min. The luminescence was recorded with a microplate reader (Infinite 200 PRO, Tecan Group, Männedorf, Switzerland). The measurements were carried out at a final temperature of 30 °C. Data were normalized to control incubations. We used Triton X (0.1%) as a positive control.

2.5. Cellular membrane permeability assay

To assess the cytotoxicity, the release of adenylate kinase (AK) of treated HEK293T cells into the surrounding medium was measured

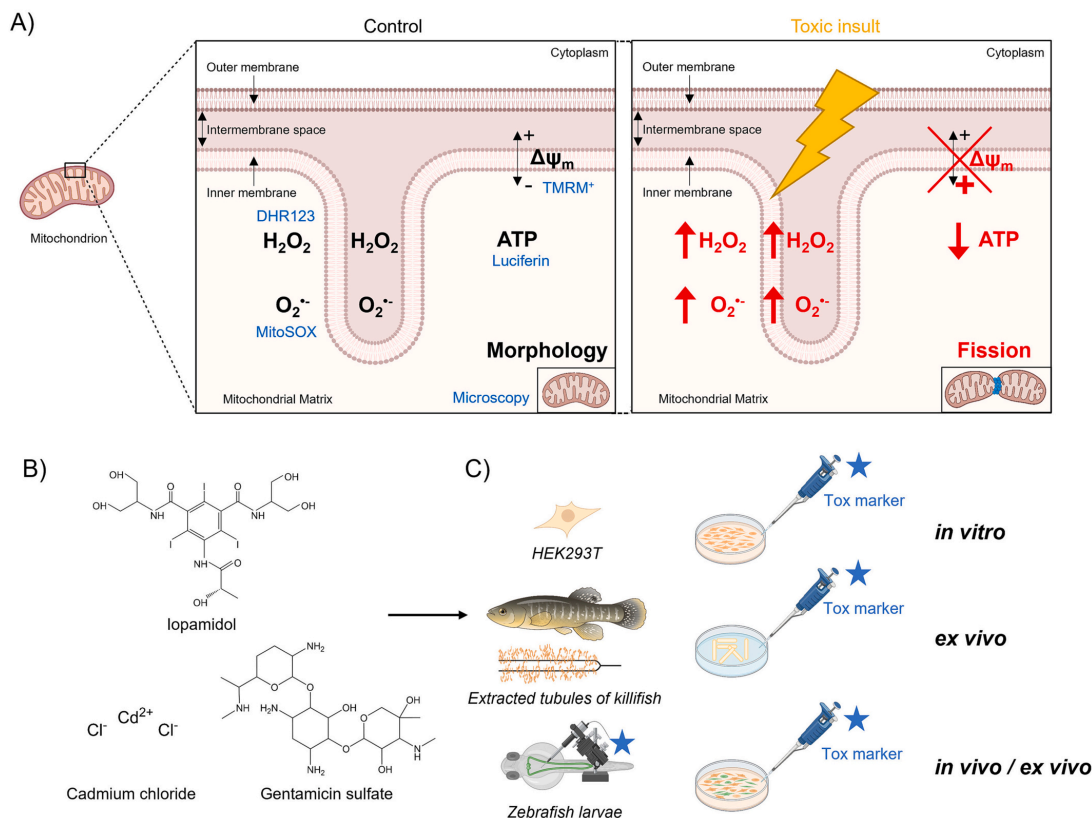


Fig. 1. Schematic illustration of the experimental setup. (A) Illustration of a mitochondrion with the outer membrane, intermembrane space, inner membrane, and mitochondrial matrix. Parameters of interest (bold), such as mitochondrial superoxide ($O_2^{\cdot-}$), cellular ROS (H_2O_2), mitochondrial membrane potential ($\Delta\psi_m$), ATP, and morphology were studied using fluorescent and luminescent assays or imaging devices (blue). Oxidative stress induced by a toxic insult leads to parameter changes, which are indicated in red. (B) Molecular structure of the tested compounds. (C) The assessment of the mitochondrial damage of (B) was studied in HEK293T cells, isolated tubules of killifish, and ZFL. In HEK293T (*in vitro*) and killifish experiments (*ex vivo*), toxic compounds and fluorescent markers were added to the media. In zebrafish experiments, substances of (B) and fluorescent markers were either intravenously injected (*in vivo*) or added to the incubation media containing single cells of lysed ZFL (*ex vivo*). (For interpretation of the references to colour in this figure legend, the reader is referred to the web version of this article.)

using the ToxiLight Bioassay Kit (Lonza, Walkersville, MD). Damaged plasma membranes result in a loss of cell integrity with leakage of intracellular content (e.g., adenylate kinase) into the surrounding cell culture medium. For the 6 h treatment experiments, 20,000 cells/well/100 μ L were seeded in poly-D-Lysine (0.1 mg/mL) coated white wall 96-well plates with a transparent ground. Cells were let to adhere for 24 h. For the 24 h experiments, 15,000 cells/well/100 μ L were seeded. Next, cells were treated with a compound solution for 6 or 24 h. After drug treatment, 20 μ L of the cell supernatant was transferred to a white 96-well plate with a white bottom. The Toxilight detection reagent (50 μ L/well) was added, followed by incubation on an orbital shaker for 5 min (400 rpm, 24 $^{\circ}$ C). The luminescence was recorded with a microplate reader (Infinite 200 PRO, Tecan Group, Männedorf, Switzerland). The measurements were carried out at a final temperature of 30 $^{\circ}$ C. Data were normalized to control incubations. Triton X (0.1%) was used as a positive control.

2.6. Assessment of mitochondrial membrane potential, mitochondrial superoxide, and reactive oxide species using flow cytometry

Flow cytometry was used to measure the fluorescent intensity of indicator dyes for mitochondrial membrane potential (TMRM, ab228569, Abcam, Cambridge, United Kingdom), mitochondrial superoxide content (MitoSOX, Thermofisher Scientific, MA), cellular ROS content (Dihydrorhodamine 123, Sigma-Aldrich, Buchs, Switzerland). For the 6 h treatment experiments, 200,000 cells/well/400 μ L were seeded in poly-D-Lysine (0.1 mg/mL) coated transparent 24-well plates for 24 h. For the 24 h experiments, 100,000 cells/well/400 μ L were seeded. After drug treatment, the fluorescent dye solution was added for 25 min (tetramethylrhodamine methyl ester, TMRM, 100 nM) or 15 min (MitoSOX, 2.5 μ M; Dihydrorhodamine 123, 1 μ M), subsequently removed, and washed with PBS. Cells were detached with trypsin (50 μ L) for 2 min, followed by blocking the trypsinization with prewarmed cell medium containing 10% FCS (150 μ L). The cell suspension (200 μ L) was transferred to a transparent v-bottom 96-well plate and centrifuged (150 \times g at 22 $^{\circ}$ C) for 4 min using a 5804 R Eppendorf centrifuge (Hamburg, Germany) equipped with a plate rotor and plate holder. Cell

supernatant was removed, and the cells were resuspended by adding PBS (200 μ L). Carbonyl cyanid-4-(trifluoromethoxy)phenylhydrazone (FCCP) and hydrogen peroxide (H_2O_2) were used as positive controls.

Samples were analyzed using a CytoFLEX flow cytometer (Beckman Coulter, Indianapolis, IN). Single cells were gated by forward scatter area (FCS-A) and side scatter area (SSC-A). The laser used were 488 nm and 638 nm with the corresponding filters FL1, FL3, and FL5. In total, 10,000 cells/well were analyzed and evaluated by Flow Jo software VX (TreeStar, Ashland, OR).

2.7. HEK293T cells imaging

The cellular morphology of HEK293T cells was evaluated after 24 h of treatment using fluorescence laser scanning confocal microscopy. Organelles such as the mitochondria network, lysosomes, and nuclei were labeled with MitoTracker Green (MTG), LysoTracker Deep Red (LTDR), and Hoechst 33342 (obtained all from ThermoFisher Scientific). In brief, cells were seeded (20,000 cells/well) into poly-D-Lysine (0.1 mg/mL) coated Ibidi μ -Slide eight well (Ibidi GmbH, Gräfelfing, Germany) for 24 h. Next, cells were treated and stained with a staining solution (100 nM MTG, 100 nM LTDR, 2 μ g/mL Hoechst) for 60 min. Then, the cell medium was removed, and the cells were washed twice and covered with prewarmed phenol red-free DMEM (300 μ L). Live cell imaging was performed by 37 °C and 5% CO_2 supply with an Olympus FV-3000 (Olympus Ltd., Tokyo, Japan) fluorescent microscope equipped with a 60 \times UPlan oil-immersion objective (numerical aperture 1.40). Confocal images were acquired using a sequential laser scanning method (1024 \times 1024 pixels), with excitation wavelengths of 405, 488, and 640 nm (argon laser) and emission wavelengths of 430–470, 500–540, and 650–750 nm, respectively. The step size between stacks was 2.5 μ m. For representative images, 2048 \times 2048 pixels, a line scanning laser setting with an average of two was chosen.

2.8. Semiquantitative image analysis of HEK293T cell images

Obtained confocal microscopy images were analyzed and edited using OMERO software 5.4.10 (<https://www.openmicroscopy.org/omero/>) as an image processing program. Quantitative signal intensities of stained cell organelles were evaluated using Fiji software 2.1.0/1.53c (<https://imagej.net/software/fiji/>). Areas of interest were measured based on a threshold applied on the average intensity projection of at least twenty z-stacks of four to sixteen HEK293T cells. Areas were normalized to one nucleus. Areas are presented as fold changes normalized to the mean of the (experimental) control. These experiments are independent ($n = 5$).

2.9. Killifish experiments

Killifish (*Fundulus heteroclitus*) proximal kidney tubules were isolated and prepared as described previously (Fricke et al., 1999). In brief, killifish were purchased from local fishermen in the vicinity of Mount Desert Island, Maine (US), and maintained at the Mount Desert Biological Laboratory (MDIBL) in tanks with naturally flowing, aerated seawater. Since no sex-related differences were observed, extracted tubules from at least 6 randomly chosen killifish were incubated in enriched marine teleost buffer (140 mM NaCl, 2.5 mM KCl, 1.5 mM $CaCl_2$, 1 mM $MgCl_2$, 20 mM TRIS pH 8.25, and 5 mM glucose). Incubations were carried out at 8 °C. To label mitochondria, Mitotracker Red was used (ThermoFisher). Tubular accumulation of the fluorescence markers was assessed using an Olympus FV1000 inverted confocal laser scanning microscope (20 \times , PlanFluo Dry, numerical aperture 0.5). Signal intensities were quantified using image capture and analysis software (NIH Image 1.61, <https://imagej.nih.gov/>).

2.10. Zebrafish husbandry & experiments

Zebrafish (*Danio rerio*) larva experiments and husbandry were carried out in accordance with Swiss animal welfare regulations. Regarding the terminology of zebrafish, we followed the life stage definitions established by Kimmel et al., 1995 (Kimmel et al., 1995), who defined >72 h-post fertilization (hpf) old zebrafish as “larvae.” Eggs from adult zebrafish were collected from different parents 0.5 to 1 hpf and kept at 28 °C in zebrafish culture media (Sieber et al., 2017b). The tg(wt1b:eGFP) and tg(cdh17:eGFP) were kindly provided by Prof. Dr. Schiffer (Erlangen, D) and Prof. Dr. Ian Drummond (MDIBL, US). Zebrafish experiments were performed as described previously (Bolten et al., 2022). In brief, randomly chosen larvae were injected with a calibrated volume of 1 to 2 nL of 25 μ M TMRM or test compounds into the cardinal vein above the heart. Organs of interest were imaged using an Olympus FV3000 confocal laser scanning microscope equipped with a 30 \times UPlanSApo (numerical aperture of 1.05) objective.

Reproducibility was verified by repeating a series of experiments on at least three different days. For each condition of each series of experiments, at least five zebrafish larvae were used.

2.11. Signal intensity quantification and post-processing of images

Quantitative signal intensities in distinct organs were evaluated using Fiji software 2.1.0/1.53c, as described recently (Bolten et al., 2022). In brief, zebrafish lines were used, which express a fluorescent marker (i.e., cdh17:eGFP or wt1b:eGFP) in renal epithelial cells. This allowed for the localization of fluorescently labeled compounds within a defined 3-dimensional anatomical structure such as the renal epithelial cells. Signals were quantified by measuring the mean signal intensities of the selected region of interest. Untreated controls and all corresponding treatment groups were analyzed using the same laser and microscopy settings, allowing a direct comparison of treatment groups. Signal intensities are presented as fold-change normalized to the mean of the (experimental) control.

Three-dimensional rendering of renal epithelial cells was done using Imaris Software V.9.9.0 (Oxford Instruments, Abingdon, UK).

2.12. Zebrafish lysis protocol

The dissociation protocol for generating ZFL single-cell suspension is based on published protocols (Bresciani et al., 2018; Samsa et al., 2016). Compared to reports, in our study, 50 to 60 ZFL were used for each treatment group and were euthanized as described previously (Cörek et al., 2020). Next, ZFL were rinsed twice with deysolting solution (5 mM glucose added to 1 \times Ringer solution) and 1 \times Ringer solution. ZFL were transferred in 4 mL of 0.3% trypsin-EDTA containing 20 μ L DNase for lysis. The solution was pipetted every 5 min for around a minute using 1000 μ L pipette tips for 20 to 25 min. Trypsin degradation was stopped by adding FCS to reach a final concentration of 10%. The solution was filtered through a 70 μ m cell strainer (ThermoFisher Scientific) followed by centrifugation at 300 rcf for 7 min at 4 °C. The supernatant was removed, and the pellet was resuspended with 2 mL of 1 \times DPBS +5% FCS. This step was done in total three times. In the last round, only 0.8 mL of 1 \times DPBS +5% FCS was added. The solution was filtered again using a 40 μ m FlowMI filter (Sigma-Aldrich), and the cell suspension was diluted in 2 mL of 1 \times DPBS +5% FCS. Confocal microscopy and hemocytometer analyses were initially carried out to verify single-cell formation. The same amount of ZFL led to the same amount of single cells, as confirmed for every experiment.

The cell suspension was transferred to a 96-well plate followed by incubation with 2.5 μ M MitoSOX (ThermoFisher Scientific) for 15 min and recommended concentration of CellroX (Cellular ROS Assay Kit Red, Abcam, Cambridge, United Kingdom) for 30 min. Fluorescence intensities were analyzed using the Cytoflex and the indicated laser and detectors. Gating was done based on wild-type (non-eGFP expressing)

CHAPTER 3. RESULTS

J.S. Bolten et al.

Toxicology and Applied Pharmacology 466 (2023) 116493

ZFL. Single cells were gated based on the area of the sideways scattering (SSC) and the FL1-eGFP detector. 1500 GFP⁺ cells were analyzed and evaluated using the Flow Jo VX software (Treestar). PBS-injected ZFL did not show any differences from non-treated ZFL.

2.13. Statistics

Statistical analyses were performed by ordinary one-way analysis of variances (ANOVA) followed by Dunnett's multi-comparison tests using

GraphPad Prism version 8.2.1 (GraphPad Software, CA). The acquired data was compared to control values. Significance against control was indicated with an asterisk (*) and the corresponding *p*-value.

3. Results

We first studied the toxic effect of iopamidol in HEK293T cells. An array of established fluorescent and luminescent assays was carried out to assess the effects of iopamidol on mitochondrial function (Fig. 1A).

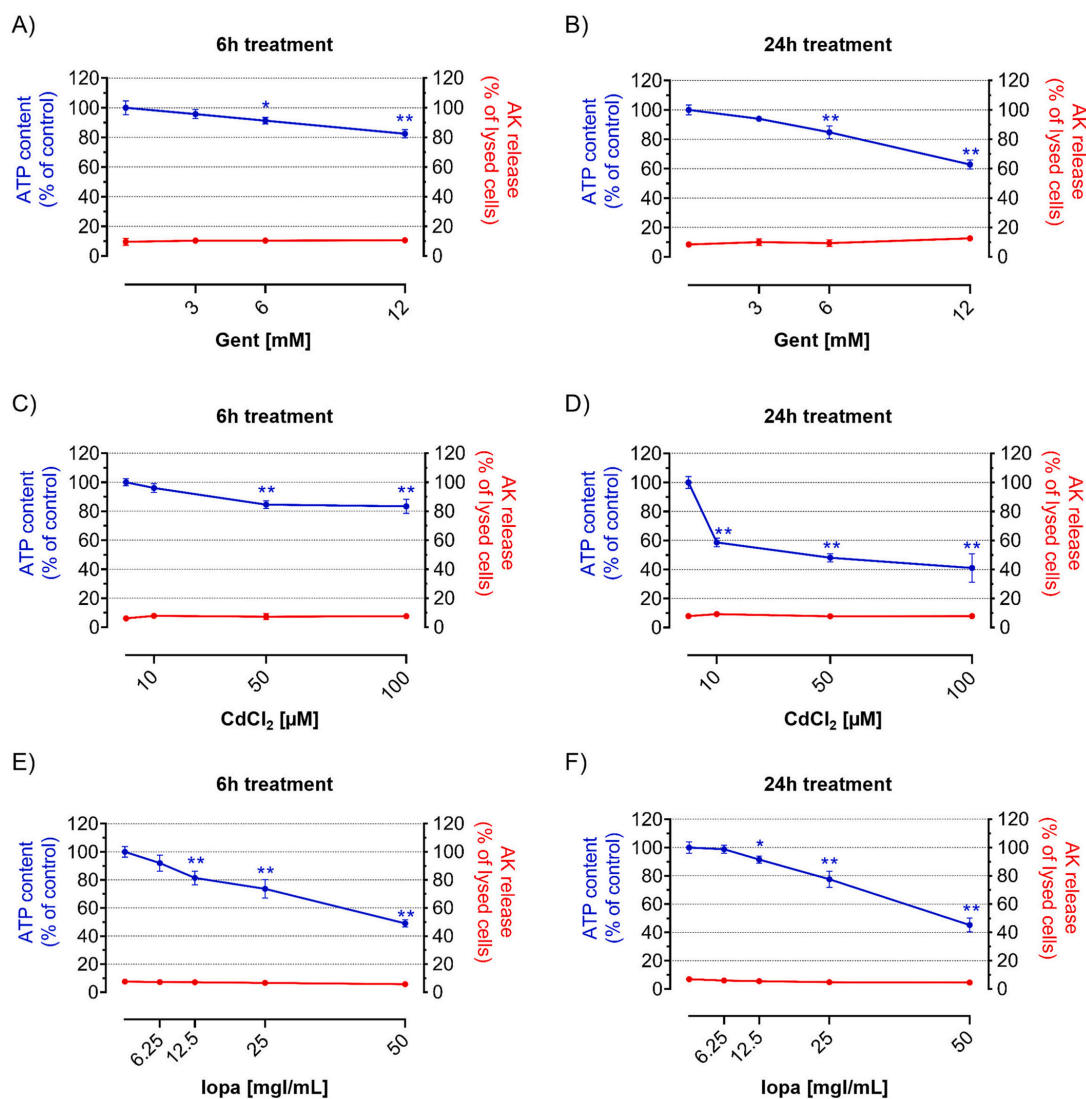


Fig. 2. Intracellular ATP content and AK release in HEK293T cells. (A) ATP content and membrane integrity (AK release) after incubation with different concentrations of gentamicin (Gent; 3, 6, 12 mM) for 6 and (B) 24 h; (C) CdCl₂ (10, 50, 100 μM) for 6 and (D) 24 h; (E) iopamidol (Iopa; 6.25, 12.5, 25, 50 mg/ml) for 6 and (F) 24 h. Data are presented as % of ATP content compared to control (set as 100%, blue) or as % of AK release of cells treated with 0.1% Triton X (set as 100%, red). Data are presented as means ± SD of at least *n* = 3 independent experiments. Statistical analyses were calculated by one-way ANOVA followed by Dunnett's multiple comparison test, and the threshold for significance was set to (*) for *p* < 0.05 and (**) for *p* < 0.001. (For interpretation of the references to colour in this figure legend, the reader is referred to the web version of this article.)

3.3. PART III: MECHANISM OF TOXICITY

J.S. Bolten et al.

Toxicology and Applied Pharmacology 466 (2023) 116493

Results on iopamidol were compared with those from two tubular toxic compounds, gentamicin and CdCl₂ (Fig. 1B). For morphological studies, confocal microscopy experiments were performed using fluorescent dyes for specific cell organelle labeling. Then, *in vitro* findings were confirmed in isolated renal tubules of killifish, followed by *in vivo/ ex vivo* experiments in ZFL (Fig. 1C).

To assess if mitochondrial dysfunction occurs prior to general cellular toxicity, intracellular ATP content (indicative of mitochondrial damage) and membrane integrity (indicative of general cellular toxicity) were assessed in the presence of the compounds. Cells were exposed to different concentrations of test compounds for 6 and 24 h. After 6 h of incubation with 3, 6, and 12 mM of gentamicin, a concentration-dependent ATP depletion was observed (Fig. 2A). The ATP content was significantly depleted at concentrations of 6 mM and 12 mM, with a drop of almost 10% between 6 mM (91% of control) and 12 mM (82% of control). We did not observe significant adenylate kinase release at these concentrations, which indicates no membrane integrity loss and hence no cellular membrane disruption. After 24 h of incubation with gentamicin, the ATP depletion was more pronounced at the three highest concentrations, with significant depletions at 6 mM (85% of control) and 12 mM (63% of control) (Fig. 2B). No AK release was observed.

Cells treated with CdCl₂ revealed a similar depletion in ATP content (Fig. 2C). The drop was significant ($p < 0.001$) and was observed at 50 μ M (84% of control) and 100 μ M (83% of control) after 6 h of incubation. No AK release at all concentrations was observed. For 24 h of incubation (Fig. 2D), there was a sharp drop in intracellular ATP content

starting at 10 μ M (59% of control), as well as for the concentration of 100 μ M (41% of control).

Cells treated with iopamidol showed similar results (Fig. 2E and F). A significant ATP depletion ($p < 0.001$) was observed at the concentration of 12.5 mg/ml (81% of control), which continued to drop to 74% compared to control with 25 mg/ml, and reached its minimum at 50 mg/ml (49% of control) after 6 h of treatment. There was a statistically significant decrease between 25 mg/ml and 50 mg/ml iopamidol after both 6 h and 24 h of incubation ($p < 0.001$). There was no statistically significant difference between 6.25 and 12.5 mg/ml and 12.5 and 25 mg/ml iopamidol. No AK release was observed throughout all concentrations and time points tested in iopamidol-treated cells, indicative of mitochondrial damage and without cellular membrane disruption (Fig. 2F). ATP values are provided relative to controls in accordance with published procedures to determine the concentration onset of toxicity (Rudin et al., 2020).

Next, the change in mitochondrial membrane potential (MMP) was investigated. The MMP is maintained by a proton gradient between the mitochondrial matrix and the intermembrane space and indicates the function of the electron transport chain [40]. The positively charged fluorescent dye TMRM accumulates inside the mitochondrial matrix due to its negative charge. Toxic effects can disturb the MMP, whereby the mitochondrial matrix gets depolarized, and TMRM accumulates less [44]. For 6 and 24 h of incubation, HEK293T cells were incubated at different concentrations of test compounds.

The signal intensity of the experimental control was set to 100%.

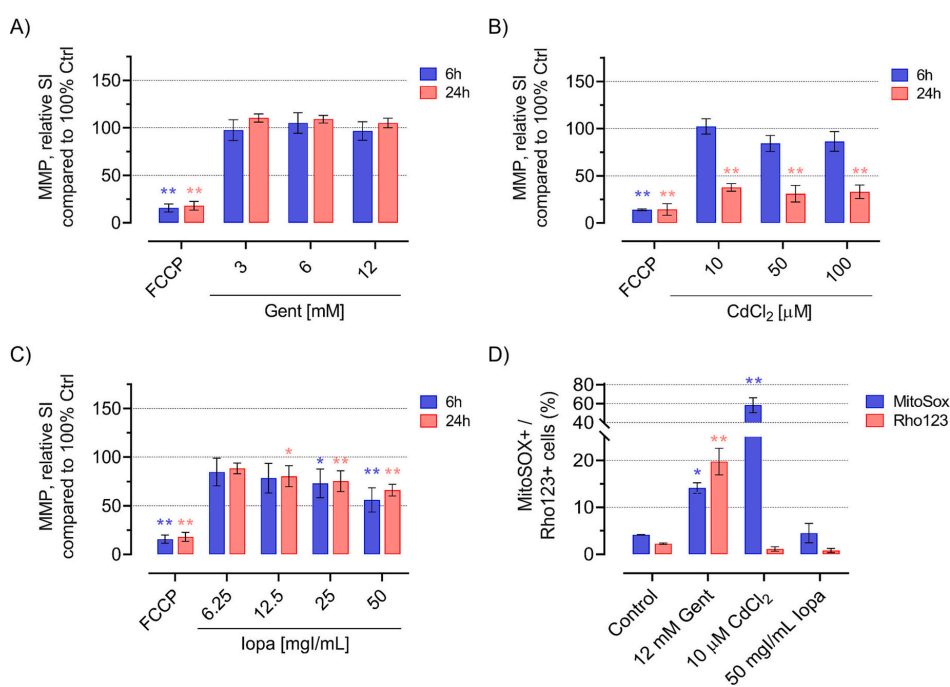


Fig. 3. Mitochondrial membrane potential and superoxide accumulation in treated HEK293T cells. (A) MMP compared to 100% control after incubation with gentamicin (Gent; 3, 6, 12 mM); (B) CdCl₂ (10, 50, 100 μ M); (C) iopamidol (Iopa; 6.25, 12.5, 25, 50 mg/ml) for 6 h (blue) and 24 h (red), respectively. Data are presented as relative signal intensity to untreated cells in PBS (set as 100%). As a positive control, cells were treated for 15 min with 10 μ M of FCCP. (D) Mitochondrial superoxide (O₂⁻) and reactive oxygen species (ROS) quantification in HEK293T cells. Data are shown as the percentage of cells containing O₂⁻ (MitoSOX+, blue) and ROS (Rhod123+, red) after treatment with PBS (control), 12 mM gentamicin, 50 mg/ml iopamidol, or 10 μ M CdCl₂ for 24 h. Data are presented as means \pm SD of $n = 3$ independent experiments. Statistical analyses were calculated by one-way ANOVA followed by Dunnett's multiple comparison test, and the threshold for significance was set to (*) for $p < 0.05$ and (**) for $p < 0.001$. (For interpretation of the references to colour in this figure legend, the reader is referred to the web version of this article.)

CHAPTER 3. RESULTS

J.S. Bolten et al.

Toxicology and Applied Pharmacology 466 (2023) 116493

Gentamicin did not reduce the MMP, neither after 6 nor 24 h of incubation, respectively (Fig. 3A). Cells treated with 10, 50, and 100 μM CdCl_2 did not show any alterations of the MMP after 6 h of incubation (Fig. 3B). However, after exposure for 24 h, all treated cells showed a highly significant drop of the MMP to 38% at 10 μM , 31% at 50 μM , and 33% at 100 μM CdCl_2 .

Iopamidol caused a reduction of the MMP for both 6 and 24 h of incubation, respectively (Fig. 3C). Cell treated for 6 h revealed a significant reduction to 73% at 25 mg/ml and 56% at 50 mg/ml iopamidol ($p < 0.05$ and 0.001). Cells treated for 24 h with 12.5 mg/ml showed a decrease to 80%. The decline continued to 75% at 25 mg/ml and 66% at 50 mg/ml compared to 100% control. Results indicate that CdCl_2 and iopamidol impaired the MMP. There was no statistically significant difference among concentrations. MMP reduction can result from a dysfunctional mitochondrial electron transport chain. Inhibition of the mitochondrial electron transport chain complexes can lead to the production of reactive oxygen species. Thus, we subsequently studied the accumulation of O_2^- and cellular ROS in HEK293T cells using the fluorescent MitoSOX and dihydrorhodamine 123 assays, respectively (Fig. 3D). 12 mM gentamicin, 50 mg/ml iopamidol, and 10 μM CdCl_2 were chosen to investigate mitochondria-specific toxicity further because they caused ATP depletion but did not impair the cellular membrane integrity.

HEK293T cells were incubated for 24 h at the mentioned concentrations. HEK293T cells treated with 12 mM gentamicin showed a significant increase in the percentage of MitoSOX positive (MitoSOX+) cells (indicating O_2^- accumulation) of around 14% compared to 4% (control) (Fig. 3D). HEK293T cells treated with 10 μM of CdCl_2 showed 58% MitoSOX+ cells. Exposure to 50 mg/ml of iopamidol did not reveal an increased number of MitoSOX+ cells.

In addition, cellular ROS formation was measured using the non-fluorescent dye dihydrorhodamine 123 (DHR123), which will be oxidized by hydrogen peroxide (H_2O_2) into the fluorescent Rhodamine 123 (Rho123). A significant increase ($p < 0.05$) of Rho123 positive (Rho123+) cells (20%) was detected for HEK293T cells treated with 12 mM of gentamicin. No elevated ROS production was detected in HEK293T cells treated with 50 mg/ml iopamidol and 10 μM CdCl_2 (Fig. 3D).

Fluorescent laser scanning confocal microscopy experiments were conducted to analyze the morphological shape, lysosomes, and mitochondrial network. HEK293T cells were treated for 24 h. Cells were stained afterward with Mitotracker (MTG), LysoTracker Deep Red (LTD), and Hoechst 33342 to highlight specific cell organelles (Fig. 4A).

Brightfield images revealed round-shaped cells for all gentamicin, CdCl_2 , and iopamidol-treated cells (Fig. 4A). Cells treated for 24 h with 12 mM gentamicin and 10 μM of CdCl_2 showed a substantial increase in red signals representing lysosomes. No lysosome-specific signs were observed for the control and iopamidol-treated cells. The mitochondrial network that continually fuses and divides can be influenced by mitochondrial toxicants (Paech et al., 2018). In iopamidol-treated cells, the mitochondria do not form a network, are round-shaped and are similar to the mitochondria in gentamicin- and CdCl_2 -treated cells. These pattern indicates mitochondrial fission or mitochondrial swelling. Furthermore, gentamicin and CdCl_2 -treated cells show colocalization of mitochondria with lysosomes (yellow) in Fig. 4B.

Quantification revealed that the size of the mitochondrial network and the cellular area is reduced in all treatment groups compared to the experimental control (100%) (Fig. 4C). Gentamicin reduced the size of mitochondria to 65%, CdCl_2 to 49%, and iopamidol to 64% compared to 100% control. The size of the cells is reduced to 58%, 54%, and 56% for gentamicin, CdCl_2 , and iopamidol. Further, gentamicin and CdCl_2 increase the area of lysosomes (272% and 288%), respectively, compared to 100% control.

Next, the killifish model was used to test these substances in a more sophisticated organ model. Isolated proximal tubules were used as an *in vivo* model to confirm *in vitro* cell experiments. First, isolated tubules

were incubated with compounds for 1 h, followed by assessing the highly sensitive mitochondrial membrane potential using the TMRM fluorescent assay. Results indicated that all three compounds reduced the mitochondrial membrane potential after 1 h of incubation, which indicates early onset of mitochondrial impairment (Supplement Fig. 1). Next, substances were incubated in renal tubules for 6 h at 4 $^\circ\text{C}$, and further mitochondrial-specific assays were performed at the same incubation time using the fluorescent marker dyes TMRM (mitochondrial membrane potential), MitoSOX (O_2^-), and DHR123 (ROS). Renal epithelial cells were imaged and compared relative to control treatments (Fig. 5A). Changes in the signal intensity of the accumulation of TMRM indicate that the MMP was significantly ($p < 0.001$) reduced in a concentration-dependent manner (Fig. 5B). Gentamicin reduced the MMP to 64% (10 μM) and 55% (3 mM), CdCl_2 to 62% (50 nM), and iopamidol to 74% (6.25 mg/ml) and 55% (50 mg/ml) compared to 100% control. Treated tubules revealed an increase in MitoSOX signal intensities for all tested concentrations (Fig. 5C). Compared to the 100% control, gentamicin increased the signal intensity of MitoSOX to 138% (10 μM) and 197% (3 mM), CdCl_2 to 397% (50 nM), and iopamidol to 182% (6.25 mg/ml) and 182% (50 mg/ml). Cellular ROS were also observed in all treatment groups (Fig. 5D). Gentamicin induced an increase of the signal intensity to 203% (10 μM) and 178% (3 mM), CdCl_2 to 153 (50 nM), and iopamidol to 133% (6.25 mg/ml) and 163% (50 mg/ml) compared to 100% control. Results revealed similar results among all treatment groups, even with lower concentrations.

In a subsequent experiment (Fig. 5E), the impact of iopamidol on ATP levels was assessed. ATP-dependent renal tubular transport mediated by the ATP-binding cassette transporters (ABC) was studied in the presence of 6.25 and 50 mg/ml iopamidol for 6 h. The accumulation of the fluorescent Sulforhodamine 101 (Sulfo101, Mrp2 substrate) in the luminal space of renal tubules correlates with the activity of apical-located ATP-dependent Mrp2 transport. Iopamidol caused a concentration-dependent impairment of renal tubular transport of Sulfo101 (75% and 44% of control). To verify that this reduction of transport is not caused by an iopamidol-specific inhibition of Mrp2, tubules were treated with a low and non-toxic concentration of iopamidol (6.25 mg/ml) for 1 h (Supplement Fig. 2). No reduction in Mrp2 transport was observed. We conclude that iopamidol did not directly inhibit Mrp2-mediated transport, but the transport was affected due to iopamidol-induced ATP depletion.

To study morphological aberrations of the mitochondrial network of renal epithelial cells, isolated tubules were exposed to Mitotracker Red after treatment with iopamidol, gentamicin, and CdCl_2 (Fig. 5F). Renal epithelial cells of treated tubules showed shrinkage in the size of the mitochondria compared to the experimental control.

The zebrafish model was used to assess the renal toxicity of iopamidol in a living organism. The change in the accumulation of intravenously injected TMRM in proximal renal epithelial cells was investigated (Fig. 6A). Furthermore, the PCT volume was analyzed using the tg(cdh17:eGFP) line that expresses eGFP in renal epithelial cells.

The fluorescent marker TMRM was *i.v.* injected, and its accumulation within renal epithelial cells is shown in Fig. 6B. Detailed colocalization within PCT is shown in a slice, maximum projection, and rendered visualization. In a subsequent experiment (Fig. 6C), the signal intensity of TMRM accumulated within renal proximal tubules was assessed in ZFL. All fish survived 6 h of treatment at the indicated concentrations. Signal intensities of TMRM showed a reduction of TMRM accumulation in PCT for all treatment groups indicating impaired MMP (Fig. 6D). Gentamicin reduced the TMRM accumulation to 59%, CdCl_2 to 61%, and iopamidol to 77% compared to 100% control. The PCT volume increased 1.31-fold in the gentamicin, 1.33-fold in the CdCl_2 , and 1.36-fold in the iopamidol treatment group ($p < 0.001$). The increase in the distal parts of the renal tubules that are metabolically less active than the proximal tubules did not show any changes in volume compared to the control (Supplement Fig. 3).

Next, O_2^- and ROS were investigated using a different approach. The

7

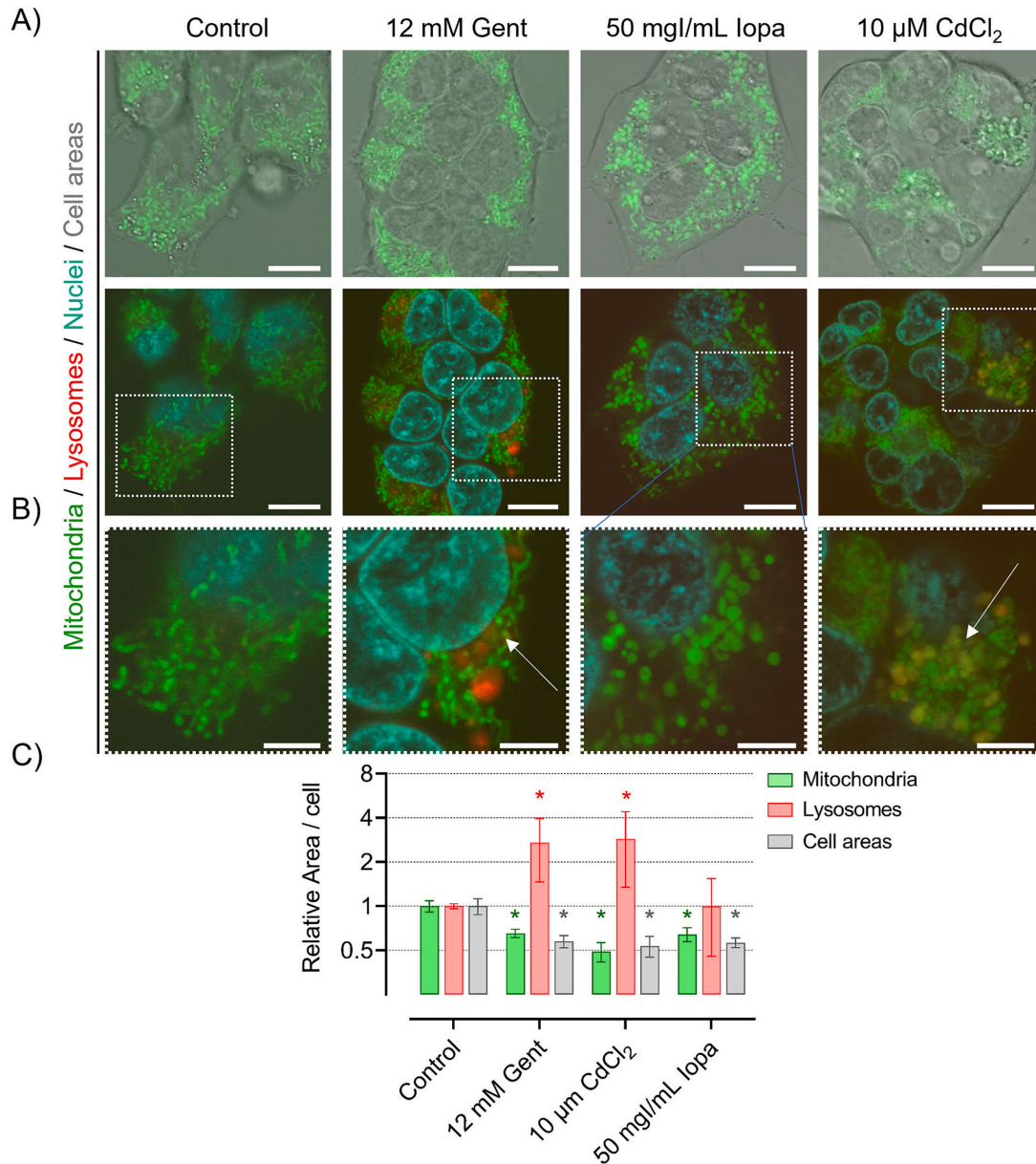


Fig. 4. Analysis and quantification of cellular morphology and organelles of treated HEK293T cells. (A) Upper panel: Qualitative analysis of cell parameters such as mitochondria (green) and cell size (grey) after incubation with buffer (control), 12 mM gentamicin, 50 mg/ml iopamidol, and 10 μ M CdCl₂ for 24 h. Lower panel: Qualitative analysis of lysosomes (red), nuclei (blue), and mitochondria (green). Zoom-in into the mitochondrial network is indicated in white dotted quadrants. Size bar: 10 μ m (B). Colocalization of lysosomes with the mitochondrial network (mitophagy) is represented in yellow for CdCl₂ and gentamicin (white arrows). Size bar: 5 μ m (C) Quantitative analysis of confocal microscopy images. Data are presented as the normalized area per cell compared to the control (set as 1). Data are presented as means \pm SD of $n = 5$ independent experiments of images containing each 4 to 35 nuclei. Statistical analyses were calculated by one-way ANOVA followed by Dunnett's multiple comparison test. The threshold for significance was set to (*) for $p < 0.05$. (For interpretation of the references to colour in this figure legend, the reader is referred to the web version of this article.)

CHAPTER 3. RESULTS

J.S. Bolten et al.

Toxicology and Applied Pharmacology 466 (2023) 116493

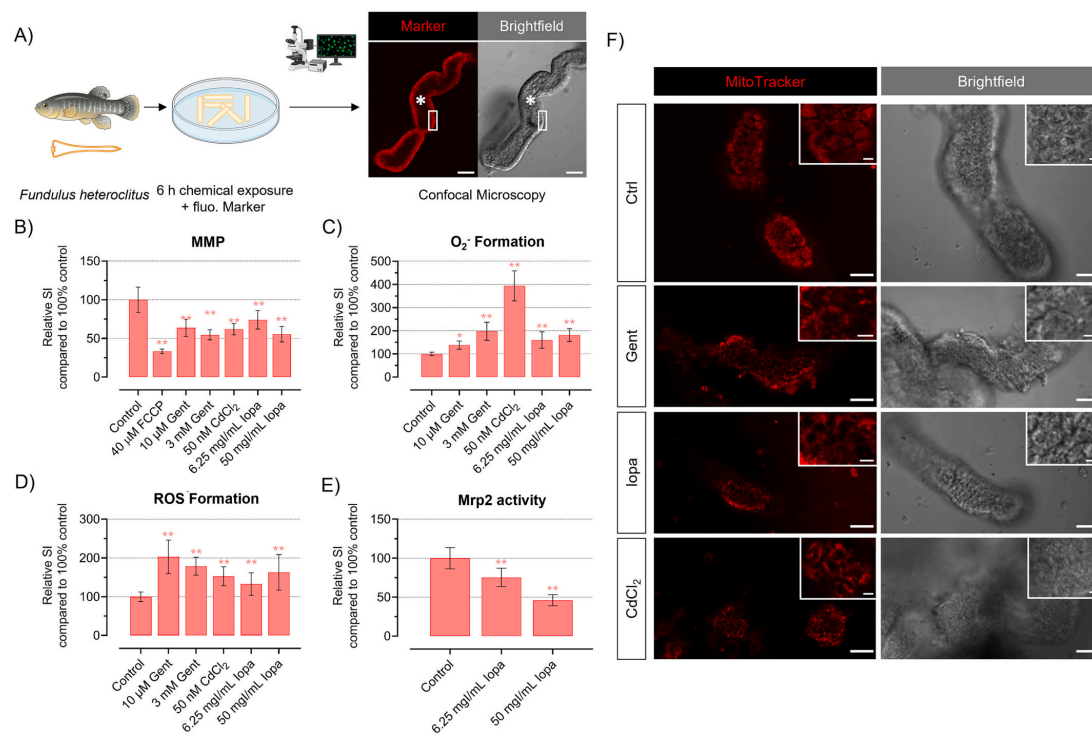


Fig. 5. Toxicity assessment in isolated renal tubules of killifish (*Fundulus heteroclitus*). (A) Freshly isolated renal tubules were incubated in chemical solutions for 6 h. Subsequently, fluorescent markers were added, and accumulation in renal epithelial cells (rectangle) and luminal space (*) were analyzed by confocal microscopy. Size bar: 50 μ m. (B) Quantification of the fluorescent signal of TMRM in epithelial cells indicating the MMP, (C) MitoSOX for O₂[•], and (D) Rhodamine123 for cellular ROS compared to the mean of the control (set as 100%). (E) Renal tubules were incubated in 6.25 or 50 mg/ml iopamidol followed by 1 h incubation of Sulfo101 (Texas Red) as a specific Mrp2 substrate. Relative signal intensity in luminal space of Sulfo101 indicating Mrp2-mediated active tubular excretion. (F) Labeling of mitochondria of renal epithelial cells using Mitotracker Red (left panel). Corresponding brightfield images (right panel). Size bar: 5 μ m and 50 μ m. Values represent means \pm SD of >15 renal tubules each. The threshold for significance was set to * p < 0.05 and ** p < 0.001. (For interpretation of the references to colour in this figure legend, the reader is referred to the web version of this article.)

commonly used markers to assess O₂[•]/ROS are weak fluorescent dyes. Therefore, iopamidol and gentamicin were i.v. injected into tg(cdh17:eGFP) ZFL or they were incubated in CdCl₂ solution (Fig. 7A). After 24 h of incubation, single cells were isolated from ZFL. Subsequently, the fluorescent markers MitoSOX or CellroX Red were added. Of note, MitoSOX⁺ and CellroX⁺ cells were measured only in eGFP⁺ cells (Fig. 7B). Gentamicin and CdCl₂-treated ZFL showed an increase in MitoSOX⁺ cells (Fig. 7C). Compared to the control (7% MitoSOX⁺ cells), gentamicin treatment caused 12% (1 nL of 21 mM Gent injected) and 15% (1 nL of 42 mM Gent injected) MitoSOX⁺ renal epithelial cells. For CdCl₂, 16% (10 μ M CdCl₂ incubation) and 19% (50 μ M CdCl₂ incubation) of eGFP⁺ cells were MitoSOX⁺. Renal epithelial cells of iopamidol-treated ZFL were less affected and showed 10% of MitoSOX⁺ cells.

Elevated ROS⁺ cells were also measured in renal epithelial cells of gentamicin and CdCl₂-treated ZFL. Compared to the control (7% ROS⁺ cells), ZFL treated with gentamicin showed 12% ROS⁺ cells (1 nL of 42 mM Gent). CdCl₂-treated ZFL revealed both 14% ROS⁺ cells (10 and 50 μ M CdCl₂). The treatment groups of iopamidol and lower concentration of gentamicin (1 nL of 21 mM Gent) did not show a significant relevant increase of ROS⁺ cells (8% and 9%). All treated ZFL survived 6 h of treatment. For 24 h of incubation, survival was 99% at control conditions (buffer only), 97% at 21 mM Gent, 92% at 42 mM Gent, 92% at 10 μ M CdCl₂, 75% at 50 μ M CdCl₂, and 99% at both iopamidol

concentrations.

4. Discussion

In the present study, we investigated the toxic effects of iopamidol. We used HEK293T cells (*in vitro*), isolated renal tubules of killifish (*ex vivo*), and three to four day old ZFL (*ex vivo/in vivo*). We compared the toxicity of iopamidol with those of the well-known tubular toxic compounds gentamicin and CdCl₂.

HEK293T cells have been used to study mitochondrial function and to assess chemical-induced damage in several toxicology studies (Cui et al., 2021; Mao et al., 2011; Sun et al., 2018). While the focus of the *in vitro* studies using HEK293T was on general mitochondrial function, the impact of iopamidol on differentiated tubular cells was studied using *ex vivo/in vivo* teleost models. To determine if and at which concentration the toxins induce mitochondrial damage, ATP content was first measured. Mitochondria are the main site of ATP production (Bertram et al., 2006). If mitochondria are directly and/or indirectly hit by toxic insults, ATP production, a marker of mitochondrial health, may decrease while maintaining an intact cell membrane, as proved here by the assessment of extracellular leakage of AK (Zhou et al., 2020). The results from HEK293T cell experiments treated with gentamicin, CdCl₂, and iopamidol similarly reveal ATP depletion but no AK release. This indicates that the tested compounds may have a direct and/or indirect

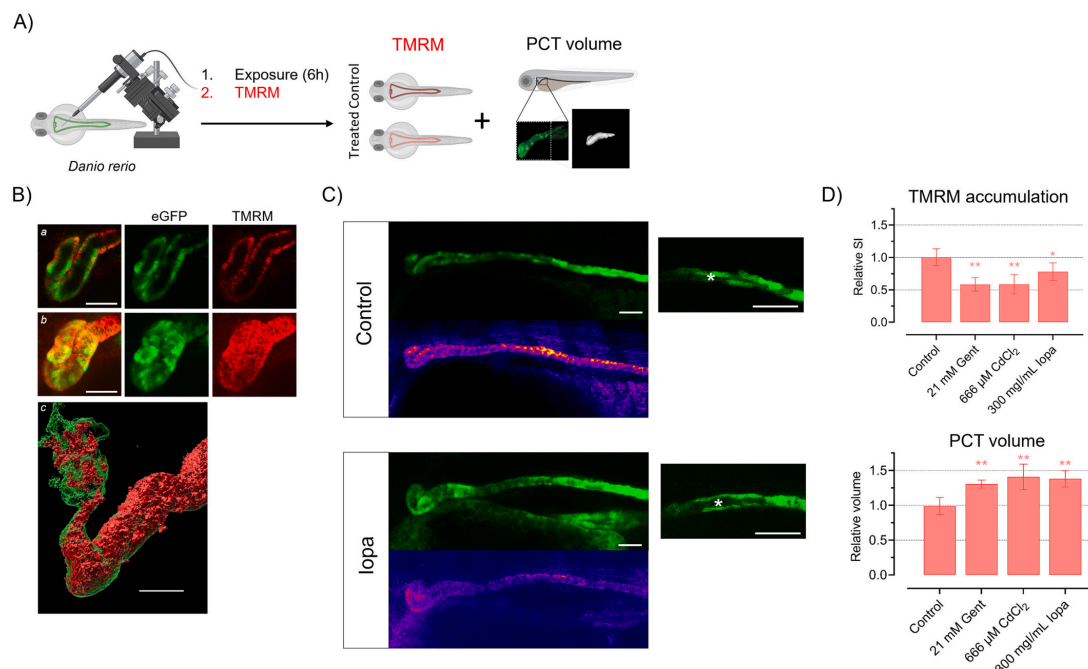


Fig. 6. Toxicity in living 72 hpf ZFL. (A) 72 hpf tg(cdh17:eGFP) ZFL were injected with 1 nL of 21 mM gentamicin, 666 μM CdCl₂, and 300 mg/ml iopamidol. Accumulation of TMRM (red) in renal epithelial cells (green) was assessed *in vivo*. The volume of PCT was quantified based on the signal intensity of the fluorescent renal epithelial cells. (B) Visualization of TMRM accumulation within renal epithelial cells of proximal tubules shown as (a) slice, (b) maximum projection, and (c) threshold-based volume rendering. Scale bar: 50 μm. (C) Representative confocal images of proximal tubules of 72 hpf control or iopamidol-treated ZFL. Renal epithelial cells are green and shown in a false colour representation of the TMRM signal intensity (blue: low signal intensity, white: strong signal intensity). Zoom-in into the lumen (*). Scale bar: 50 μm. (D) The relative signal intensity (SI) of TMRM accumulation and relative volume of the PCT as compared to the control is shown. Values represent means ± SD of 3 independent experiments with 4 to 11 fish each. The threshold for significance was set to **p* < 0.05 and ***p* < 0.001. (For interpretation of the references to colour in this figure legend, the reader is referred to the web version of this article.)

negative impact on mitochondria. Of note, an increase in ATP consumption and/or inhibition of glycolysis can also influence ATP levels. Therefore, several mitochondria-specific assays were performed to further investigate mitochondrial damage. Reduction in MMP and comparative microscopy images of HEK293T cell experiments treated with nephrotoxicants revealed aberrations in the mitochondrial network. Iopamidol-treated cells showed round-shaped mitochondria, a morphological finding suggesting an iopamidol-induced shift from fusion to fission and/or mitochondrial swelling. This shift can be interpreted as an impairment of the mitochondrial respiratory chain followed by removing damaged mitochondria (Youle and van der Bliek, 2012). This is supported by data showing an iopamidol-induced ATP depletion and loss of MMP. In the gentamicin and CdCl₂ treatment groups, morphological fission and lysosomal-mediated clearance of mitochondria (mitophagy) were also observed. Notably, the more pronounced enlargement and activation of lysosomes in gentamicin, which is known to be accumulated and trapped in lysosomes (Servais et al., 2005), and CdCl₂-treated HEK293T cells indicate lysosomal accumulation and/or damage (Zhao et al., 2021). These findings suggest that iopamidol-treated HEK293T may respond better to lysosomal and mitochondrial insults and/or iopamidol did not accumulate within lysosomes.

In the killifish model, mitochondrial damage was confirmed but at lower concentrations of toxicants compared to the HEK293T *in vitro* settings. This highlights a higher sensitivity of the *ex vivo* model to the toxicants studied, which can be explained by the presence of relevant

physiological processes, such as functional excretion and reabsorption via membrane transporters (e.g., OCT, megalin/cubilin machinery, etc.), as well as more differentiated cell types (Anzenberger et al., 2006; Bolten et al., 2022; Miller et al., 1997). Moreover, the need for a more complex model (*i.e.*, *ex vivo*) can also explain why iopamidol-induced O₂^{•-} and ROS production and gentamicin-induced reduction of MMP were detected in killifish tubules but not in HEK293T cells.

Since isolated renal tubules of killifish are more sensitive to toxic insults, confocal microscopy is sufficient to detect changes in mitochondrial energizations in entire tubules by avoiding stressful single-cell formation. For HEK293T cellular studies, we decided to use flow cytometry since it is a very sensitive and quantitative method. In addition, it allows for higher throughput than fluorescence microscopy.

In the living ZFL model, toxicity in the proximal renal tubules was indicated by TMRM accumulation in the tubular epithelial cells, which was also observed with a selection of other positively charged fluorescent dyes, such as Rhodamine 123, Rhodamine 6G, and Cy5. The following reasons provide an explanation for this organ-specific accumulation pattern. First, ZFL renal epithelial cells are functional, as shown previously (Bolten et al., 2022). They are equipped with several ATP-consuming ATP-binding cassettes (ABC) transporters, solute carriers (SLC), and folate and megalin/cubilin tubular reabsorption transporters (Anzenberger et al., 2006; Bolten et al., 2022; Luckenbach et al., 2014). Second, the kidney is an excretory organ. Consequently, high concentrations of some positively charged compounds can pass renal epithelial cells and get trapped. Third, positively charged dyes are

CHAPTER 3. RESULTS

J.S. Bolten et al.

Toxicology and Applied Pharmacology 466 (2023) 116493

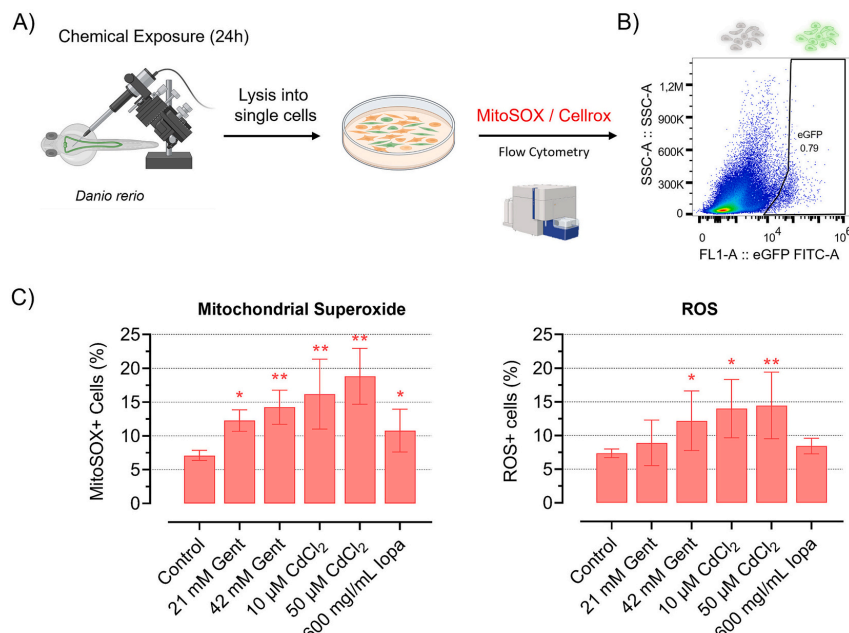


Fig. 7. Toxicity analysis in isolated renal epithelial cells of ZFL. (A) 72 hpf tg(cdh17:eGFP) ZFL were injected with 1 nL of 21 mM or 42 mM of gentamicin, 2 nL of 300 mg/ml iopamidol or incubated in 10 or 50 μM CdCl₂. After 24 h, ZFL were lysed into single cells, and fluorescent MitoSOX or CellroX Red was added. (B) Using flow cytometry and gating tools, signal intensities of MitoSOX and CellroX in GFP+ cells were analyzed. (C) Amount of MitoSOX+ and CellroX+ cells in (%). Values represent mean ± SD of at least $n = 5$ independent experiments. The threshold for significance was set to * $p < 0.05$ and ** $p < 0.001$. (For interpretation of the references to colour in this figure legend, the reader is referred to the web version of this article.)

substrates of organic cationic transporters (OCT) located in renal epithelial cells on the basolateral (blood) side. These transporters facilitate the uptake of positively charged molecules by renal epithelial cells. In both teleost models, OCT transport was verified (Sweet et al., 2000; Mihaljević et al., 2017; Yamashita et al., 2013).

Studies investigating the clearance of TMRM revealed fast and efficient cellular uptake within 10 min after injection (Supplementary Fig. 4). However, the fluorescent signal could not be detected in any other organs due to the trapping of the dye within the mitochondria of renal epithelial cells for >48 h. Incubations longer than 48 h were not performed because the use of 120 hpf ZFL is restricted by guidelines for animal permission. Interestingly, this renal epithelial cell-specific accumulation can be exploited to label pronephros of ZFL, a relevant approach for researchers who do not have access to transgenic lines that express GFP in renal epithelial cells.

Based on the presented data, we conclude that iopamidol falls into the same category as a tubular cell toxic compound, as shown for gentamicin and CdCl₂ (Campos et al., 2018; Mao et al., 2011; Markowitz and Perazella, 2005; Patel and Sapra, 2020; Servais et al., 2005). This conclusion is supported by the following lines of evidence:

First, mitochondrial damage was observed in all tested renal models. It is important to assess if mitochondria are affected and not the cellular integrity. Indeed, ATP and AK release assays in HEK293T cells (Fig. 2) provided evidence that mitochondrial damage was observed but not the cellular integrity at the indicated concentrations. In killifish models, cell integrity was verified by confocal microscopy images of renal epithelial cells (Fig. 5). In ZFL, for 6 h of treatment, no larva showed any toxic signs, such as altered heartbeat, heart edema, or changes in viability. For the 24 h treatment, only viable fish were used.

Second, gentamicin and CdCl₂ are well-known compounds affecting

proximal renal epithelial cells in ZFL and humans (Hentschel et al., 2005; Jado et al., 2020; Järup et al., 1998; Patel and Sapra, 2020). Our studies revealed similar toxicity of iopamidol, gentamicin, and CdCl₂ on mitochondria using visual inspection-assisted fluorescent assays in teleost models.

Third, the high-water solubility and low molecular weight of iopamidol would preclude renal damage induced by insoluble crystal formation within renal tissue. This was observed for antivirals, such as acyclovir (Markowitz and Perazella, 2005). Most commonly, the precipitation of crystals occurs in distal tubular lumens due to the insolubility of the chemical in acidic urine (Markowitz and Perazella, 2005).

Fourth, the dose range of iopamidol chosen for these studies is clinically relevant. The concentration used in the study is comparable with concentrations found in patients. For experiments in teleost models, we used concentrations ranging from 6.25 mg/ml to 50 mg/ml, which are in line with the concentration used in clinics given 1 to 2 mg/kg (Hardiek et al., 2001). This equals a clinical plasma concentration of 3 to 10 mg/ml. Higher doses are not uncommon leading to plasma concentrations up to 25 mg/ml. It should be noted that the concentration of iopamidol in renal epithelial cells is higher due to renal excretion. It was reported that concentrations of 120 mg/ml of a nonionic low-osmolality contrast agent were found in the urine of rabbits after 60 min given a clinically relevant dose (Spataro et al., 1982). Therefore, we decided to use a range of iopamidol concentrations that potentially include patients given higher doses and patients with normal and impaired renal function (6.25 mg/ml – 50 mg/ml). ZFL experiments were carried out by injecting 1 or 2 nL of a 300 mg/ml solution intravenously into a blood volume of approximately 70 nL. This correlates to an initial plasma concentration of 8.5 mg/ml. Concentrations of gentamicin sulfate and CdCl₂ used for *in vitro* studies are comparable

with the literature (Campos et al., 2018; Cui et al., 2021; Servais et al., 2005; Wang et al., 2022). In the *ex vivo*/*in vivo* part, the concentrations are in the range being relevant to human beings after CdCl₂ intoxication (Järup et al., 1998) and in clinical settings for gentamicin (Boyer et al., 2021; Halstenson et al., 1992).

It should be mentioned that iopamidol is a small-molecular weight, water-soluble, not metabolized drug given as a single bolus injection. Chronic exposure and inflammation can therefore be neglected. According to the manufacturer, the human half-life is 2 h but can be up to 33 h in patients with impaired kidney function, such as peritoneal dialysis patients (Hatakeyama et al., 2011).

Teleost models have several limitations. Notably, chronic and immune-mediated inflammation effects cannot be studied in both teleost models because a longer exposition would be needed, which would be considered an animal experiment. Renal tubules of killifish can be used up to 30 h after isolation. ZFL are legally and ethically only allowed to be used up to five days post fertilization (3R principles – reduce, refine, and replace animal experiments). Further, the mentioned method to lyse ZFL to perform single-cell experiments using flow cytometry is harsh. Therefore, small changes in, for instance, O₂⁻ and ROS are hardly detectable. This is due to the fact that the trypsin-induced isolation of renal epithelial cells from their natural cell-to-cell network affects cellular integrity. Also, the species-specific difference in response to toxicants, involved transport proteins, and the site of initial toxic action may differ among species. Furthermore, extracted epithelial cells of the tg(cdh17:eGFP) line include proximal and distal epithelial cells. Here, the distal tubule, which is not affected by the tested compounds, can ameliorate the toxic readout from this *ex vivo* method, such as ROS.

5. Conclusion & outlook

Due to the complex anatomy of vertebrates such as rats and mice, mechanistic studies in isolated cells are challenging. The question arises if *in vitro* findings can be extrapolated to higher vertebrates and humans. We showed that the killifish *ex vivo* model and the ZFL *in vivo* model are excellent models for studying renal tubular toxicity. Chemical-induced mitochondrial damage can be assessed in real-time visual observation using fluorescence assays. By lysing ZFL into a single-cell solution, GFP emitting renal epithelial cells of the tg(cdh17:eGFP) enable single-cell analysis using flow cytometry. These established models are closer to human beings than *in vitro* cell-based assays. Therefore, we propose using isolated renal tubules of killifish and ZFL as preclinical (*ex vivo*/*in vivo*) screening models.

It remains to be elucidated if initial toxic insults are limited to mitochondria or if other cellular functions are affected as well. Additional mechanistic insight could be obtained by analysis of oxidative phosphorylation, oxygen consumption rate analysis, or by a metabolomics screening approach. For gentamicin, there are hypotheses that key mitochondrial components, including cytochrome c and complex-I and II activity are affected (Morales et al., 2010; O'Reilly et al., 2019). For CdCl₂, complexes III and V might be affected (Wang et al., 2022). Using isolated mitochondria of renal epithelial cells of iopamidol-treated killifish renal tubules, ZFL, and patients would ultimately confirm the translational relevance of this study.

CRedit authorship contribution statement

Jan Stephan Bolten: Conceptualization, Methodology, Validation, Formal analysis, Investigation, Resources, Writing – original draft, Visualization, Project administration, Funding acquisition. **Riccardo Vincenzo Mancuso:** Conceptualization, Methodology, Validation, Formal analysis, Investigation, Resources, Writing – review & editing. **Noëmi Johanna Roos:** Conceptualization, Methodology, Validation, Formal analysis, Investigation. **Aline Mayr:** Formal analysis, Investigation, Visualization. **Ramya Deepthi Puligilla:** Investigation, Formal

analysis, Funding acquisition. **Lisa Kraus:** Formal analysis, Investigation. **Alex Odermatt:** Conceptualization, Resources, Writing – review & editing. **Gert Fricker:** Formal analysis, Investigation, Resources, Project administration, Funding acquisition, Writing – review & editing. **Jörg Huwyler:** Conceptualization, Methodology, Validation, Resources, Writing – original draft, Visualization, Project administration, Funding acquisition, Writing – review & editing.

Declaration of Competing Interest

The authors declare the following financial interests/personal relationships which may be considered as potential competing interests:

Jan Stephan Bolten reports financial support, equipment, drugs, or supplies, and travel were provided by PhD Program of Pharmaceutical Sciences of the University of Basel. Ramya Deepthi Puligilla reports financial support, equipment, drugs, or supplies, and travel were provided by PhD Program of Pharmaceutical Sciences of the University of Basel. Ramya Deepthi Puligilla reports financial support was provided by Swiss Centre for Applied Human Toxicology, SCAHT. Joerg Huwyler reports equipment, drugs, or supplies was provided by Maine INBRE grant (GM103423) from the National Institute of General Medical Sciences at the National Institutes of Health. Gert Fricker reports financial support, equipment, drugs, or supplies, and travel were provided by Salisbury Cove Research Foundation. Gert Fricker reports equipment, drugs, or supplies was provided by Maine INBRE grant (GM103423) from the National Institute of General Medical Sciences at the National Institutes of Health.

Data availability

Data will be made available on request.

Acknowledgment

We thank the PhD Program of Pharmaceutical Sciences of the University of Basel for the generous financial support of the present project. The authors thank Dr. Kai Schleicher from the Imaging Core Facility (University of Basel) for support with confocal microscopy and image analysis. Prof. Dr. Markus Affolter and Dr. Heinz Georg Belting (University of Basel) are acknowledged for providing support for zebrafish experiments. We thank Dr. Joaquin Navajas Acedo (University of Basel, Biocenter) and Dr. Janine Bögli (FACS Core Facility, University of Basel) for support with the protocol for single cell formation. Prof. Dr. Daniel Ricklin and Dr. Ekaterina Umnyakova are acknowledged for support with flow cytometry experiments. We thank Dr. Milienko Panajatovic for the helpful scientific discussions and manuscript proofreading. Killifish images were acquired using equipment of the Light Microscopy Facility at the MDIBL, which is supported by the Maine INBRE grant (GM103423) from the National Institute of General Medical Sciences at the National Institutes of Health. In addition, we thank the Salisbury Cove Research Foundation for its support of this work. The project was supported by a grant (SCAHT-GL 21-09) from the Swiss Centre for Applied Human Toxicology – SCAHT.

Appendix A. Supplementary data

Supporting information is available in a public data repository (<https://zenodo.org>. DOI: <https://doi.org/10.5281/zenodo.7387093>). Supplementary data to this article can be found online at [<https://doi.org/10.1016/j.taap.2023.116493>].

References

- Allen, D.D., Caviedes, R., Cárdenas, A.M., Shimahara, T., Segura-Aguilar, J., Caviedes, P. A., 2005. Cell lines as *in vitro* models for drug screening and toxicity studies. *Drug Dev. Ind. Pharm.* 31, 757–768. <https://doi.org/10.1080/03639040500216246>.

CHAPTER 3. RESULTS

J.S. Bolten et al.

Toxicology and Applied Pharmacology 466 (2023) 116493

- Andreucci, M., Faga, T., Pisani, A., Sabbatini, M., Russo, D., Michael, A., 2014. Prevention of contrast-induced nephropathy through a knowledge of its pathogenesis and risk factors. *Sci. World J.* 2014, 823169 <https://doi.org/10.1155/2014/823169>.
- Anzenberger, U., Bit-Avragim, N., Rohr, S., Rudolph, F., Dehmel, B., Willnow, T.E., Abdellah-Seyfried, S., 2006. Elucidation of megalin/LRP2-dependent endocytic transport processes in the larval zebrafish pronephros. *J. Cell Sci.* 119, 2127–2137. <https://doi.org/10.1242/jcs.02954>.
- Bertram, R., Gram Pedersen, M., Luciani, D.S., Sherman, A., 2006. A simplified model for mitochondrial ATP production. *J. Theor. Biol.* 243, 575–586. <https://doi.org/10.1016/j.jtbi.2006.07.019>.
- Bolten, J.S., Pratsinis, A., Alter, C.L., Fricker, G., Huwyler, J., 2022. Zebrafish (Danio rerio) larva as an in vivo vertebrate model to study renal function. *Am. J. Physiol.-Ren. Physiol.* 322, F280–F294. <https://doi.org/10.1152/ajprenal.00375.2021>.
- Bottinor, W., Polkampally, P., Jovin, I., 2013. Adverse reactions to iodinated contrast media. *Int. J. Angiol. Off. Publ. Int. Coll. Angiol. Inc* 22, 149–154. <https://doi.org/10.1055/s-0033-1348885>.
- Boyer, A., Timsit, J.-F., Klouche, K., Canet, E., Phan, T., Bohé, J., Rubin, S., Orieux, A., Lautrette, A., Gruson, D., Souweine, B., 2021. Aminoglycosides in critically ill septic patients with acute kidney injury receiving continuous renal replacement therapy: a multicenter, observational study. *Clin. Ther.* 43, 1116–1124. <https://doi.org/10.1016/j.clinthera.2021.04.011>.
- Bresciani, E., Broadbridge, E., Liu, P.P., 2018. An efficient dissociation protocol for generation of single cell suspension from zebrafish embryos and larvae. *MethodsX* 5, 1287–1290. <https://doi.org/10.1016/j.mex.2018.10.009>.
- Bush, W.H., Swanson, D.P., 1991. Acute reactions to intravascular contrast media: types, risk factors, recognition, and specific treatment. *Am. J. Roentgenol.* 157, 1153–1161. <https://doi.org/10.2214/ajr.157.6.1950858>.
- Campos, M.A.A., de Almeida, L.A., Grossi, M.F., Tagliati, C.A., 2018. In vitro evaluation of biomarkers of nephrotoxicity through gene expression using gentamicin. *J. Biochem. Mol. Toxicol.* 32, e22189. <https://doi.org/10.1002/jbt.22189>.
- Cörek, E., Rodgers, G., Siegrist, S., Einfalt, T., Detampel, P., Schlepütz, C.M., Sieber, S., Fluder, P., Schulz, G., Unterwiesing, H., Alexiou, C., Müller, B., Puchkov, M., Huwyler, J., 2020. Shedding light on metal-based nanoparticles in zebrafish by computed tomography with micrometer resolution. *Small* 16, 2000746. <https://doi.org/10.1002/smll.202000746>.
- Cui, J., Yin, S., Zhao, C., Fan, L., Hu, H., 2021. Combining Patulin with cadmium induces enhanced hepatotoxicity and nephrotoxicity in vitro and in vivo. *Toxins* 13, 221. <https://doi.org/10.3390/toxins13030221>.
- Deray, G., 2006. Dialysis and iodinated contrast media. *Kidney Int.* 69, S25–S29. <https://doi.org/10.1038/sj.ki.5000371>.
- Fricker, G., Gutmann, H., Droule, A., Drewe, J., Miller, D., 1999. Epithelial transport of antihelminthic ivermectin in a novel model of isolated proximal kidney tubules. *Pharm. Res.* 16, 1570–1575. <https://doi.org/10.1023/A:1018956621376>.
- Gomi, T., Nagamoto, M., Hasegawa, M., Katoh, A., Sugiyama, M., Murata, N., Kunihiro, T., Kohda, E., 2010. Are there any differences in acute adverse reactions among five low-osmolar non-ionic iodinated contrast media? *Eur. Radiol.* 20, 1631–1635. <https://doi.org/10.1007/s00330-009-1698-6>.
- Halstenson, C.E., Wong, M.O., Herman, C.S., Heim-Duthoy, K.L., Teal, M.A., Afrime, M. B., Kelloway, J.H., Keane, W.F., Awini, W.M., 1992. Effect of concomitant administration of piperacillin on the dispositions of isepamicin and gentamicin in patients with end-stage renal disease. *Antimicrob. Agents Chemother.* 36, 1832–1836.
- Hardiek, K., Katholi, R.E., Ramkumar, V., Deitrick, C., 2001. Proximal tubule cell response to radiographic contrast media. *Am. J. Physiol.-Ren. Physiol.* 280, F61–F70. <https://doi.org/10.1152/ajprenal.2001.280.1.F61>.
- Hatakeyama, S., Abe, A., Suzuki, T., Hashimoto, Y., Koie, T., Funyu, T., Satoh, S., Habuchi, T., Ohyama, C., Matsuo, S., 2011. Clearance and safety of the radiocontrast medium iopamidol in peritoneal Dialysis patients. *Int. J. Nephrol.* 2011, 657051. <https://doi.org/10.4061/2011/657051>.
- He, X., Yang, J., Li, L., Tan, H., Wu, Y., Ran, P., Sun, S., Chen, J., Zhou, Y., 2017. Atorvastatin protects against contrast-induced nephropathy via anti-apoptosis by the upregulation of Hsp27 in vivo and in vitro. *Mol. Med. Rep.* 15, 1963–1972. <https://doi.org/10.3892/mmr.2017.6251>.
- Hentschel, D.M., Park, K.M., Cilenti, L., Zervos, A.S., Drummond, I., Bonventre, J.V., 2005. Acute renal failure in zebrafish: a novel system to study a complex disease. *Am. J. Physiol.-Ren. Physiol.* 288, F923–F929. <https://doi.org/10.1152/ajprenal.00386.2004>.
- Jado, J.C., Humanes, B., González-Nicolás, M.Á., Camaño, S., Lara, J.M., López, B., Cercenado, E., García-Bordas, J., Tejedor, A., Lázaro, A., 2020. Nephroprotective effect of Cilastatin against gentamicin-induced renal injury in vitro and in vivo without altering its bactericidal efficiency. *Antioxidants* 9. <https://doi.org/10.3390/antiox9090821>.
- Järup, L., Berglund, M., Elinder, C.G., Nordberg, G., Vahter, M., 1998. Health effects of cadmium exposure – a review of the literature and a risk estimate. *Scand. J. Work Environ. Health* 24, 1–51.
- Jiang, W., Hu, S., Che, D., An, H., Liu, R., 2019. A mast-cell-specific receptor mediates iopamidol induced immediate IgE-independent anaphylactoid reactions. *Int. Immunopharmacol.* 75, 105800. <https://doi.org/10.1016/j.intimp.2019.105800>.
- Katayama, H., Yamaguchi, K., Kozuka, T., Takashima, T., Seez, P., Matsuura, K., 1990. Adverse reactions to ionic and nonionic contrast media. A report from the Japanese committee on the safety of contrast media. *Radiology.* <https://doi.org/10.1148/radiology.175.3.2343107>.
- Kim, S.R., Lee, J.H., Park, K.H., Park, H.J., Park, J.W., 2017. Varied incidence of immediate adverse reactions to low-osmolar non-ionic iodide radiocontrast media used in computed tomography. *Clin. Exp. Allergy* 47, 106–112. <https://doi.org/10.1111/cea.12803>.
- Kimmel, C.B., Ballard, W.W., Kimmel, S.R., Ullmann, B., Schilling, T.F., 1995. Stages of embryonic development of the zebrafish. *Dev. Dyn.* 203, 253–310. <https://doi.org/10.1002/aja.1002030302>.
- Luckenbach, T., Fischer, S., Sturm, A., 2014. Current advances on ABC drug transporters in fish. *Comp. Biochem. Physiol. Part C Toxicol. Pharmacol.* 165, 28–52. <https://doi.org/10.1016/j.cbpc.2014.05.002>.
- Mao, W., Zhang, N., Zhou, F., Li, W., Liu, H., Feng, J., Zhou, L., Wei, C., Pan, Y., He, Z., 2011. Cadmium directly induced mitochondrial dysfunction of human embryonic kidney cells. *Hum. Exp. Toxicol.* 30, 920–929. <https://doi.org/10.1177/0960327110384286>.
- Markowitz, G.S., Perazella, M.A., 2005. Drug-induced renal failure: a focus on tubulointerstitial disease. *Clin. Chim. Acta* 351, 31–47. <https://doi.org/10.1016/j.cccn.2004.09.005>.
- Mihaljević, I., Popović, M., Zaja, R., Maraković, N., Šinko, G., Smital, T., 2017. Interaction between the zebrafish (Danio rerio) organic cation transporter 1 (Oct1) and endo- and xenobiotics. *Aquat. Toxicol.* 187, 18–28. <https://doi.org/10.1016/j.aquatox.2017.03.012>.
- Miller, D.S., Fricker, G., Drewe, J., 1997. P-glycoprotein-mediated transport of a fluorescent rapamycin derivative in renal proximal tubule. *J. Pharmacol. Exp. Ther.* 282, 440–444.
- Morales, A.I., Dettaille, D., Prieto, M., Puente, A., Briones, E., Arévalo, M., Lervere, X., López-Novoa, J.M., El-Mir, M.-Y., 2010. Metformin prevents experimental gentamicin-induced nephropathy by a mitochondria-dependent pathway. *Kidney Int.* 77, 861–869. <https://doi.org/10.1038/ki.2010.11>.
- Naughton, C.A., 2008. Drug-induced nephrotoxicity. *Am. Fam. Physician* 78, 743–750.
- Niu, G., 1993. Experimental histopathological studies of renal lesions induced by high- or low-osmolality contrast media. *Nihon Ika Daigaku Zasshi* 60, 390–405. <https://doi.org/10.1272/jnms1923.60.390>.
- Oezen, G., Schentarra, E.-M., Bolten, J.S., Huwyler, J., Fricker, G., 2022. Sodium arsenite but not aluminum chloride stimulates ABC transporter activity in renal proximal tubules of killifish (*Fundulus heteroclitus*). *Aquat. Toxicol. Amst. Neth.* 252, 106314. <https://doi.org/10.1016/j.aquatox.2022.106314>.
- Oh, H.J., Oh, H., Nam, B.Y., You, J.S., Ryu, D.-R., Kang, S.-W., Chung, Y.E., 2019. The protective effect of klotho against contrast-associated acute kidney injury via the antioxidant effect. *Am. J. Physiol.-Ren. Physiol.* 317, F881–F889. <https://doi.org/10.1152/ajprenal.00297.2018>.
- O'Reilly, M., Young, L., Kirkwood, N.K., Richardson, G.P., Kros, C.J., Moore, A.L., 2019. Gentamicin affects the bioenergetics of isolated mitochondria and collapses the mitochondrial membrane potential in cochlear sensory hair cells. *Front. Cell. Neurosci.* 13.
- Paeck, F., Mingard, C., Grünig, D., Abegg, V.F., Bouitbir, J., Krähenbühl, S., 2018. Mechanisms of mitochondrial toxicity of the kinase inhibitors ponatinib, regorafenib and sorafenib in human hepatic HepG2 cells. *Toxicology* 395, 34–44. <https://doi.org/10.1016/j.tox.2018.01.005>.
- Patel, J.B., Sapra, A., 2020. Nephrotoxic medications. In: *StatPearls*. StatPearls Publishing, Treasure Island (FL).
- Roos, N.J., Aliu, D., Bouitbir, J., Krähenbühl, S., 2020. Lapatinib activates the Kelch-like ECH-associated protein 1-nuclear factor erythroid 2-related factor 2 pathway in HepG2 cells. *Front. Pharmacol.* 11, 944. <https://doi.org/10.3389/fphar.2020.00944>.
- Rudin, D., Schmutz, M., Roos, N.J., Bouitbir, J., Krähenbühl, S., 2020. Reactive Metabolite metabolites enhance the toxicity of hemin on the ATP Pool in HL60 cells by inhibition of glycolysis. *Biomedicines* 8, 212. <https://doi.org/10.3390/biomedicines8070212>.
- Samsa, L.A., Fleming, N., Magness, S., Qian, L., Liu, J., 2016. Isolation and characterization of single cells from zebrafish embryos. *J. Vis. Exp. JoVE.* <https://doi.org/10.3791/53877>.
- Servais, H., Van Der Smissen, P., Thirion, G., Van der Essen, G., Van Bambeke, F., Tulkens, P.M., Mingeot-Leclercq, M.-P., 2005. Gentamicin-induced apoptosis in LLC-PK1 cells: involvement of lysosomes and mitochondria. *Toxicol. Appl. Pharmacol.* 206, 321–333. <https://doi.org/10.1016/j.taap.2004.11.024>.
- Sieber, S., Grossen, P., Detampel, P., Siegfried, S., Witzigmann, D., Huwyler, J., 2017a. Zebrafish as an early stage screening tool to study the systemic circulation of nanoparticulate drug delivery systems in vivo. *J. Control. Release* 264, 180–191. <https://doi.org/10.1016/j.jconrel.2017.08.023>.
- Sieber, S., Siegrist, S., Schwarz, S., Porta, F., Schenk, S.H., Huwyler, J., 2017b. Immobilization of enzymes on PLGA sub-micrometer particles by crosslinked layer-by-layer deposition. *Macromol. Biosci.* 17, 1700015. <https://doi.org/10.1002/mabi.201700015>.
- Sieber, S., Grossen, P., Bussmann, J., Campbell, F., Kros, A., Witzigmann, D., Huwyler, J., 2019. Zebrafish as a preclinical in vivo screening model for nanomedicines. *Adv. Drug Deliv. Rev.* <https://doi.org/10.1016/j.addr.2019.01.001>.
- Spataro, R.F., Fischer, H.W., Boylan, L., 1982. Urography with low-osmolality contrast media: comparative urinary excretion of iopamidol, Hexabrix, and Diatrizoate. *Investig. Radiol.* 17, 494.
- Sugitara, T., Hirasawa, Y., Toyoshi, T., Matsumura, Y., 2020. Effects of Agmatine on contrast-induced nephropathy in rats and rabbits. *Biol. Pharm. Bull.* 43, 1556–1561. <https://doi.org/10.1248/bpb.b20-00405>.
- Sun, H., Yang, H., Ruan, H., Li, W., He, X., Wang, L., Liu, F., Zhang, J., 2018. The protective effect of sika deer antler protein on gentamicin-induced nephrotoxicity in vitro and in vivo. *Cell. Physiol. Biochem.* 50, 841–850. <https://doi.org/10.1159/000494471>.

3.3. PART III: MECHANISM OF TOXICITY

J.S. Bolten et al.

Toxicology and Applied Pharmacology 466 (2023) 116493

- Sweet, D.H., Miller, D.S., Pritchard, J.B., 2000. Basolateral localization of organic cation transporter 2 in intact renal proximal tubules. *Am. J. Physiol.-Ren. Physiol.* 279, F826–F834. <https://doi.org/10.1152/ajprenal.2000.279.5.F826>.
- Wang, Y., Chi, H., Xu, F., He, Z., Li, Z., Wu, F., Li, Y., Zhang, G., Peng, X., Yu, S., Yang, J., Zhang, W., Yang, X., 2022. Cadmium chloride-induced apoptosis of HK-2 cells via interfering with mitochondrial respiratory chain. *Ecotoxicol. Environ. Saf.* 236, 113494 <https://doi.org/10.1016/j.ecoenv.2022.113494>.
- Wolf, G., Arenson, R., Cross, A., 1989. A prospective trial of ionic vs nonionic contrast agents in routine clinical practice: comparison of adverse effects. *Am. J. Roentgenol.* 152, 939–944. <https://doi.org/10.2214/ajr.152.5.939>.
- Yamashita, M., Yamashita, Y., Suzuki, T., Kani, Y., Mizusawa, N., Imamura, S., Takemoto, K., Hara, T., Hossain, M.A., Yabu, T., Touhata, K., 2013. Selenoneine, a novel selenium-containing compound, mediates detoxification mechanisms against methylmercury accumulation and toxicity in zebrafish embryo. *Mar. Biotechnol. N. Y.* 15, 559–570. <https://doi.org/10.1007/s10126-013-9508-1>.
- Youle, R.J., van der Blik, A.M., 2012. Mitochondrial fission, fusion, and stress. *Science* 337, 1062–1065. <https://doi.org/10.1126/science.1219855>.
- Zaremba, A., Miller, D.S., Fricker, G., 2017. Zinc chloride rapidly stimulates efflux transporters in renal proximal tubules of killifish (*Fundulus heteroclitus*). *Toxicol. Appl. Pharmacol.* 334, 88–99. <https://doi.org/10.1016/j.taap.2017.09.001>.
- Zhao, Y., Li, Z.-F., Zhang, D., Wang, Z.-Y., Wang, L., 2021. Quercetin alleviates cadmium-induced autophagy inhibition via TFEB-dependent lysosomal restoration in primary proximal tubular cells. *Ecotoxicol. Environ. Saf.* 208, 111743 <https://doi.org/10.1016/j.ecoenv.2020.111743>.
- Zhou, X., Bouitbir, J., Liechti, M.E., Krähenbühl, S., Mancuso, R.V., 2020. Parahalogenation of amphetamine and Methcathinone increases the mitochondrial toxicity in undifferentiated and differentiated SH-SY5Y cells. *Int. J. Mol. Sci.* 21, 2841. <https://doi.org/10.3390/ijms21082841>.

3.3.2 Publication 2

Sodium arsenite but not aluminum chloride stimulates ABC transporter activity in renal proximal tubules of killifish (*Fundulus heteroclitus*)

Goezde Oezen, Eva-Maria Schentarra, **Jan Stephan Bolten**, Jörg Huwyler, Gert Fricker

Aquat Toxicol. 2022 Nov;252:106314.

doi: 10.1016/j.aquatox.2022.106314.

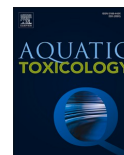
Personal contribution:

My contribution to this research article includes conducting scientific experiments using isolated proximal tubules of killifish. Furthermore, I reviewed the manuscript and created a striking image.



Contents lists available at ScienceDirect

Aquatic Toxicology

journal homepage: www.elsevier.com/locate/aqtox

Sodium arsenite but not aluminum chloride stimulates ABC transporter activity in renal proximal tubules of killifish (*Fundulus heteroclitus*)

Goezde Oezen^{a,b}, Eva-Maria Schentarra^{a,b}, Jan Stephan Bolten^{b,c}, Joerg Huwyler^{b,c}, Gert Fricker^{a,b,*}

^a Institute of Pharmacy and Molecular Biotechnology, Heidelberg University, Heidelberg 69120, Germany

^b Mount Desert Island Biological Laboratory, Salisbury Cove, ME 04672, United States

^c Department of Pharmaceutical Sciences, University of Basel, Basel 4056, Switzerland

ARTICLE INFO

Keywords:

Arsenic
Aluminum
Multidrug resistance-related protein 2 (Mrp2)
Drug efflux
Transport regulation
Renal proximal tubules

ABSTRACT

ABC export proteins including Multidrug resistance-related protein 2 (Mrp2) serve as detoxification mechanism in renal proximal tubules due to active transport of xenobiotics and metabolic waste products into primary urine. The environmental pollutants aluminum and arsenic interfere with a multitude of regulatory mechanisms in the body and here their impact on ABC transporter function was studied. NaAsO₂ but not AlCl₃ rapidly stimulated Mrp2-mediated Texas Red (TR) transport in isolated renal proximal tubules from killifish, a well-established laboratory model for the determination of efflux transporter activity by utilizing fluorescent substrates for the ABC transporters of interest and confocal microscopy followed by image analysis. This observed stimulation remained unaffected by the translation inhibitor cycloheximide (CHX), but it was abrogated by antagonists and inhibitors of the endothelin receptor type B (ET_B)/nitric oxide synthase (NOS)/protein kinase C (PKC) signaling pathway. NaAsO₂-triggered effects were abolished as a consequence of PKC α inhibition through G66976 and PKC α inhibitor peptide C2-4. Phosphatidylinositol 3-kinase (PI3K) inhibitor LY 294,002 as well as the mammalian target of rapamycin (mTOR) inhibitor rapamycin suppressed NaAsO₂-triggered stimulation of luminal TR transport. In addition, the stimulatory effect of NaAsO₂ was abolished by GSK650394, an inhibitor of serum- and glucocorticoid-inducible kinase 1 (SGK1), which is an important downstream target. Environmentally relevant concentrations of NaAsO₂ further stimulated transport function of P-glycoprotein (P-gp), Multidrug resistance-related protein 4 (Mrp4) and Breast cancer resistance protein (Bcrp) while AlCl₃ was ineffective. To our knowledge, this is the first report engaging in the impact of NaAsO₂ on efflux transporter signaling and it may contribute to the understanding of defense mechanisms versus this worrying pollutant.

1. Introduction

The euryhaline mummichog or Atlantic killifish (*Fundulus heteroclitus*) is a fish living in estuaries and salt marshes along the Atlantic coast. It is known for its tolerance versus high fluctuations of water salinity, temperature, low oxygen levels and highly polluted ecosystems. Therefore, it became an interesting research subject for physiological, ecotoxicological and developmental studies (Lau et al., 2021; Eide et al., 2021; Whitehead et al., 2017; Lister et al., 2011). Isolation of renal proximal tubules leads to broken tubule ends, which rapidly close off, forming closed compartments whereby the luminal accumulation of secreted substances can be measured (Schramm et al., 1995).

Maintaining the functional activity and the structural organization of a whole tissue, these isolated tubules represent an ideal model to study excretory transport processes. They are superior to isolated cells and cell lines, which often change or lose functional properties during culture time.

Just as in mammals, the ABC transport proteins P-glycoprotein (P-gp, ABCB1), Multidrug resistance-related proteins 2 and 4 (Mrp2, 4; ABCG2, 4) and Breast cancer resistance protein (Bcrp, ABCG2) act as ATP-driven efflux pumps at the luminal membrane in renal proximal tubules of killifish, where they contribute to body detoxification (Schramm et al., 1995; Miller et al., 1997; Masereeuw et al., 2000; Reichel et al., 2007; Mahringer et al., 2019). Our experiments showed that these ABC

* Corresponding author at: Department Pharmaceutical Technology and Biopharmacy, Institute of Pharmacy and Molecular Biotechnology, Heidelberg University, Im Neuenheimer Feld 329, Heidelberg 69120, Germany.
E-mail address: gert.fricker@uni-hd.de (G. Fricker).

<https://doi.org/10.1016/j.aquatox.2022.106314>

Received 2 July 2022; Received in revised form 12 September 2022; Accepted 23 September 2022

Available online 25 September 2022

0166-445X/© 2022 Elsevier B.V. All rights reserved.

transporters respond in a very sensitive way to metallic environmental contaminants. Whereas acute exposure of isolated killifish tubules to CdCl₂ or HgCl₂ resulted in a significant decrease of Mrp2 mediated transport (Terlouw et al., 2002; Notenboom et al., 2002), ZnCl₂ led to a significant increase of ABC transporter function causing augmented luminal accumulation of Texas Red (TR) (Zaremba et al., 2017). Interestingly, the same effect was observed in human brain capillary endothelial cells (hCMEC/D3) and functionally active brain capillaries from rodents *in vitro* and *in vivo* (Zaremba et al., 2019).

The focus of our present studies was set on the impact of environmental metallic/metalloid pollutants, namely aluminum and arsenic, on ABC transporter function. Arsenic is a life-threatening environmental toxicant, to which millions of people are exposed (Ratnaik, 2003; Ng et al., 2003; Singh et al., 2015). Its trivalent form (As^{III}) has been shown to be highly toxic (Hughes, 2002; Sharma and Sohn, 2009). The World Health Organization and the Environmental Protection Agency have classified arsenic into IARC group 1 and as group A carcinogen to humans respectively and therefore set a limit of 10 µg/L (0.01 ppm) arsenic in drinking water. However, in many countries arsenic levels in drinking water are several fold higher, e.g. in India, Bangladesh or Sri Lanka (Sharma and Sohn, 2009; Singh et al., 2015). In extreme cases concentrations between 4 and 8 ppm have been observed (Ng et al., 2003). Due to its colorless, scentless and tasteless properties as well as the restricted access to water supply many people are using arsenic-contaminated water in everyday life. Furthermore, in the New England States Maine and New Hampshire, almost 30% of wells produce water that exceeds arsenic concentrations of 10 µg/L (Ayotte et al., 2003). Trivalent arsenic reacts particularly with thiols and vicinal sulfhydryl groups causing dysregulation and inhibition of proteins (Hughes, 2002). Carcinogenicity of arsenic might be caused by oxidative stress and alteration of DNA repair or cell proliferation (Hughes, 2002).

Aluminum is the most abundant metal in the earth surface and humans have manifold contact to it, e.g. with lubricants, pharmaceuticals, detergents, cosmetics, vaccines, waterproofing clothes, anticorrosion agents, food additives, colorants and many others. However, overexposure may result in a broad variety of disabilities and several diseases have been associated with aluminum toxicosis including Alzheimer's disease, toxic myocarditis, inflammatory bowel disease, osteomalacia, cancer, diabetes, and others (Igbokwe et al., 2019). On a cellular level increased lipid peroxidation (Christen, 2000), lymphocyte dysfunction (Zhu et al., 2014), impaired glycolysis (Kaur et al., 2021), fibrillation of α -synuclein (Uversky et al., 2001), amyloidogenic effects (Xiaoling et al., 2016), inhibition of membrane ATPases (de Sautu et al., 2018) and many other effects have been observed in the context of aluminum overexposure.

Very little is known about the impact of these metallic/metalloid pollutants on ABC transporter function and their underlying signaling cascades. Our foregoing studies suggest that metals salts under investigation (CdCl₂, HgCl₂, ZnCl₂) modulate the function of Mrp2 in killifish proximal tubules through a Ca²⁺-dependent signaling pathway involving ET_B/NOS/PKC (Terlouw et al., 2002; Notenboom et al., 2002; Zaremba et al., 2017). Thereby, signaling starts with a release of endothelin-1 (ET-1) in a Ca²⁺-dependent manner, whereas ET-1 itself acts via an endothelin B receptor (ET_B) located at the basolateral membrane (Terlouw et al., 2002; Notenboom et al., 2002; Zaremba et al., 2017). ET_B then mediates an activation of PKC through stimulation of NOS (Terlouw et al., 2002; Notenboom et al., 2002; Zaremba et al., 2017). Dependent on the activated isoform of PKC Mrp2-mediated transport is reduced (CaCl₂ and HgCl₂) or stimulated (ZnCl₂) after short-term treatment of proximal tubules (Terlouw et al., 2002; Notenboom et al., 2002; Zaremba et al., 2017). In order to determine acute effects of aluminum and arsenic, respectively, on transporter function freshly isolated killifish renal tubules were incubated with these metal/metalloid ions and modulators of transporter function to monitor the excretion of fluorescent substrates into the tubular lumen.

2. Materials and methods

2.1. Chemicals

Cadmium chloride (CdCl₂), cycloheximide (CHX), dimethylsulfoxide (DMSO), GSK650394, LY 294,002 hydrochloride, rapamycin, sodium (meta)arsenite (NaAsO₂), Texas Red (sulforhodamine 101 - free acid, TR) and zinc chloride (ZnCl₂) were obtained from Sigma-Aldrich (St. Louis, MO, USA). Aldosterone, Bisindolylmaleimide I (BIM), G66976, MK-571 (sodium salt), okadaic acid, PKC α (C2-4) inhibitor peptide and phosphoramidon were purchased from Cayman Chemical (Ann Arbor, MI, USA). Nifedipine was purchased from Calbiochem (La Jolla, CA, USA). BODIPY FL verapamil and N^G-methyl-L-arginine, acetate salt (L-NMMA) were obtained from Molecular Probes (Eugene, OR, USA). Aluminum chloride hexahydrate was purchased from Caesar & Loretz GmbH (Hilden, Germany). BODIPY FL prazosin was obtained from Invitrogen (Carlsbad, CA, USA). RES-701-1 was purchased from Enzo Life Sciences (Farmingdale, NY, USA). NBD-CSA was custom-synthesized by R. Wenger (Basel, Switzerland). 8-[Fluo]-cAMP was purchased from Biolog Life Science Institute (Bremen, Germany). All other chemicals were obtained from Cayman Chemical or Sigma-Aldrich in highest available quality.

2.2. Animals

All animals were sacrificed by decapitation in accordance with regulations for the protection of laboratory animals by the Institutional Animal Care and Use Committee of the Mount Desert Island Biological Laboratory (MDIBL). Male and female killifish (*Fundulus heteroclitus*) from 3.5 to 6.0 cm were caught in Northeast Creek on Mount Desert Island, Maine, and maintained in 100% seawater at 12–15 °C at the MDIBL for one week before experiments.

2.3. Isolation of kidneys and tissue preparation

All procedures for kidney dissection and preparation of isolated, intact tubules were performed as described previously (Masereeuw et al., 2000; Prevo et al., 2011). Briefly, killifish were sacrificed and cut along the belly with sharp small scissors. Kidneys were carefully transferred with fine forceps to a dish containing marine teleost saline buffer (MTS): 140 mM NaCl, 2.5 mM KCl, 1.5 mM CaCl₂, 1.0 mM MgCl₂ and 20 mM Tris base at pH 7.8 (Forster and Taggart, 1950). Adherent connective tissue and hematopoietic tissue were detached using a dissecting microscope and forceps to expose proximal tubules. The isolated and pooled kidney tubules were transferred to tissue culture dishes with cover glass bottoms (FluoroDish®, dish Ø 35 mm, glass Ø 23 mm, WPI) containing 2.0 ml MTS. All tissue isolations were performed at room temperature (20–22 °C).

2.4. Transport experiments screening for potential modulation of ABC transporter activity

Pooled tubules from 6 to 12 fish were incubated in FluoroDish culture dishes containing 1.0 ml MTS with/without NaAsO₂ or AlCl₃ (0.5–10.0 µM) and a corresponding fluorescent substrate for 60 min to reach steady-state distribution if not stated otherwise. Metal/metalloid concentrations were chosen in accordance with our previous experiments with other metal salts (CdCl₂, HgCl₂, ZnCl₂) (Terlouw et al., 2002; Notenboom et al., 2002; Zaremba et al., 2017). All dishes were kept in dark and at a temperature from 4 to 8 °C during the incubation time. Texas Red (1.0 µM; TR) was used as probe substrate of Mrp2 transport, as it had already been used previously as suitable substrate (Masereeuw et al., 1996; Miller et al., 2002). The cyclosporin A derivative NBD-CSA (2.0 µM) as well as BODIPY FL verapamil (2.0 µM) were used as fluorescent substrates to measure P-gp transport activity (Schramm et al., 1995; Miller et al., 2014; Nobmann et al., 2001). Fluo-cAMP (2.0 µM)

was used as probe for Mrp4 (Reichel et al., 2007) and BODIPY FL prazosin (1.0 μM) served as substrate of Bcrp (Reichel et al., 2011). Used substances were directly added from stock solutions in either DMSO or MTS to the dishes. In case of DMSO the final concentration of the solvent never passed 0.5%. In preliminary studies a DMSO concentration \leq 1.0% did not show an impact on the transport function of isolated tubules. All experiments at the microscope were carried out at room temperature (20–22 °C).

2.5. Transport experiments assessing potential influence on specific signaling events

Experiments were performed as described above with the exception that tubules were pre-incubated in MTS without (control) or with indicated transport modulators for 30 min at 4–8 °C. Then 1.0–2.0 μM of the fluorescent probe substrates were added to the incubation medium for another 60 min at 4–8 °C.

2.6. Confocal microscopy

Fluorodishes containing proximal tubules were observed with a 20X (NA 0.5) dry objective of an inverted confocal laser scanning microscope Olympus Fluoview FV1000 (Tokyo, Japan). Only intact proximal tubules were chosen via transmitted light. Excitation and emission parameters for Texas Red were set at 559 nm (diode laser) and 612 nm. For the substrates NBD-CSA, BODIPY FL verapamil, Fluo-cAMP and BODIPY FL prazosin the excitation was set at 473 nm (diode laser) and the emission was observed at 520 nm. Adjustment of the photomultiplier gain was done separately for every experiment to preclude background fluorescence and auto-fluorescence of the examined tissue. Confocal images with 512×512 pixels were generated based on four scans with 2 s each. Bits per pixel were set at 12. For each treatment 8–15 images of various tubules were taken. The images were analyzed with ImageJ software version 1.53c for Windows as described previously (Maser-euw et al., 1996; Miller et al., 1996). Briefly, after background subtraction three adjacent cellular and luminal regions of all selected tubules were tagged for calculation of average pixel intensities. Only intact tubules were chosen for the analysis.

2.7. Statistical analyses

All results are given as mean fluorescence intensity \pm S.E.M. in relation to the average fluorescence measured in control tubules. Statistical analyses were done by performing one-way ANOVA and afterwards Bonferroni's multiple comparison test (GraphPad Prism 9.3.1, GraphPad Software, CA, USA). Mean values were determined as significantly different when $p < 0.05$.

3. Results

3.1. Effect of AlCl_3 and NaAsO_2 on ABC export protein transport in killifish proximal tubules

To quantify excretion, renal tubules were incubated with the fluorescent substrates of P-gp, Mrp2, Mrp4 and Bcrp in absence and in presence of increasing doses of AlCl_3 and NaAsO_2 or inhibitors of the transporters. In preliminary experiments no significant differences between tubules from male and female fish were observed (data not shown). Therefore, there is no gender distinction in the presented data.

Incubation of the tubules with 10 μM of the Mrp2 inhibitor MK-571 yielded a very similar decrease of Texas Red (TR) excretion as observed before (Zaremba et al., 2017). Foregoing studies had shown that incubation of tubules with 10–50 μM of the heavy metal salt CdCl_2 for both 30 min and 90 min resulted in a decreased accumulation of the Mrp2 substrates fluorescein-methotrexate (FL-MTX) and Texas Red in the tubular lumens and hence a reduction of Mrp2 transport activity

(Terlouw et al., 2002; Zaremba et al., 2017). Therefore, these inhibitions caused by MK-571 and CdCl_2 were repeated as a control experiment with the same results (Figs. 1A, 6C). However, proximal tubules exposed to 0.5–10 μM AlCl_3 showed no difference in excretion of TR when compared to control (Fig. 1B), whereas incubation of the tubules with 0.5–10 μM NaAsO_2 , respectively yielded a significant increase of TR excretion (Fig. 1C). In comparison to untreated tubules, NaAsO_2 significantly enhanced the luminal accumulation of TR to $243 \pm 23\%$ (mean \pm S.E.M.), $294 \pm 18\%$, $309 \pm 35\%$ and $215 \pm 23\%$ using concentrations of 0.5, 1.0, 5.0 and 10.0 μM . Since this stimulatory effect appeared to reach a saturation niveau at 1 μM NaAsO_2 , this concentration was used in following experiments. Figs. 2 and 3 show representative images of untreated proximal tubules (control) in comparison to tubules treated with either 1.0 μM AlCl_3 or 1.0 μM NaAsO_2 to illustrate the findings. For each example transmitted-light (first panel) and confocal images (second panel) are depicted followed by the overlay of both (third panel). The findings regarding NaAsO_2 are in accordance with previously performed studies in which enhanced Mrp2 transport activity was detected in isolated renal proximal tubules after maintaining killifish in water with sublethal doses of arsenic (Miller et al., 2007). When tubules were preincubated with 100 $\mu\text{g}/\text{ml}$ cycloheximide (CHX), a protein translation inhibitor, the stimulation of TR transport into the tubular lumens caused by 1.0 μM NaAsO_2 was not reduced, suggesting that the increased Mrp2 transport activity was not initiated by a de novo synthesis of the ABC transporter (Fig. 1D).

Possible influence of NaAsO_2 and AlCl_3 on P-gp-, Bcrp- and Mrp4-mediated transport in killifish proximal tubules was also investigated using BODIPY FL verapamil (Miller et al., 2014) and the cyclosporin A derivative NBD-CSA as fluorescent probe substrates for P-gp (Schramm et al., 1995), BODIPY FL prazosin as a probe substrate for Bcrp (Reichel et al., 2011) and fluo-cAMP as probe substrate of Mrp4 (Reichel et al., 2007). Like the findings on Mrp2-mediated transport, NaAsO_2 enhanced luminal accumulation of all four substrates, BODIPY FL verapamil (Fig. 4A), NBD-CSA (Fig. 4B), BODIPY FL prazosin (Fig. 4C) and fluo-cAMP (Fig. 4D) significantly with concentrations of 0.5 and 1.0 μM , whereas 1.0 μM and 10.0 μM AlCl_3 had no effect on the secretion of these substrates.

As comparable results were observed for all ABC transporters, we concentrated in the following studies on excretion of the Mrp2 substrate TR.

3.2. Involvement of NaAsO_2 in signaling cascades modulating Mrp2-mediated transport

3.2.1. Signaling via an $\text{ET}_B/\text{NOS}/\text{PKC}$ pathway

In order to determine, whether NaAsO_2 is involved in the $\text{ET}_B/\text{NOS}/\text{PKC}$ signaling cascade as discussed in the introduction, we investigated whether nifedipine (L-type Ca^{2+} channel blocker), RES-701-1 (ET_B receptor antagonist), L-NMMA (NOS inhibitor) and the PKC inhibitor bisindolylmaleimide I (BIM) are able to reduce the NaAsO_2 -induced stimulation of Mrp2-mediated transport (Fig. 5). 10 μM nifedipine had no effect on Mrp2-mediated transport of Texas Red, but reduced luminal accumulation induced by NaAsO_2 down to control levels (Fig. 5A). Thus, we conclude that the effect of NaAsO_2 depends on a rise in free intracellular Ca^{2+} levels, similar to the effect recently observed for Mrp2 stimulation by ZnCl_2 (Zaremba et al., 2017). The used MTS buffer contained 1.5 mM CaCl_2 but this ingredient by itself does not implicate a Ca^{2+} influx causing a change in Mrp2-mediated transport of TR. Experiments in total absence of Ca^{2+} were not accomplishable, because tubules collapsed and disintegrated during incubation. As described before (Zaremba et al., 2017; Terlouw et al., 2001), increasing the CaCl_2 concentration to 3 mM lowered Mrp2-mediated transport. The previous explanation was a Ca^{2+} -induced stimulation of ET-1 release with a subsequent activation of PKC resulting in a fast decrease of Mrp2 efflux activity (Terlouw et al., 2001). In the present study RES-701-1, an ET_B receptor antagonist and furthermore the NOS inhibitor L-NMMA and the

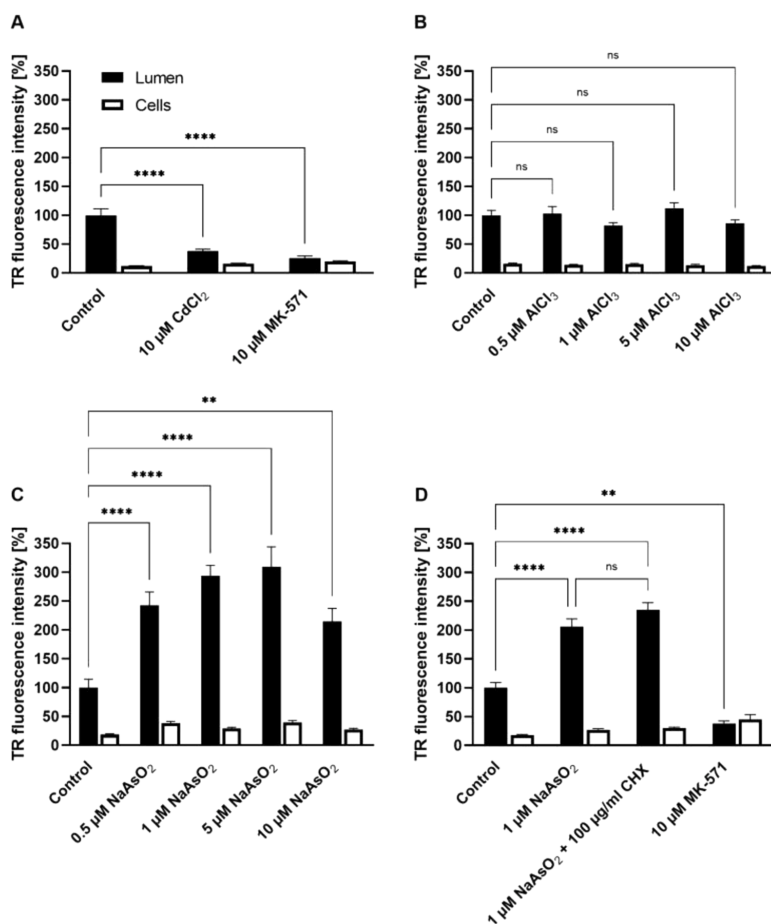


Fig. 1. Effects of CdCl₂, AlCl₃ and NaAsO₂ on the luminal TR accumulation in proximal tubules of killifish. (A) Inhibition of luminal TR transport caused by CdCl₂. Proximal tubules were pre-incubated in MTS (control) or MTS with indicated treatments for 30 min previous to another 60 min with 1.0 μM TR. (B) AlCl₃ did not show any significant influence on TR transport. Tubules were incubated in MTS (control) or MTS with indicated treatments as well as 1.0 μM TR for 60 min. (C) Dose-dependent stimulation of TR transport by NaAsO₂. The experiment was performed as described for (B). (D) The NaAsO₂-induced stimulation of TR transport could not be abolished by the translation inhibitor CHX. Proximal tubules were incubated with MTS (control) or MTS with indicated treatments for 30 min previous to another 90 min with 1.0 μM TR. Mean values ± S.E.M. for 15–19 (A), 15–24 (B), 9–30 (C), 15–26 (D) tubules. *P* values depicted by following scheme: ns ≥ 0.05, * < 0.05, ** < 0.01, *** < 0.001, **** < 0.0001.

PKC inhibitor BIM abolished NaAsO₂-triggered TR efflux stimulation in the kidney tubules (Fig. 5B, C). The ineffectiveness of these used compounds against Mrp2-mediated transport activity was shown either as a part of the presented experiments or published previously (Masereeuw et al., 2000; Notenboom et al., 2002). The stimulatory effect of NaAsO₂ was also reduced in the presence of 200 μM phosphoramidon (Fig. 5D), which inhibits ECE (endothelin-converting enzyme) that participates in ET-1 processing (Oppenorth et al., 1992). In summary, these data suggest that NaAsO₂ is acting very similar to ZnCl₂, namely by modulation of the ET_B/NOS/PKC cascade. Thus, next to ZnCl₂ (Zaremba et al., 2017, 2019) it is the second compound in the group of metals and metalloids that has a rapid stimulatory effect on Mrp2 transport function in contrast to CdCl₂, the presence of which resulted in decreased Mrp2 transport (Terlouw et al., 2001, 2002; Notenboom et al., 2002; Masereeuw et al., 2000).

3.2.2. Signaling via PKC isoform alpha

Protein kinase C (PKC) is an umbrella term for various subtypes of serine/threonine kinases including conventional PKCs (cPKC: α, β1, β2, γ), novel PKCs (nPKC: δ, ε, η, θ) and atypical PKCs (aPKC: ι, λ) (Steinberg, 2008). Bisindolylmaleimide I (BIM) is an unselective and general PKC inhibitor (Toullec et al., 1991), however, the indolocarbazole

Gö6976 has a high selectivity for PKCα and PKCβ1 (Martiny-Baron et al., 1993). To determine whether incubation of tubules with these PKC inhibitors has a similar effect on NaAsO₂-induced function of Mrp2 as on ZnCl₂-induction, we examined TR excretion in proximal tubules after NaAsO₂ treatment with or without Gö6976. The inhibitor abolished NaAsO₂-triggered stimulation of Mrp2 transport activity (Fig. 6A) as previously described for ZnCl₂ (Zaremba et al., 2017), indicating a participation of either PKCα or PKCβ1. For further examination of the involved PKC isoform in NaAsO₂-triggered stimulation of Mrp2 transport activity, we incubated the tubules with C2-4, a specific PKCα inhibitor peptide. C2-4 blocked the stimulatory effect of NaAsO₂ on Mrp2-mediated TR transport, suggesting an activation of PKCα as a result of NaAsO₂ treatment of the proximal tubules (Fig. 6B). In contrast, the CdCl₂-induced reduction of Mrp2 activity was not blocked by C2-4 while the unspecific PKC inhibitor BIM abolished it, enhancing luminal fluorescence of CdCl₂-treated tubules to control levels (Fig. 6C). The kinase activity of PKCα is dependent on phosphorylation. It can be stopped by protein phosphatase 2A (PP2A) via dephosphorylation (Nakashima, 2002). Treatment of proximal tubules with NaAsO₂ and 10 nM okadaic acid, a potent and selective inhibitor of PP2A (Fernández et al., 2002) resulted in an abolishment of the stimulatory effect of NaAsO₂ on Mrp2 efflux activity (Fig. 6D). This result is distinct from the

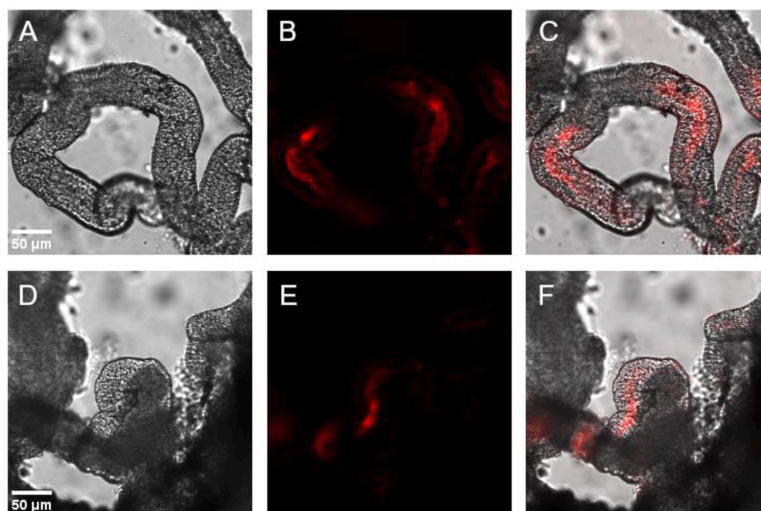


Fig. 2. Representative examples of proximal tubules from killifish presented with transmitted-light (first panel) and confocal images (second panel) as well as an overlay of both (third panel). Tubules were incubated 60 min with 1.0 μM TR in MTS, containing no further substances (control; A–C) or 1.0 μM AlCl_3 (D–F). Luminal TR accumulation in AlCl_3 -treated tubules is at control levels, indicating no alteration in Mrp2 transport activity.

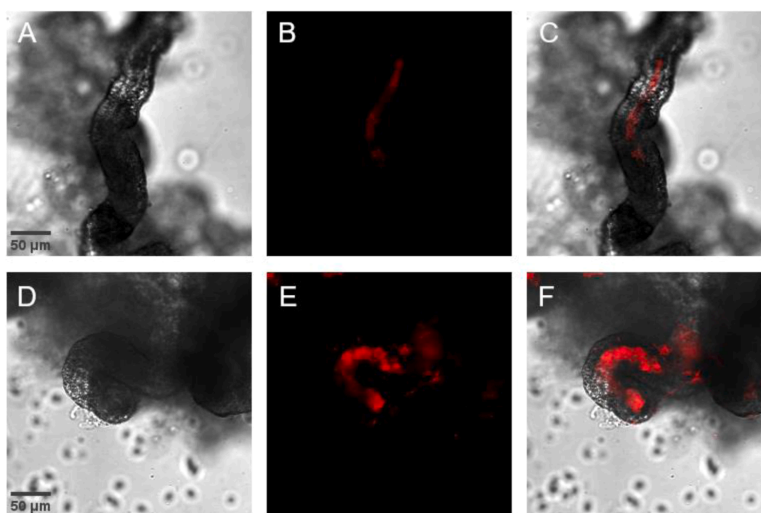


Fig. 3. Representative examples of proximal tubules from killifish presented with transmitted-light (first panel) and confocal images (second panel) as well as an overlay of both (third panel). Tubules were incubated 60 min with 1.0 μM TR in MTS, containing no further substances (control; A–C) or 1.0 μM NaAsO_2 (D–F). Treatment of tubules with NaAsO_2 resulted in enhanced luminal fluorescence, suggesting increased Mrp2 efflux activity.

recently observed ineffectiveness of okadaic acid against ZnCl_2 -induced stimulation of Mrp2 transport (Zaremba et al., 2017). Mrp2 transport function was not modified by okadaic acid itself.

3.2.3. Signaling via PI3K/mTOR and SGK1 activation

Compared to previous studies (Zaremba et al., 2017, 2019) we found a striking similarity between the effects of ZnCl_2 and NaAsO_2 upon the activity of Mrp2 in killifish proximal tubules. Zinc has been described to be involved in phosphatidylinositol 3-kinase (PI3K)/mammalian target

of rapamycin (mTOR) pathway (Ryu et al., 2008; Nimmanon et al., 2017). Therefore, we examined, whether NaAsO_2 also has an impact on this pathway. PI3K inhibitor LY 294,002 (Kong and Yamori, 2008) significantly reduced the stimulating effect of NaAsO_2 on Mrp2-mediated TR transport but did not modify Mrp2 efflux function by itself (Fig. 7A). Further on, the stimulation caused by NaAsO_2 was also inhibited by rapamycin, a potent inhibitor of mTOR, while rapamycin itself did not show an impact on Mrp2 activity (Fig. 7B).

Downstream PI3K/mTOR, several additional signaling cascades are

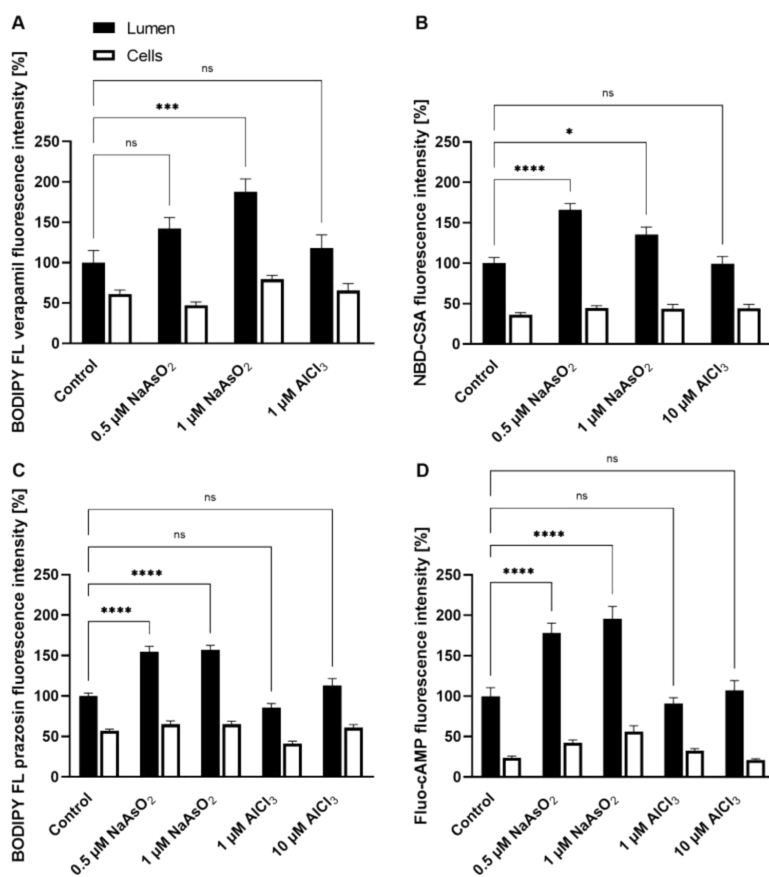


Fig. 4. Effects of NaAsO₂ and AlCl₃ on the luminal accumulation of BODIPY FL verapamil (A), NBD-CSA (B), BODIPY FL prazosin (C) and fluo-cAMP (D) in proximal tubules of killifish. Tubules were incubated in MTS (control) or MTS with indicated treatments as well as a fluorescent substrate, namely 2.0 μM BODIPY FL verapamil (A), 2.0 μM NBD-CSA (B), 1.0 μM BODIPY FL prazosin (C) or 2.0 μM fluo-cAMP (D) for 60 min. Mean values ± S.E.M. for 6–9 (A), 6–9 (B), 10–16 (C), 8–15 (D) tubules. P values depicted by following scheme: ns ≥ 0.05, * < 0.05, ** < 0.01, *** < 0.001, **** < 0.0001.

active including serum- and glucocorticoid-inducible kinase 1 (SGK1), which is a serine/threonine kinase (Lang et al., 2014; Kobayashi and Cohen, 1999). SGK1 is responsible for the regulation of a great number of carriers and ion channels (Lang et al., 2014; Kobayashi and Cohen, 1999). Treatment of proximal tubules with NaAsO₂ and GSK650394, a potent SGK1 inhibitor, led to an abolishment of NaAsO₂-induced Mrp2 transport stimulation (Fig. 7C), similar to what we had observed before for ZnCl₂ (Zaremba et al., 2017). Therefore, these data suggest that NaAsO₂ and ZnCl₂ mediate SGK1 activation and they are accordant with ZnCl₂ and NaAsO₂ on one side as both substances show a stimulation of Mrp2 transport activity. CdCl₂ on the other side initiates a signaling pathway that modifies Mrp2 transport activity in the opposite way and it was shown previously that its signaling events do not include a participation of SGK1 (Zaremba et al., 2017). Moreover, SGK1 is also induced by the mineralocorticoid aldosterone in the kidney (Shigaev et al., 2000; McCormick et al., 2005). Treatment of proximal tubules with 100 nM aldosterone leads to a rapid rise of luminal TR accumulation compared to control (Fig. 7D). This observed effect is reversed by GSK650394, suggesting that the aldosterone-induced enhancement of Mrp2 efflux activity is due to SGK1 activation. These data give countenance to the thesis that Mrp2 transport activity is mediated by SGK1 and that NaAsO₂-induced signaling includes SGK1 activation. An overview of the proposed signaling pathway causing NaAsO₂-induced Mrp2 transport stimulation is depicted in Fig. 8.

4. Discussion

The function and signaling pathways of export proteins can be examined with proximal tubules from the euryhaline teleost killifish as they turned out to be an excellent model system for a comparative method of approach (Notenboom et al., 2002, 2005; Terlouw et al., 2001; Masereeuw et al., 1996; Miller, 1987; Schramm et al., 1995; Mahringer et al., 2019; Zaremba et al., 2017). Here, we particularly studied the effect of AlCl₃ and NaAsO₂ on the transport activity of the ABC transporter Mrp2 and its regulation and compared it to the previously observed effects of ZnCl₂. Whereas AlCl₃ had no effect at all on the function of the studied ABC transporters, NaAsO₂ – similar to ZnCl₂ – rapidly stimulated Mrp2 transport function. The same effect was observed for the other ABC transporters in killifish proximal tubules, P-gp, Mrp4 and Bcrp, suggesting a general effect rather than an effect being specific to Mrp2. Furthermore, the ABC transporter stimulation was induced by environmentally relevant concentrations of NaAsO₂ (Neff, 1997; Ng et al., 2003). As described by these reviews, concentrations between 4 and 8 ppm have been registered in highly polluted areas. Our results agree with studies conducted with arsenic-treated rat liver epithelial cells which revealed an up-regulation of Mrp1, Mrp2, P-gp and the phase II drug metabolizing enzyme glutathione S-transferase II as a defense mechanism to reduce intracellular arsenic levels (Liu et al., 2001).

CHAPTER 3. RESULTS

G. Oezen et al.

Aquatic Toxicology 252 (2022) 106314

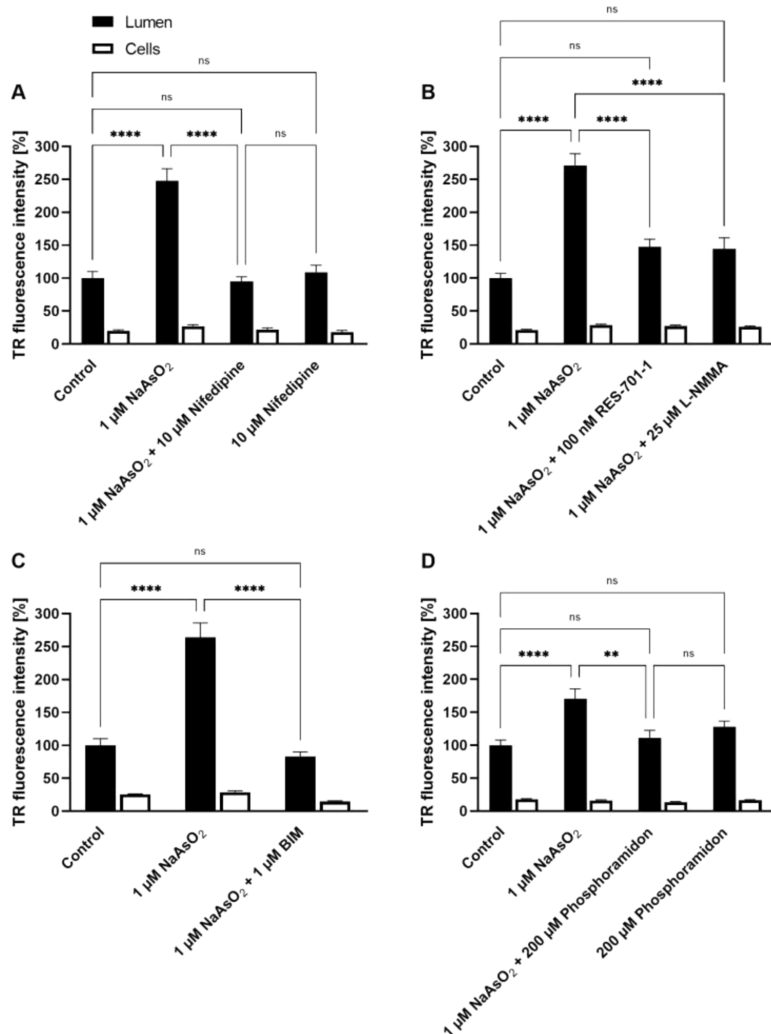


Fig. 5. The stimulating effect of NaAsO₂ on luminal TR efflux in proximal tubules of killifish involves the ET_B/NOS/PKC pathway. Tubules were pre-incubated in MTS (control) or MTS with indicated treatments for 30 min previous to another 60 min with 1.0 μM TR. (A) The Ca²⁺-channel blocker nifedipine abolished the stimulation of luminal TR transport caused by NaAsO₂. (B) RES-701-1, an ET_B receptor antagonist, and L-NMMA, a NOS inhibitor, blocked the effect of NaAsO₂ on luminal TR efflux. (C) The NaAsO₂-induced stimulation of TR transport is also abolished by PKC inhibitor BIM. (D) The endothelin-converting enzyme inhibitor phosphoramidon blocked the enhanced luminal TR accumulation caused by NaAsO₂. Mean values \pm S.E.M. for 14–18 (A), 15–25 (B), 15–23 (C), 17–29 (D) tubules. *P* values depicted by following scheme: ns \geq 0.05, * < 0.05, ** < 0.01, *** < 0.001, **** < 0.0001.

Mrp2 stimulation caused by NaAsO₂ was not reduced when translation was blocked with cycloheximide, indicating that the observed effect is not caused by a de novo synthesis of the transporter. Our data show that the signaling event induced by NaAsO₂ is similar to the one by ZnCl₂. First of all, the effect is Ca²⁺-dependent and appears to trigger a signaling cascade via the ET_B/NOS/PKC pathway. Nifedipine, a Ca²⁺-channel blocker, as well as the ET_B antagonist RES-701-1, the NOS inhibitor L-NMMA and furthermore the PKC inhibitor BIM were able to reduce the stimulatory effect of NaAsO₂. These effects of both NaAsO₂ and ZnCl₂ appear to be mediated by the same signaling cascade which results in reduced Mrp2 transport function in presence of CdCl₂ or HgCl₂ (Terlouw et al., 2002). The reason for these contrary findings may be due to different PKC isoforms that are selectively activated and in turn induce varying signaling events causing contrastive modulation of Mrp2 transport activity. In another teleost, the zebrafish *Danio rerio*, several diverse isoforms of PKC have been described (Patten et al., 2007). Both ZnCl₂-induced signaling and NaAsO₂-induced signaling involve PKC α

activation since cPKC inhibitor Gö6976, which is selective for PKC α and PKC β 1, as well as the specific PKC α inhibitor peptide C2-4 abolished the stimulatory effect of the two substances on Mrp2 transport activity. CdCl₂, on the contrary, involves another PKC isoform since BIM was able to abolish CdCl₂-induced decrease in Mrp2-mediated TR transport while C2-4 was not. In addition, previous studies showed that Gö6976 cannot block the inhibitory effect of CdCl₂ either (Zaremba et al., 2017). These results are supported by another study with rat brain capillaries, in which 12-deoxyphorbol-13-phenylacetate-20-acetate (dPPA), that is an activator of PKC β 1 and PKC β 2, had no influence on the transport activity of Mrp2 (Rigor et al., 2010), indicating that neither PKC β 1 nor PKC β 2 participate in the rapid modulation of Mrp2 function. It is not yet clear how distinct PKC isoforms are activated as a consequence of treatment with NaAsO₂ or ZnCl₂ on one side or with CdCl₂ on the other side as all three substances seem to have a similar signaling pathway involving ET_B and NOS. One possibility may be the protein phosphatase 2A (PP2A) which is able to block the activity of PKC α by dephosphorylation

3.3. PART III: MECHANISM OF TOXICITY

G. Oezen et al.

Aquatic Toxicology 252 (2022) 106314

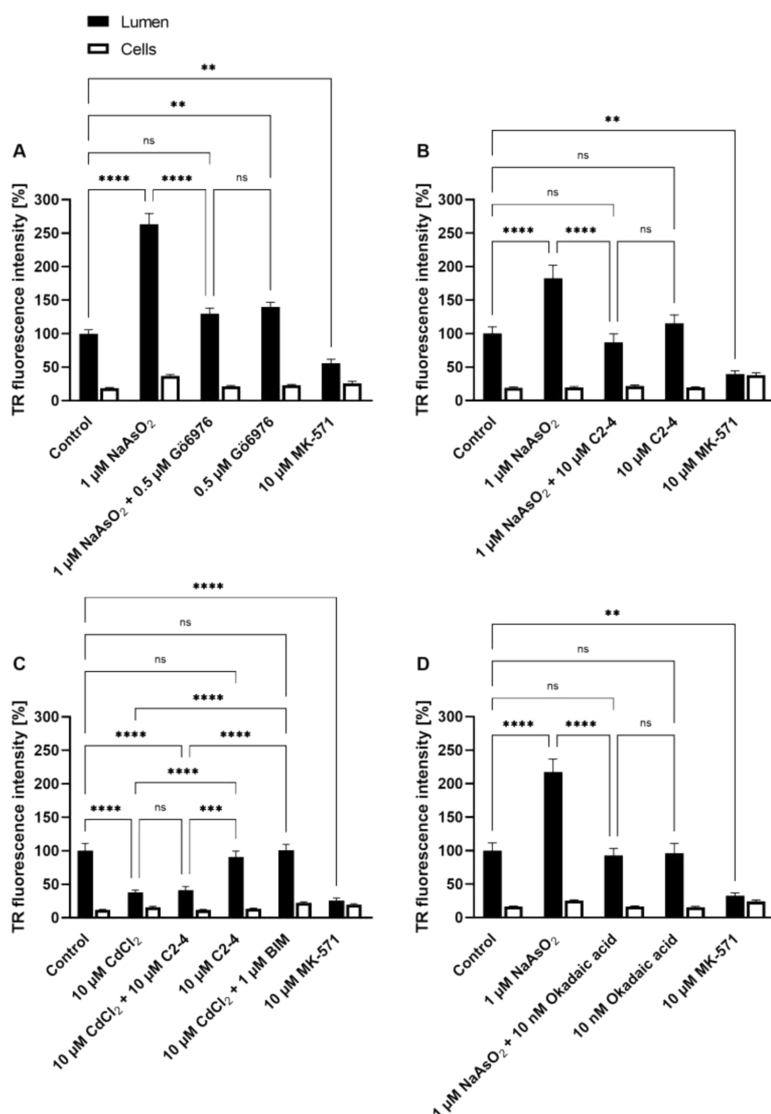


Fig. 6. NaAsO₂ and CdCl₂ involve different PKC subtypes in their signaling events inducing an alteration of Mrp2 transport activity. Killifish proximal tubules were pre-incubated in MTS (control) or MTS with indicated treatments for 30 min previous to another 60 min with 1.0 μM TR. (A) NaAsO₂-induced stimulation of luminal TR accumulation is blocked by G66976. (B) C2-4, a specific inhibitor of PKCα, abolished the induction of TR efflux caused by NaAsO₂. (C) CdCl₂-induced inhibition of TR transport is blocked by PKC inhibitor BIM while C2-4 did not show an influence. (D) The protein phosphatase 2A inhibitor okadaic acid abolished NaAsO₂-induced stimulation of luminal TR transport. Mean values ± S.E.M. for 19–32 (A), 16–23 (B), 15–19 (C), 14–29 (D) tubules. *P* values depicted by following scheme: ns ≥ 0.05, * < 0.05, ** < 0.01, *** < 0.001, **** < 0.0001.

(Parekh et al., 2000; Hansra et al., 1996) and thus modulate its kinase activity. There is evidence that Zn²⁺ binds to PP2A leading to a direct inhibition of the phosphatase, similar to okadaic acid, which is a potent PP2A inhibitor (Xiong et al., 2013). Given that CdCl₂-triggered decrease of Mrp2 transport activity was blocked by okadaic acid while ZnCl₂-induced enhancement of Mrp2 function remained unaffected, we reasoned that PP2A is involved in the selective activation of a specific PKC isoform (Zaremba et al., 2017). However, since the NaAsO₂-induced stimulation of Mrp2 was suppressed by okadaic acid, this step in the signaling cascade needs to be further investigated.

In accordance with the observed impact of ZnCl₂ on Mrp2 activity, the NaAsO₂-induced stimulation appears to include a participation of PI3K/mTOR and a subsequent activation of SGK1. Arsenic appears to interact with the PI3K/mTOR pathway as shown for the murine

hepatocyte cell line AML-12 (Yuan et al., 2021) and the malignant lymphocyte cell line NALM-6 (Toosi et al., 2018). Our findings indicate the involvement of PI3K in the examined stimulation of Mrp2 transport activity caused by NaAsO₂ since LY 294,002, a PI3K inhibitor, abolished the stimulatory effect. There is evidence that mTOR can trigger distinct signaling pathways depending on the formation of either mTORC1 or mTORC2, two different multiprotein complexes (Laplante and Sabatini, 2009). It is described in literature that mTORC2 is less sensitive to rapamycin than mTORC1 and that a prolonged treatment with the drug is required to achieve mTORC2 inhibition (Sarbassov et al., 2006). mTOR inhibitor rapamycin was able to block the NaAsO₂-induced stimulation of Mrp2 transport activity in our studies with fairly short incubation times, suggesting the participation of mTORC1. It is currently unknown, whether PI3K/mTOR is in direct connection to

CHAPTER 3. RESULTS

G. Oezen et al.

Aquatic Toxicology 252 (2022) 106314

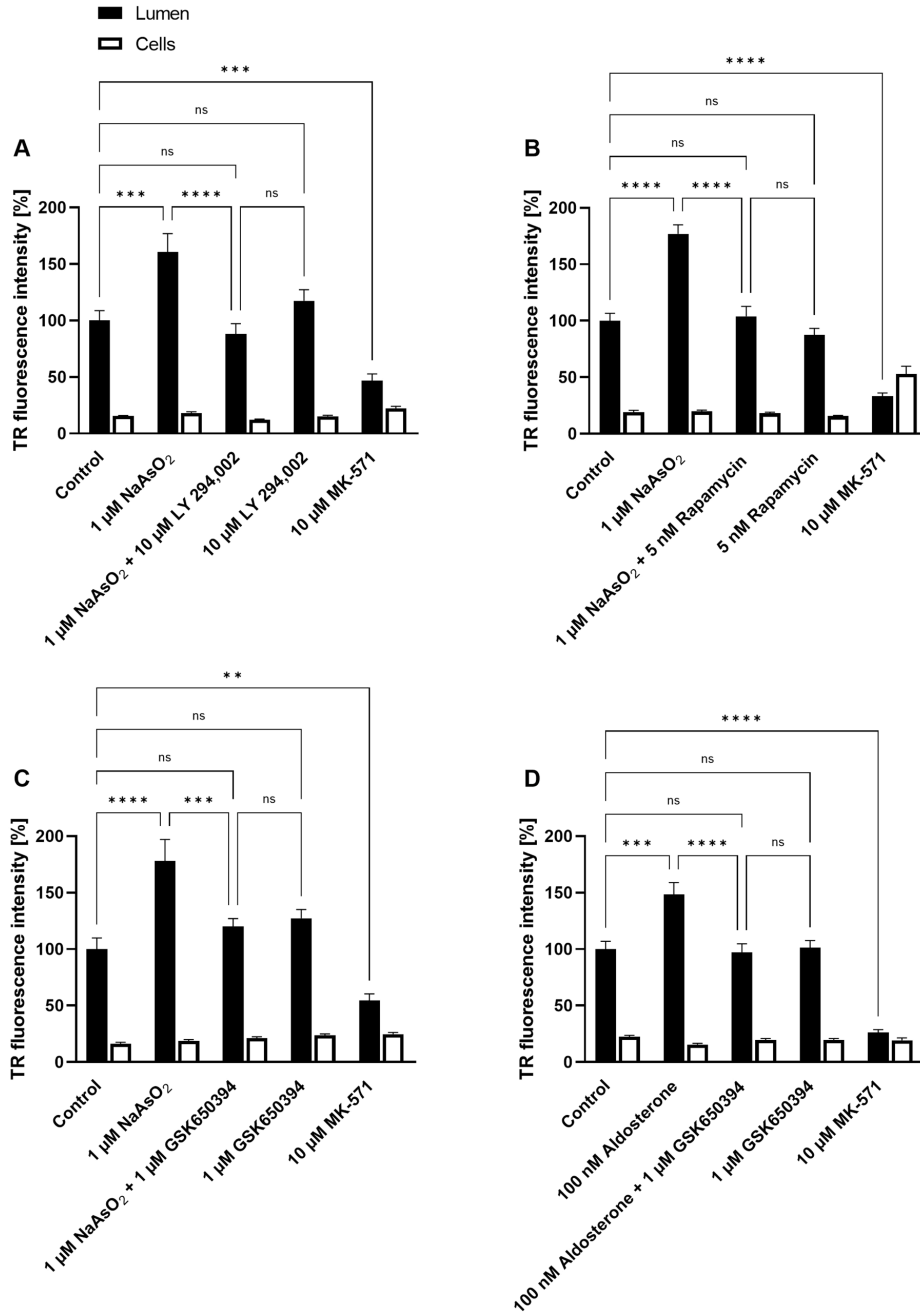


Fig. 7. Involvement of PI3K/mTOR pathway and SGK1 activation in proximal tubules of killifish as a result of NaAsO₂ treatment. Tubules were pre-incubated in MTS (control) or MTS with indicated treatments for 30 min previous to another 60 min with 1.0 μM TR. (A) The PI3K inhibitor LY 294,002 abolished the stimulatory effect of NaAsO₂ on luminal TR efflux. (B) NaAsO₂-induced stimulation of TR efflux is blocked by rapamycin, a well-known inhibitor of mTOR. (C) The SGK1 inhibitor GSK650394 abolished the induction of luminal TR transport caused by NaAsO₂. (D) The aldosterone-induced stimulation of luminal TR efflux is abolished by GSK650394. Mean values \pm S.E.M. for 16–35 (A), 15–28 (B), 15–33 (C), 12–24 (D) tubules. *P* values depicted by following scheme: ns \geq 0.05, * < 0.05, ** < 0.01, *** < 0.001, **** < 0.0001.

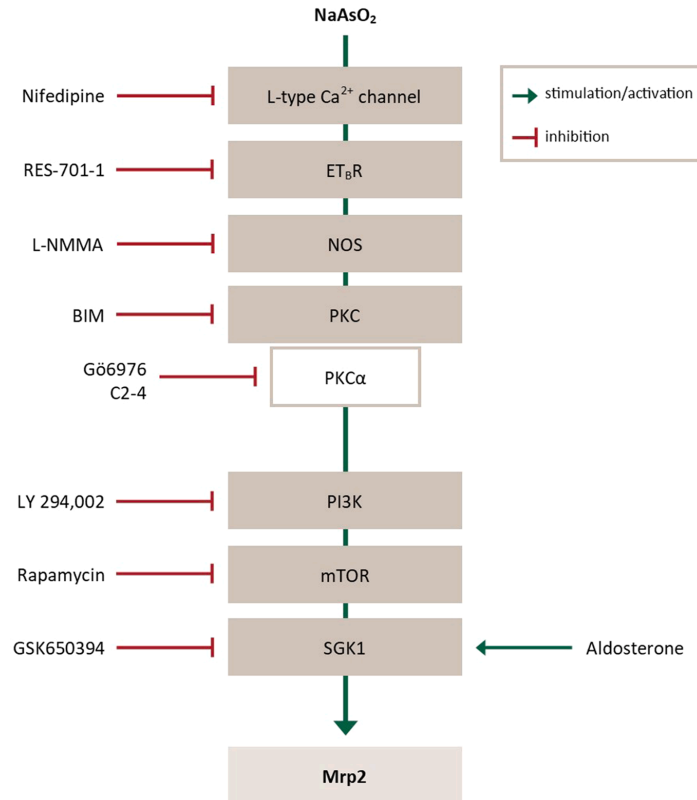


Fig. 8. Overview screen of the proposed signaling pathway resulting in enhanced Mrp2 transport activity in killifish proximal tubules due to treatment with NaAsO₂. The presented results suggest involvement of the ET_B/NOS/PKC cascade with participation of PKC α . In addition, the data indicate that NaAsO₂ interacts with PI3K/mTOR pathway and induces SGK1 activation. Currently, it is not known if there is a connection between PKC α and the PI3K/mTOR pathway.

PKC α activation within the investigated signaling pathway. Similar to our study with ZnCl₂ (Zaremba et al., 2017) a link between PKC α and PI3K/mTOR regarding the NaAsO₂-triggered stimulation of Mrp2 transport activity seems suppressable, but this needs to be clarified by further experiments.

The serine/threonine kinase SGK1 is induced by a broad spectrum of extracellular stimuli (Loffing et al., 2006) and being a stimulator of many ion channels and carriers itself, it is involved in regulating epithelial transport (Lang and Stourmaras, 2013; Lang et al., 2014). Here, we show that GSK650394, a SGK1 inhibitor, suppressed Mrp2 transport stimulation by NaAsO₂, suggesting that SGK1 activity is a crucial part in the investigated NaAsO₂-induced signaling pathway. It has been shown previously that the activity of SGK1 is regulated by PI3K activation (Park et al., 1999). Several considerations support the hypothesis that SGK1 might be indispensable in the NaAsO₂-induced signaling events causing Mrp2 stimulation. First of all, rapid SGK1 activation in the kidney can be induced via aldosterone (McCormick et al., 2005). In our studies, the mineralocorticoid also stimulated Mrp2-mediated transport and this observed effect was inhibited by the SGK1 inhibitor GSK650394. In addition, induction of SGK1 is accomplished by a lot of external stimuli including xenobiotics and SGK1 in turn can induce many other proteins as mentioned before. This also includes the activation of other kinases leading to the regulation of further targets (Gehring et al., 2009). Following investigations will concentrate on the mechanism that enables SGK1 to mediate

NaAsO₂-triggered stimulation of Mrp2 transport activity in killifish proximal tubules.

5. Conclusion

All in all, our data indicate that AlCl₃ has no impact on acute ABC transporter function in killifish proximal tubules. In contrast, NaAsO₂ exhibits a rapid stimulatory effect on the efflux activity of ABC transporters, namely Mrp2, Mrp4, P-gp and Bcrp in killifish proximal tubules. The enhancement of Mrp2 transport function shows a striking similarity to the recently observed ZnCl₂-triggered signaling events. With arsenic being a worrying environmental toxin, these findings might be interesting with respect to understand the body's defense mechanisms in response to this pollutant.

CRedit authorship contribution statement

Goezde Oezen: Investigation, Validation, Writing – original draft. **Eva-Maria Schentarra:** Investigation, Validation, Writing – original draft. **Jan Stephan Bolten:** Investigation, Validation, Writing – original draft. **Joerg Huwyler:** Investigation, Validation, Writing – original draft, Conceptualization. **Gert Fricker:** Conceptualization, Investigation, Validation, Writing – original draft, Project administration, Funding acquisition.

CHAPTER 3. RESULTS

G. Oezen et al.

Aquatic Toxicology 252 (2022) 106314

Declaration of Competing Interest

On behalf of all co-authors I declare that we have no conflict of interest.

Data availability

Data will be made available on request.

Acknowledgments

Research reported in this publication was supported by the Salsbury Cove Research Fund, the Ulrich Dahlgren Fund, and the National Institute of General Medical Sciences of the National Institutes of Health under award numbers P20GM103423 and P20GM104318. The content is solely the responsibility of the authors and does not necessarily represent the official views of the National Institutes of Health. Image collection, processing and analysis for this manuscript was performed with the assistance of Dr. Frederic Bonnet and the MDI Biological Laboratory Light Microscopy Facility, which is supported by the Maine INBRE grant (GM103423) from the NIGMS at the NIH.

References

- Ayotte, J.D., Montgomery, D.L., Flanagan, S.M., Robinson, K.W., 2003. Arsenic in groundwater in eastern New England: occurrence, controls, and human health implications. *Environ. Sci. Technol.* 37 (10), 2075–2083.
- Christen, Y., 2000. Oxidative stress and Alzheimer disease. *Am. J. Clin. Nutr.* 71 (2), 621S–629S.
- de Sautu, M., Saffioti, N.A., Ferreira-Gomes, M.S., Rossi, R.C., Rossi, J.P.F.C., Mangialavori, I.C., 2018. Aluminum inhibits the plasma membrane and sarcoplasmic reticulum Ca^{2+} -ATPases by different mechanisms. *Biochim. Biophys. Acta Biomembr.* 1860 (8), 1580–1588.
- Eide, M., Zhang, X., Karlsen, O.A., Goldstone, J.V., Stegeman, J., Jonassen, I., Goksøyr, A., 2021. The chemical defenses of five model teleost fish. *Sci. Rep.* 11 (1), 10546.
- Fernández, J.J., Cadenas, M.L., Souto, M.L., Trujillo, M.M., Norte, M., 2002. Okadaic acid: useful tool for studying cellular processes. *Curr. Med. Chem.* 9, 229–262.
- Forster, R., Taggart, J., 1950. Use of isolated renal tubules for the examination of metabolic processes associated with active cellular transport. *J. Cell. Physiol.* 36, 251–270.
- Gehring, E.M., Lam, R.S., Siraskar, G., Koutsouki, E., Seebom, G., Ureche, O.N., Ureche, L., Baltaev, R., Tavare, J.M., Lang, F., 2009. PIKfyve upregulates CFTR activity. *Biochem. Biophys. Res. Commun.* 390, 952–957.
- Hansra, G., Bormancin, F., Whelan, R., Hemmings, B.A., Parker, P.J., 1996. 12-O-Tetradecanoylphorbol-13-acetate-induced dephosphorylation of protein kinase C α correlates with the presence of a membrane associated protein phosphatase 2A heterotrimer. *J. Biol. Chem.* 271, 32785–32788.
- Hughes, M.F., 2002. Arsenic toxicity and potential mechanisms of action. *Toxicol. Lett.* 133 (1), 1–16.
- Igbokwe, I.O., Igwenu, E., Igbokwe, N.A., 2019. Aluminium toxicosis: a review of toxic actions and effects. *Interdiscip. Toxicol.* 12 (2), 45–70.
- Kaur, I., Behl, T., Aleya, L., Rahman, M.H., Kumar, A., Arora, S., Akter, R., 2021. Role of metallic pollutants in neurodegeneration: effects of aluminum, lead, mercury, and arsenic in mediating brain impairment events and autism spectrum disorder. *Environ. Sci. Pollut. Res. Int.* 28 (8), 8989–9001.
- Kong, D., Yamori, T., 2008. Phosphatidylinositol 3-kinase inhibitors: promising drug candidates for cancer therapy. *Cancer Sci.* 99 (9), 1734–1740.
- Kobayashi, T., Cohen, P., 1999. Activation of serum- and glucocorticoid-regulated protein kinase by agonists that activate phosphatidylinositol 3-kinase is mediated by 3-phosphoinositide-dependent protein kinase-1 (PDK1) and PDK2. *Biochem. J.* 339, 319–328.
- Lang, F., Stoumgaras, C., Alesutan, I., 2014. Regulation of transport across cell membranes by the serum- and glucocorticoid-inducible kinase SGK1. *Mol. Membr. Biol.* 31, 29–36.
- Lang, F., Stoumgaras, C., 2013. Serum and glucocorticoid inducible kinase, metabolic syndrome, inflammation, and tumor growth. *Hormones* 12, 160–171. *Hormones*.
- Laplante, M., Sabatini, D.M., 2009. mTOR signaling at a glance. *J. Cell Sci.* 122, 3589–3594.
- Lau, S.C., Mehdi, H., Bragg, L.M., Servos, M.R., Balshine, S., Scott, G.R., 2021. Exposure to waste-water effluent disrupts hypoxia responses in killifish (*Fundulus heteroclitus*). *Environ. Pollut.* 284, 117373.
- Liu, J., Chen, H., Miller, D.S., Saavedra, J.E., Keefer, L.K., Johnson, D.R., Klaassen, C.D., Waalkes, M.P., 2001. Overexpression of glutathione S-Transferase II and multidrug resistance transport proteins is associated with acquired tolerance to inorganic arsenic. *Mol. Pharmacol.* 60 (2), 302–309.
- Lister, A.L., Van Der Kraak, G.J., Rutherford, R., MacLatchy, D., 2011. *Fundulus heteroclitus*: ovarian reproductive physiology and the impact of environmental contaminants. *Comp. Biochem. Physiol. C Toxicol. Pharmacol.* 154 (4), 278–287.
- Loffing, J., Flores, S.Y., Staub, O., 2006. Sgk kinases and their role in epithelial transport. *Annu. Rev. Physiol.* 68, 461–490.
- Mahringer, A., Bernd, A., Miller, D.S., Fricker, G., 2019. Aryl hydrocarbon receptor ligands increase ABC transporter activity and protein expression in killifish (*Fundulus heteroclitus*) renal proximal tubules. *Biol. Chem.* 400 (10), 1335–1345.
- Martiny-Baron, G., Kazanietz, M.G., Mischak, H., Blumberg, P.M., Kochs, G., Hug, H., Marmé, D., Schächtele, C., 1993. Selective inhibition of protein kinase C isozymes by the indolocarbazole Gö 6976. *J. Biol. Chem.* 268, 9194–9197.
- Masereeuw, R., Russel, F.G., Miller, D.S., 1996. Multiple pathways of organic anion secretion in renal proximal tubule revealed by confocal microscopy. *Am. J. Physiol.* 271, F1173–F1182.
- Masereeuw, R., Terlouw, S.A., van Aubel, R.A., Russel, F.G., Miller, D.S., 2000. Endothelin B receptor-mediated regulation of ATP-driven drug secretion in renal proximal tubule. *Mol. Pharmacol.* 57 (1), 59–67.
- McCormick, J.A., Bhalla, V., Pao, A.C., Pearce, D., 2005. SGK1: a rapid aldosterone-induced regulator of renal sodium reabsorption. *Physiology* 20, 134–139.
- Miller, D.S., 1987. Aquatic models for the study of renal transport function and pollutant toxicity. *Environ. Health Perspect.* 71, 59–68.
- Miller, D.S., Letcher, S., Barnes, D.M., 1996. Fluorescence imaging study of inorganic anion transport from renal proximal tubule cell to lumen. *Am. J. Physiol.* 271, F508–F520.
- Miller, D.S., Fricker, G., Drewe, J., 1997. p-Glycoprotein-mediated transport of a fluorescent rapamycin derivative in renal proximal tubule. *J. Pharmacol. Exp. Ther.* 282 (1), 440–444.
- Miller, D.S., Masereeuw, R., Karnaky, K.J., 2002. Regulation of MRP2-mediated transport in shark rectal salt gland tubules. *Am. J. Physiol. Regul. Integr. Comp. Physiol.* 282, 774–781.
- Miller, D.S., Shaw, J.R., Stanton, C.R., Barnaby, R., Karlson, K.H., Hamilton, J.W., Stanton, B.A., 2007. MRP2 and acquired tolerance to inorganic arsenic in the kidney of killifish (*Fundulus heteroclitus*). *Toxicol. Sci.* 97 (1), 103–110.
- Miller, D.S., 2014. Sphingolipid signaling reduces basal P-glycoprotein activity in renal proximal tubule. *J. Pharmacol. Exp. Ther.* 348, 459–464.
- Nakashima, S., 2002. Protein kinase C α (PKC α): regulation and biological function. *J. Biochem.* 132, 669–675.
- Neff, J.M., 1997. Ecotoxicology of arsenic in the marine environment—review. *Environ. Toxicol. Chem.* 16, 917–927.
- Ng, J.C., Wang, J., Shraim, A., 2003. A global health problem caused by arsenic from natural sources. *Chemosphere* 52 (9), 1353–1359.
- Nimmanon, T., Ziliotto, S., Morris, S., Flanagan, L., Taylor, K.M., 2017. Phosphorylation of zinc channel ZIP7 drives MAPK, PI3K and mTOR growth and proliferation signalling. *Metallomics* 9, 471–481.
- Nobmann, S., Bauer, B., Fricker, G., 2001. Ivermectin excretion by isolated functionally intact brain endothelial capillaries. *Br. J. Pharmacol.* 132 (3), 722–728.
- Notenboom, S., Miller, D.S., Smits, P., Russel, F.G.M., Masereeuw, R., 2002. Role of NO in endothelin-regulated drug transport in the renal proximal tubule. *Am. J. Physiol. Renal. Physiol.* 282 (3), F458–F464.
- Notenboom, S., Miller, D.S., Kuik, L.H., Smits, P., Russel, F.G.M., Masereeuw, R., 2005. Short-term exposure of renal proximal tubules to gentamicin increases long-term multidrug resistance protein 2 (Abcc2) transport function and reduces nephrotoxicant sensitivity. *J. Biol. Chem.* 315, 912–920.
- Ogpenorth, T.J., Wu-Wong, J.R., Shiosaki, K., 1992. Endothelin-converting enzymes. *FASEB J.* 6, 2653–2659.
- Parekh, D.B., Ziegler, W., Parker, P.J., 2000. Multiple pathways control protein kinase C phosphorylation. *EMBO J.* 19, 496–503.
- Park, J., Leong, M.L.L., Buse, P., Maiyar, A.C., Firestone, G.L., Hemmings, B.A., 1999. Serum and glucocorticoid-inducible kinase (SGK) is a target of the PI 3-kinase-stimulated signaling pathway. *EMBO J.* 18, 3024–3033.
- Patten, S.A., Sihra, R.K., Dhama, K.S., Coutts, C.A., Ali, D.W., 2007. Differential expression of PKC isoforms in developing zebrafish. *Int. J. Dev. Neurosci.* 25, 155–164.
- Prevo, B., Miller, D.S., van de Water, F.M., Wever, K.E., Russel, F.G.M., Flik, G., Masereeuw, R., 2011. Rapid, nongenomic stimulation of multidrug resistance protein 2 (Mrp2) activity by glucocorticoids in renal proximal tubule. *J. Pharmacol. Exp. Ther.* 338, 362–371.
- Ratnaik, R.N., 2003. Acute and chronic arsenic toxicity. *Postgrad. Med. J.* 79 (933), 391–396.
- Reichel, V., Masereeuw, R., van den Heuvel, J.J., Miller, D.S., Fricker, G., 2007. Transport of a fluorescent cAMP analog in teleost proximal tubules. *Am. J. Physiol. Regul. Integr. Comp. Physiol.* 293 (6), R2382–R2389.
- Reichel, V., Burghard, S., John, I., Huber, O., 2011. P-glycoprotein and breast cancer resistance protein expression and function at the blood-brain barrier and blood-cerebrospinal fluid barrier (choroid plexus) in streptozotocin-induced diabetes in rats. *Brain Res.* 1370, 238–245.
- Rigor, R.R., Hawkins, B.T., Miller, D.S., 2010. Activation of PKC isoform beta(I) at the blood-brain barrier rapidly decreases P-glycoprotein activity and enhances drug delivery to the brain. *J. Cereb. Blood Flow Metab.* 30, 1373–1383.
- Ryu, J.M., Lee, M.Y., Yun, S.P., Han, H.J., 2008. Zinc chloride stimulates DNA synthesis of mouse embryonic stem cells: involvement of PI3K/Akt, MAPKs, and mTOR. *J. Cell. Physiol.* 218, 558–567.
- Sarbasov, D.D., Ali, S.M., Sengupta, S., Sheen, J.H., Hsu, P.P., Bagley, A.F., Markhard, A.L., Sabatini, D.M., 2006. Prolonged rapamycin treatment inhibits mTORC2 assembly and Akt/PKB. *Mol. Cell.* 22, 159–168.

3.3. PART III: MECHANISM OF TOXICITY

G. Oezen et al.

Aquatic Toxicology 252 (2022) 106314

- Schramm, U., Fricker, G., Wenger, R., Miller, D.S., 1995. P-glycoprotein-mediated secretion of a fluorescent cyclosporin analogue by teleost renal proximal tubules. *Am. J. Physiol.* 268 (1 Pt 2), F46–F52.
- Sharma, V.K., Sohn, M., 2009. Aquatic arsenic: toxicity, speciation, transformations, and remediation. *Environ Int.* 35, 743–759.
- Shigaev, A., Asher, C., Latter, H., Garty, H., Reuveny, E., 2000. Regulation of sgk by aldosterone and its effects on the epithelial Na⁺ channel. *Am. J. Physiol. Ren. Physiol.* 278, 613–619.
- Singh, R., Singh, S., Parihar, P., Singh, V.P., Prasad, S.M., 2015. Arsenic contamination, consequences and remediation techniques: a review. *Ecotoxicol. Environ. Saf.* 112, 247–270.
- Steinberg, S.F., 2008. Structural basis of protein kinase C isoform function. *Physiol. Rev.* 88, 1341–1378.
- Terlouw, S.A., Masereeuw, R., Russel, F.G., Miller, D.S., 2001. Nephrotoxicants induce endothelin release and signaling in renal proximal tubules: effect on drug efflux. *Mol. Pharmacol.* 59, 1433–1440.
- Terlouw, S.A., Graeff, C., Smeets, P.H., Fricker, G., Russel, F.G., Masereeuw, R., Miller, D.S., 2002. Short- and long-term influences of heavy metals on anionic drug efflux from renal proximal tubule. *J. Pharmacol. Exp. Ther.* 301 (2), 578–585.
- Toullec, D., Pianetti, P., Coste, H., Bellevergue, P., Grand-Perret, T., Ajakane, M., Baudet, V., Boissin, P., Boursier, E., Loriolle, F., et al., 1991. The bisindolylmaleimide GF 109203X is a potent and selective inhibitor of protein kinase C. *J. Biol. Chem.* 266, 15771–15781.
- Toosi, B., Zaker, F., Alikarami, F., Kazemi, A., Teremmahi Ardestani, M., 2018. VS-5584 as a PI3K/mTOR inhibitor enhances apoptotic effects of subtoxic dose arsenic trioxide via inhibition of NF-kappaB activity in B cell precursor-acute lymphoblastic leukemia. *Biomed. Pharmacother.* 102, 428–437.
- Uversky, V.N., Li, J., Fink, A.L., 2001. Metal-triggered Structural Transformations, aggregation, and fibrillation of human α -synuclein. *J. Biol. Chem.* 276 (47), 44284–44296.
- Whitehead, A., Clark, B.W., Reid, N.M., Hahn, M.E., Nacci, D., 2017. When evolution is the solution to pollution: key principles, and lessons from rapid repeated adaptation of killifish (*Fundulus heteroclitus*) populations. *Evol. Appl.* 10 (8), 762–783.
- Xiaoling, Z., Yifei, L., Xiaozhe, S., Chun, M., 2016. An overview on therapeutics attenuating amyloid β level in Alzheimer's disease: targeting neurotransmission, inflammation, oxidative stress and enhanced cholesterol levels. *Am. J. Transl. Res.* 8 (2), 246–269.
- Xiong, Y., Jing, X.P., Zhou, X.W., Wang, X.L., Yang, Y., Sun, X.Y., Qiu, M., Cao, F.Y., Lu, Y.M., Liu, R., Wang, J.Z., 2013. Zinc induces protein phosphatase 2A inactivation and tau hyperphosphorylation through Src dependent PP2A (tyrosine 307) phosphorylation. *Neurobiol. Aging* 34, 745–756.
- Yuan, M., Sun, Z., Manthari, R.K., Zhao, Y., Guo, Q., Yang, K., Wang, J., 2021. Arsenic-induced autophagy regulates apoptosis in AML-12 cells. *Toxicol. In Vitro* 72, 105074.
- Zaremba, A., Miller, D.S., Fricker, G., 2017. Zinc chloride rapidly stimulates efflux transporters in renal proximal tubules of killifish (*Fundulus heteroclitus*). *Toxicol. Appl. Pharmacol.* 334, 88–99.
- Zaremba, A., Helm, F., Fricker, G., 2019. Impact of Zn²⁺ on ABC transporter function in intact isolated rat brain microvessels, human brain capillary endothelial cells, and in rat *in vivo*. *Mol. Pharm.* 16 (1), 305–317.
- Zhu, Y., Li, Y., Miao, L., Wang, Y., Liu, Y., Yan, X., Cui, X., Li, H., 2014. Immunotoxicity of aluminum. *Chemosphere* 104, 1–6.

3.4 Part IV: Application of the zebrafish model

3.4.1 Publication 1

Virus-Derived Peptides for Hepatic Enzyme Delivery

Anna Pratsinis, Philipp Uhl, **Jan Stephan Bolten**, Patrick Hauswirth, Susanne Heidi Schenk, Stephan Urban, Walter Mier, Dominik Witzigmann, Jörg Huwyler

Mol Pharm. 2021 May 3;18(5):2004-2014.

doi: 10.1021/acs.molpharmaceut.0c01222.

Personal contribution:

My contribution to this research article includes zebrafish larvae experiments to assess pharmacokinetic aspects. Thus, I was involved in PEGylation strategies to enhance biodistribution. I wrote parts of the method section and proofread the manuscript.

Virus-Derived Peptides for Hepatic Enzyme Delivery

Anna Pratsinis, Philipp Uhl, Jan Stephan Bolten, Patrick Hauswirth, Susanne Heidi Schenk, Stephan Urban, Walter Mier, Dominik Witzigmann, and Jörg Huwlyer*

Cite This: *Mol. Pharmaceutics* 2021, 18, 2004–2014

Read Online

ACCESS |

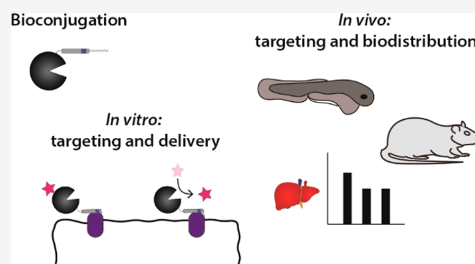
Metrics & More

Article Recommendations

Supporting Information

ABSTRACT: Recently, a lipopeptide derived from the hepatitis B virus (HBV) large surface protein has been developed as an HBV entry inhibitor. This lipopeptide, called MyrcludexB (MyrB), selectively binds to the sodium taurocholate cotransporting polypeptide (NTCP) on the basolateral membrane of hepatocytes. Here, the feasibility of coupling therapeutic enzymes to MyrB was investigated for the development of enzyme delivery strategies. Hepatotropic targeting shall enable enzyme prodrug therapies and detoxification procedures. Here, horseradish peroxidase (HRP) was conjugated to MyrB via maleimide chemistry, and coupling was validated by SDS-PAGE and reversed-phase HPLC. The specificity of the target recognition of HRP-MyrB could be shown in an NTCP-overexpressing liver parenchymal cell line, as demonstrated by competitive inhibition with an excess of free MyrB and displayed a strong linear dependency on the applied HRP-MyrB concentration. *In vivo* studies in zebrafish embryos revealed a dominating interaction of HRP-MyrB with scavenger endothelial cells vs xenografted NTCP expressing mammalian cells. In mice, radiolabeled ^{125}I -HRP-MyrB, as well as the non-NTCP targeted control HRP-peptide-construct (^{125}I -HRP-alaMyrB) demonstrated a strong liver accumulation confirming the nonspecific interaction with scavenger cells. Still, MyrB conjugation to HRP resulted in an increased and NTCP-mediated hepatotropism, as revealed by competitive inhibition. In conclusion, the model enzyme HRP was successfully conjugated to MyrB to achieve NTCP-specific targeting *in vitro* with the potential for *ex vivo* diagnostic applications. *In vivo*, target specificity was reduced by non-NTCP-mediated interactions. Nonetheless, tissue distribution experiments in zebrafish embryos provide mechanistic insight into underlying scavenging processes indicating partial involvement of *stabilin* receptors.

KEYWORDS: bioconjugation, enzyme targeting, hepatic drug delivery, zebrafish screening, hepatitis B virus



INTRODUCTION

Multiple therapeutic enzymes have already entered the clinic,¹ and several others are being investigated for a range of indications, including metabolic disorders,^{2,3} poisoning,^{4–7} and cancer therapy.^{8,9} Targeted enzyme delivery is particularly relevant, as systemic administration and related side effects lower the therapeutic index.¹⁰ The mechanisms of enzymatic action are mainly focused on substrate depletion^{3,9,11} or conversion of prodrugs.^{12–14} By locally confining therapeutic enzymes by active targeting, side effects may be minimized to increase treatment efficacy.¹⁵ Even though different ligands have been described for targeted enzyme delivery,^{16,17} enzymes are typically linked to antibodies targeting noninternalizing antigens as in Antibody Directed Enzyme Prodrug Therapy (ADEPT).^{14,15} Following local conversion, free drugs can penetrate deeper into the target tissue when compared to targeting ligand–drug conjugates.¹³ Indeed, several antibody–drug conjugates (ADC) targeting noninternalizing antigens have recently emerged using cleavable linkers.^{18–20} This strategy is based on extracellular liberation of the drug payload, thereby increasing target tissue accumulation and penetration.²¹ Importantly, such strategies require a specific

target within the extracellular matrix or, that is, confined to poorly internalizing cellular receptors.²¹

A liver-specific target that meets this requirement is the sodium taurocholate cotransporting polypeptide (NTCP)²² expressed on the basolateral membrane of hepatocytes.²³ Interestingly, MyrcludexB (MyrB), a recently developed viromimetic lipopeptide derived from the hepatitis B virus (HBV) large surface protein, selectively targets the NTCP with high affinity ($K_D = 67$ nM) and a relatively slow dissociation ($t_{1/2}$ of 11 h).²⁴ This is the basis for clinical trials to prevent HBV and hepatitis D virus (HDV) binding to hepatocytes^{24,25} for the management of chronic HBV and HDV infections.^{26,27} Beyond the antiviral application, this sustained NTCP association may also provide a novel avenue for targeted

Received: December 16, 2020

Revised: March 27, 2021

Accepted: March 29, 2021

Published: April 12, 2021



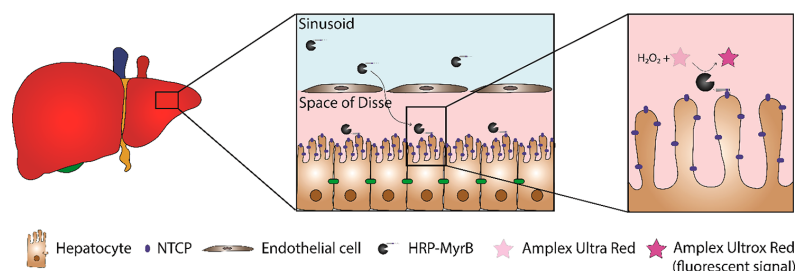


Figure 1. Suggested hepatotropism of enzymes tagged to viromimetic peptides. MyrB-tagged enzymes (i.e., HRP-MyrB) enter the space of Disse from the bloodstream through the fenestrae of the liver sinusoidal endothelium, specifically recognizing and binding NTCP on the basolateral membrane of hepatocytes. This enables targeted delivery of enzymes as demonstrated with HRP that catalyzes the reaction of a fluorogenic substrate with H_2O_2 on the cell surface to produce a fluorescent signal.

enzyme delivery for the treatment of liver diseases or toward detoxification to exploit the high hepatic accumulation, enabling enzymatic conversion on the extracellular surface of hepatocytes.

Indeed, various hepatic drug delivery platforms using MyrB or its derivatives have been proposed as targeting ligands.^{28–30} These efforts have focused primarily on liposome-based strategies, demonstrating effective delivery of small molecule drugs such as paclitaxel²⁸ or doxorubicin.³⁰ Similarly, we optimized virus-mimetic lipid nanocarriers coupled to a MyrB derivative.³¹ Notably, we observed that the nanocarrier is readily endocytosed, while MyrB remains largely associated with the cell surface,³¹ resulting in the typical MyrB cell membrane staining.^{24,32}

Capitalizing on the previously demonstrated ability to employ derivatives of MyrB as a targeting agent for the hepatocyte-specific delivery of small molecule drugs,³¹ the aim of this work was to explore the feasibility of linking a therapeutic enzyme to MyrB for targeted enzyme (large molecule) delivery to the surface of hepatocytes. To this end, horseradish peroxidase (HRP) was selected as a model enzyme due to its commercial availability, its fluorogenic substrates, and its previous use in enzyme prodrug therapy.^{33,34} As illustrated in Figure 1, HRP coupled to the viromimetic peptide MyrB (HRP-MyrB) enters the space of Disse through the fenestrated capillaries formed by the liver sinusoidal endothelial cells (EC). Within the space of Disse, the conjugate associates with NTCP, exerting its targeted enzymatic activity, demonstrated here by oxidation of Amplex Ultra Red (AUR) to Amplex Ultrox Red, yielding a fluorescent signal. The binding efficacy and ability to specifically deliver the enzymatic activity was investigated *in vitro* in liver parenchymal cells engineered to overexpress NTCP.³⁵ To preassess the *in vivo* targeting ability and to predict hepatic clearance mechanisms via macrophages or liver sinusoidal EC in mammals, the zebrafish embryo (*Danio rerio*) model was used, xenotransplanted with mammalian cells expressing NTCP. In previous contributions, we demonstrated the utility of this early, high-throughput pharmacokinetic (PK) prescreening model.^{36–39} The biodistribution of radiolabeled HRP-MyrB conjugates was evaluated in mice, and the PK properties were compared to those observed in zebrafish embryos.

EXPERIMENTAL PROCEDURES

Preparation of Enzymes Coupled to Viromimetic Peptides. All peptides were synthesized via solid-phase

peptide synthesis on a chlorotrityl resin (2-CTC) employing the fluorenylmethyloxycarbonyl/*tert*-butyl (Fmoc/*t*Bu) strategy and modified with myristic acid.^{31,40} The peptides were purified via preparative HPLC (Reprosil Pur 120 C18-AQ, 5 μ m (250 mm \times 25 mm)), and the purity of the peptides was confirmed by LC-MS.

EZ-Link maleimide-activated horseradish peroxidase (HRP-mal), derived from plants, and MyrBC were solubilized in the conjugation buffer (100 mM NaPi, 150 mM NaCl, 5 mM EDTA, pH 7.2) to 0.5 mg/mL HRP-mal with a 1- to 5-fold molar excess of the peptide. Solutions were kept at room temperature at constant shaking and incubated for 4–16 h, yielding HRP-MyrB. For subsequent preparations, HRP-mal was solubilized at 0.5–5 mg/mL, and viromimetic peptides were added using a molar excess of 2–2.5.

For fluorescent labeling, NHS-Rhodamine (5/6-carboxytetramethyl-rhodamine succinimidyl ester) was predissolved to 10 mg/mL in anhydrous DMSO and added to the HRP-peptide constructs at a 10 to 20-fold molar excess. Solutions were kept at room temperature for 2 to 16 h at constant agitation. Free dye was removed by dialysis (12–14 kDa MWCO) against 10 mM phosphate-buffered saline (PBS) or by size exclusion chromatography using an XK16/20 column packed with Sephadex G-50 fine medium eluted with PBS. MyrBC was fluorescently labeled as previously described.³¹

Characterization of Enzymes Coupled to Viromimetic Peptides. The HRP concentration and dye coupling ratio were determined with UV–Vis spectroscopy. The efficacy of HRP-peptide coupling was investigated by 10% SDS-PAGE.⁴¹ Samples were diluted in a nonreducing loading buffer, and the gels were stained with Coomassie blue R-250.

The HRP-peptide constructs were analyzed by RP-HPLC-UV using a Nexera X2 (Shimadzu) instrument equipped with an SPD-M30A Diode Array detector connected to a Bioresolve RP mAb Polyphenyl Column. Buffer A consisted of 0.1% trifluoroacetic acid (TFA) in water, and buffer B consisted of 0.1% TFA in acetonitrile. The proteins were eluted in 20 min at a flow rate of 0.2 mL/min from 15 to 55% buffer B and detected by UV–Vis at 220 nm.

The enzymatic activity was monitored by following the oxidation of AUR. HRP (0.25–5 mU/mL) was incubated with 1 mM hydrogen peroxide (H_2O_2) and 50 μ M AUR in PBS in 96-well plates. Upon mixing, the fluorescence (λ_{Ex}/Em : 490/585 nm) was immediately recorded over 5 min using a Spectramax M2e plate reader (Molecular Devices). The activity of the

HRP-peptide constructs was normalized to that of HRP-mal, measured at the same concentration, set to 100%.

In Vitro Cell Binding. A549, HEK293, and HepG2 cell lines (ATCC) were grown in Dulbecco's modified Eagle medium (high glucose, 4500 mg/L) supplemented with 10% fetal calf serum (FCS, Amimed) and 1% penicillin–streptomycin, referred to as the complete cell culture medium. Cells were kept in culture over 20 passages. Cells were grown at 37 °C in a humidified atmosphere containing 5% CO₂. The stable human NTCP-expressing HepG2 cell line was generated by lentiviral transfection (HepG2 *hNTCP*).³⁵ HEK293 cells stably expressing GFP⁴² were cultured in complete cell culture media containing 0.5 mg/mL Geneticin (G418).

For *in vitro* imaging, cells were seeded at a concentration of 50,000 cells/well on 8-well μ -slides (Ibidi) previously coated with 9 μ g/cm² of collagen I, rat tail. The following day, HRP-MyrB-Rho and HRP-alaMyrB-Rho were added at a final concentration of 200 nM for 15–30 min. The cells were washed, and the nuclei were stained with 0.5 μ g/mL Hoechst 33342. The cells were again washed and incubated with Cell Mask deep red membrane stain for 2 min. Cells were washed and imaged using a Zeiss LSM880 inverted confocal microscope, equipped with a 63 \times PlanApo oil-immersion objective (numerical aperture 1.4).

In Vitro Delivery of Enzymatic Activity to Target Cells. HepG2 and HepG2 *hNTCP* cells were diluted to 1,000,000 cells/mL, and 0.5 mL was transferred to 1.5 mL Eppendorf tubes. The cells were then centrifuged for 4 min at 200g and resuspended in 0.5 mL of HRP-MyrB or HRP-alaMyrB diluted in complete cell culture media (enzyme concentrations of 25–200 mU/mL) and incubated for 30 min at 37 °C under constant rotation. To remove unbound HRP, the cells were washed three times with 1.5 mL of DPBS by centrifugation. The final cell pellet was suspended in 0.5 mL of DPBS, and 50 μ L were transferred to 96-well plates, where 50 μ L of an AUR/H₂O₂ solution was added to measure the HRP activity. For blocking experiments, HepG2 *hNTCP* cells were incubated with 2 μ M MyrB for 30 min before adding 200 mU/mL HRP-MyrB, corresponding to approximately 10 nM protein–peptide conjugate.

Transient Transfection of Cell Lines. HEK293 cells stably expressing GFP were seeded at a concentration of 280,000 cells/well in a 6-well plate, previously coated with 4.2 μ g/cm² of poly-D-lysine. After 2 days, the cells were transfected with an *hNTCP*-pEF6 plasmid³¹ using Lipofectamine 3000 according to the manufacturer's recommendations (2.5 μ g plasmid per well at a 2:1 w/v ratio of DNA to Lipofectamine 3000). Transfected cells and nontransfected control cells were harvested the following day for xenografting.

In Vivo NTCP Targeting Using Xenografted Zebrafish Embryos. The zebrafish (*Danio rerio*) AB/Tübingen (wild type) embryos were kindly provided by Prof. Dr. M. Affolter and Dr. H. Belting (University of Basel, Switzerland) and were maintained according to the Swiss animal welfare regulations.^{36,38} The embryos obtained from adult zebrafish were kept in zebrafish culture media at 28 °C, and the formation of pigment cells was prevented by adding 30 μ g/mL 1-phenyl 2-thiourea (PTU) 0, 1, and 2 days post fertilization (dpf). At 2 dpf, zebrafish embryos were anaesthetized with 0.01% tricaine, dechorionized, and embedded in 0.3% agarose containing tricaine and PTU.³⁶

Control- and *hNTCP* overexpressing HEK293 cells were detached from the 6-well plates with trypsin-EDTA, and the

cell suspension was centrifuged for 4 min at 150g. The cell pellet was resuspended to an approximate cell concentration of 10,000,000 cells/mL and injected into the duct of Cuvier using a micromanipulator and a pneumatic Pico Pump PV830.³⁶ Calibrated volumes of 1 nL of MyrB-Atto565, HRP-MyrB-Rho, and HRP-alaMyrB-Rho at 0.2 mg/mL were subsequently injected into the duct of Cuvier. The tail region of the zebrafish embryos was imaged 1 h post injection (hpi) using a Leica SP5-II-Matrix inverted confocal microscope equipped with an HCX IRAPO 25 \times (numerical aperture 0.95) objective. Colocalization of the fluorescently labeled proteins with the control and *hNTCP*-overexpressing cells was evaluated in FIJI using the JaCoP plug-in to quantify the Pearson's Correlation Coefficient (PCC).⁴⁵

Radioactive Labeling of Protein–Peptide Conjugates with ¹²⁵I. HRP was coupled to MyrB-derived peptides containing an additional D-tyrosine residue for radioactive labeling and subsequent planar imaging and biodistribution studies in mice. To characterize the biodistribution of HRP, the linkage peptide (CAy) was added to HRP-mal at a 5-fold molar excess in conjugation buffer and incubated overnight at room temperature. Protein–peptide conjugates were exchanged into 0.25 M phosphate, pH 7.5, using centrifugal filter units. Radioactive iodine-125 (¹²⁵I) was added to 100 μ L of a 0.15 mM solution of the respective HRP-peptide conjugate. Ten μ L of a 1 mg/mL chloramine T solution was added to effectuate the radioiodination of the tyrosine residues, and 20 μ L of saturated methionine was added after 30 s to stop the reaction.⁴⁴ The reaction mixture was purified by using NAP-5 columns by elution with sterile saline and subsequently concentrated with centrifugal filter units.

Biodistribution of Protein–Peptide Conjugates in Mice. All mouse experiments were performed in accordance with procedures approved by the German authorities, using female SWISS mice (6–8 weeks) obtained from Janvier Laboratories (Le Genest-Saint-Isle, France). HRP-peptide conjugates were injected into the tail vein at an HRP dose of 8.3 mg/kg and a total radioactivity of approximately 1 MBq per animal. For blocking experiments, 2 mg/kg MyrB was administered into the tail vein 10 min prior to HRP-peptide injection. Mice were euthanized 1 h post HRP-peptide injection by CO₂ asphyxia. The radioactivity in the peripheral blood and major organs was quantified using a Cobra Auto γ -Counter. The organ-associated radioactivity was calculated using published values for organ weights.⁴⁵

Planar Imaging of Mice. Mice were anaesthetized using isoflurane (Baxter), and ¹²⁵I-HRP-alaMyrB and ¹²⁵I-HRP-MyrB were injected into the tail vein at a total radioactivity of 1–3 MBq. Blocking of the NTCP was performed as described above. For scintigraphic imaging, mice were placed in the prone position on a planar gamma-imager (Biospace) equipped with a high-energy collimator.^{25,46} Images were recorded at 10, 30, and 60 min with a 10 min acquisition time, during which the mice were under isoflurane anesthesia.

Statistical Analysis. Statistical analysis was performed with OriginPro 2018 using a one-way ANOVA followed by a Tukey posthoc test for pairwise comparison. A *p*-value smaller than 0.05 was considered statistically significant.

RESULTS AND DISCUSSION

Linkage of Viromimetic Targeting Ligands to HRP. To investigate the feasibility of coupling therapeutic enzymes to the viromimetic peptide MyrB for targeted hepatic enzyme

Table 1. Overview of the Synthesized MyrB-Derived Peptides^a

name	sequence
MyrBC	Myr-GT <u>NLSV</u> <u>NPLGFF</u> PDHQLDPAFGANSNNPDWSFNPNKDHWPEANKVGC
MyrByC	Myr-GT <u>NLSV</u> <u>NPLGFF</u> PDHQLDPAFGANSNNPDWSFNPNKDHWPEANKVGC
alaMyrBC	Myr-GT <u>NLSV</u> <u>NAAAAA</u> PDHQLDPAFGANSNNPDWSFNPNKDHWPEANKVGC
alaMyrByC	Myr-GT <u>NLSV</u> <u>NAAAAA</u> PDHQLDPAFGANSNNPDWSFNPNKDHWPEANKVGC
MyrB-Atto565	Myr-GT <u>NLSV</u> <u>NPLGFF</u> PDHQLDPAFGANSNNPDWSFNPNKDHWPEANKVGC-Atto565
linkage peptide	CAy

^aThe amino acids constituting the pharmacophore, 9-NPLGFFP-15, are underlined.^{25,40} Myr represents myristic acid.

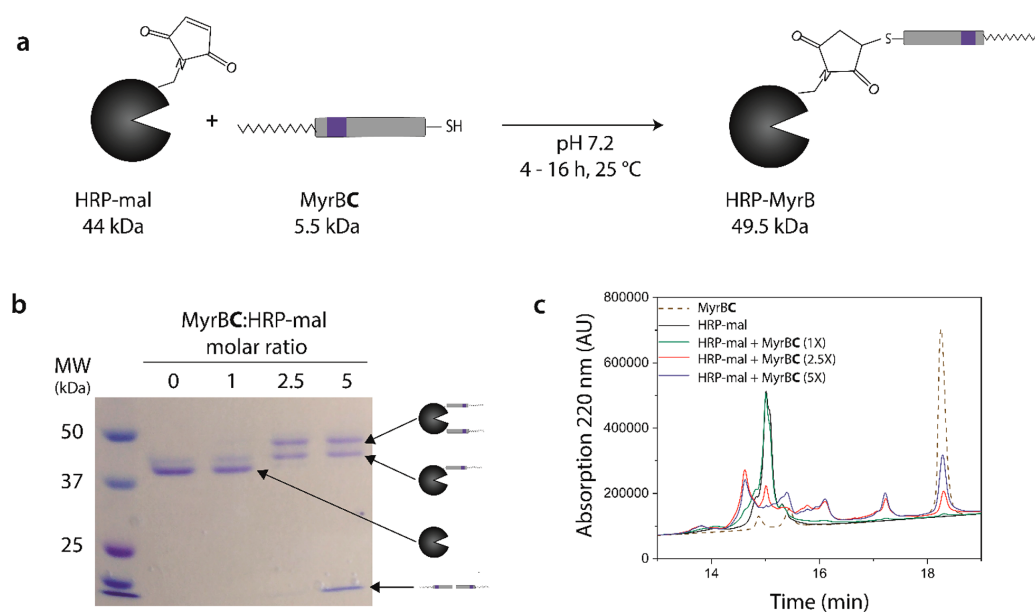


Figure 2. Effective ligand-enzyme coupling of MyrB to HRP. (a) Coupling reaction: MyrB-cysteine (MyrBC) is added to HRP-mal at 1- to 5-fold molar excess. (b) Effective linkage is shown by SDS-PAGE, where unconjugated HRP, HRP coupled to 1–2 MyrBC, and free MyrBC, are marked by an arrow and a schematic illustration. Left lane: molecular weight markers. (c) RP-HPLC elution profile of HRP-mal (black-), HRP-mal conjugated with MyrBC at 1- (green-), 2.5- (red-), and 5-fold molar excess (blue-) as well as noncoupled MyrBC (brown dashed line).

delivery, different peptide derivatives were prepared by solid-phase synthesis. In the present work, nonmyristoylated MyrB derivatives were not considered since we could previously demonstrate that they show poor binding to NTCP *in vitro*³¹ and *in vivo*.²⁵ An overview of the prepared peptide sequences is shown in Table 1. MyrB consists of 47 amino acids with an N-terminal myristic acid. The peptide sequence is identical to the active pharmaceutical ingredient currently under clinical investigation^{26,27} with minor exceptions. A cysteine residue was attached to the C-terminus to allow efficient, reproducible, and directed coupling to HRP. Of note, C-terminal cysteine modification does not interfere with target recognition.²⁵ With respect to the choice of MyrB derivatives used in the present study, it is important to note that exchanging amino acids within the pharmacophore 9-NPLGFFP-15 leads to abrogation of effect, as has been demonstrated in multiple contributions.^{24,25,40,47} Schulze et al. had exchanged the residues 11–15 with alanine, leading to a complete loss of inhibitory effect of HBV infection when tested up to a concentration of 2.5 μM .⁴⁰ By comparison, the nonmodified sequence displays an IC₅₀ of 0.4 nM.⁴⁰ Also, deletion of the residues 11–15 could not prevent HBV infection when tested up to 500 nM.⁴⁷ Replacing

MyrB amino acid residues 11–15 within the pharmacophore with alanines abrogates specific NTCP target recognition both *in vitro*^{24,40} and *in vivo*,²⁵ therefore providing an ideal negative control peptide³¹ (alaMyrB) with comparable physicochemical properties.

The viromimetic peptides were coupled to maleimide-activated HRP (HRP-mal) via their C-terminal cysteine residue, forming a metabolically stable thioether bond,⁴⁸ as illustrated in Figure 2a. A molecular weight of 44 kDa for HRP⁴⁹ and 5.5 kDa for the viromimetic peptide MyrB enables direct monitoring of the coupling by a change in molecular weight. To determine the optimal coupling ratio, the viromimetic peptide MyrBC was added to HRP-mal at an increasing molar ratio, ranging from 1- to 5-fold molar excess (Figure 2a). Effective linkage of MyrB to HRP at a 2.5- to 5-fold molar peptide excess is observed by SDS-PAGE as a result of the increase in molecular weight by 5.5 to 11 kDa, depending on whether one or two MyrB peptides are coupled to HRP (Figure 2b). Of note, the starting HRP-mal material displays a double band just above 37 kDa due to different glycosylation. The same applies to the MyrB-coupled HRP, resulting in blurred bands.

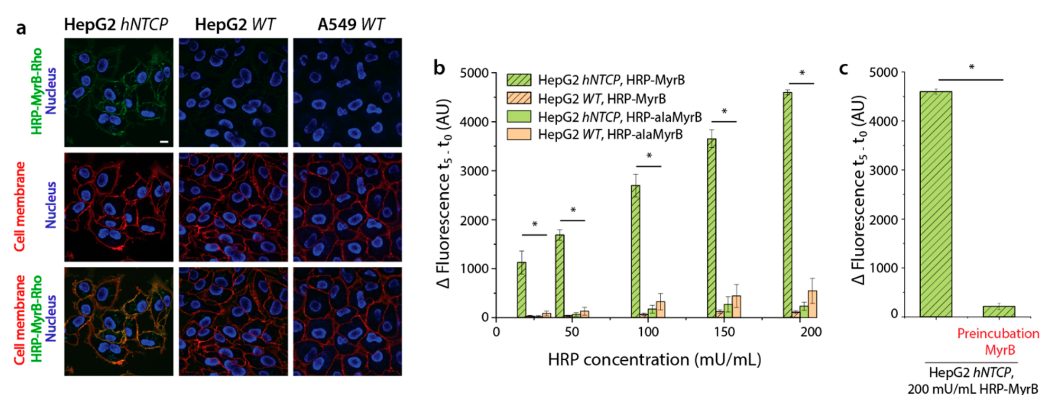


Figure 3. Specific binding of enzymatically active HRP-MyrB to NTCP expressing hepatic cells. (a) Representative confocal laser scanning microscopy images of HepG2 *hNTCP* (left column), HepG2 *WT* (middle column) and A549 *WT* (right column) cells incubated with HRP-MyrB-Rho. Upper row: HRP-MyrB-Rho. Middle row: Cell Mask. Lower row: merged images. Blue signal: Hoechst nuclear staining. Scale bar = 10 μm . (b) HRP-MyrB (hatched pattern) and HRP-alaMyrB (solid pattern) were added to HepG2 *hNTCP* (green bars) and HepG2 (orange bars). After 30 min, HRP activity was measured. Mean \pm St. Dev ($n = 3$). * $p \leq 0.001$ as compared to HepG2 *hNTCP* plus HRP-MyrB. (c) Specificity of NTCP-targeting by competitive inhibition of HRP-MyrB binding to HepG2 *hNTCP* cells using free MyrB at a 200-fold molar excess of free MyrB. Mean \pm SD ($N = 3$). * $p \leq 0.001$.

Considering that one or two MyrB are linked to each HRP moiety, the effective coupling is observed at almost equimolar maleimide to thiol ratio at 2.5-fold molar MyrB to HRP excess. The high coupling efficiency detected here is in line with reports on maleimide protein chemistry with effective coupling at 1-⁵⁰ to 5-fold molar⁵¹ excess when linking DOTA⁵⁰ or fluorophores⁵¹ to proteins. To further characterize the linkage of MyrB to HRP, the above-described coupling reaction mixture was subjected to RP-HPLC analysis.

Linkage is also observed by RP-HPLC, as shown in Figure 2c, where the addition of MyrB at 2.5- or 5-fold molar excess leads distinctly to a delayed retention time. HRP linked to MyrB elutes later, presumably due to increased interaction of the myristic acid with the solid phase of the column, as previously shown for hydrophobic enzyme modification⁵ and with ADCs.⁵² Interestingly, linkage of the MyrB to HRP again leads to two distinct peaks, with a retention time of 16.2 and 17.3 min, compared to HRP-mal eluting at 15.1 min (Figure 2c). This is in line with the observations made by SDS-PAGE (Figure 2b), further supporting the notion that the here described coupling reaction yields HRP coupled to either one or two MyrB lipopeptides. In addition, by increasing the molar excess of MyrB from 2.5- (red line, Figure 2c) to 5-fold molar excess (blue line), the amount of coupled HRP does not seem to significantly increase according to the peaks at 16.2 and 17.3 min. It is possible that coupling two MyrB ligands promote superior targeting, aligned with a recent report¹⁶ demonstrating increased target binding by multivalent interactions. We, however, believe that one MyrB ligand suffices, considering its high specificity and affinity ($K_D = 67 \text{ nM}^{24}$).

The free peptide elutes around 15 and 18.3 min (dashed line, Figure 2c). The last peak corresponds to its dimeric form that rapidly forms in the absence of maleimide residues due to disulfide bonding of C-terminal cysteine residue.⁴⁸ Now, while increasing the proportion of MyrB from 2.5- to 5-fold molar excess, the coupling degree remains comparable. This is due to the starting material, HRP-mal, which displays a fixed and differential amount of maleimide residues per HRP molecule. An increase in free MyrB eluting at 18.3 min is obvious. The

coupling ratio was therefore set to 2–2.5-fold molar MyrB excess for all subsequent experiments to limit any potential interference stemming from the free lipopeptide. Subsequent experiments revealed that the present coupling protocol was applicable to the other viromimetic peptides employed here, yielding effective linkage as evaluated by SDS-PAGE (Figure S1).

Since previous reports have demonstrated that coupling moieties to enzymes may lead to a change in catalytic activity,¹¹ the HRP activity was evaluated based on the enzyme's ability to catalyze the reaction of hydrogen peroxide with AUR.⁵³ A residual activity of approximately 80% (Figure S2) indicates that the enzymatic activity is hardly impacted by the peptide linkage and in line with a previous report,⁵⁴ where the covalent modification of HRP at 3 positions did not influence the catalytic activity.

In Vitro Assessment of HRP-MyrB Target Recognition.

The NTCP target specificity of viromimetic peptides linked to HRP was investigated *in vitro*. To visualize the cellular binding, HRP-MyrB and HRP-alaMyrB were coupled to rhodamine, yielding HRP-MyrB-Rho and HRP-alaMyrB-Rho with an average of 1–2 fluorophores per enzyme. The cellular target protein (NTCP) is responsible for the sodium-dependent uptake of bile salts, and its expression is highly specific to hepatocytes.⁵⁵ This integral membrane protein is, however, not detectable in the human liver cancer-derived HepG2 or HuH7 cell lines as its expression is downregulated during oncogenic transformation.^{24,35} Recently, the HepG2 cell line was engineered to express the human NTCP (*hNTCP*) by lentiviral transduction,³⁵ thereby enabling the study of NTCP target recognition using this HepG2 *hNTCP* cell line. The NTCP overexpressing HepG2 cell line was used due to the defined expression levels of the receptor of interest. This in contrast to primary cultures of primary human hepatocytes, which rapidly lose liver-specific function and morphology in cell culture.⁵⁶

To investigate the *in vitro* binding efficacy and specificity, the present protein–peptide conjugates were exposed to different cell lines including hepatic HepG2 wild type (*WT*), HepG2 *hNTCP* and nonhepatic, lung endothelial A549 *WT* cells.

Figure 3a shows representative live-cell images of HRP-MyrB-Rho added to HepG2 *hNTCP*-, HepG2 *WT*-, and A549 *WT* cells. As it can be deduced from Figure 3a, HRP-MyrB-Rho readily associates with the HepG2 *hNTCP* cells, manifested by the distinct plasma membrane staining (green) overlapping with that stemming from Cell Mask Deep Red Plasma Membrane Stain (red). In contrast, *hNTCP*-specific cell membrane labeling is not observed for HepG2 *WT* and A549 *WT* cells (Figure 3a), nor when HRP-alaMyrB-Rho is added to HepG2 *hNTCP* (Figure S3).

These observations are well aligned with previous reports for free MyrB, where a plasma membrane-specific binding pattern was observed when exposed to NTCP expressing cells.^{24,32} Our *in vitro* experiments indicate that the NTCP target specificity of MyrB is maintained following the attachment of a protein with approximately 10-fold higher molecular weight.

We further investigated the capability of the HRP-viromimetic peptide conjugates to specifically deliver enzymatic activity to target cells. Figure 3b shows the targeted delivery of enzymatic activity to HepG2 *hNTCP* cells when MyrB is linked to HRP. By comparison, hardly any enzymatic activity was detected when the slightly modified viromimetic peptide alaMyrB is linked to HRP, nor when HRP-MyrB and HRP-alaMyrB are incubated with the NTCP-deficient HepG2 *WT* cells, confirming the observed lack of cellular binding.

To further investigate whether the interaction of HRP-MyrB with the HepG2 *hNTCP* cell line is specifically mediated via NTCP, we preincubated the cells with a 200-fold molar excess of MyrB before adding HRP-MyrB and measured the enzymatic activity (Figure 3c). By competitive inhibition, the catalytic activity following HRP-MyrB exposure is significantly reduced, further demonstrating that the interaction is NTCP-mediated. Noteworthy, the binding of HRP-MyrB to HepG2 *hNTCP* cells is directly proportional to the applied HRP-Myr concentration (Figures 3b and S4). This strong linear dependency is characterized by an R^2 of 0.99 and does not show any saturation over the concentration ranges used in the present work.

Since HRP-MyrB was demonstrated to specifically interact with NTCP, this construct may be utilized as an immunoassay reagent to detect and quantify the NTCP expression level in patient tumor biopsies during biomarker analysis of hepatocellular carcinoma tissue. This is important since a higher NTCP expression level was found to correlate with a superior survival rate and has, therefore, been suggested as a novel prognostic marker during the management of hepatocellular carcinoma.⁵⁷ This HRP-MyrB construct could therefore enable simple and straightforward quantitation of NTCP expression without a secondary antibody, as is conventionally done in enzyme-linked immunosorbent assays (ELISA) or during immunohistochemical staining of biological tissues.⁴⁸ Thereby potentially extending its application to *ex vivo* diagnostic purposes.

To summarize, by analyzing the interaction of various HRP-viromimetic peptide conjugates with different cell lines *in vitro* using confocal microscopy, we qualitatively demonstrated that the ability of MyrB to specifically recognize the NTCP target is maintained following enzyme linkage. In addition, we quantitatively showed a concentration-dependent and NTCP target-specific delivery of enzymatic activity. Nonetheless, future studies involving primary hepatocytes, maintained under optimized culture conditions, should be applied to better characterize the hepatocyte-specific interaction, espe-

cially in view of the development of potential *ex vivo* diagnostics.

Investigating NTCP Targeting in Xenografted Zebrafish Embryos. To investigate the circulation properties of protein-peptide conjugates as well as their ability to target the NTCP *in vivo*, we used the zebrafish embryo model. Recently, we and others have demonstrated that zebrafish embryos are a valid *in vivo* tool to assess nanocarrier's PK parameters.^{36–38,58} The question, however, remains whether such screening in zebrafish embryos can be extended to therapeutic proteins and enzymes. Since zebrafish embryos do not express NTCP, human HEK293 cells stably expressing the green fluorescent protein (GFP) were transiently transfected with a plasmid encoding NTCP and xenotransplanted in wild-type ABC/TU zebrafish embryos.³¹ This enabled the expression of the target protein NTCP and facilitated target cell detection *in vivo* via GFP fluorescence detection. As soon as the HEK293 settled within the zebrafish embryo vasculature, the protein-peptide conjugates HRP-MyrB-Rho and HRP-alaMyrB-Rho were subsequently injected. Given that MyrB has shown effective target recognition in rodents and higher vertebrate species²⁵ and is currently under clinical investigation,²⁶ fluorescent labeled MyrB-Atto565 was included as a positive control.

Figure 4a shows the circulation pattern of MyrB-Atto565, HRP-MyrB-Rho, and HRP-alaMyrB-Rho in the tail region of the zebrafish embryos xenografted with control HEK293 cells and expressing human NTCP (HEK293 *hNTCP*). Indeed, MyrB-Atto565 demonstrates a clear association with the HEK293 *hNTCP* cells, as confirmed by statistical analysis using at least five embryos per sample. This is manifested by a pronounced fluorescent signal on the cellular membrane (yellow) of a high proportion of xenografted cells. Importantly, MyrB-Atto565 does not show any interaction with the control HEK293 cells, indicating that the association is NTCP-mediated.

The effective colocalization of MyrB-Atto565 with *hNTCP* was quantitatively analyzed by Pearson's Correlation Coefficient (PCC), a measure of the linear correlation between injected conjugate and xenografted cells.⁴³ The colocalization was significantly elevated for the interaction of MyrB-Atto565 with the HEK293 *hNTCP* cells compared to control cells (Figure 4b). This validates the utility of the current setup to investigate the *in vivo* targeting ability of protein-peptide conjugates to NTCP.

In contrast to MyrB-Atto565, both HRP-MyrB-Rho and HRP-alaMyrB-Rho do not show any appreciable interaction with the HEK293 *hNTCP* cells, neither by qualitative image evaluation (Figure 4a) nor by quantitative colocalization analysis (PCC) (Figures 4b). This is surprising, considering the strong NTCP target association of HRP-MyrB observed *in vitro* (Figure 3). To ensure the lack of *in vivo* targeting was not provoked by the here employed cell line, we investigated the *in vitro* interaction of HRP-MyrB-Rho with HEK293 *hNTCP* cells. As expected, HRP-MyrB-Rho demonstrates an NTCP-specific plasma membrane staining (Figure S5).

When we compare the caudal vasculature of the tail region of the two fluorescently labeled protein-peptide conjugates to that of MyrB-Atto565 (Figure 4a), a markedly different circulation profile becomes apparent. Upon injection, MyrB-Atto565 displays a homogeneous signal distribution within the vasculature with fluorescence intensity clearly visible within the dorsal aorta. Both HRP-MyrB-Rho and HRP-alaMyrB-Rho, on the other hand, display a scattered, nonspecific vasculature

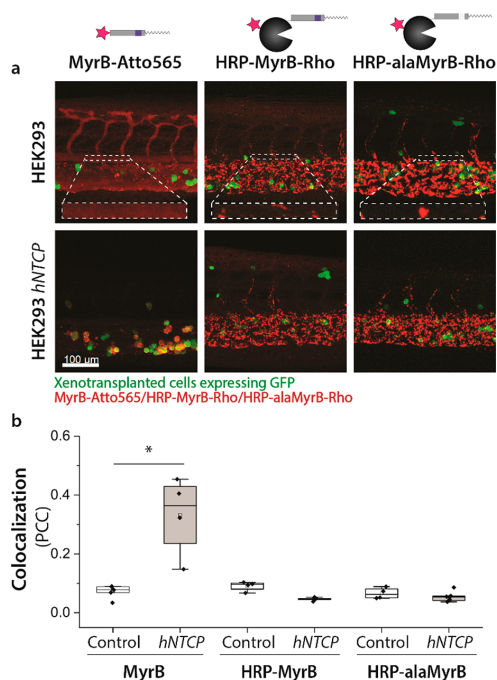


Figure 4. Assessment of *in vivo* targeting ability using xenografted zebrafish embryos. (a) Wildtype zebrafish embryos xenografted 2 dpf with HEK293 control cells (HEK293) or HEK293 overexpressing hNTCP (HEK293 hNTCP) are shown in the upper- and lower panels, respectively. The xenografted cells expressed GFP (green signal). Red signal: MyrB-Atto565 (left column), and the enzyme-ligand conjugates HRP-MyrB-Rho (middle column) and HRP-alaMyrB-Rho (right column) were subsequently injected, and the zebrafish embryos were imaged in the caudal vasculature tail region 1 hpi. Dashed white box: magnification of the dorsal aorta. For each group, a representative image is shown. Scale bar (applicable to all images) = 100 μm . (b) The interaction of MyrB-Atto565, HRP-MyrB-Rho, and HRP-alaMyrB-Rho with HEK293 cells analyzed by PCC. All values are shown as box plots with median values. $n \geq 5$. * $p \leq 0.01$.

binding pattern with hardly any signal detectable in the dorsal aorta lumen (lined and enlarged box, Figure 4a). It is tempting to speculate that the scavenging mechanisms (via macrophages or EC) encountered upon systemic exposure preclude *in vivo* target recognition.

The adaptive immune system is not matured in the zebrafish embryos, though macrophage precursors are already present at 20 hpf⁵⁹ and may contribute to the observed scavenging. In a previous study, we demonstrated macrophage clearance of nanoparticles in zebrafish embryos with GFP-expressing macrophages Tg(mpeg1:Gal4;UAS:Kaede).³⁷ We therefore injected HRP-MyrB-Rho into zebrafish embryos with this genetic modification. Notably, we did not observe any macrophage colocalization at 1 hpi (Figure S6a). This indicates that scavenging is not dominated by macrophages in zebrafish embryos at this development stage. This is aligned with previous investigations where HRP did not colocalize with macrophages when imaged 24 hpi.⁵³

With a dotted staining pattern in the posterior caudal vein, the scavenging pattern here resembles more that of nano-

formulations with a short circulation time, for example, mediated by phospholipids with a higher transition temperature³⁶ or by negative charge.⁵⁸ Campbell et al.⁵⁸ identified the role of endothelial *stabilin 1* and *stabilin 2* scavenger receptors, also present on mammalian liver sinusoidal EC, during sequestration of negatively charged particles. It was further shown that *stabilin* interaction could be blocked by preinjection of dextran sulfate, ameliorating the circulation pattern for the tested negatively charged vehicles.⁵⁸

Considering that the present protein-peptide conjugates are negatively charged, stabilin receptors on EC may contribute to the here observed scavenging (Figure 4a). We, therefore, preinjected zebrafish embryos expressing GFP in the vasculature Tg(kdrl:EGFP) with dextran sulfate. After 20 min, HRP-MyrB-Rho was injected, and zebrafish were imaged 1 hpi. The circulation of HRP-MyrB-Rho was markedly improved following dextran sulfate preinjection due to reduced scavenging, with signal also visible within the dorsal aorta (white dashed box, Figure S6a). For better understanding, a schematic representation of the vasculature present in the tail region of zebrafish embryos is depicted in Figure S6b. A distinct staining pattern was still visible following dextran sulfate injection, albeit altered in appearance with larger accumulations of HRP-MyrB-Rho visible (arrow, lower panel, Figure S6a). We, therefore, conclude that endothelial scavenging is in part stabilin-mediated, indicative of liver accumulation in mammals, while additional scavenging mechanisms may also play a role.

Biodistribution of Protein-Peptide Conjugates in Mice. While specific NTCP-targeting was clearly observed *in vitro* (Figure 3), this could not be demonstrated *in vivo* using xenografted zebrafish embryos (Figure 4). Therefore, we envisaged investigating whether HRP-MyrB is capable of NTCP-targeting in mice or if indeed the nontarget mediated scavenging observed in zebrafish embryos significantly contributes to hepatic accumulation. Viromimetic peptides with a C-terminal D-tyrosine-cysteine residue, MyrByC and alaMyrByC, were coupled to HRP-mal and subsequently radiolabeled with [¹²⁵I] iodine.⁴⁴ This enabled site-specific labeling without perturbing target recognition.²⁵ The radioactively labeled protein-peptide conjugates were administered intravenously. The mice were either imaged by scintigraphical imaging or subjected to a biodistribution analysis at 1 hpi. A short analysis was selected to maximize insight into NTCP specific binding, considering that MyrB associates with NTCP within 5 min following injection.²⁵ Of note, the cell- and zebrafish experiments were performed with hNTCP. Mouse NTCP (mNTCP), on the other hand, has a slightly different sequence with a lower MyrB binding efficiency.⁶⁰ Nonetheless, the mouse model is capable of detecting NTCP-specific target recognition,^{24,25,60} where the ability to prevent HBV infection was found to correlate with accumulation in mouse livers, supporting the use of this animal model to investigate NTCP-specific binding.²⁵

Figure 5a shows whole-body scintigraphy images of mice recorded 10, 30, and 60 min after injection of ¹²⁵I-HRP-MyrBy and ¹²⁵I-HRP-alaMyrBy. Upon injection, ¹²⁵I-HRP-MyrBy rapidly accumulates within the liver. Interestingly, a similar hepatic accumulation is also observed for ¹²⁵I-HRP-alaMyrBy. This is surprising, as previous studies involving this control peptide in its free form did not lead to significant liver accumulation.²⁵ In both groups, a steady increase in bladder accumulation is observed, indicating renal clearance.

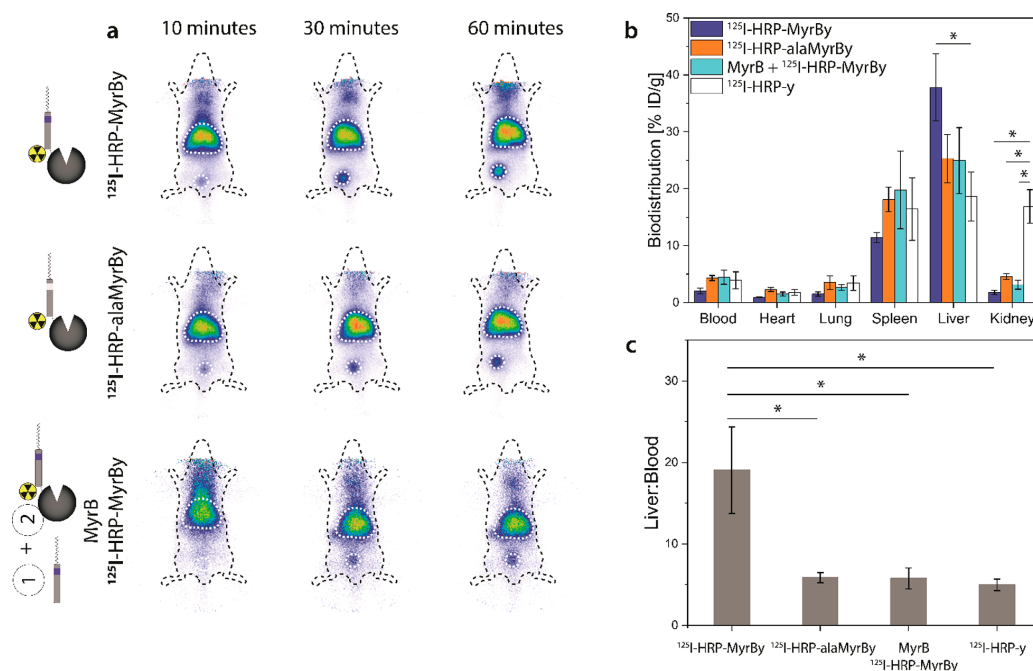


Figure 5. *In vivo* targeting and biodistribution of HRP-MyrB conjugates in mice. Radiolabeled peptide–protein conjugates (^{125}I -HRP-MyrB-y, ^{125}I -HRP-alaMyrB-y, and ^{125}I -HRP-y) were injected iv to study their biodistribution. A subset of mice was injected with free MyrB prior to administration of ^{125}I -HRP-MyrB-y to competitively inhibit NTCP recognition. (a) Whole body scintigraphy images were recorded 10 (left column), 30 (middle column), and 60 min (right column) post injection of ^{125}I -HRP-MyrB-y (upper row), ^{125}I -HRP-alaMyrB-y (middle row) or ^{125}I -HRP-MyrB-y, and competing free MyrB (lower row). The liver and bladder are marked with white dotted lines. (b) Biodistribution of ^{125}I -HRP-MyrB-y (dark blue bars), ^{125}I -HRP-alaMyrB-y (orange bars), and a combination of ^{125}I -HRP-MyrB-y and competing free MyrB (light blue bars) and ^{125}I -HRP-y (white bars). Mean \pm St. Dev ($n = 3$). * $p \leq 0.01$. (c) Liver to blood concentration ratios 1 hpi. Mean \pm SD ($n = 3$). * $p \leq 0.01$.

Indeed, the biodistribution analysis (Figure 5b) shows an enriched liver accumulation for both groups, quantitatively confirming the trend observed by scintigraphical imaging. The high liver accumulation associated with both constructs strongly suggests that hepatic enzyme delivery is not dominated by NTCP-target recognition and is perhaps imparted by alternative liver-specific scavenging mechanisms. It is important to recall that experiments in zebrafish embryos (Figure 4) suggested that scavenging processes might be a major contributor to liver accumulation in mice.

Nonetheless, to further elucidate whether the liver accumulation observed with ^{125}I -HRP-MyrB-y was at least partially mediated by NTCP-specific interaction, another group of mice was preinjected with nonradiolabeled MyrB to competitively inhibit NTCP before administering ^{125}I -HRP-MyrB-y. The corresponding images are shown in the lower panels of Figure 5a. The organ biodistribution (Figure 5b) is comparable to that of ^{125}I -HRP-alaMyrB-y. This indicates that the PK properties of the protein–peptide conjugates are dictated to a greater extent by the coupled protein rather than the MyrB peptide sequence. Despite this, ^{125}I -HRP-MyrB-y shows a higher liver accumulation when injected alone than after blocking NTCP, with 37% and 25% of the injected dose (ID/g) detected in the liver, respectively. Furthermore, comparing the liver to blood radioactivity ratio for each group reveals a significantly elevated liver association for ^{125}I -

HRP-MyrB-y (Figure 5c). Conclusively, a fraction of ^{125}I -HRP-MyrB-y is specifically recognized by the NTCP target, confirming the NTCP-specific association observed *in vitro* (Figure 3). While NTCP-specific targeting could be observed in this short-term biodistribution study, a long-term study would be required to better understand the duration of NTCP association as well as the metabolism of the here applied constructs.

To better understand the pharmacokinetic properties of HRP, which in fact accounts for the majority of the molecular weight of the present conjugates, a biodistribution analysis of ^{125}I -HRP-y was performed. As expected, ^{125}I -HRP-y also accumulates within the liver (Figure 5b), though to a significantly lower degree than ^{125}I -HRP-MyrB-y, thereby providing a clearer distinction between HRP- and NTCP-mediated effects. Furthermore, ^{125}I -HRP-y alone exhibits a significantly higher accumulation in the kidneys, suggestive of a slightly elevated renal clearance. The reduced kidney association of protein–peptide conjugates is presumably due to the higher molecular weight and change in surface charge lowering glomerular filtration.⁶¹

The non-NTCP mediated association of the present protein–peptide conjugates observed in zebrafish embryos (Figure 4) seems to also be relevant in mice, considering that the greater part of the liver association was not due to NTCP-interaction (Figure 5). The injection of HRP-MyrB-Rho in

zebrafish embryos revealed vascular scavenging (Figure S6a), which is in part stabilin-mediated (Figure S6a). Orthologues to *stabilin 1* and *stabilin 2* are selectively expressed in mammalian liver sinusoidal EC.⁵⁸ However, since the scavenging is not fully eliminated by dextran sulfate blockage in zebrafish embryos, additional interactions are likely pertinent in precluding target receptor association in this setup. Such interactions may be mediated by the strong glycosylation profile of HRP, accounting for approximately 18–22% of the protein's molecular weight,^{62,63} which may be recognized by Kupffer cells and liver sinusoidal EC.^{64,65}

The biodistribution analysis of the present protein–peptide conjugates revealed a strong liver-accumulation, mediated by NTCP-specific targeting as well as unspecific off-target interactions. Observations made in zebrafish embryos provided a mechanistic insight and were instrumental for interpreting findings in the mouse, i.e., a higher vertebrate species. By this approach, qualitative as well as quantitative results were combined to study the targeting capability of novel protein and peptide drug carriers.

CONCLUSIONS

In the present study, the feasibility of extending the functionality of the lipopeptide MyrB as a targeting ligand for hepatocyte-specific enzyme delivery was explored. Linkage of MyrB with distinct modifications to the enzyme HRP yielded HRP-MyrB and was followed by a detailed analytical characterization. By coupling the enzyme HRP to MyrB, successful NTCP-targeting was demonstrated *in vitro*, indicating that the peptide's targeting specificity was well maintained. Upon exposure of fluorescently labeled HRP-MyrB to NTCP expressing cells, a distinct cell membrane-specific staining was observed, typical for the interaction of MyrB with NTCP expressing cells. In addition, specific delivery of enzymatic activity to target cells was demonstrated, which was effectively blocked by adding free MyrB. The *in vitro* targeting specificity may ultimately enable straightforward quantitation of NTCP expression as an immunoassay reagent for improved hepatocellular carcinoma biomarker analysis. A detailed characterization with patient tumor biopsies and matched control tissues will be required to explore the feasibility of this approach.

With respect to a potential *in vivo* use of our enzyme-peptide conjugates, significant scavenging of HRP-MyrB precluded exclusive target recognition *in vivo*. Indeed, biodistribution analysis in mice revealed that liver accumulation was only in part NTCP-mediated. Experiments in transgenic zebrafish embryos suggest that interactions between HRP-MyrB and stabilin receptors expressed in mammalian liver sinusoidal EC play an important role. Several potential strategies could be employed to further improve target recognition. First, HRP can be replaced by an alternative therapeutic protein with favorable PK properties. Second, the enzyme may be sterically stabilized by covalent coupling of polyethylene glycol (PEG).⁶⁶ Third, enzymes could be encapsulated within nano-^{53,67} or microcarriers.⁶⁸ The screening and evaluation strategies presented in this work can then be applied to the characterization and optimization of such alternative protein–peptide conjugates and to design strategies for therapeutic applications.

ASSOCIATED CONTENT

Supporting Information

The Supporting Information is available free of charge at <https://pubs.acs.org/doi/10.1021/acs.molpharmaceut.0c01222>.

Transfection of HEK293 cells and *in vitro* imaging; circulation of HRP-MyrB-Rho in transgenic zebrafish embryos; effective coupling of MyrBC and alaMyrBC to HRP-mal; enzymatic activity of HRP conjugates measured after peptide linkage; interaction of HRP-alaMyrB with HepG2 hNTCP; regression analysis of HRP-MyrB activity measurements when exposed to HepG2 hNTCP cells; specific binding of HRP-MyrB to HEK293 cells genetically engineered to express hNTCP; examining mechanisms underlying scavenging of HRP-MyrB (PDF)

AUTHOR INFORMATION

Corresponding Author

Jörg Huwyler – Department of Pharmaceutical Sciences, University of Basel, Basel 4056, Switzerland; orcid.org/0000-0003-1748-5676; Email: joerg.huwyler@unibas.ch

Authors

Anna Pratsinis – Department of Pharmaceutical Sciences, University of Basel, Basel 4056, Switzerland

Philipp Uhl – Department of Nuclear Medicine, Heidelberg University Hospital, Heidelberg 69120, Germany; orcid.org/0000-0002-8616-5599

Jan Stephan Bolten – Department of Pharmaceutical Sciences, University of Basel, Basel 4056, Switzerland

Patrick Hauswirth – Department of Pharmaceutical Sciences, University of Basel, Basel 4056, Switzerland

Susanne Heidi Schenk – Department of Pharmaceutical Sciences, University of Basel, Basel 4056, Switzerland

Stephan Urban – Department of Infectious Diseases, Heidelberg University Hospital, Heidelberg 69120, Germany

Walter Mier – Department of Nuclear Medicine, Heidelberg University Hospital, Heidelberg 69120, Germany;

orcid.org/0000-0002-3901-5061

Dominik Witzigmann – Department of Biochemistry and Molecular Biology and NanoMedicines Innovation Network (NMN), University of British Columbia, Vancouver, British Columbia V6T 1Z3, Canada; orcid.org/0000-0002-8197-8558

Complete contact information is available at:

<https://pubs.acs.org/doi/10.1021/acs.molpharmaceut.0c01222>

Notes

The authors declare no competing financial interest.

ACKNOWLEDGMENTS

This work was financially supported by the Swiss National Science Foundation (SNF, 31003A-165964). D.W. is supported by the SNF (Postdoc Mobility Fellowship, grant no. 183923). The authors thank Dr. Alexia Ferrand and Dr. Kai Schleicher from the Biozentrum Imaging facility for support with confocal microscopy and Karin Leotta, Heidelberg University Hospital, for her excellent support with the mice experiments. Prof. Dr. Markus Affolter and Dr. Heinz Georg Belting are acknowledged for providing support for zebrafish experiments.

REFERENCES

- (1) Labrou, N. *Therapeutic Enzymes: Function and Clinical Implications*; Springer Nature, 2019.
- (2) Liu, X.; Zhang, Z.; Zhang, Y.; Guan, Y.; Liu, Z.; Ren, J.; Qu, X. Artificial Metalloenzyme-Based Enzyme Replacement Therapy for the Treatment of Hyperuricemia. *Adv. Funct. Mater.* **2016**, *26* (43), 7921–7928.
- (3) Platt, F. M. Emptying the Stores: Lysosomal Diseases and Therapeutic Strategies. *Nat. Rev. Drug Discovery* **2018**, *17* (2), 133–150.
- (4) Liu, Y.; Du, J.; Yan, M.; Lau, M. Y.; Hu, J.; Han, H.; Yang, O. O.; Liang, S.; Wei, W.; Wang, H.; Li, J.; Zhu, X.; Shi, L.; Chen, W.; Ji, C.; Lu, Y. Biomimetic Enzyme Nanocomplexes and Their Use as Antidotes and Preventive Measures for Alcohol Intoxication. *Nat. Nanotechnol.* **2013**, *8* (3), 187–192.
- (5) Pratsinis, A.; Zuercher, S.; Forster, V.; Fischer, E. J.; Luciani, P.; Leroux, J.-C. Liposome-Supported Enzymatic Peritoneal Dialysis. *Biomaterials* **2017**, *145*, 128–137.
- (6) Wei, W.; Du, J.; Li, J.; Yan, M.; Zhu, Q.; Jin, X.; Zhu, X.; Hu, Z.; Tang, Y.; Lu, Y. Construction of Robust Enzyme Nanocapsules for Effective Organophosphate Decontamination, Detoxification, and Protection. *Adv. Mater. (Weinheim, Ger.)* **2013**, *25* (15), 2212–2218.
- (7) Fang, L.; Chow, K. M.; Hou, S.; Xue, L.; Chen, X.; Rodgers, D. W.; Zheng, F.; Zhan, C.-G. Rational Design, Preparation, and Characterization of a Therapeutic Enzyme Mutant with Improved Stability and Function for Cocaine Detoxification. *ACS Chem. Biol.* **2014**, *9* (8), 1764–1772.
- (8) Beckett, A.; Gervais, D. What Makes a Good New Therapeutic L-Asparaginase? *World J. Microbiol. Biotechnol.* **2019**, *35* (10), 152.
- (9) Zou, S.; Wang, X.; Liu, P.; Ke, C.; Xu, S. Arginine Metabolism and Deprivation in Cancer Therapy. *Biomed. Pharmacother.* **2019**, *118*, 109210.
- (10) Kratz, F.; Müller, I. A.; Rypka, C.; Warnecke, A. Prodrug Strategies in Anticancer Chemotherapy. *ChemMedChem* **2008**, *3* (1), 20–53.
- (11) Liu, M.; Johansen, P.; Zabel, F.; Leroux, J.-C.; Gauthier, M. A. Semi-Permeable Coatings Fabricated from Comb-Polymers Efficiently Protect Proteins in Vivo. *Nat. Commun.* **2014**, *5* (1), 1–8.
- (12) Sharma, S. K.; Bagshawe, K. D. Antibody Directed Enzyme Prodrug Therapy (ADEPT): Trials and Tribulations. *Adv. Drug Delivery Rev.* **2017**, *118*, 2–7.
- (13) Senter, P. D.; Wallace, P. M.; Svensson, H. P.; Vrudehula, V. M.; Kerr, D. E.; Hellstroem, I.; Hellstroem, K. E. Generation of Cytotoxic Agents by Targeted Enzymes. *Bioconjugate Chem.* **1993**, *4* (1), 3–9.
- (14) Allen, T. M. Ligand-Targeted Therapeutics in Anticancer Therapy. *Nat. Rev. Cancer* **2002**, *2* (10), 750–763.
- (15) Cheng, T.-L.; Wu, P.-Y.; Wu, M.-F.; Chern, J.-W.; Roffler, S. R. Accelerated Clearance of Polyethylene Glycol-Modified Proteins by Anti-Polyethylene Glycol IgM. *Bioconjugate Chem.* **1999**, *10* (3), 520–528.
- (16) Lieser, R. M.; Chen, W.; Sullivan, M. O. Controlled Epidermal Growth Factor Receptor Ligand Display on Cancer Suicide Enzymes via Unnatural Amino Acid Engineering for Enhanced Intracellular Delivery in Breast Cancer Cells. *Bioconjugate Chem.* **2019**, *30* (2), 432–442.
- (17) Ulbrich, K.; Holá, K.; Šubr, V.; Bakandritsos, A.; Tuček, J.; Zbořil, R. Targeted Drug Delivery by Polymers and Magnetic Nanoparticles: Covalent and Noncovalent Approaches, Release Control, and Clinical Studies. *Chem. Rev.* **2016**, *116* (9), 5338–5431.
- (18) Bernardes, G. J. L.; Casi, G.; Trüssel, S.; Hartmann, I.; Schwager, K.; Scheuermann, J.; Neri, D. A Traceless Vascular-Targeting Antibody-Drug Conjugate for Cancer Therapy. *Angew. Chem., Int. Ed.* **2012**, *51* (4), 941–944.
- (19) Cazzamalli, S.; Ziffels, B.; Widmayer, F.; Murer, P.; Pellegrini, G.; Pretto, F.; Wulhfard, S.; Neri, D. Enhanced Therapeutic Activity of Non-Internalizing Small-Molecule-Drug Conjugates Targeting Carbonic Anhydrase IX in Combination with Targeted Interleukin-2. *Clin. Cancer Res.* **2018**, *24* (15), 3656–3667.
- (20) Rossin, R.; Versteegen, R. M.; Wu, J.; Khasanov, A.; Wessels, H. J.; Steenberg, E. J.; Hoeve, W. T.; Janssen, H. M.; Onzen, A. H. A. M.; van Hudson, P. J.; Robillard, M. S. Chemically Triggered Drug Release from an Antibody-Drug Conjugate Leads to Potent Antitumour Activity in Mice. *Nat. Commun.* **2018**, *9* (1), 1–11.
- (21) Dal Corso, A.; Cazzamalli, S.; Neri, D.; Damelin, M. Antibody-Drug Conjugates: Targeting the Tumor Microenvironment. *Innovations for Next-Generation Antibody-Drug Conjugates* **2018**, 299–319.
- (22) Yan, H.; Zhong, G.; Xu, G.; He, W.; Jing, Z.; Gao, Z.; Huang, Y.; Qi, Y.; Peng, B.; Wang, H.; Fu, L.; Song, M.; Chen, P.; Gao, W.; Ren, B.; Sun, Y.; Cai, T.; Feng, X.; Sui, J.; Li, W. Sodium Taurocholate Cotransporting Polypeptide Is a Functional Receptor for Human Hepatitis B and D Virus. *eLife* **2012**, *1*, 1.
- (23) Slijepcevic, D.; Kaufman, C.; Wichers, C. G. K.; Gilgioni, E. H.; Lempp, F. A.; Duijst, S.; Waart, D. R.; de Elferink, R. P. J. O.; Mier, W.; Stieger, B.; Beuers, U.; Urban, S.; van de Graaf, S. F. J. Impaired Uptake of Conjugated Bile Acids and Hepatitis b Virus PreS1-Binding in Na⁺-Taurocholate Cotransporting Polypeptide Knockout Mice. *Hepatology* **2015**, *62* (1), 207–219.
- (24) Meier, A.; Mehrle, S.; Weiss, T. S.; Mier, W.; Urban, S. Myristoylated PreS1-Domain of the Hepatitis B Virus L-Protein Mediates Specific Binding to Differentiated Hepatocytes. *Hepatology* **2013**, *58* (1), 31–42.
- (25) Schieck, A.; Schulze, A.; Gähler, C.; Müller, T.; Haberkorn, U.; Alexandrov, A.; Urban, S.; Mier, W. Hepatitis B Virus Hepatotropism Is Mediated by Specific Receptor Recognition in the Liver and Not Restricted to Susceptible Hosts. *Hepatology* **2013**, *58* (1), 43–53.
- (26) Blank, A.; Markert, C.; Hohmann, N.; Carls, A.; Mikus, G.; Lehr, T.; Alexandrov, A.; Haag, M.; Schwab, M.; Urban, S.; Haefeli, W. E. First-in-Human Application of the Novel Hepatitis B and Hepatitis D Virus Entry Inhibitor Myrcludex B. *J. Hepatol.* **2016**, *65* (3), 483–489.
- (27) Bogomolov, P.; Alexandrov, A.; Voronkova, N.; Macievich, M.; Kokina, K.; Petrachenkova, M.; Lehr, T.; Lempp, F. A.; Wedemeyer, H.; Haag, M.; Schwab, M.; Haefeli, W. E.; Blank, A.; Urban, S. Treatment of Chronic Hepatitis D with the Entry Inhibitor Myrcludex B: First Results of a Phase Ib/IIa Study. *J. Hepatol.* **2016**, *65* (3), 490–498.
- (28) Zhang, Q.; Zhang, X.; Chen, T.; Wang, X.; Fu, Y.; Jin, Y.; Sun, X.; Gong, T.; Zhang, Z. A Safe and Efficient Hepatocyte-Selective Carrier System Based on Myristoylated PreS1/21–47 Domain of Hepatitis B Virus. *Nanoscale* **2015**, *7* (20), 9298–9310.
- (29) Zhang, X.; Zhang, Q.; Peng, Q.; Zhou, J.; Liao, L.; Sun, X.; Zhang, L.; Gong, T. Hepatitis B Virus PreS1-Derived Lipopeptide Functionalized Liposomes for Targeting of Hepatic Cells. *Biomaterials* **2014**, *35* (23), 6130–6141.
- (30) Liu, Q.; Somya, M.; Iijima, M.; Tatematsu, K.; Kuroda, S. A Hepatitis B Virus-Derived Human Hepatic Cell-Specific Heparin-Binding Peptide: Identification and Application to a Drug Delivery System. *Biomater. Sci.* **2019**, *7* (1), 322–335.
- (31) Witzigmann, D.; Uhl, P.; Sieber, S.; Kaufman, C.; Einfalt, T.; Schöneweis, K.; Grossen, P.; Buck, J.; Ni, Y.; Schenk, S. H.; Hussner, J.; Meyer zu Schwabedissen, H. E.; Québatte, G.; Mier, W.; Urban, S.; Huwyler, J. Optimization-by-Design of Hepatotropic Lipid Nanoparticles Targeting the Sodium-Taurocholate Cotransporting Polypeptide. *eLife* **2019**, *8*, No. e42276.
- (32) Gripon, P.; Cannie, I.; Urban, S. Efficient Inhibition of Hepatitis B Virus Infection by Acylated Peptides Derived from the Large Viral Surface Protein. *J. Virol.* **2005**, *79* (3), 1613–1622.
- (33) Greco, O.; Folkes, L. K.; Wardman, P.; Tozer, G. M.; Dachs, G. U. Development of a Novel Enzyme/Prodrug Combination for Gene Therapy of Cancer: Horseradish Peroxidase/Indole-3-Acetic Acid. *Cancer Gene Ther.* **2000**, *7* (11), 1414–1420.
- (34) Folkes, L. K.; Wardman, P. Oxidative Activation of Indole-3-Acetic Acids to Cytotoxic Species— a Potential New Role for Plant Auxins in Cancer Therapy. *Biochem. Pharmacol.* **2001**, *61* (2), 129–136.
- (35) Ni, Y.; Lempp, F. A.; Mehrle, S.; Nkongolo, S.; Kaufman, C.; Fälth, M.; Stindt, J.; König, C.; Nassal, M.; Kubitz, R.; Sültmann, H.

- Urban, S. Hepatitis B and D Viruses Exploit Sodium Taurocholate Co-Transporting Polypeptide for Species-Specific Entry into Hepatocytes. *Gastroenterology* **2014**, *146* (4), 1070–1083.
- (36) Sieber, S.; Grossen, P.; Detampel, P.; Siegfried, S.; Witzigmann, D.; Huwyler, J. Zebrafish as an Early Stage Screening Tool to Study the Systemic Circulation of Nanoparticulate Drug Delivery Systems in Vivo. *J. Controlled Release* **2017**, *264*, 180–191.
- (37) Sieber, S.; Grossen, P.; Uhl, P.; Detampel, P.; Mier, W.; Witzigmann, D.; Huwyler, J. Zebrafish as a Predictive Screening Model to Assess Macrophage Clearance of Liposomes in Vivo. *Nanomedicine* **2019**, *17*, 82–93.
- (38) Sieber, S.; Grossen, P.; Bussmann, J.; Campbell, F.; Kros, A.; Witzigmann, D.; Huwyler, J. Zebrafish as a Preclinical in Vivo Screening Model for Nanomedicines. *Adv. Drug Delivery Rev.* **2019**, *151–152*, 152.
- (39) Kantae, V.; Krekels, E. H. J.; Ordas, A.; González, O.; van Wijk, R. C.; Harms, A. C.; Racz, P. I.; van der Graaf, P. H.; Spaink, H. P.; Hankemeier, T. Pharmacokinetic Modeling of Paracetamol Uptake and Clearance in Zebrafish Larvae: Expanding the Allometric Scale in Vertebrates with Five Orders of Magnitude. *Zebrafish* **2016**, *13* (6), 504–510.
- (40) Schulze, A.; Schieck, A.; Ni, Y.; Mier, W.; Urban, S. Fine Mapping of Pre-S Sequence Requirements for Hepatitis B Virus Large Envelope Protein-Mediated Receptor Interaction. *J. Virol.* **2010**, *84* (4), 1989–2000.
- (41) Laemmli, U. K. Cleavage of Structural Proteins during the Assembly of the Head of Bacteriophage T4. *Nature* **1970**, *227* (5259), 680–685.
- (42) Witzigmann, D.; Wu, D.; Schenk, S. H.; Balasubramanian, V.; Meier, W.; Huwyler, J. Biocompatible Polymer-Peptide Hybrid-Based DNA Nanoparticles for Gene Delivery. *ACS Appl. Mater. Interfaces* **2015**, *7* (19), 10446–10456.
- (43) Bolte, S.; Cordelières, F. P. A Guided Tour into Subcellular Colocalization Analysis in Light Microscopy. *J. Microsc.* **2006**, *224* (3), 213–232.
- (44) Uhl, P.; Helm, F.; Hofhaus, G.; Brings, S.; Kaufman, C.; Leotta, K.; Urban, S.; Haberkorn, U.; Mier, W.; Fricker, G. A Liposomal Formulation for the Oral Application of the Investigational Hepatitis B Drug Myrcludex B. *Eur. J. Pharm. Biopharm.* **2016**, *103*, 159–166.
- (45) Mühlfeld, A. S.; Segerer, S.; Hudkins, K.; Carling, M. D.; Wen, M.; Farr, A. G.; Ravetch, J. V.; Alpers, C. E. Deletion of the Fcγ Receptor IIb in Thymic Stromal Lymphopoietin Transgenic Mice Aggravates Membranoproliferative Glomerulonephritis. *Am. J. Pathol.* **2003**, *163* (3), 1127–1136.
- (46) Müller, T.; Mehrle, S.; Schieck, A.; Haberkorn, U.; Urban, S.; Mier, W. Liver Imaging with a Novel Hepatitis B Surface Protein Derived SPECT-Tracer. *Mol. Pharmaceutics* **2013**, *10* (6), 2230–2236.
- (47) Engelke, M.; Mills, K.; Seitz, S.; Simon, P.; Gripon, P.; Schnölzer, M.; Urban, S. Characterization of a Hepatitis B and Hepatitis Delta Virus Receptor Binding Site. *Hepatology* **2006**, *43* (4), 750–760.
- (48) Hnasko, R. M.; Hnasko, R. Bioconjugation of Antibodies to Horseradish Peroxidase (HRP). *Methods Mol. Biol.* **2015**, *1318*, 43–50.
- (49) Lane, S. M.; Kuang, Z.; Yom, J.; Arifuzzaman, S.; Genzer, J.; Farmer, B.; Naik, R.; Vaia, R. A. Poly(2-Hydroxyethyl Methacrylate) for Enzyme Immobilization: Impact on Activity and Stability of Horseradish Peroxidase. *Biomacromolecules* **2011**, *12* (5), 1822–1830.
- (50) Ahlgren, S.; Orlova, A.; Rosik, D.; Sandström, M.; Sjöberg, A.; Baastrup, B.; Widmark, O.; Fant, G.; Feldwisch, J.; Tolmachev, V. Evaluation of Maleimide Derivative of DOTA for Site-Specific Labeling of Recombinant Affibody Molecules. *Bioconjugate Chem.* **2008**, *19* (1), 235–243.
- (51) Kim, Y.; Ho, S. O.; Gassman, N. R.; Korlann, Y.; Landorf, E. V.; Collart, F. R.; Weiss, S. Efficient Site-Specific Labeling of Proteins via Cysteines. *Bioconjugate Chem.* **2008**, *19* (3), 786–791.
- (52) Wakankar, A.; Chen, Y.; Gokarn, Y.; Jacobson, F. S. Analytical Methods for Physicochemical Characterization of Antibody Drug Conjugates. *mAbs* **2011**, *3* (2), 161–172.
- (53) Einfalt, T.; Witzigmann, D.; Edlinger, C.; Sieber, S.; Goers, R.; Najer, A.; Spulber, M.; Onaca-Fischer, O.; Huwyler, J.; Palivan, C. G. Biomimetic Artificial Organelles with in Vitro and in Vivo Activity Triggered by Reduction in Microenvironment. *Nat. Commun.* **2018**, *9* (1), 1–12.
- (54) Mogharrab, N.; Ghourchian, H.; Amininasab, M. Structural Stabilization and Functional Improvement of Horseradish Peroxidase upon Modification of Accessible Lysines: Experiments and Simulation. *Biophys. J.* **2007**, *92* (4), 1192–1203.
- (55) Döring, B.; Lütke, T.; Geyer, J.; Petzinger, E.; Bevenssee, M. O. Chapter Four - The SLC10 Carrier Family: Transport Functions and Molecular Structure. *Curr. Top. Membr.* **2012**, *70*, 105–168.
- (56) Su, S.; Di Poto, C.; Roy, R.; Liu, X.; Cui, W.; Kroemer, A.; Resson, H. W. Highlight Article: Long-Term Culture and Characterization of Patient-Derived Primary Hepatocytes Using Conditional Reprogramming. *Exp. Biol. Med. (London, U. K.)* **2019**, *244* (11), 857–864.
- (57) Kang, J.; Wang, J.; Cheng, J.; Cao, Z.; Chen, R.; Li, H.; Liu, S.; Chen, X.; Sui, J.; Lu, F. Down-Regulation of NTCP Expression by Cyclin D1 in Hepatitis B Virus-Related Hepatocellular Carcinoma Has Clinical Significance. *Oncotarget* **2017**, *8* (34), 56041–56050.
- (58) Campbell, F.; Bos, F. L.; Sieber, S.; Arias-Alpizar, G.; Koch, B. E.; Huwyler, J.; Kros, A.; Bussmann, J. Directing Nanoparticle Biodistribution through Evasion and Exploitation of Stab2-Dependent Nanoparticle Uptake. *ACS Nano* **2018**, *12* (3), 2138–2150.
- (59) Torraca, V.; Masud, S.; Spaink, H. P.; Meijer, A. H. Macrophage-Pathogen Interactions in Infectious Diseases: New Therapeutic Insights from the Zebrafish Host Model. *Dis. Models & Mech.* **2014**, *7* (7), 785–797.
- (60) Yan, H.; Peng, B.; He, W.; Zhong, G.; Qi, Y.; Ren, B.; Gao, Z.; Jing, Z.; Song, M.; Xu, G.; Sui, J.; Li, W. Molecular Determinants of Hepatitis B and D Virus Entry Restriction in Mouse Sodium Taurocholate Cotransporting Polypeptide. *Journal of Virology* **2013**, *87* (14), 7977–7991.
- (61) Venkatachalam, M. A.; Rennke, H. G. The Structural and Molecular Basis of Glomerular Filtration. *Circ. Res.* **1978**, *43* (3), 337–347.
- (62) Veitch, N. C. Horseradish Peroxidase: A Modern View of a Classic Enzyme. *Phytochemistry* **2004**, *65* (3), 249–259.
- (63) Gray, J. S. S.; Yang, B. Y.; Montgomery, R. Heterogeneity of Glycans at Each N-Glycosylation Site of Horseradish Peroxidase. *Carbohydr. Res.* **1998**, *311* (1), 61–69.
- (64) Mahler, H.-C. *Protein Pharmaceutics: Formulation, Analytics and Delivery*; ECV, Editio-Cantor-Verlag, 2010.
- (65) Stahl, P. D. The Mannose Receptor and Other Macrophage Lectins. *Curr. Opin. Immunol.* **1992**, *4* (1), 49–52.
- (66) Taipa, M. A.; Fernandes, P.; de Carvalho, C. C. C. R. Production and Purification of Therapeutic Enzymes. *Adv. Exp. Med. Biol.* **2019**, *1148*, 1–24.
- (67) Gaspar, M. M.; Perez-Soler, R.; Cruz, M. E. M. Biological Characterization of L-Asparaginase Liposomal Formulations. *Cancer Chemother. Pharmacol.* **1996**, *38* (4), 373–377.
- (68) Gay, F.; Agüera, K.; Sénéchal, K.; Tainturier, A.; Berlier, W.; Maucourt-Boulch, D.; Honnorat, J.; Horand, F.; Godfrin, Y.; Bourgeaux, V. Methionine Tumor Starvation by Erythrocyte-Encapsulated Methionine Gamma-Lyase Activity Controlled with per Os Vitamin B6. *Cancer Med.* **2017**, *6* (6), 1437–1452.

3.4.2 Publication 2

Optimized Photoactivatable Lipid Nanoparticles Enable Red Light Triggered Drug Release

Nisha Chander, Johannes Morstein, **Jan S Bolten**, Andrej Shemet, Pieter R Cullis, Dirk Trauner, Dominik Witzigmann

Small. 2021 May;17(21):e2008198.

doi: 10.1002/sml.202008198.

Personal contribution:

My contribution to this research article includes zebrafish larvae experiments to assess pharmacokinetic aspects. I was involved in the design and planning of *in vivo* studies. Thus, I wrote parts of the method, results, and discussion sections and proofread the manuscript.

Optimized Photoactivatable Lipid Nanoparticles Enable Red Light Triggered Drug Release

Nisha Chander, Johannes Morstein, Jan S. Bolten, Andrej Shemet, Pieter R. Cullis,*
Dirk Trauner,* and Dominik Witzigmann*

Encapsulation of small molecule drugs in long-circulating lipid nanoparticles (LNPs) can reduce toxic side effects and enhance accumulation at tumor sites. A fundamental problem, however, is the slow release of encapsulated drugs from these liposomal systems at the disease site resulting in limited therapeutic benefit. Methods to trigger release at specific sites are highly warranted. Here, it is demonstrated that incorporation of ultraviolet (UV-A) or red-light photoswitchable-phosphatidylcholine analogs (AzoPC and redAzoPC) in conventional LNPs generates photoactivatable LNPs (paLNPs) having comparable structural integrity, drug loading capacity, and size distribution to the parent DSPC-cholesterol liposomes. It is shown that 65–70% drug release (doxorubicin) can be induced from these systems by irradiation with pulsed light based on *trans*-to-*cis* azobenzene isomerization. In vitro it is confirmed that paLNPs are non-toxic in the dark but convey cytotoxicity upon irradiation in a human cancer cell line. In vivo studies in zebrafish embryos demonstrate prolonged blood circulation and extravasation of paLNPs comparable to clinically approved formulations, with enhanced drug release following irradiation with pulsed light. Conclusively, paLNPs closely mimic the properties of clinically approved LNPs with the added benefit of light-induced drug release making them promising candidates for clinical development.

1. Introduction

Lipid nanoparticles (LNP) are the leading drug delivery platform in the clinic for systemic applications.^[1–3] Unilamellar LNPs with diameters less than 100 nm are favored for delivery of small molecular drugs. Solid core systems are better suited for delivery of macromolecular genetic drugs, such as siRNA or mRNA.^[4–6] More than 10 LNP therapeutics have been approved by the US FDA and other regulatory agencies. Most of these are liposomes containing anticancer drugs that exhibit reduced toxicity and enhanced efficacy compared to the free drug.^[4,7–9]

Robust techniques exist for achieving efficient drug encapsulation in <100 nm diameter liposomal systems that exhibit long half-lives in the circulation (up to 24 h in humans) and preferential accumulation at tumor sites following intravenous injection.^[9–11] However, a major limitation is that they do not selectively leak their contents after arrival at the target site. This severely limits the improvement in therapeutic index that can be gained by liposomal delivery.^[1,10] Technologies that


trigger release of liposomal contents either at or near the target site would have significant benefits. This is particularly true given that liposomes containing cancer drugs can exhibit maximum tolerated doses that are up to five times higher than those of free drug and thus are systemically much less toxic.^[10–12]

There have been many attempts to develop triggered release systems for liposomal systems containing anticancer drugs.^[13] To this end, thermosensitive lipids or metallic nanoparticles (such as or gold nanoparticles or iron oxide nanoparticles) tethered to the liposome have been employed.^[14–16] These systems give rise to liposomes that leak contents in response to local heating or irradiation. Many systems, however, are quite complex, limiting their manufacturing scalability or require the development of a specific device to trigger release. In addition, several reported systems exhibit poor drug loading/retention and relatively short circulation lifetimes resulting in off-target release and reduced ability to access the desired target tissues.^[13,17] As a result, only one triggered release technology has progressed to late stage clinical trials to date: ThermoDox—a liposomal doxorubicin (Dox) formulation for the treatment of

N. Chander, Dr. P. R. Cullis, Dr. D. Witzigmann
Department of Biochemistry and Molecular Biology
University of British Columbia
2350 Health Sciences Mall, Vancouver, BC V6T 1Z3, Canada
E-mail: pieterc@mail.ubc.ca; dominik.witzigmann@ubc.ca

J. Morstein, Dr. A. Shemet, Dr. D. Trauner
Department of Chemistry
New York University
100 Washington Square East, Room 712, New York, NY 10003, USA
E-mail: dirktrauner@nyu.edu

J. S. Bolten
Department of Pharmaceutical Technology
University of Basel
Klingelbergstrasse 50, Basel 4056, Switzerland
Dr. P. R. Cullis, Dr. D. Witzigmann
NanoMedicines Innovation Network (NMIN)
University of British Columbia
2350 Health Sciences Mall, Room 5451, Vancouver, BC V6T 1Z3, Canada

 The ORCID identification number(s) for the author(s) of this article can be found under <https://doi.org/10.1002/smll.202008198>.

DOI: 10.1002/smll.202008198

inoperable hepatocellular carcinoma, where drug release is stimulated by a mild hyper-thermic trigger.^[17,18] The lipid composition of ThermoDox is significantly different as compared to the approved Doxil formulation to ensure a relatively sharp transition temperature. However, this resulted in a formulation with different pharmacokinetics and a relatively short circulation lifetime.^[19,20] Despite more than 30 years of efforts, the only triggered release system (in response to local heating) that had made it into the clinic failed in phase III.^[20,21]

Alternative attempts to develop approaches for light-triggered drug release from liposomal targets have not progressed to a clinical setting due to inefficient drug encapsulation and release, lack of straightforward and scalable methods of manufacture, and difficulty in selecting the clinical entry point.^[22,23] In addition, there is a range of competitive technologies including simple and effective device-only ablative methods such as microwave and radiofrequency ablation, as well as surgery and radiotherapy. The implementation of light-triggered drug release systems, however, could benefit from approved phototherapies and photodynamic therapies (PDT) as well as emerging technologies to deliver light deep within patients.^[24,25]

Ideally, new systems for light-triggered release should closely mimic the composition and properties of clinically approved LNPs in terms of composition, size, loading, and stability. The approved systems Doxil, Ambisome, and Marqibo, all use saturated lipids that contain choline headgroups at approximately equimolar levels with cholesterol as the primary lipid constituents.^[9,18] Such phosphatidylcholine lipid-cholesterol compositions can be readily formulated into liposomal systems with diameters <100 nm that can be efficiently loaded with weakly basic drugs, such as Dox, and display long circulation lifetimes following i.v. administration. With the constantly evolving field of photo pharmacology, approaches to include photosensitizers like porphyrin into stealth liposomes have helped advance the light-triggered drug release concept to have more clinical

translatability. These types of systems take advantage of the well-established field of PDT.^[26,27] The investigation of non-porphyrin based photosensitizers as novel PDT agents has been considerably less extensive than porphyrin-based compounds.

Here, we report a liposomal light-triggered release system containing photoswitchable phosphatidylcholine analogs with azobenzenes incorporated into the lipid tail, compounds termed AzoPC and red-AzoPC.^[28,29] This strategy enables the design of an exterior lipid composition that allows long circulation lifetimes, incorporation of an agent responsive to light, and an aqueous interior offering small molecule drugs to be encapsulated. We show that DSPC-cholesterol systems incorporating AzoPC (in the trans-form) at low (10 mol%) levels result in liposomes that have similar size and drug (Dox) loading properties as parent LNPs. When stimulated to adopt the cis-form, the AzoPC containing liposomes exhibit triggered release properties resulting in enhanced cytotoxic effects *in vitro*. The responsiveness of photoactivatable LNPs (paLNPs) to a different wavelength is easily tuned by substituting AzoPC with a red-shifted variant red-AzoPC. *In vivo* studies confirmed long blood circulation half-lives and triggered release properties of paLNP system. This proof-of-concept study demonstrates the potential therapeutic utility of liposomal systems containing AzoPC.

2. Results and Discussion

2.1. Design of Dox-Loaded paLNP Liposomes

In order to design a light-triggered release system enabling efficient drug loading and long-circulation properties, we first modified conventional DSPC-cholesterol liposomes (55 mol% DSPC, 45 mol% Chol) by incorporating a UV-A photo-switchable AzoPC (Figure 1A).^[22] The use of such azobenzene photoswitches in biology and medicine is well established.^[23,30]

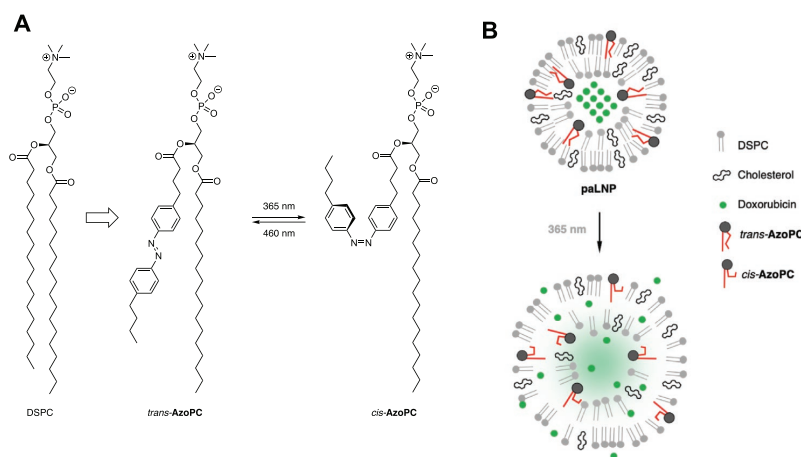


Figure 1. Design of a light-triggered drug release system. A) Chemical structure of DSPC and its photoswitchable analog AzoPC. The azobenzene can be isomerized from the trans to the cis form at 365 nm. B) Schematic for light induced drug release from paLNPs. Low levels of trans AzoPC are incorporated in a DSPC-cholesterol liposomal system loaded with Dox. Photoisomerization of AzoPC induces drug release.

Stimulation of paLNPs at 365 nm should trigger trans to cis isomerization resulting in Dox release (Figure 1B).

2.2. Synthesis and Characterization of Dox-Loaded paLNP Liposomes

DSPC-cholesterol liposomes were prepared employing ethanol dilution-rapid mixing techniques and subsequent dialysis steps to contain 300 mM ammonium sulphate in their aqueous core and phosphate buffered saline (PBS) as an exterior buffer and were used as control formulations (control-LNP). A range of paLNP liposomes were synthesized by titrating varying amounts of AzoPC (2.5, 5, 10, 15, 20, 30 mol%) into the control DSPC-cholesterol liposomes where the added AzoPC substituted for DSPC. Dynamic light scattering (DLS) analysis of the particles showed a monodisperse population (PDI <0.1) of uniformly sized ≈ 55 –60 nm particles (Table 1). The trans to cis photoswitching kinetics of AzoPC incorporated into paLNPs was comparable to that observed in the stock ethanol solution as observed by measuring absorbance at 340 nm at 30 s intervals ($\lambda = 365$ nm) (Figure 2A).

The LNP formulations were loaded with Dox using the pH gradient (interior acidic) generated by encapsulated ammonium sulphate. The LNP were incubated at 65 °C for 30 min with free drug to achieve a maximum encapsulated drug:lipid ratio (wt/wt) of 0.1 after which untrapped Dox was removed via dialysis. Drug:lipid ratios were assayed for samples taken before and after drug loading and used to calculate percent entrapment. Efficient loading was achieved for liposomes containing up to 10% Azo-PC. Formulations containing higher mol% of AzoPC (15–30 mol%) were unable to maintain the ammonium sulphate gradient effectively, which resulted in lower drug loading (Figure 2B). The dependence of drug loading efficiency on the ammonium sulphate gradient in the paLNP system was confirmed by switching the AzoPC conformation to the cis form prior to drug loading which resulted in a significant reduction in entrapment efficiency in cis-paLNPs ($\approx 20\%$ entrapment) as compared to trans-paLNPs ($\approx 100\%$ entrapment) (Figure 2C,D). The control LNP did not show any change in encapsulation efficiency upon irradiation (Figure 2E).

Table 1. Physicochemical characterization of LNPs. Hydrodynamic diameter and size distribution (PDI) of control-LNP (DSPC-Chol system) and paLNPs containing various amounts of AzoPC.

Lipid composition	Mean diameter \pm SD [nm]	PDI
Control-LNP	52.83 \pm 2.588	0.038
AzoPC 2.5%	55.49 \pm 0.732	0.064
AzoPC 5%	56.33 \pm 1.811	0.083
AzoPC 10%	57.89 \pm 1.150	0.072
AzoPC 15%	59.20 \pm 1.689	0.097
AzoPC 20%	59.86 \pm 4.118	0.105
AzoPC 30%	63.44 \pm 2.988	0.101

2.3. Liposomes containing 10 mol% AzoPC Exhibit up to 80% Light-Triggered Release of Dox when AzoPC is Switched to the cis Form

Drug release from paLNPs following irradiation was measured in PBS at room temperature. paLNPs loaded with Dox at a drug:lipid ratio of 0.1 (wt/wt) and a concentration of 3 mg mL⁻¹ total lipid were irradiated with the UV-A light source (365 nm) for 5 min followed by storage in the dark for 1 h. Samples were assayed for drug release by measuring absorbance at 492 nm. Limited release was observed in paLNPs containing 2.5–5 mol% AzoPC while paLNPs containing 10–30 mol% AzoPC showed up to 20% drug release at the 1 h timepoint (Figure 3A). paLNP containing 10% AzoPC in the trans form showed drug loading and drug release properties that were similar to the control LNP system (DSPC-cholesterol), whereas paLNP systems with higher trans AzoPC contents exhibited decreased drug loading capabilities that may be attributed to increased permeability of the liposome bilayer. We therefore chose to move forward with the paLNP systems containing 10 mol% AzoPC for subsequent experiments.

Initial work was performed to determine whether triggered release could be achieved in response to irradiation to switch the azo-PC from the trans to the cis form. It was found that significant triggered release of up to 40% could be achieved for paLNP containing 10 mol% Azo-PC following 5 min irradiation at 365 nm at room temperature when the paLNP were suspended in PBS (Figure 3B). We next tested whether light triggered release was influenced by the presence of serum proteins. It is well known that serum proteins adsorb to liposomal surfaces forming a protein corona that can influence membrane permeability and other properties such as accessibility of light to membrane surface.^[31,32] We therefore evaluated light-triggered release from paLNPs containing 10 mol% AzoPC following dilution into cell culture medium (DMEM) containing serum (10% fetal bovine serum, FBS). It was found that the presence of serum proteins inhibited light-triggered drug release significantly compared to paLNP in PBS. After an initial irradiation time of 5 min at 365 nm followed by storage in the dark, $\approx 25\%$ of Dox was released after a 24 h time period as compared to 40% of Dox released in PBS (Figure 3B).

Of note, AzoPC in the cis form will spontaneously revert to its trans form over time, potentially reducing leakage from the irradiated paLNP. We therefore investigated whether the amount of drug release could be increased through pulsed irradiation following the 5 min initial irradiation to prevent re-isomerization keeping the AzoPC in its cis form for a longer period of time. The paLNP were subjected to pulses of LED light (wavelength 365 nm) of 75 ms duration every 15 s over a 24 h period (Figure 4A,B). We found that this pulsed irradiation protocol led to increased drug release within 24 h compared with initial irradiation. This result could be explained by thermal relaxation and repeated switching over time. While constant irradiation over the same time frame could potentially produce a similar effect in terms of release, the pulsed method allows for successful switching and maintenance of the AzoPC in cis conformation at >100 times less irradiation time, preventing any side effects associated with prolonged exposure to

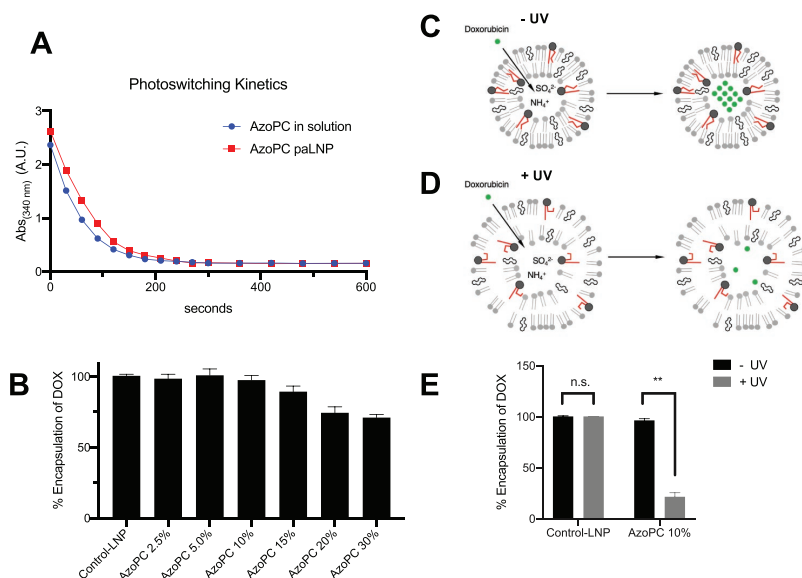


Figure 2. Substitution of up to 10 mol% trans AzoPC for DSPC in DSPC-cholesterol liposomes allows for efficient loading of Dox. A) AzoPC photo-switching kinetics in paLNPs versus free dissolved AzoPC. Samples at 3 mg mL^{-1} AzoPC concentration were used for absorbance measurements. B) Dox entrapment efficiency of paLNP formulations with increasing amounts of AzoPC. C) Schematic for remote loading of Dox into paLNPs incorporating AzoPC in the trans form. paLNPs containing 300 mM ammonium sulphate in the aqueous core and suspended in PBS were mixed with Dox at a drug to lipid (wt/wt) ratio of 0.1. The mixture was heated in a water bath at 65°C for 30 min, following removal of untrapped Dox via dialysis. D) Schematic for remote loading of Dox into paLNPs with AzoPC in the cis form. paLNPs were subject to UV irradiating at 365 nm for 5 min, following the same drug loading procedure as above. E) Comparison of Dox loading efficiency in paLNP formulations containing 10% AzoPC before and after photoswitching via irradiation with UV-A light (365 nm). Error bars represent SEM $**p < 0.01$, n.s., not significant, Student's *t*-test.

UV-A light such as increase in temperature of irradiated area or cytotoxicity.

Correspondingly, the *in vitro* drug release experiments were repeated on paLNP in PBS and DMEM, where the initial irradiation time of 5 min was followed by pulsed irradiation. This pulsed irradiation enabled significantly improved drug release of 75–80% from paLNPs in PBS (Figure 4C) and 65–70% from paLNPs in serum containing medium (DMEM with 10% FBS) (Figure 4D). The control LNP demonstrated a relatively low Dox

release and did not show any change in drug release on irradiation (Figure 4C,D).

2.4. The Morphology of Doxorubicin-Loaded Liposomes Containing AzoPC Following Pulsed Irradiation is Consistent with Drug Release

Liposomes loaded with Dox employing pH loading techniques exhibit characteristic “coffee bean” morphology as detected by

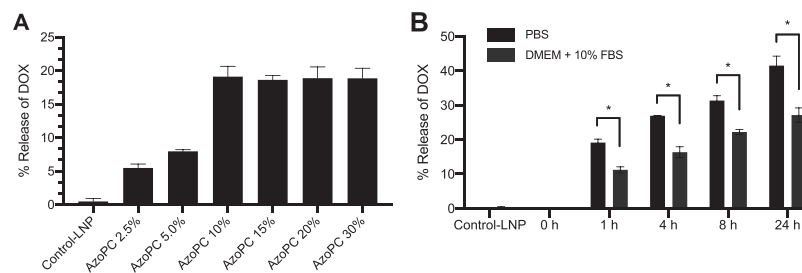


Figure 3. Presence of serum proteins significantly inhibited drug release from paLNP compared to paLNP in PBS. A) paLNP particles containing a substitution of 10–30 mol% trans AzoPC for DSPC in control DSPC-cholesterol liposomes suspended in PBS were irradiated with a UV-A light source (365 nm) for 5 min followed by storage in the dark at room temperature for 1 h. Samples were assayed for drug release (Dox by measuring absorbance at 492 nm). B) paLNP particles containing 10 mol% AzoPC suspended in PBS or DMEM media containing 10% FBS were irradiated with a UV-A light source (365 nm) for 5 min followed by storage in the dark at room temperature for 24 h. Samples were assayed for drug release (Dox) by measuring absorbance at 492 nm at 0, 1, 4, 8, and 24 h timepoints. Error bars represent SEM $*p < 0.1$, Student's *t*-test.

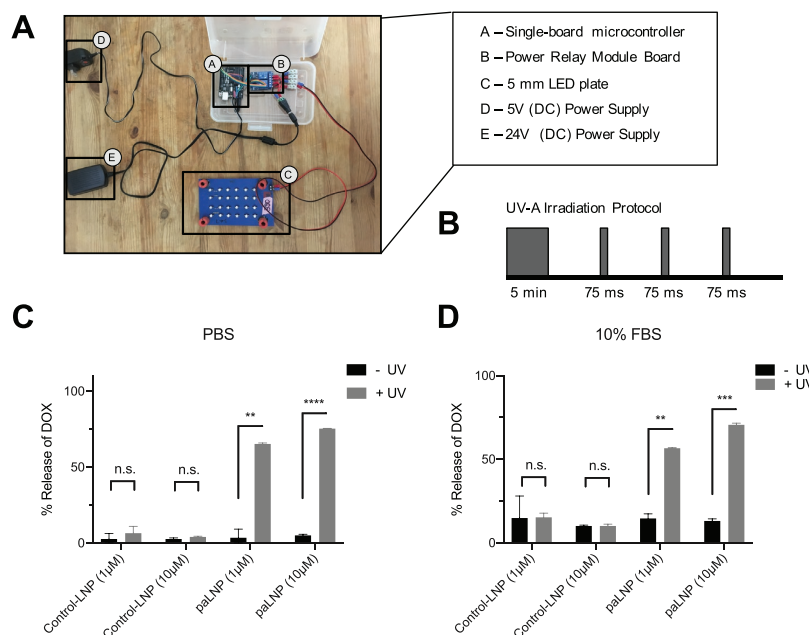


Figure 4. Pulsed irradiation (365 nm) of paLNP (10 mol% AzoPC) results in triggered release of Dox both in the absence and presence of serum. A) “Cell-DISCO” setup for pulsed irradiation using a single-board microcontroller (e.g., Arduino), power relay module board, LED plate, and power supplies. B) Irradiation protocol for pulsed LED starting with a 5 min initial irradiation followed by 75 ms irradiation pulses. C) Light-triggered Dox release from control-LNP and paLNP (10 mol% AzoPC) using pulsed LED irradiation (365 nm) for 24 h at 20 °C in PBS or D) DMEM media containing 10% FBS. Error bars represent SEM $**p < 0.01$, $***p < 0.001$, $****p < 0.0001$, n.s., not significant, Student’s *t*-test.

cryo-TEM due to the formation of nano-sized crystals of precipitated Dox in the center of the liposomes.^[33] It is of interest to determine whether similar morphology is exhibited by the loaded paLNP and whether this morphology is affected by the light-triggered release of Dox. We performed structural evaluation of the paLNP formulation using cryo-TEM imaging.

As shown in Figure 5A, paLNPs showed a typical bilayer structure, indistinguishable from the control DSPC-cholesterol liposomes, with sizes in agreement with those obtained via DLS (≈ 55 –60 nm). Control-LNPs and paLNPs loaded with Dox showed Dox crystallized within the liposome interior. After light-triggered release using pulsed irradiation at 365 nm over 24 h, there is a clear decrease in the number of entrapped drug crystals within the paLNPs, while the control DSPC-cholesterol liposomes show no visible changes. This was also confirmed through quantification of crystal thickness within the various samples (Figure 5B).

2.5. Dox Released from Loaded paLNP Following Irradiation is Biologically Active

Dox is a cytotoxic agent and its release from paLNP following irradiation would be expected to result in cytotoxic effects on nearby tissues. In order to demonstrate this, we investigated the effects of light-released Dox on the viability of a human derived liver cancer cell line (i.e., HuH7 cells) *in vitro*. We compared the cell viability effects of Dox in its free versus liposome

encapsulated forms with and without light-triggered drug release. HuH7 cells were treated with either free Dox (dissolved in PBS), Dox-loaded control-LNP or paLNP at drug concentrations up to 100 μM . Cells were subjected to irradiation at 365 nm for 5 min at 6 h post exposure to trigger drug release, followed by pulsed irradiation at 365 nm for 24 h to keep the AzoPC in its *cis* form. As expected, control-LNP (with or without UV irradiation) did not result in a decrease in viable cells due to their limited drug release properties. In contrast, treatments using paLNPs were highly dependent on the light-trigger. Whereas paLNP without UV irradiation did not affect cell viability, photoswitched paLNP resulted in a dose-dependent decrease in the number of viable cells 24 h after treatment similar to that of free Dox (Figure 6A). To confirm the significant light-triggered release of Dox from paLNP, HuH7 cells were treated with control-LNP or paLNP at a Dox concentration of 10 μM as stated above and analyzed through confocal microscopy with and without UV treatment. The confocal images demonstrate that only paLNPs result in effective release of Dox after irradiation. Once released, Dox accumulates in the nucleus and is fluorescent. (Figure 6B).

2.6. Formulation and Characterization of Red-Shifted paLNP Incorporating Tetra-Ortho-Chloro-Azobenzene Modified AzoPC

Incorporation of AzoPC sensitive to 365 nm could be perceived as a challenge for *in vivo* translation due to the limitation in

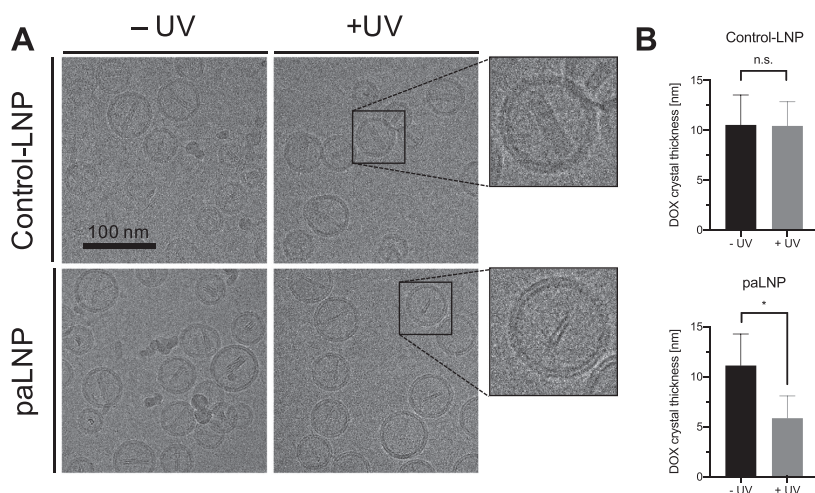


Figure 5. Dox loaded paLNP show evidence of drug release following pulsed irradiation (365 nm) as detected employing cryo-TEM. A) Representative cryo-TEM images of control DSPC-cholesterol liposomes and paLNP containing 10 mol% AzoPC prior to UV irradiation and post UV irradiation using a pulsed LED at 365 nm over a 24 h period. B) Comparison of thickness of Dox crystal within the liposomes pre and post UV irradiation. Error bars represent SEM $*p < 0.1$, n.s., not significant, Student's *t*-test.

tissue penetration depth and low tolerance to UV-A light. To extend the applicability of our light-triggered release system, we developed a red-shifted version of AzoPC, termed redAzoPC (synthesis described elsewhere), that undergoes a switch from the *cis* to the *trans* conformation at 660 nm (Figure 7A). Red-paLNPs were prepared using the previously established procedures (Section 2.1) by adding 10 mol% redAzoPC into the control DSPC-cholesterol liposomes (substituting DSPC for redAzoPC). Characterization of the red-paLNP particles showed a monodisperse population (PDI < 0.1) of uniformly sized ≈ 56 – 58 nm nanoparticles with $>98\%$ entrapment efficiency of

Dox, matching the physicochemical characteristics of control and paLNPs.

Drug release from red-paLNPs following irradiation was measured in PBS and cell culture medium (DMEM) containing serum (10% FBS) at room temperature. The red-paLNP were subjected to pulses of LED light (wavelength 660 nm) of 75 ms duration every 15 s over a 24 h period. This pulsed irradiation enabled a 75–80% Dox release from red-paLNPs in PBS (Figure 7B) and 70–75% release from red-paLNPs in serum containing medium (Figure 7C). In contrast, control-LNPs did not show any change in drug release following deep-red light irradiation (Figure 7B,C).

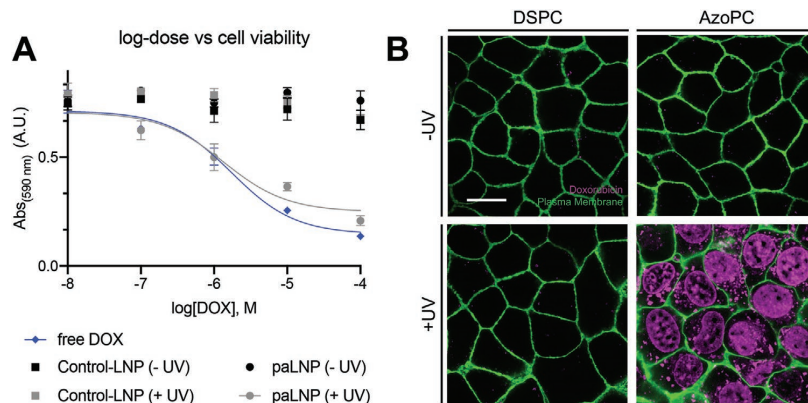


Figure 6. Dox released from drug loaded paLNP following irradiation is biologically active. A) Influence of irradiation on the viability of HuH7 cells incubated with increasing concentrations of Dox in free form or encapsulated in control-LNP or paLNP. Cells were incubated in the presence of 0, 0.1, 1, 10, and 100 μM Dox concentrations and were irradiated for 5 min at 365 nm and then subjected to pulsed irradiation at 365 nm for 24 h. Drug release was reflected by decreased cell viability. B) Confocal images of HuH7 cells treated with control-LNP and paLNP with and without UV irradiation. Samples with 10 μM Dox concentrations were irradiated for 5 min at 365 nm following, after which samples were subjected to pulsed irradiation at 365 nm for 24 h.

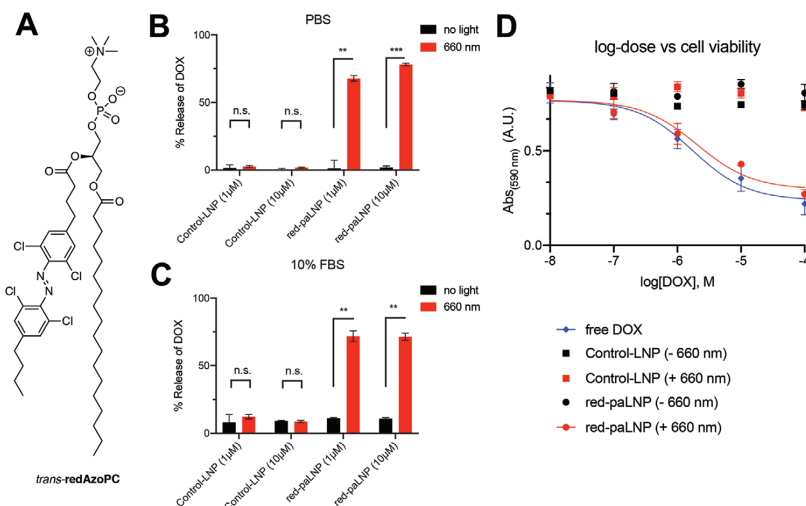


Figure 7. Pulsed deep-red light irradiation (660 nm) of red-paLNP (10 mol% redAzoPC) results in triggered release of Dox. A) Chemical structure of photoswitchable analog redAzoPC. The tetra-ortho-chloro-azobenzene can be isomerized from the trans to the cis form at 660 nm. B) Light-triggered Dox release from control-LNP and red-paLNP (10 mol% redAzoPC) using pulsed LED irradiation (660 nm) for 24 h at 20 °C in PBS or C) DMEM media containing 10% FBS. Error bars represent SEM $**p < 0.01$, $***p < 0.001$, n.s., not significant, Student's *t*-test. D) Influence of irradiation on the viability of HuH7 cells incubated with increasing concentrations of Dox in its free form or encapsulated in control-LNP or red-paLNP. Cells were incubated in the presence of 0, 0.1, 1, 10, and 100 μM Dox concentrations and were irradiated for 5 min at 660 nm and then subjected to pulsed irradiation at 660 nm for 24 h. Dox release was reflected by decreased cell viability.

To assess the effects of Dox in its free versus red-paLNP encapsulated forms (with and without light-trigger) on the viability of a human derived liver cancer cell line (i.e., HuH7 cells), an *in vitro* study was performed (similar to Section 2.4). HuH7 cells were treated with either free Dox (dissolved in PBS), Dox-loaded control-LNP or red-paLNP at drug concentrations up to 100 μM . Cells were subjected to irradiation at 660 nm for 5 min at 6 h post exposure to trigger drug release, followed by pulsed irradiation at 660 nm for 24 h to keep the redAzoPC in its cis isoform. As seen previously, control-LNP (with or without irradiation) did not result in a decrease in viable cells due to their limited drug release properties. In contrast, cytotoxic effects of red-paLNPs were highly dependent on the light-trigger. Similar to the results seen with the paLNP (UV-A light), the red-paLNP did not affect cell viability without irradiation whereas the photoswitched red-paLNP resulted in a dose-dependent decrease in the number of viable cells 24 h after treatment similar to that of free Dox (Figure 7D).

2.7. paLNP and Red-paLNP Display Long Circulation Lifetimes In Vivo Following I.V. Administration

To assess the pharmacokinetic properties of developed paLNP systems (i.e., influence of incorporating AzoPC analogs into conventional liposomes), we used the zebrafish embryo model. As demonstrated previously by our team, zebrafish embryos are a reliable and predictive *in vivo* tool to investigate liposomal circulation behavior and clearance mechanisms.^[34,35] First, we intravenously injected fluorescently labeled control-LNP, paLNP, and red-paLNP (1 nL) into transgenic zebrafish expressing

green fluorescent protein in their vascular endothelial cells (Tgkdr1:EGFP) at total lipid concentrations of 10 mg mL⁻¹. Next, we performed confocal microscopy imaging of the tail region 2 and 24 h post-injection (hpi). All liposomal systems (with and without irradiation) demonstrated excellent circulation properties within blood vessels 2 hpi (Figure 8A,B and Figure S3, Supporting Information) without any signs of agglomeration within the intersegmental vessels (ISV) and dorsal longitudinal anastomotic vessels. At 24 hpi, significant extravasation of LNPs into surrounding tissue and accumulations in the posterior caudal vein region (indicating macrophage clearance) was observed (Figure 8A–C). These pharmacokinetic characteristics, that is, excellent systemic circulation resulting in pronounced tissue extravasation, are typical for long-circulating liposomes. Importantly, incorporation of photoswitchable AzoPC analogs into LNP did not affect the pharmacokinetic properties thereby confirming the ideal characteristics for a light-triggered release system.

2.8. Light-Triggered Release of Doxorubicin from paLNP Systems In Vivo

In assessing the light-triggered release of Dox from paLNPs, various factors must be considered to enable its detection. Upon *in vivo* injection, Dox is entrapped in circulating LNPs (fluorescence is quenched). Release of Dox into circulation does not result in increased fluorescence due to low quantum efficiency and rapid clearance. Release into tissue however, is detectable due to fluorescence de-quenching and enhanced penetration (fluorescent area). Based on these considerations, we injected

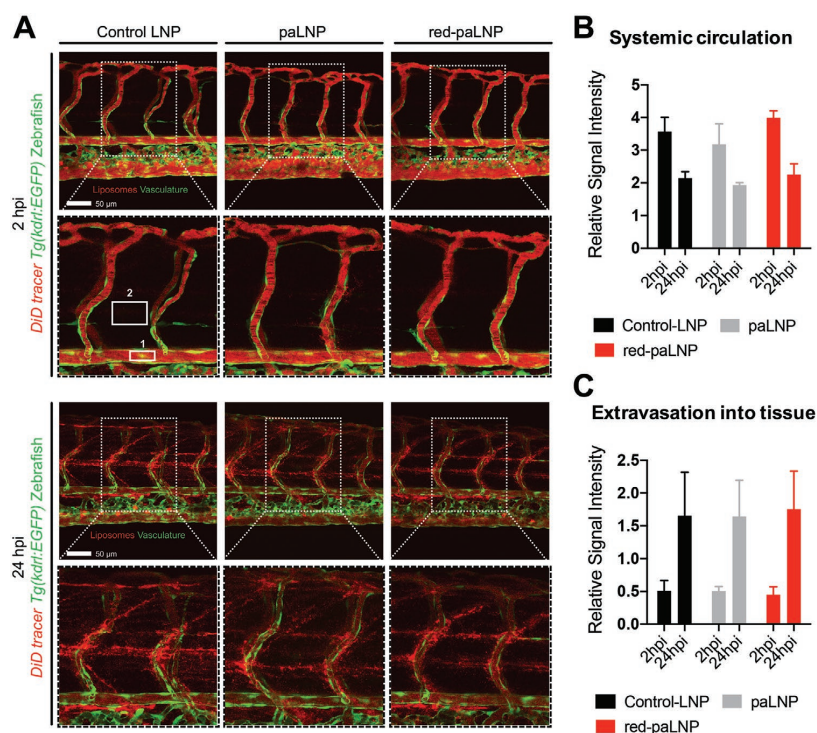


Figure 8. Assessment of LNP pharmacokinetics in vivo in transgenic zebrafish. Control LNP and paLNPs were injected intravenously into transgenic Tg(kdr:EGFP) zebrafish expressing enhanced green fluorescent protein in their vasculature. LNPs were fluorescently labeled with DiD. A) Confocal images of tail region were acquired at 2 and 24 hpi. B) Systemic circulation properties were quantified based on fluorescence signals in the dorsal aorta (box 1). C) LNP extravasation into tissue was quantified between the ISV (box 2). Error bars represent SEM.

control-LNP, paLNP, and red-paLNP (2 nL) at a Dox concentration of 3 mg mL⁻¹ into wildtype Tg(abc/tübingen) zebrafish embryos. Following tissue extravasation and accumulation, we exposed one set of zebrafish to pulsed UV-A (365 nm) or deep-red light (660 nm) irradiation for 24 h. Next, we performed confocal microscopy imaging of the tail region and analyzed the penetration area of free Dox.

All tested LNPs released Dox 48 hpi (Figure 9A,B). Although similar Dox signals in the absence of light-trigger were detected for all LNPs, paLNP, and red-paLNP triggered with UV-A or deep red pulsed light, respectively, demonstrated significantly enhanced Dox release in zebrafish embryos (Figure 9C). This result highlights the potential of paLNPs for triggered drug release in vivo.

3. Conclusion

This work demonstrates that DSPC-cholesterol liposomes containing 10 mol% photoswitchable phosphatidylcholines (substituting for DSPC) enable light-triggered Dox release in a physiological context. These paLNPs exhibit similar size-distribution, stability, and loading efficiencies as the parent DSPC-cholesterol systems which are clinically approved and widely

used in human cancer therapy. They have the added benefit of being able to release contents upon UV-A or deep-red light irradiation inducing a trans to cis isomerization in photoswitchable phosphatidylcholine analogs. This results in up to 80% release of encapsulated Dox over 24 h. The triggered release could potentially be made more rapid in response to a higher intensity light source.^[22] The described characteristics in combination with their long blood circulation half-lives make the paLNPs interesting and promising candidates for clinical development. It will be an important task in the future to demonstrate the local release in specific regions using rodent models. With regard to the utility of irradiation at 365 nm, the field of optoelectronics is currently undergoing significant advances, for example, through the development of fully implantable optoelectronic systems^[36] that could help overcome the issue of limited tissue penetration. This limitation can also be overcome by incorporating red-shifted analogs of AzoPC as demonstrated in our work or by using methods for upconversion of light.^[37]

In summary, in addition to the triggered release properties exhibited by the paLNP systems developed here, an important feature is their compositional simplicity and similarity to the well-studied clinical formulations. This allows us to be able to predict their physicochemical properties, nano-bio interactions, and pharmacokinetics in vivo. As such, this proof-of-concept

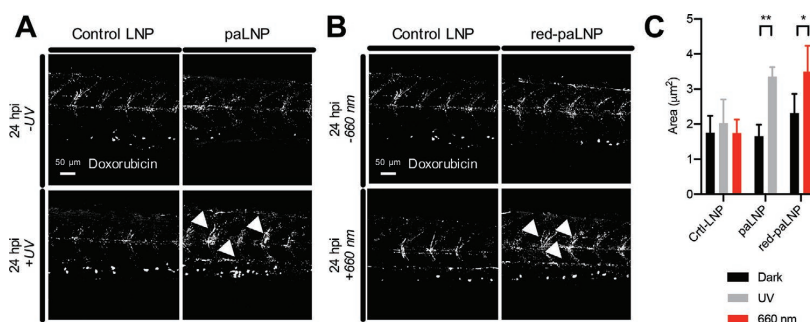


Figure 9. Dox release in zebrafish embryos in presence or absence of pulsed light trigger. Control LNP and paLNPs were injected intravenously into wildtype zebrafish embryos 48 hpf (2 nL, 3 mg mL⁻¹ Dox). After 24 h, zebrafish were exposed to pulsed irradiation and confocal images of tail region were acquired at 48 hpi. A,B) Representative images of Dox release (white signal) from control LNP, paLNP, or red-paLNP in presence or absence of pulsed UV-A (365 nm, A) or deep-red light (660 nm, B) irradiation. White arrows indicate exemplified areas with enhanced Dox release. C) Quantitative image analysis of Dox release. Errors bars represent SEM. * $p < 0.1$, ** $p < 0.01$.

study, and in particular the tools and methods employed, will potentially allow for rational design of new, simple, and effective systems with enhanced drug release capabilities that will have a significant impact on the therapeutic index gained by liposomal delivery of cytotoxic drugs.

4. Experimental Section

Materials: Phospholipids used for liposome preparation 1,2-distearoyl-sn-glycero-3-phosphocholine (DSPC) was purchased from Avanti Polar Lipids (Alabaster, AL). Cholesterol and MS-222 (Tricaine) and agarose was purchased from Sigma-Aldrich (Saint Louis, MO). AzoPC and redAzoPC was provided by the lab of Dr. Dirk Trauner (New York University). Ammonium sulphate, Dulbecco's PBS, FBS, and Triton x-100 were purchased from Sigma-Aldrich (Saint Louis, MO). Doxorubicin hydrochloride (Dox) was purchased from Cayman Chemicals (Ann Arbor, MI).

The Cell-DISCO was engineered in the Trauner lab and used as described.^[38] A 365 nm/660 nm LED (Roithner Lasertechnik) plate was used at one 75 ms flash per 15 s.

Liposome Preparation: Lipid stocks of cholesterol and DSPC were co-dissolved in ethanol at appropriate molar ratios. In some cases, AzoPC or redAzoPC was incorporated into the lipid mix at varying molar ratios, keeping the DSPC to cholesterol ratio constant. All the LNPs were made using the T-tube formulation method at total flow rate of 20 mL min⁻¹ and flow rate ratio of 3:1 aqueous: organic phases (v/v) with an initial lipid concentration of 10 µmol in 25% ethanol and 300 mM ammonium sulphate. Following formulation, particles were dialyzed against 300 mM ammonium sulphate using 12–14 kDa regenerated cellulose membranes (Spectrum Labs, Rancho Dominguez, 38 CA) overnight to remove residual EtOH. Prior to drug loading (see Section 4.3 Remote loading of Dox into preformed liposomes), particles were dialyzed against Dulbecco's PBS (pH 7.4) overnight using 12–14 kDa regenerated cellulose membranes. Cholesterol concentration of the particles was measured using the Wako Cholesterol E assay (Mountain View, CA) and used to determine the total lipid concentration.

Remote Loading of Dox into Preformed Liposomes: Prepared liposomes with ammonium sulphate gradient (see previous section) were combined with Dox dissolved in PBS to a final concentration of 3 mg mL⁻¹ total lipid and a drug:lipid (molar) ratio of 0.1. Loading mixture was incubated at 65 °C for 30 min before being dialyzed against PBS overnight to remove any unencapsulated Dox. Dialyzed particles were sterile filtered using a 0.2 µm syringe filter (Pall, Ville St. Laurent, QB).

Characterization of Dox-paLNP and Dox-Red-paLNP: Particle size and polydispersity index (PDI) were determined through DLS using the Malvern Zetasizer NanoZS (Worcestershire, UK). Reported values correspond to number mean diameters. Cholesterol concentration of the Dox-LNP particles was determined using the Wako Cholesterol E assay (Mountain View, CA) and used to determine the total lipid concentration. The concentration of Dox in the loaded particles was measured using absorbance at 492 nm. Dox-control LNP, dox-paLNP or dox-red-paLNP samples were collected prior to the incubation step in the loading procedure as well as post-loading and dialysis. The samples were mixed with 0.5% Triton x-100 in PBS at a dilution 1:20 dilution in a 96 well plate. After shaking briefly and incubating at room temperature for 5 min, absorbance values were measured at 492 nm. Encapsulation efficiency (percent encapsulation) was determined through comparison of the drug:lipid ratio of Dox-LNP pre-loading and post-loading and dialysis to remove unencapsulated Dox (see Section 2.3 Remote loading of Dox into preformed liposomes). Drug:lipid ratios were determined using the molar concentrations of Dox and total lipid determined through A492 and Wako Cholesterol E assay, respectively.

Cryo-TEM Imaging of Dox-Control LNP and Dox-paLNP: Control-LNP and paLNPs loaded with Dox (0.1 drug:lipid, molar) were concentrated (Amicon Ultra-15 Centrifuge Filter Units, Millipore, Billerica, MA) to a total lipid concentration of ≈25 mg mL⁻¹ prior to analysis. Some samples were subject to light-triggered drug release (see Section 4.6) and compared to non-UV treated samples. Morphological liposome characteristics and Dox loading were investigated by Cryo-TEM as described previously.^[39–41] In brief, liposome formulations were deposited onto glow-discharged copper grids and vitrified using a FEI Mark IV Vitrobot (FEI, Hillsboro, OR). Cryo-TEM imaging was performed using a 200 kV Glacios microscope equipped with a Falcon III camera at the UBC High Resolution Macromolecular Cryo-Electron Microscopy facility (Vancouver, BC).

Drug Release Assay of Dox-LNP Incubated in PBS: Control-LNP and paLNP particles diluted to a final concentration of 3 mg mL⁻¹ total lipid in PBS were irradiated with a UV-A light source (365 nm) for 5 min followed by storage in the dark at room temperature. At the 1 h time point, the incubated sample was passed down a size exclusion column to remove free drug. The drug:lipid ratio of purified LNPs was determined as detailed in the previous section and percent retention calculated relative to the $t = 0$ h time point. Release experiments were repeated using pulsed irradiation at 365 nm over a 24 h period in the dark at room temperature, following which drug release was determined based on drug:lipid ratio as detailed in the previous section and percent retention calculated relative to the $t = 0$ h time point.

Drug Release Assay of Dox-LNP Incubated in DMEM Media Containing 10% FBS: Control-LNP and paLNP particles loaded with Dox

(0.1 drug:lipid ratio) at a final concentration of 3 mg mL⁻¹ total lipid in DMEM media containing 10% FBS were irradiated with a UV-A light source (365 nm) for 15 min followed by pulsed irradiation at 365 nm over a 24 h period in the dark at room temperature. After 24 h, an aliquot was passed down a size exclusion column to remove free drug, followed by addition of a fixed ratio of isopropanol to precipitate the proteins. The supernatant was analyzed to determine the drug:lipid ratio as detailed in the previous section and percent retention calculated relative to the $t = 0$ h time point.

In Vitro Cell Viability Assay: Cell viability assay was performed using HuH7 cells—hepatocyte derived carcinoma cell line. Growth media was composed of DMEM with FBS (10%). Cells were plated in 96-well cell culture treated plates (Falcon/Corning Inc., Corning, NY) at a density of 12500 cells/well \approx 24 h prior to treatment. Either free Dox, control-LNP, paLNPs, or red-paLNPs (0.1 drug:lipid ratio) in PBS were diluted as necessary with PBS and added to the appropriate volume of media to obtain final treatment concentrations of 0, 0.1, 1, 10, and 100 μ M Dox (free drug, control-LNP or paLNP). Treated cells were subject to irradiation with UV-A light (365 nm) or deep-red light (660 nm) for 15 min following by pulsed irradiation (365 or 660 nm) incubated at 37 °C and 5% CO₂ for a total of 24 h. At the 24 h time point, cell viability was analyzed using an MTT assay (Abcam Inc.) comparing UV irradiated and non-UV irradiated cells.

Confocal Imaging: Imaging was performed using HuH7 cells—hepatocyte derived carcinoma cell line. Growth media was composed of DMEM with FBS (10%). Cells were plated in confocal imaging plates at a density of 40000 cells/well 24 h prior to treatment. Either free Dox, control-LNP or paLNPs (0.1 drug:lipid ratio) in PBS were diluted as necessary with PBS and added to the appropriate volume of media to obtain final treatment concentrations of 10 μ M Dox (free drug, control-LNP, or paLNP). Treated cells were subject to irradiation with UV-A light (365 nm) for 15 min following by pulsed irradiation (365 nm) incubated at 37 °C and 5% CO₂ for a total of 24 h. At the 24 h time point, cell membranes were stained with cell mask deep red plasma membrane stain (1.0 mg mL⁻¹, Thermo Fisher Scientific). Live cell imaging comparing UV irradiated and non-UV irradiated cells was conducted using a Leica TCS SP8 laser scanning confocal microscope (Leica, Germany), equipped with a 60 \times oil-immersion objective (numerical aperture 1.40). Dox was excited at 488 nm argon laser and CellMask was excited with a 633 nm.^[42]

Zebrafish Pharmacokinetic Studies: Embryos from Tg(kdrl:eGFP) and Tg(AB/Tübingen) adult zebrafish (*Danio rerio*) were bred at 28 °C in zebrafish culture media containing 30.4 μ g mL⁻¹ 1-phenyl-2-thiourea (PTU) and maintained according to Swiss animal welfare regulations. Embryos were embedded in 0.3% agarose containing tricaine and PTU and injected with a calibrated volume of 1 nL into Duct of Cuvier (48 h post fertilization, hpf) and cardinal vein (72 hpf) using a micromanipulator (Wagner Instrumentenbau KG), a pneumatic Pico Pump PV830 (WPI) and a Leica S8APO microscope (Leica). A portion of the injected fish was exposed, starting 0.16 hpi, to the corresponding pulsed light trigger at 28 °C for 24 h. The tail region of zebrafish embryos was imaged 2 and 24 hpi using an Olympus FV3000 confocal laser scanning microscope equipped with a 30 \times UPlanSApo oil-immersion objective (NA 1.35). Quantitative image analysis was performed as previously described.^[34,42]

Dox Release Studies in Zebrafish Embryos: 48 hpf embryos from Tg(abc/tu) were injected with 2 nL of 3 mg mL⁻¹ Dox containing LNPs into the duct of Cuvier and incubated at 28 °C in PTU containing zebrafish culture media. 24 hpi, one set of zebrafish was irradiated with pulsed-light for additional 24 h. For quantitative analysis, confocal images of five fishes were processed applying a defined threshold, followed by area calculation in Fiji (ImageJ) 2.1.0.

Supporting Information

Supporting Information is available from the Wiley Online Library or from the author.

Acknowledgements

N.C. and J.M. contributed equally to this work. The authors acknowledge Dr. Natalie Strynadka and Dr. Claire Atkinson from the UBC High Resolution Macromolecular Cryo-Electron Microscopy facility for support. Further, the authors acknowledge Dr. M. Affolter and Dr. H.G. Belting (Biozentrum, University of Basel, Switzerland) for providing zebrafish eggs, Dr. Jörg Huwyler (Pharmazentrum) for support with zebrafish injection and imaging, and Dr. Kai Schleicher (IMCF) for supporting quantitative image analysis of zebrafish studies (all University of Basel, Switzerland). J.M. thanks the NCI for a F99/K00 award (1F99CA253758-01). D.W. was supported by the Swiss National Science Foundation (#183923). This work was supported by NMIN (the NanoMedicines Innovation Network), a member of the Networks of Centres of Excellence Canada program.

Conflict of Interest

The authors declare no conflict of interest.

Data Availability Statement

The data that support the findings of this study are available from the corresponding author upon reasonable request.

Keywords

cancer, doxorubicin, liposome, photoswitch, triggered drug release

Received: December 30, 2020

Revised: February 25, 2021

Published online: April 20, 2021

- [1] T. M. Allen, P. R. Cullis, *Adv. Drug Delivery Rev.* **2013**, *65*, 36.
- [2] A. Wicki, D. Witzigmann, V. Balasubramanian, J. Huwyler, *J. Controlled Release* **2015**, *200*, 138.
- [3] J. Buck, P. Grossen, P. R. Cullis, J. Huwyler, D. Witzigmann, *ACS Nano* **2019**, *13*, 3754.
- [4] G. Bozzuto, A. Molinari, *Int. J. Nanomed.* **2015**, *10*, 975.
- [5] J. A. Kulkarni, D. Witzigmann, S. Chen, P. R. Cullis, R. van der Meel, *Acc. Chem. Res.* **2019**, *52*, 2435.
- [6] A. Akinc, M. A. Maier, M. Manoharan, K. Fitzgerald, M. Jayaraman, S. Barros, S. Ansell, X. Du, M. J. Hope, T. D. Madden, *Nat. Nanotechnol.* **2019**, *14*, 1084.
- [7] A. Gabizon, R. Catane, B. Uzieli, B. Kaufman, T. Safra, R. Cohen, F. Martin, A. Huang, Y. Barenholz, *Cancer Res.* **1994**, *54*, 987.
- [8] R. T. Chlebowski, *West. J. Med.* **1979**, *131*, 364.
- [9] D. Bobo, K. J. Robinson, J. Islam, K. J. Thurecht, S. R. Corrie, *Pharm. Res.* **2016**, *33*, 2373.
- [10] D. Papahadjopoulos, T. M. Allen, A. Gabizon, E. Mayhew, K. Matthay, S. K. Huang, K. D. Lee, M. C. Woodle, D. D. Lasic, C. Redemann, *Proc. Natl. Acad. Sci. USA* **1991**, *88*, 11460.
- [11] A. Gabizon, H. Shmeeda, Y. Barenholz, *Clin. Pharmacokinet.* **2003**, *42*, 419.
- [12] L. D. Mayer, L. C. Tai, D. S. Ko, D. Masin, R. S. Ginsberg, P. R. Cullis, M. B. Bally, *Cancer Res.* **1989**, *49*, 5922.
- [13] S. Bibi, E. Lattmann, A. R. Mohammed, Y. Perrie, *J. Microencapsulation* **2012**, *29*, 262.
- [14] A. Dabbagh, B. J. J. Abdullah, H. Abdullah, M. Hamdi, N. H. A. Kasim, *J. Pharm. Sci.* **2015**, *104*, 2414.

- [15] M. E. Lorkowski, P. U. Atukorale, K. B. Ghaghada, E. Karathanasis, *Adv. Healthcare Mater.* **2020**, *10*, e2001044.
- [16] N. Forbes, A. Pallaoro, N. O. Reich, J. A. Zasadzinski, *Part. Part. Syst. Charact.* **2014**, *31*, 1158.
- [17] D. Needham, G. Anyarambhatla, G. Kong, M. W. Dewhirst, *Cancer Res.* **2000**, *60*, 1197.
- [18] U. Bulbake, S. Doppalapudi, N. Kommineni, W. Khan, *Pharmaceutics* **2017**, *9*, 12.
- [19] C. D. Landon, J.-Y. Park, D. Needham, M. W. Dewhirst, *Open Nanomed. J.* **2011**, *3*, 24.
- [20] Y. Dou, K. Hynynen, C. Allen, J. *Controlled Release* **2017**, *249*, 63.
- [21] Celsion, *A Phase III, Randomized, Double Blind, Clinicaltrials.Gov* **2018**.
- [22] C. Pernpeintner, J. A. Frank, P. Urban, C. R. Roeske, S. D. Pritzl, D. Trauner, T. Lohmüller, *Langmuir* **2017**, *33*, 4083.
- [23] K. Hüll, J. Morstein, D. Trauner, *Chem. Rev.* **2018**, *118*, 10710.
- [24] D. Miranda, J. F. Lovell, *Bioeng. Transl. Med.* **2016**, *1*, 267.
- [25] R. H. Bisby, C. Mead, C. G. Morgan, *Photochem. Photobiol.* **2000**, *72*, 57.
- [26] D. Luo, K. A. Carter, A. Razi, J. Geng, S. Shao, D. Giraldo, U. Sunar, J. Ortega, J. F. Lovell, *Biomaterials* **2016**, *75*, 193.
- [27] K. A. Carter, D. Luo, J. Geng, S. T. Stern, J. F. Lovell, *Mol. Cancer Ther.* **2019**, *18*, 592.
- [28] J. Morstein, A. C. Impastato, D. Trauner, *ChemBioChem* **2021**, *22*, 73.
- [29] D. B. Konrad, J. A. Frank, D. Trauner, *Chem. Eur. J.* **2016**, *22*, 4364.
- [30] M. M. Lerch, M. J. Hansen, G. M. van Dam, W. Szymanski, B. L. Feringa, *Angew. Chem., Int. Ed.* **2016**, *55*, 10978.
- [31] R. Pattiellu, S. Crielaard, I. Klein-Schiphorst, B. I. Florea, A. Kros, F. Campbell, *ACS Cent. Sci.* **2020**, *6*, 535.
- [32] G. Caracciolo, *Nanoscale* **2018**, *10*, 4167.
- [33] Y. Barenholz, *J. Controlled Release* **2012**, *160*, 117.
- [34] S. Bleher, J. Buck, C. Muhl, S. Sieber, S. Barnert, D. Witzigmann, J. Huwyler, M. Barz, R. Süß, *Small* **2019**, *15*, 1904716.
- [35] S. Sieber, P. Grossen, J. Bussmann, F. Campbell, A. Kros, D. Witzigmann, J. Huwyler, *Adv. Drug Delivery Rev.* **2019**, *151–152*, 152.
- [36] S. H. Yun, S. J. J. Kwok, *Nat. Biomed. Eng.* **2017**, *1*, 0008.
- [37] J. Morstein, D. Trauner, *Curr. Opin. Chem. Biol.* **2019**, *50*, 145.
- [38] M. Borowiak, W. Nahaboo, M. Reynders, K. Nekolla, P. Jalinot, J. Hasserodt, M. Rehberg, M. Delattre, S. Zahler, A. Vollmar, *Cell* **2015**, *162*, 403.
- [39] D. Witzigmann, S. Sieber, F. Porta, P. Grossen, A. Bieri, N. Strelnikova, T. Pfohl, C. Prescianotto-Baschong, J. Huwyler, *RSC Adv.* **2015**, *5*, 74320.
- [40] S. Sieber, P. Grossen, P. Detampel, S. Siegfried, D. Witzigmann, J. Huwyler, *J. Controlled Release* **2017**, *264*, 180.
- [41] J. A. Kulkarni, D. Witzigmann, J. Leung, R. van der Meel, J. Zaifman, M. M. Darjuan, H. M. Grisch-Chan, B. Thöny, Y. Y. C. Tam, P. R. Cullis, *Nanoscale* **2019**, *11*, 9023.
- [42] D. Witzigmann, P. Uhl, S. Sieber, C. Kaufman, T. Einfalt, K. Schöneweis, P. Grossen, J. Buck, Y. Ni, S. H. Schenk, *eLife* **2019**, *8*, e42276.

3.4.3 Publication 3

Incorporation of phosphatidylserine improves efficiency of lipid based gene delivery systems

Claudia Lotter, Claudio Luca Alter, **Jan Stephan Bolten**, Pascal Detampel, Cornelia G Palivan, Tomaz Einfalt, Jörg Huwyler

Eur J Pharm Biopharm. 2022 Mar;172:134-143.

doi: 10.1016/j.ejpb.2022.02.007.

Personal contribution:

My contribution to this research article includes zebrafish larvae experiments to assess pharmacokinetic aspects. I was involved in the design and planning of *in vivo* studies. Thus, I wrote parts of the method, results, and discussion sections and proofread the manuscript.



Contents lists available at ScienceDirect

European Journal of Pharmaceutics and Biopharmaceutics

journal homepage: www.elsevier.com/locate/ejpb

Incorporation of phosphatidylserine improves efficiency of lipid based gene delivery systems

Claudia. Lotter^{a,1}, Claudio. Luca. Alter^{a,b,1}, Jan. Stephan. Bolten^a, Pascal. Detampel^a, Cornelia. G. Palivan^{b,c}, Tomaž. Einfalt^{a,2}, Jörg. Huwyler^{a,*}

^a Department of Pharmaceutical Sciences, Division of Pharmaceutical Technology, University of Basel, Klingelbergstrasse 50, 4056 Basel, Switzerland

^b Swiss Nanoscience Institute, University of Basel, Klingelbergstrasse 82, 4056 Basel, Switzerland

^c Department of Chemistry, University of Basel, Mattenstrasse 24a, BPR 1096, 4003 Basel, Switzerland

ARTICLE INFO

Keywords:

Lipid nanoparticles
Nucleic acid delivery
Transfection efficiency
Transfection potency
Lipid composition
Phosphatidylserine

ABSTRACT

The essential homeostatic process of dead cell clearance (efferocytosis) is used by viruses in an act of apoptotic mimicry. Among others, viruses leverage phosphatidylserine (PS) as an essential “eat me” signal in viral envelopes to increase their infectivity. In a virus-inspired biomimetic approach, we demonstrate that PS can be incorporated into non-viral lipid nanoparticle (LNP) pDNA/mRNA constructs to enhance cellular transfection. The inclusion of the bioactive PS leads to an increased ability of LNPs to deliver nucleic acids *in vitro* to cultured HuH-7 hepatocellular carcinoma cells resulting in a 6-fold enhanced expression of a transgene. Optimal PS concentrations are in the range of 2.5 to 5% of total lipids. PS-decorated mRNA-LNPs show a 5.2-fold enhancement of *in vivo* transfection efficiency as compared to mRNA-LNPs devoid of PS. Effects were less pronounced for PS-decorated pDNA-LNPs (3.2-fold increase). Incorporation of small, defined amounts of PS into gene delivery vectors opens new avenues for efficient gene therapy and can be easily extended to other therapeutic systems.

1. Introduction

There is a growing interest in solid lipid nanoparticles (LNPs) as a drug delivery system for nucleic acids. The FDA approval in 2018 of the first LNP based siRNA drug (Patisiran) and the worldwide approval of COVID-19 mRNA LNP based vaccines were the first clinical applications of LNPs for non-viral nucleic acid therapy [1,2]. Classic LNP formulations are composed of charged lipids and lipid-like adjuvants. Cationic lipids bind and condense the negatively charged nucleic acids. This is a prerequisite to enable cellular uptake and subsequently their release from the endosomal compartment to the cytoplasm. Due to the high

systemic toxicity and poor pharmacokinetic properties of permanently charged cationic LNPs [3,4], current clinically translated LNP therapies are based on ionizable lipids. The chemical nature of ionizable lipids with a pK_a around 6.7 (i.e. 1,2-dioleoyloxy-3-(dimethylamino)propane (DODMA)) can be leveraged to formulate pH-responsive LNPs [5,6]. In this regard, extensive chemical optimization of ionizable lipids has been conducted to improve the delivery efficiency of LNPs [7,8]. Besides charged lipids, additional “helper lipids” are needed for the formation of solid nanoparticles. Altering the helper lipid composition of LNP formulations reduces their cytotoxicity and leads to increased potencies *in vitro* and *in vivo* [9–15]. For example, it has been shown that the

Abbreviations: CLSM, confocal laser scanning microscopy; D_h, hydrodynamic diameter; DLS, dynamic light scattering; DODMA, 1,2-dioleoyloxy-3-(dimethylamino)propane; DOPC, 1,2-dioleoyl-*sn*-glycero-3-phosphocholine; DOTAP, 2,3-dioleoyloxy-propyl-trimethylammoniumchlorid; DMPE-PEG2000, 1,2-dimyristoyl-*sn*-glycero-3-phosphoethanolamine-N-[methoxy (polyethylene glycol)-2000]; EE, encapsulation efficiency; EGFP, enhanced green fluorescent protein; i.v., intravenous; hpi, hours post injection; LNP, lipid nanoparticle; mRNA, messenger RNA; MTS, 3-(4,5-dimethylthiazol-2-yl)-5-(3-carboxymethoxyphenyl)-2-(4-sulfophenyl)-2H-tetrazolium; N/P, lipid-nitrogen (N) to oligonucleotide-phosphate (P) ratio; PDI, polydispersity index; pDNA, plasmid DNA; PEG, polyethylene glycol; PS, L- α -phosphatidylserine; TE, transfection efficiency, number of EGFP positive cells; TP, transfection potency, mean EGFP signal intensity expressed as single-cell relative fluorescence units; ZFE, zebrafish embryo.

* Corresponding author at: Department of Pharmaceutical Sciences, University of Basel, Klingelbergstrasse 50, CH-4056 Basel, Switzerland.

E-mail address: joerg.huwyler@unibas.ch (Jörg. Huwyler).

¹ Contributed equally.

² T.E. and J.H. have contributed equally to this work as senior last authors.

<https://doi.org/10.1016/j.ejpb.2022.02.007>

Received 5 November 2021; Received in revised form 11 February 2022; Accepted 11 February 2022

Available online 15 February 2022

0939-6411/© 2022 The Authors. Published by Elsevier B.V. This is an open access article under the CC BY license (<http://creativecommons.org/licenses/by/4.0/>).

implementation of specific polyethylene glycol-functionalized (PEG) lipids can control the circulation time and influence LNP biodistribution [9,10]. The replacement of the classical cholesterol with bioactive phytosterols has been proven to alter the morphology, the internalization mechanisms, and the subcellular trafficking of LNPs [11–14]. Similarly, with the substitution of the helper lipid 1,2-distearoyl-*sn*-glycero-3-phosphocholine (DSPC) with 1,2-dioleoyl-*sn*-glycero-3-phosphocholine (DOPC) or 1-stearoyl-2-oleoyl-*sn*-glycero-3-phosphocholine (SOPC), a notable increase in LNP effectiveness has been achieved [13,14]. Furthermore, the substitution of DSPC by unsaturated PCs had a strong impact on transfection efficiency and toxicity of LNPs although effects were different for LNP-siRNA and LNP-pDNA systems [13].

Despite all of these efforts, the efficiency of LNP based formulations is still suboptimal and not comparable to the one of viral vectors. Unlike LNPs, viral envelopes have complex lipidomic compositions [16]. In the present study, we introduce a new strategy to improve the LNP efficacy that is inspired by virus envelopes. In particular, we focus on the bioactive phospholipid phosphatidylserine (PS) [17], which affects cellular internalization and intracellular processing. We selected PS as it represents an essential co-factor during the infection process of several viral types [18–20], including the Ebola, Epstein Barr, and Hepatitis B virus [21]. By inclusion of PS in their membranes, virions camouflage themselves as dead cells in an act referred to as apoptotic cell mimicry [21]. In mammalian cells, PS is actively kept on the inner leaflet of the cellular membrane by the flippase enzyme family. However, through the induction of apoptosis or necrosis, PS gets gradually exposed to the outer leaflet. This in turn induces PS recognition and apoptotic cell clearance. This process called efferocytosis is highly evolutionarily conserved due to the constant turnover of cells [22,23]. Efferocytosis is performed by both professional (i.e. macrophages) and non-professional phagocytes (i.e. tissue cells) [22,24,25]. The key receptor families to which PS has been reported to bind include G-protein-coupled TIM (TIM1, TIM3, TIM4) and TAM (Gas6, ProS) receptors [26]. Surface presentation of PS and interaction with TIM receptors is also exploited by other parasitic organisms [27] and is an essential bioactive molecule in the entry of exosomes [28–30]. Furthermore, PS bearing liposomes were previously demonstrated to effectively alter subcellular trafficking of liposomes to

the endoplasmic reticulum of non-phagocytic cells in a viral-like manner [31].

It was therefore the aim of the present study to explore whether the decoration of LNPs with PS increases transfection. We incorporated PS in both cationic and ionizable LNPs. Using optimized lipid-nitrogen to oligonucleotide-phosphate (N/P) ratios, we used a screening approach to design PS-decorated LNPs with desired physico-chemical properties such as particle size and size distribution, surface charge, and nucleic acid condensation efficiency. Mechanistic studies were used to investigate the impact of PS on transfection efficiency (TE) as well as transfection potency (TP), cellular LNP uptake, viability, and subcellular trafficking of LNPs. Uptake and cellular processing of both pDNA and mRNA encoding for an enhanced green fluorescent protein transgene (EGFP) were studied. Lead PS-LNPs formulations were tested with respect to TP and TE *in vivo* in a vertebrate zebrafish embryo (ZFE) model (Fig. 1).

2. Material and methods

2.1. Materials and chemicals

1,2-dioleoyloxy-3-dimethylaminopropane (DODMA), 1,2-dioleoyl-*sn*-glycero-3-phosphocholine (DOPC), L- α -phosphatidylserine (brain derived PS), 1,2-dimyristoyl-*sn*-glycero-3-phosphoethanolamine-N-[methoxy(polyethylene glycol)-2000] (DMPE-PEG200) were purchased from Avanti Polar Lipids (Alabaster, AL). 2,3-dioleoyloxy-propyl-trimethylammoniumchlorid (DOTAP) was purchased from Corden Pharma (Frankfurt am Main, Germany). Cholesterol, DiI, Hoechst 33342 and 7-Aminoactinomycin D (7-AAD) were obtained from Sigma Aldrich (Schaffhausen, Switzerland). SYBR Gold Nucleic Acid Gel Stain (SYBR gold reagent), DiO, Chlorpromazine, Polyinosinic acid (Poly I), Colchicine, Nystatin and Dynasore were acquired by Thermo Fisher Scientific (Zug, Switzerland). AnnexinV was purchased from Biolegend (San Diego, CA), Label IT Cy5 Kit from Mirus Bio (Madison, WI) and Chol-PEG-FITC-5k from Nanocs (New York, NY). The minicircle plasmid DNA encoding for EGFP under the control of a liver-specific p3 promoter [32] was kindly provided by the University Children's Hospital Zurich.

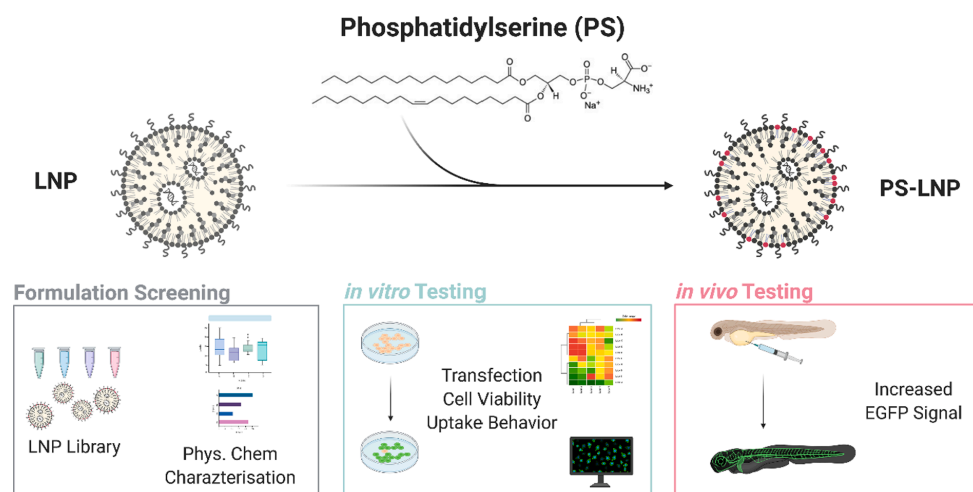


Fig. 1. Design and evaluation of lipid nanoparticles (LNPs) equipped with phosphatidylserine (PS). LNPs were formulated with PS, DOPC, and cholesterol as helper lipids and DOTAP or DODMA as cationic or ionizable nucleic acid condensation agents, respectively. PS-LNPs had a defined hydrodynamic diameter and ζ -potential. Cellular uptake, transfection potency, and transfection efficiency of PS-LNPs were evaluated *in vitro* (i.e., HuH-7 hepatic carcinoma cell line) as well as *in vivo* (i.e., zebrafish embryo). EGFP: enhanced green fluorescent protein transgene. (For interpretation of the references to color in this figure legend, the reader is referred to the web version of this article.)

NTC9385R (3xCpG)-CAG EGFP-CpG free BGH pA nanovector plasmid DNA was obtained from Nature Technology Corp (Lincoln, NE). Mini-circle plasmid DNA used for *in vitro* experiments and nanovector plasmid DNA used for *in vivo* experiments are referred to as pDNA. 5' capped CleanCap EGFP mRNA was purchased from TriLink Biotechnologies (San Diego, CA). Dulbecco's modified Eagle's medium (DMEM) high glucose (4500 mg L⁻¹) was obtained from Sigma Aldrich and supplemented with 10% FCS (BioConcept, Allschwil, Switzerland), penicillin (100 units mL⁻¹), and streptomycin (100 µg mL⁻¹) (Sigma Aldrich). Trypsin/EDTA (0.25%) was purchased from Gibco. FACS buffer, composed of DPBS (Sigma Aldrich), was supplemented with 1% FCS, 2.5 mM EDTA, 0.05% NaN₃.

2.2. Preparation of LNPs

Lipid nanoparticles used for *in vitro* experiments were prepared using a bulk mixing method as described elsewhere [32]. Briefly, lipid solutions (DODMA/DOTAP, Cholesterol, DOPC and PS at molar ratios of 50:40:10:0, 50:40:9.5:0.5, 50:40:9:1, 50:40:7.5:2.5, 50:40:5:5 and 50:30:20:10) were solved in CHCl₃, taken to dryness by rotational evaporation under reduced pressure for 1 h and rehydrated using 5% glucose, 20 mM sodium acetate, pH 4 (LNP sample buffer). The final lipid concentration was 0.8 mM. Liposomes were extruded 13 times using a manual mini extruder (Avanti Polar Lipids) and polycarbonate membranes (Nucleopore, Whatman, North Bend, OH) with a pore size of 100 nm. For LNP complexation with pDNA or mRNA, LNPs were combined at the desired N/P ratio with nucleic acids solved in LNP sample buffer. They were incubated at 22 °C for 30 min at 300 rpm. For *in vivo* experiments, LNPs containing PEGylated lipids were used. The lipid composition was DODMA:Cholesterol:DOPC:DMPE-PEG2000 = 50:39:10:1. Where indicated, DOPC was partially substituted with PS to reach the indicated final percentage of this lipid. The total amount of DOPC and PS was 10% of total lipids. The dry film was rehydrated at 70 °C using methanol:ethanol = 20:80. The lipid solution (organic phase) was combined with the nucleic acids solved in LNP sample buffer (aqueous phase) at the desired N/P ratio by microfluidics (Nano-Assembler; Precision Nanosystems, San Jose, CA). Flow rate was 20 mL min⁻¹ with an organic:aqueous phase ratio of 1:3. Buffer was exchanged at 4 °C to 0.9% NaCl, 1 mM HEPES, at pH 7.4 (*in vivo* sample buffer) by dialysis (Millipore, 12,000–14,000 molecular weight cut-off). Dialyzed samples were collected and characterized by a nucleic acid exclusion assay using SYBR gold reagent. Where indicated, LNPs were labeled with fluorescent dyes. No particle aggregation was observed upon storage at 4 °C for at least one week. For all experiments, only freshly prepared LNPs were used. All formulations showed colloidal stability.

2.3. LNP size, size distribution and ζ-potential

PS-LNP size distribution and ζ-potential were determined by dynamic light scattering using a Zetasizer Ultra (Malvern Analytical, Volketswil, Switzerland). For ζ-potential measurement: PS-LNPs were diluted 1:40 in either LNP sample buffer or 5% glucose/10 mM HEPES, pH 7.4.

2.4. Evaluation of nucleic acid encapsulation efficiency

The encapsulation efficiency (EE) of the particles was determined by a nucleic acid exclusion assay using SYBR gold reagent. Briefly, 190 µL diluted fluorescent dye was added to 10 µL LNP solution in the presence or absence of 0.2% (w/v) Triton-X100 and incubated for 5 min. A linear calibration curve was obtained for each of the tested nucleic acids. Fluorescence was measured at λ_{ex} = 485 nm, λ_{em} = 530 nm and λ_{Cutoff} = 515 nm.

2.5. Cell culture

HuH-7 cells were obtained from American Type Culture Collection (ATCC, Manassas, VA) and cultured in DMEM (55 cm² dishes, 37 °C, 5% CO₂, saturated humidity). The cells were harvested at 80% confluency.

2.6. Flow cytometry

2 × 10⁴ HuH-7 cells were seeded onto Collagen (Collagen I, rat tail) coated 24-well plates and allowed to adhere overnight. Cell medium was removed, cells were trypsinized for 5 min and further uptake was blocked by addition of 300 µL FACS buffer containing 7-AAD (2 µg mL⁻¹) at least 20 min prior use. Samples were kept on ice until analyzed. Experiments were analyzed by flow cytometry using a FACS Canto II (BD Bioscience, San Jose, CA). Doublets were excluded using FSC-A and SSC-A detectors. The apoptotic cells were excluded using FL2-A (695/40). A total of 10'000 single cells for each sample were analyzed and data were processed using Flow Jo VX software (TreeStar, Ashland, OR).

2.7. In vitro transfection experiments

In these experiments, “transfection efficiency” (TE) refers to the number of transfected cells. “Transfection potency” (TP) refers to the mean signal intensity of the whole cell population expressed in terms of relative fluorescent units. Cells were incubated with 100 µL PS-LNPs for 48 h for pDNA and 24 h for mRNA in 500 µL DMEM at the indicated final nucleic acid concentrations/well (0.28 µg mL⁻¹ or 0.83 µg mL⁻¹). TE and EGFP signal intensity in cells were analyzed using flow cytometry. A TE value of 100% thereby would indicate that 100% (number) of target cells were transfected. Furthermore, a normalized signal intensity value of 100% refers to the highest observed median EGFP signal in a given experiment.

2.8. Time dependent uptake

100 µL PS-LNPs condensing a mixture of 1:4 Cy5-labeled nucleic acid:non-labeled nucleic acid were added to HuH-7 cells at a final nucleic acid concentration of 0.034 µg mL⁻¹, incubated for 4 h, and washed three times with DPBS. Cells were analyzed by flow cytometry. A normalized signal intensity of 100% thereby refers to the highest observed median Cy5 signal in an individual experiment.

2.9. Inhibition study

Inhibitors were used to block endocytosis pathways and were added prior 100 µL 0.1 mol% DiO PS-LNP (0.28 µg mRNA mL⁻¹) addition (Chlorpromazine (10 µg mL⁻¹) for 30 min, Poly I (10 µg mL⁻¹) for 30 min, Colchicine (10 µg mL⁻¹) for 2 h, Nystatin (50 µg mL⁻¹) for 15 min and Dynasore (80 µM) for 30 min). PS-LNPs were incubated for 4 h and washed three times with DPBS. Signal intensity of DiO expression in cells were analyzed by flow cytometry. Change in uptake was measured as a DiO signal intensity reduction of samples compared to non-inhibited median DiO signal intensity.

2.10. Cell viability assay

3.3 × 10³ HuH-7 cells were plated onto Collagen (Collagen I, rat tail) pre-treated clear bottom 96-multiwell plates 24 h prior transfection. An adjusted amount of sample volume compared to TE experiment with nucleic acid concentrations of 0.28 µg mL⁻¹ and 0.83 µg mL⁻¹ were added to the cells. Terfenadine (50–1 nM) was used as a negative control. After 48 h or 24 h depending on the used nucleic acid, 20 µL MTS [3-(4,5-dimethylthiazol-2-yl)-5-(3-carboxymethoxyphenyl)-2-(4-sulfophenyl)-2H-tetrazolium] reagent was added to each well and was incubated for 1 h at 37 °C and 5% CO₂. The absorbance was measured at 490 nm whereby the obtained results were normalized according to the

untreated cells which were defined as 100% viable.

2.11. Confocal laser scanning microscopy

CLSM was performed using an Olympus FV 1000 inverted microscope (Olympus Ltd, Tokyo, Japan) equipped with a 60x UPlanFLN oil immersion objective (numerical aperture 1.40). To minimize spectral cross talk, the samples were scanned using sequential mode. For confocal fluorescence and live cell imaging, HuH-7 cells were seeded into microscopy microslides (Ibidi GmbH, Gräfelfing, Germany; coated with rat tail collagen I). HuH-7 cells were incubated with LNP complexed nucleic acid at a concentration of $0.28 \mu\text{g mL}^{-1}$. Cells nuclei were post-stained with Hoechst 33342 ($2.5 \mu\text{g mL}^{-1}$ in PBS, for 5 min). Live-Images were acquired at a controlled temperature of 37°C using DMEM. Images were visualized by IMARIS software (Bitplane, Belfast, United Kingdom). Single-particle track speeds were analyzed using the IMARIS Tracking and Statistic Module. Spot detection was set to $0.5 \mu\text{m}$ and tracking parameters were set to autoregressive motion, max. distance = $5 \mu\text{m}$, max gap = 3 and track duration = 120 s.

2.12. Zebrafish embryo (ZFE) experiments

For ZFE experiments, PEGylated LNPs were produced using the microfluidics protocol. LNPs were concentrated using an Amicon Ultra-4 centrifugal filter ($10^4/000$ molecular weight cut-off; Merck Millipore). Eggs of wildtype (abc/Tübingen) and Tg(kdrl:EGFP) adult zebrafish were collected and raised at 28°C in $30 \mu\text{g mL}^{-1}$ 1-phenyl-2-thiourea (PTU) added zebrafish culture medium. 36 h post-fertilization, ZFE were manually dechlorinated and embedded in ethyl-3-aminobenzoate methanesulfonate (MS-222, Tricaine) and PTU containing 0.3% agarose. $2 \times 3 \text{ nL}$ of $75 \mu\text{g mL}^{-1}$ mRNA or $150 \mu\text{g mL}^{-1}$ pDNA coding for EGFP and complexed with PEGylated LNPs were intravenously injected into the Duct of Cuvier by using a micromanipulator (Wagner Instrumentenbau, Schöffengrund, Germany), a pneumatic Pico Pump PV830 (WPI, Sarasota, FL) and a Leica S8APO microscope (Leica, Wetzlar, Germany). Successfully injected ZFE were transferred into 28°C PTU containing zebrafish culture medium. Injected ZFE were imaged between 30 and 62 h post-injection (hpi) using an Olympus FV 1000 inverted laser scanning microscope (Olympus, Tokyo, Japan) equipped with a 30x objective (UPlanSApo, 1.05NA). ZFE images were stitched using the Grid-collection stitching plug-in semi-quantitative analysis was done using a threshold in Fiji 2.1.0/1.53c software. Fluorescent signals were analyzed in the tail region of the ZFE to monitor circulating particles only [33,34]. Image were assembled in OMERO software 5.4.10 (University of Dundee & Open Microscopy Environment). To reduce intraexperimental variability, comparative experiments were performed during the same day by the same operator and using the same stage. Reproducibility was verified by repeating series of experiments on at least three different days. For each condition of each series of experiments at least 9 ZFE were used ($n = 9$). For the preparation of Figures and the corresponding semi-quantitative analysis, data from one representative series of experiments were used [34].

For biodistribution studies, $2 \times 3 \text{ nL}$ of $75 \mu\text{g mL}^{-1}$ pDNA coding for EGFP DiI fluorescent labelled LNPs were injected into wild type ZFE and imaged from 2 to 11 hpi with a time interval of 1 h. For vasculature localization studies, Tg(kdrl:EGFP) were injected with $2 \times 3 \text{ nL}$ of $75 \mu\text{g mL}^{-1}$ mRNA DiI fluorescently labelled LNPs and were imaged 4 hpi. To determine DiI PS-LNP – vasculature association, the IMARIS manual surface, measurement point and statistic modules was used. DiI PS-LNP signal within a distance of $0.5 \mu\text{m}$ and $-6 \mu\text{m}$ to the EGFP vasculature signal, was defined to be associated with it.

2.13. Statistical analysis

If not otherwise indicated, data values are means \pm SD, $n = 3$ independent sets of experiments. Groups were compared by ANOVA

followed by Tukey post-hoc test. Analyses were performed with OriginPro 2021 software (OriginLab, Northampton, MA).

3. Results and discussion

3.1. Physico-chemical characterization of PS-LNPs

During the initial step of PS-LNP development and *in vitro* evaluation, we incorporated PS into first and second-generation LNPs by changing the lipid composition of LNPs. First generation LNPs were formulated using the permanently charged lipid DOTAP (Dioleoyl-3-trimethylammonium-propane), while the second-generation LNPs contained the ionizable lipid DODMA (1,2-dioleoyloxy-3-(dimethylamino)propane), which is characterized by a pK_a of 7.0 [5]. We tested different helper lipid compositions (PS, DOPC (1,2-dioleoyl-*sn*-glycerol-3-phosphocholine) and Cholesterol) while using a constant amount (50 mol%) of either DOTAP or DODMA. These lipid formulations served to condense both plasmid DNA (pDNA) and messenger RNA (mRNA) encoding for enhanced green fluorescence protein (EGFP). Formulations were prepared by a time-efficient bulk mixing method, which is amenable to formulation screening [32]. However, our protocol does not support the use of PEGylated lipids and was therefore applied for *in vitro* screening experiments only. It was the aim of these screening experiments to identify the most promising formulations. One cell line was used (HuH-7) and loading efficiency was verified to be in the range of 50% to 100%, which was sufficient for decision making during the screening process. A total of 36 formulations were thus characterized by a combination of dynamic light scattering and ζ -potential measurements. Data for N/P 6 (DOTAP) and N/P 10 (DODMA) are shown in Table 1. Since PS carries a net negative charge, we were interested in its effects on nucleic acid condensation [35,36]. At N/P 6, LNPs formulated with the permanently charged lipid DOTAP condensed nucleic acids in presence of up to 10% PS. LNPs formulated with DODMA required an increased N/P ratio of 10 to reach encapsulation efficiencies (EE) of above 50% at all tested PS concentrations. Of note, mRNA EE seemed to be lower as compared to pDNA EE, which can be attributed to different nucleic acid topologies [37]. The latter study suggests that surface potentials of DNA or RNA differ, leading to a different binding and surface distribution of ions.

Our results demonstrate that PS containing LNPs with defined physico-chemical properties can be prepared using a simple bulk mixing protocol. LNPs used in the present study had a monodisperse size distribution ($\text{PDI} \leq 0.2$) and a D_H in the range of 120 to 170 nm, regardless of the encapsulated nucleic acid. This is important since *in vitro* and *in vivo* interactions of nanoparticles with biological systems critically depend on particle size. Clathrin-mediated endocytosis is typically observed for particles with a size of 120–150 nm and an upper size limit of 200 nm [38]. Extravasation of macromolecules and nanoparticles through, for example, the sinusoids of the liver into the space of Disse is limited by the size of the endothelial fenestrae of 100 to 175 nm [39]. Mechanisms of cellular uptake are discussed below. A slight but not significant increase in D_H distribution was obtained when LNPs were incubated with fetal calf serum (Supplementary Fig. 1). This can be attributed to the previously described interaction of non-PEG LNPs with serum proteins [40]. However, no detrimental agglomeration and formation of large particles ($>1 \mu\text{m}$) did occur.

The apparent surface charge or ζ -potential of particles is of similar importance for internalization. A positive charge of particles favors adsorptive mediated endocytosis but leads to unspecific cell interactions and a high plasma clearance and volume of distribution *in vivo* [38]. Whereas neutral to slightly negatively charged particles lead to an increased circulation half-life. Furthermore, they are expected to be less toxic as well as more stable compared to their positively charged counterparts [41,42].

ζ -potential measurements were performed at pH 4 (i.e., a pH smaller than the pK_a of the ionizable lipid DODMA) and at physiological pH. As expected, at pH 7.4, a significant reduction in surface charge was

CHAPTER 3. RESULTS

Claudia. Lotter et al.

European Journal of Pharmaceutics and Biopharmaceutics 172 (2022) 134–143

Table 1

LNP screening and physico-chemical characterization. LNPs were prepared by bulk mixing and contained DOPC, Cholesterol, DOTAP or DODMA nucleic acid condensing lipids, nucleic acids at different N/P ratios, and different amounts of incorporated PS. pDNA: plasmid DNA, mRNA: 5' capped messenger RNA. Values are means \pm SD, $n \geq 3$.

Formulation	% PS	N/P	pDNA			mRNA		
			D _H [nm] ^{a)}	PDI ^{b)}	ζ-potential [mV] ^{c)}	D _H [nm] ^{a)}	PDI ^{b)}	ζ-potential [mV] ^{c)}
DOTAP	0	6	138 \pm 1	0.06 \pm 0.01	55 \pm 8	122 \pm 1	0.09 \pm 0.01	10 \pm 3
	0.5	6	129 \pm 2	0.05 \pm 0.02	49 \pm 3	120 \pm 1	0.11 \pm 0.01	13 \pm 5
	1	6	122 \pm 2	0.04 \pm 0.03	47 \pm 4	125 \pm 0	0.06 \pm 0.02	12 \pm 1
	2.5	6	137 \pm 3	0.06 \pm 0.02	39 \pm 9	122 \pm 1	0.10 \pm 0.01	7 \pm 1
	5	6	130 \pm 1	0.07 \pm 0.01	28 \pm 2	134 \pm 1	0.06 \pm 0.01	3 \pm 1
DODMA	0	10	150 \pm 1	0.13 \pm 0.01	35 \pm 1	147 \pm 1	0.10 \pm 0.01	8 \pm 1
	0.5	10	126 \pm 1	0.10 \pm 0.02	21 \pm 1	134 \pm 0	0.11 \pm 0.01	10 \pm 1
	1	10	141 \pm 3	0.15 \pm 0.01	-3 \pm 2	136 \pm 1	0.16 \pm 0.02	5 \pm 1
	2.5	10	150 \pm 1	0.13 \pm 0.01	-17 \pm 3	138 \pm 1	0.14 \pm 0.02	-9 \pm 0
	5	10	136 \pm 2	0.13 \pm 0.02	-3 \pm 0	128 \pm 1	0.13 \pm 0.01	-13 \pm 1
	10	170 \pm 3	0.11 \pm 0.01	-4 \pm 1	135 \pm 1	0.13 \pm 0.01	-3 \pm 1	
	10	144 \pm 2	0.11 \pm 0.02	-6 \pm 2	132 \pm 1	0.13 \pm 0.01	-10 \pm 1	

^{a)} Hydrodynamic diameter.

^{b)} Polydispersity index.

^{c)} ζ-potential at pH 7.4.

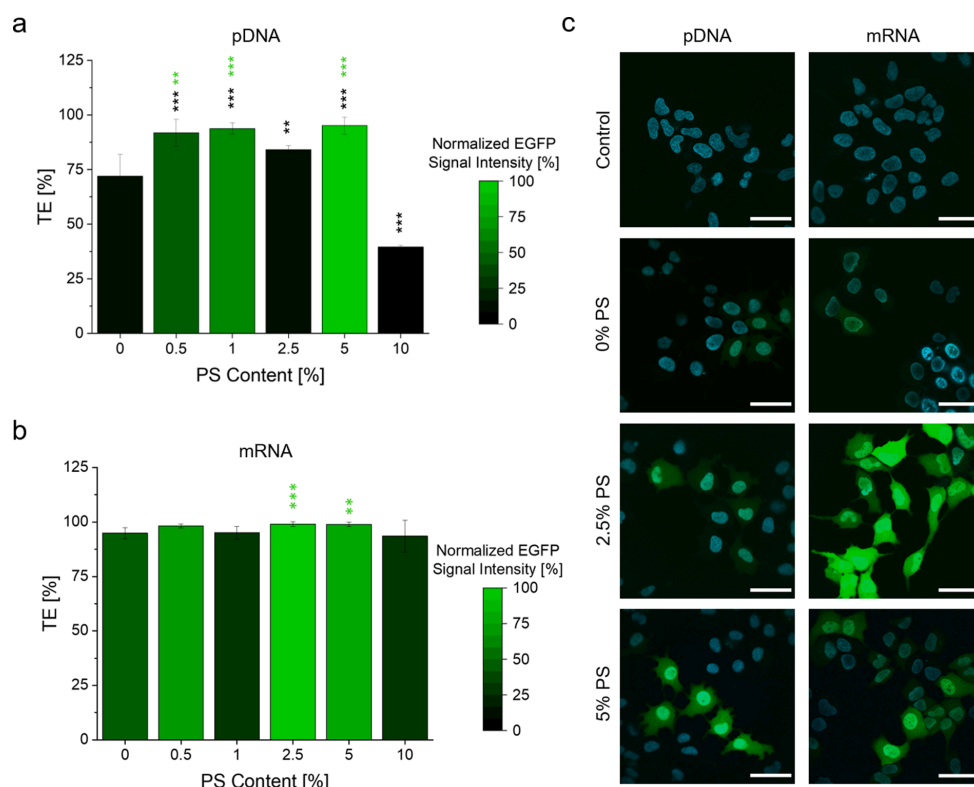


Fig. 2. Cellular transfection of PS-LNPs *in vitro*. Transfection efficiency (TE) and transfection potency (TP, expressed as normalized EGFP signal intensity) of HuH-7 cells treated with DODMA LNPs containing increasing amounts of incorporated PS at N/P 10. a) 0.28 μg pDNA mL⁻¹, 48 h incubation. b) 0.28 μg mRNA mL⁻¹, 24 h incubation. Values are means \pm SD, $n = 3$. Level of significance compared to 0% PS-LNPs: *; $p \leq 0.05$, **; $p \leq 0.01$, ***; $p \leq 0.001$; Black stars: TE. Green stars: normalized EGFP signal intensity. c) Representative CLSM images of untreated control HuH-7 cells and cells treated with DODMA LNPs with 0%, 2.5%, and 5% incorporated PS. 0.28 μg nucleic acid mL⁻¹. Left row: pDNA and 48 h incubation. Right row: mRNA and 24 h incubation. Green signal: EGFP. Cyan signal: Hoechst 33342 nuclear stain. Scale bar: 50 μm. (For interpretation of the references to color in this figure legend, the reader is referred to the web version of this article.)

observed for DODMA based formulations. The addition of PS, which has a net charge of -1 per molecule at pH 7.4, had a direct influence on the surface charge of DODMA LNPs but no effect on nucleic acid condensation or colloidal stability. This is in contrast to previous reports using systems with different lipid compositions devoid of PS [35,36]. In presence of PS, DODMA LNPs condensing pDNA at N/P 10 a reduction from 21 ± 1 mV for 0% PS to -4 ± 1 mV for 5% PS was observed. In comparison to DODMA, DOTAP is characterized by a tertiary amine and holds a higher charge density due to its non-ionizable nature. As a consequence, an N/P ratio of 6 was sufficient to condensate nucleic acids. The ζ -potential of DOTAP LNPs with incorporated PS also decreased up to 30 mV. The resulting ζ -potentials for DOTAP PS-LNPs were still highly positive. Overall, for DODMA-based LNPs, a clear trend towards negative ζ -potentials upon addition of PS was observed. In contrast, this trend was not observed for the ζ -potential of DOTAP LNPs. At pH 4, regardless of the type of lipid, the ζ -potential was positive and approximately 30 mV (data not shown).

3.2. *In vitro* cell transfection and cell viability

Integration of PS into LNPs enhanced their ability to transfect cells *in vitro*. HuH-7 liver-derived cells were used as a cell culture model. HuH-7 cells have previously been reported to express high levels of TIM/TAM receptors and were used to study the role of PS as an apoptotic mimicry strategy of enveloped dengue and EBOLA viruses [20,43,44]. For the *in vitro* screening, EGFP encoding pDNA LNP formulations were added to cells at a final nucleic acid concentration of $0.28 \mu\text{g mL}^{-1}$ or $0.83 \mu\text{g mL}^{-1}$ and were analyzed by flow cytometry for LNP effectiveness i.e., transfection efficiency (TE; i.e., number of EGFP positive cells) and transfection potency (TP; i.e., mean EGFP signal intensity expressed as single-cell relative fluorescence units). While DODMA LNPs were used at an N/P ratio of 10, DOTAP LNPs had an N/P ratio of 6 due to their enhanced EE as mentioned before. These experiments revealed a strong effect of incorporated PS on the transfection ability of LNPs formulated with DODMA as well DOTAP (Fig. 2 and Supplementary Fig. 2).

These results can be summarized as follows:

First, the TE of DODMA LNPs is considerably higher than the one of DOTAP LNPs confirming previous studies [45]. In absence of PS, DOTAP containing LNPs with up to $0.83 \mu\text{g mL}^{-1}$ pDNA cannot be used to transfect cells. This is in contrast to DODMA containing LNPs with $0.28 \mu\text{g mL}^{-1}$ pDNA, where a high number of cells were transfected (i.e., high TE) albeit TP were low. Using mRNA complexed LNPs with mRNA concentration of $0.28 \mu\text{g mL}^{-1}$ for DODMA and $0.83 \mu\text{g mL}^{-1}$ for DOTAP containing LNPs showed high TE values. However, EGFP signal intensities were again low in both cases. Due to the poor performance of DOTAP LNPs, it was therefore decided to focus for the subsequent experiments on DODMA LNP formulations only.

Second, the TP of LNPs can be enhanced considerably using defined amounts of PS. Optimal results were obtained using 1 to 5% PS. Lower PS concentrations had no effect. Excessive concentrations of PS (i.e. PS content > 5%) had no or even detrimental effects as observed by a sharp decrease in TE for pDNA containing PS-LNPs. This can be attributed to the negative charge of PS interfering with pDNA condensation. With respect to DOTAP containing PS-LNPs complexed with $0.83 \mu\text{g mL}^{-1}$ pDNA, cells could now be transfected using 1% PS (Supplementary Fig. 2b). However, despite the 3-fold increase of TE as well as the increased EGFP signal intensity, TP was still much weaker as compared to the DODMA containing LNPs. With respect to DODMA containing PS-LNPs, EGFP signal intensities could be considerably enhanced by a factor of three (PS-LNPs with mRNA) to six (PS-LNPs with pDNA) (Fig. 2a and b). It should be noted that TE values of DODMA mRNA-LNPs had already reached saturation, thus preventing a further increase in presence of PS. The increase in TP when incorporating PS into DODMA containing LNPs was visualized and confirmed by confocal scanning microscopy (Fig. 2c). Furthermore, as a general trend, overall TE is higher for mRNA since only the delivery to the cytoplasm is needed in

contrast to pDNA, where the additive permeability barrier of the nuclear membrane has to be overcome. We conclude that PS at concentrations between 1 and 5% potentiate EGFP expression in target cells. Optimal PS concentrations to be used depend on the used nucleic acids and may vary depending on the experimental conditions.

Third, it is important to note that incorporation of PS into LNPs had no effect on cell viability as determined by the MTS assay (Supplementary Fig. 3). Of note, relatively low concentrations of all LNPs were used in the present study. We therefore observed high cell viability despite the three-fold higher concentrations and the higher ζ -potential of the DOTAP based LNPs. However, concentration dependent toxicity was not further evaluated since the focus of our attention shifted to the more promising DODMA based formulations during the course of the project.

3.3. Cellular uptake of PS-LNPs

Since PS promotes receptor interactions of viral and exosomal particles, we investigated if the increased TP of PS-LNPs is a consequence of enhanced cellular uptake. Therefore, PS-LNPs condensing either fluorescently labeled Cy5-pDNA or Cy5-mRNA were incubated with HuH-7 cells at a final nucleic acid concentration of $0.034 \mu\text{g mL}^{-1}$ and were analyzed by flow cytometry (Fig. 3a and b). For pDNA LNPs 4 h post-incubation, only slight changes regarding the amount of Cy5 + cells were observed (>10%). Nevertheless, an almost 1.6- respectively 1.3-fold increased Cy5 signal intensity was observed for formulations with 2.5% PS and 5% PS as compared to the 0% PS formulation. A similar trend was observed using mRNA PS-LNPs. Again, Cy5 + cells could be increased by 13% using 2.5% PS-LNPs compared to 0% PS formulations, whereas 5% PS-LNPs lead to 15% fewer Cy5 + cells. Furthermore, Cy5 signal intensity increased 1.6-fold for 2.5% PS formulation, and again no significant difference for 5% PS formulations compared to 0% PS was observed. In these experiments, the amount of Cy5 + cells was lower using mRNA LNPs compared to LNPs condensing pDNA. This could be due to faster processing of mRNA LNPs since first EGFP signals were already observed after 4 h of incubation and were significantly higher for 2.5% PS compared to the other formulations. Overall it can be summarized that a well-defined amount of PS (i.e., 2.5 to 5% PS) was needed to induce cellular uptake confirming previous results.

To analyze the intracellular fate of PS-LNPs, we applied a combination of confocal laser scanning microscopy and differential interference contrast (DIC) live-cell microscopy (Fig. 3c) using fluorescently labeled PS-LNPs. Intracellular tracking of PS-LNPs reveals considerable differences between PS-LNPs and LNPs devoid of PS. Tracking of > 120 single particles containing 2.5 to 5% PS revealed a median particle speed of $0.11 \pm 0.04 \mu\text{m s}^{-1}$ for 2.5% PS and $0.09 \pm 0.06 \mu\text{m s}^{-1}$ for 5% PS, respectively. These median speeds were significantly higher than those of LNPs without PS ($0.06 \pm 0.05 \mu\text{m s}^{-1}$) (Supplementary Figure 4). While cellular uptake of the latter lead to their accumulation at the cell periphery, a clear accumulation in the perinuclear region of PS-LNPs is observed. It remains to be elucidated if PS has a beneficial effect on intracellular processing and cytosolic liberation of nucleic acids.

Our findings thus suggest that PS-LNPs interact with target cells in a highly specific manner. To elucidate mechanisms of cellular uptake and intracellular processing in the presence and absence of PS, we conducted a series of cellular uptake inhibition experiments (Supplementary Fig. 5). An arbitrary threshold of at least 50% inhibition was considered to be significant. Uptake of PS-LNPs (in contrast to LNPs) was specifically inhibited by Annexin V (which was previously demonstrated to bind to PS and therefore blocks the uptake of apoptotic cells [46]) and by Chlorpromazine (a known clathrin-mediated endocytosis inhibitor). Uptake of both PS-LNPs and LNPs was specifically inhibited by Colchicine (inhibitor of tubulin polymerization), Dynasore (inhibition of clathrin-mediated endocytosis), and Poly I:C (a synthetic single-stranded RNA that can competitively bind to the scavenger receptor SR-A [47]). Remarkably, Poly I:C inhibited cellular uptake of LNPs by

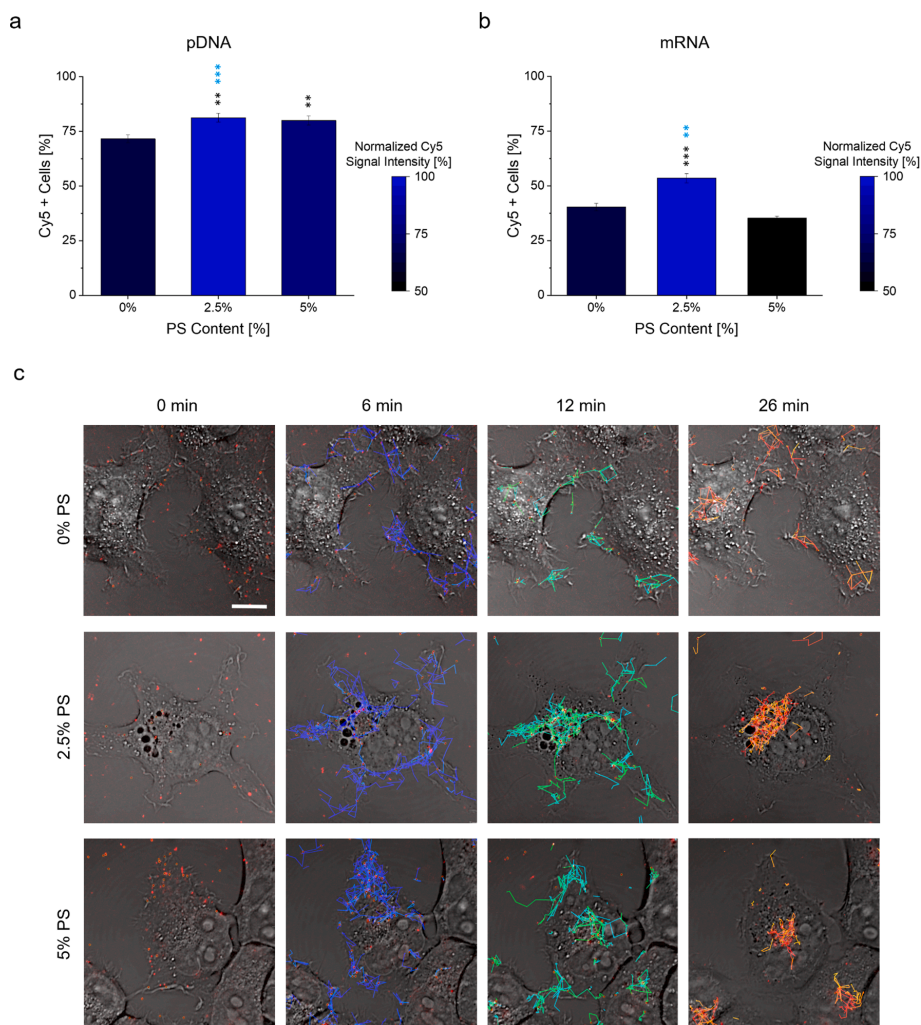


Fig. 3. Cellular uptake of PS-LNPs. HuH-7 cells were incubated with fluorescently labeled PS-LNPs (0 to 5% PS). Quantitation of cellular uptake of PS-LNPs condensing fluorescently labeled a) Cy5-pDNA or b) Cy5-mRNA at a final nucleic acid concentration of $0.034 \mu\text{g mL}^{-1}$ by flow cytometry (N/P 10, 4 h incubation). Values are means \pm SD, $n = 3$. Level of significance compared to 0% PS-LNPs: *: $p \leq 0.05$, **: $p \leq 0.01$, ***: $p \leq 0.001$; Black stars: Cy5 + cells. Blue stars: normalized Cy5 signal intensity. c) Representative CLSM images of DII-PS-LNP tracking analysis (N/P 10, $0.28 \mu\text{g pDNA mL}^{-1}$). Particle tracks are heat-mapped from blue (6 min) to red (26 min). Scale Bar: $10 \mu\text{m}$. (For interpretation of the references to color in this figure legend, the reader is referred to the web version of this article.)

50% but almost completely blocked the uptake of PS-LNPs.

These experiments indicate that LNPs and PS-LNPs share cellular uptake pathways such as clathrin-mediated endocytosis, a process that depends on microtubules [48]. In addition, PS-LNPs activate PS-specific uptake mechanisms, as demonstrated by the inhibitory action of Annexin V. Our studies with Annexin V suggest that this effect contributes by 50% to the total observed cellular uptake. Interestingly, PS seems to potentiate the inhibitory effect of Poly I:C, suggesting a strong involvement of the scavenger receptor SR-A. This receptor acts as a pathogen sensor of extracellular dsRNA and recognizes a range of ligands including low density lipoproteins and nucleic acids [47,49]. Our results seem to suggest that SR-A facilitates cellular entry of LNPs and

that PS facilitates this process.

3.4. *In vivo* evaluation of PS-LNPs

The increased ability of PS-LNP to transfect cells observed *in vitro* was verified *in vivo* using the developing zebrafish embryo (ZFE) as an *in vivo* vertebrate screening model [50]. Formulations were injected intravenously into the Duct of Cuvier of ZFE 36 h post-fertilization. In these experiments (and in contrast to the *in vitro* experiments), PS-LNPs were modified with PEGylated phospholipids (i.e., DMPE-PEG2000). This modification is necessary to suppress opsonization and agglomeration in presence of plasma protein. In addition, immune interactions

3.4. PART IV: APPLICATION OF THE ZEBRAFISH MODEL

Claudia Lotter et al.

European Journal of Pharmaceutics and Biopharmaceutics 172 (2022) 134–143

can be suppressed such as inflammatory reactions or recognition of LNPs by cells of the mononuclear phagocyte system [51]. Since PEGylation interferes with the condensation of nucleic acids, these LNPs were prepared using a microfluidics protocol [52] and not bulk mixing. PEGylated LNPs were characterized by a mean D_H of approximately 105 nm and a monodisperse PDI of 0.15 (Supplementary Table 1). PEGylated LNPs have a slightly lower surface charge at physiological pH as compared to their non-PEGylated counterparts with values in the range of -3 mV to -12 mV. This is indicative of the shielding of the negative charge of PS by DMPE-PEG2000. The EE was in the range of 87–100% for pDNA and 54–78% for mRNA. For all *in vivo* studies, the same amounts of nucleic acids were administered (i.e., 6 nL injection volume, $75 \mu\text{g mL}^{-1}$ mRNA, $150 \mu\text{g mL}^{-1}$ pDNA).

In vivo experiments in ZFE confirmed our *in vitro* results (Fig. 4). In our study, we have focused on an analysis of the ZFE tail region in the vicinity of the caudal vein since this tissue, but not the teleost liver, harbors macrophages, and scavenger endothelial cells. It can therefore be considered to have the same functionality as the mammalian liver sinusoids [53]. Furthermore, the head region of the ZFE was excluded from analysis since passive trapping of particles within the ocular vasculature cannot be excluded. As expected and in agreement with previous *in vitro* results, free nucleic acids or LNPs devoid of PS show minimal activity 42 h post-injection (hpi). The addition of PS to pDNA-LNPs led to 1.3-fold enhanced EGFP expression in the tail region of the ZFE compared to 0% PS formulation. In contrast, the addition of PS to mRNA-LNPs resulted in a strong and widely distributed EGFP signal throughout the ZFE, leading to a 3.7-fold increased TP (Fig. 4b). A semi-quantitative analysis of the tail region of the ZFE revealed 3.2-fold versus 5.2-fold increase in TE between pDNA PS-LNP and mRNA PS-LNP treated ZFE compared to 0% PS formulations. It can be concluded that PS enhances TE for both types of LNPs, however, to a higher extent

for mRNA-LNPs as compared to pDNA-LNP. Even though the evaluation of TP reveals less pronounced differences, the same trends are observed. Concerning the biodistribution of LNPs, we observed an increased EGFP signal in the tail region for PS containing LNP formulations. This distribution pattern is indicative of PS-LNP deposition in the ZFE tail vasculature which could be localized starting from 4 to 8 hpi. Semi-quantitative image analysis of confocal image stacks revealed enhanced extravasation and penetration of PS-LNPs into tissues surrounding the vasculature (Fig. 4c). In these experiments, $62\% \pm 4\%$ of DiI PS-LNP signal was associated with the ZFE vasculature. This is in contrast to LNPs devoid of PS (Supplementary Fig. 6), which were retained to a higher degree within the vasculature ($46\% \pm 9\%$ association). These interactions with the vasculature are similar to the previously reported biodistribution of PS marked exosomes and negatively charged liposomes [54]. Overall no toxic effects were observed in ZFE after LNP administration.

4. Conclusion

In the present study, we could demonstrate that the biomimetic incorporation of PS into LNPs enhances transfection efficiency and transfection potency *in vitro* as well as *in vivo*. Furthermore, PS-LNPs have a distinct intracellular mobility, which is similar to enveloped viruses, exosomes, and PS equipped liposomes. PS enhances interactions with scavenger receptors of target cells leading to an enhanced cellular uptake by clathrin-mediated endocytosis. PS enhances the transfection efficiency and transfection potency of both pDNA and mRNA based LNPs. Further optimization of PS-LNPs can presumably be achieved by the use of more complex viral-like compositions [31]. Additional studies will focus on the beneficial anti-inflammatory and tolerogenic effects of PS [55] when combined with LNPs. The incorporation of the bioactive

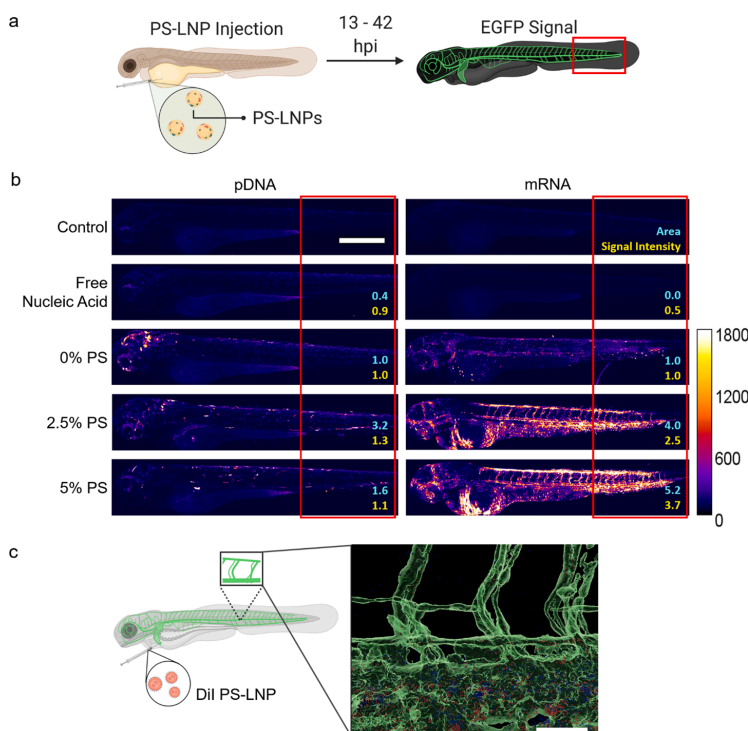


Fig. 4. *In vivo* evaluation of PS-LNP uptake and transfection in the zebrafish embryo (ZFE). Transfection efficiency (TE), transfection potency (TP), and biodistribution of LNPs were studied using ZFE. a) Schematic representation of the experimental procedure. After intravenous injection of LNPs, EGFP signal were visualized by CLSM within 13 hpi (for mRNA) to 42 hpi (for pDNA). Red: area of interest. b) Representative CLSM images of ZFE injected with PS-LNPs condensing either EGFP coding pDNA or mRNA. Color-coding according to EGFP signal intensity. Cyan: TE-fold difference as compared to 0% PS formulation; Yellow: TP-fold difference as compared to 0% PS formulation. Scale Bar: 100 μm . c) Representative 3D-rendered image of a ZFE Tg(kdrl:EGFP) injected with DiI-labeled 2.5% PS-LNPs condensing pDNA. ZFE were analyzed 4 hpi. Green signal: ZFE vasculature, Red signal: DiI PS-LNPs associated with ZFE vasculature, Blue signal: DiI PS-LNPs not associated with ZFE vasculature. Scale Bar: 50 μm . (For interpretation of the references to color in this figure legend, the reader is referred to the web version of this article.)

CHAPTER 3. RESULTS

Claudia. Lotter et al.

lipid PS in LNPs is a promising strategy to enhance the efficacy of gene delivery systems and can serve for enhancement of other delivery systems by the decoration of the carriers.

5. Ethical regulations

Animals were maintained according to Swiss animal welfare regulations and were handled according to approved institutional animal care and use protocols of the University of Basel.

Declaration of Competing Interest

The authors declare that they have no known competing financial interests or personal relationships that could have appeared to influence the work reported in this paper.

Data availability statement

Supporting and raw data is included in the Supplementary Materials or can be retrieved from the public data repository Zenodo (<https://zenodo.com>).

Acknowledgment

The authors thank Dr. S. Schenk (University of Basel) for providing valuable scientific advice and support. We thank Dr. K. Schleicher (Imaging Core Facility, University of Basel) for his valuable help with imaging processing and analysis. We thank Prof. Dr. M. Affolter and Dr. H.G. Belting for providing zebrafish eggs. Furthermore, the authors acknowledge Nicole Rimann (University Children's Hospital Zurich) for the supply with pDNA. Schemes were created using BioRender.com.

Funding

This work was supported by the Swiss Nanoscience Institute (Grant P1801), the Swiss National Science Foundation (Sinergia Grant CRSII5_180257), and the Phospholipid Research Center Heidelberg (Grant JHU-2021-094/2-1).

Author contributions

J.H., T.E., C.L., C.A. contributed to the apoptotic cell mimicry LNP concept, experiment planning, and writing the manuscript. C.L. and C.A. contributed equally to LNP formulation, characterization, tissue-culture work, and ZFE work. J.B. contributed to ZFE experiments. P.D. and C.P. contributed to the experimental design and editing of the manuscript.

Appendix A. Supplementary data

Supplementary data to this article can be found online at <https://doi.org/10.1016/j.ejpb.2022.02.007>.

References

- [1] A. Akinc, et al., The Onpatro story and the clinical translation of nanomedicines containing nucleic acid-based drugs, *Nat. Nanotechnol.* 14 (2019) 1084–1087.
- [2] J. Buck, P. Grossen, P.R. Cullis, J. Huwyler, D. Witzigmann, Lipid-Based DNA Therapeutics: Hallmarks of Non-Viral Gene Delivery, *ACS Nano* 13 (4) (2019) 3754–3782.
- [3] M.J. Stewart, et al., Gene Transfer In Vivo with DNA-Liposome Complexes: Safety and Acute Toxicity in Mice, *Hum. Gene Ther.* 3 (1992) 267–275.
- [4] H. San, et al., Safety and Short-Term Toxicity of a Novel Cationic Lipid Formulation for Human Gene Therapy, *Hum. Gene Ther.* 4 (1993) 781–788.
- [5] J. Heyes, L. Palmer, K. Bremner, I. MacLachlan, Cationic lipid saturation influences intracellular delivery of encapsulated nucleic acids, *J. Controlled Release* 107 (2) (2005) 276–287.
- [6] S.C. Semple, S.K. Klimuk, T.O. Harasym, M.J. Hope, Lipid-based formulations of antisense oligonucleotides for systemic delivery applications, in: *Methods in Enzymology*, vol. 313, Academic Press, 2000, pp. 322–341.

European Journal of Pharmaceutics and Biopharmaceutics 172 (2022) 134–143

- [7] A. Akinc, et al., A combinatorial library of lipid-like materials for delivery of RNAi therapeutics, *Nat. Biotechnol.* 26 (2008) 561–569.
- [8] C.D. Sago, et al., High-throughput in vivo screen of functional mRNA delivery identifies nanoparticles for endothelial cell gene editing, *Proc. Natl. Acad. Sci.* 115 (2018) E9944–E9952.
- [9] Y. Xia, J. Tian, X. Chen, Effect of surface properties on liposomal siRNA delivery, *Biomaterials* 79 (2016) 56–68.
- [10] A. Akinc, M. Goldberg, J. Qin, J.R. Dorkin, C. Gamba-Vitalo, M. Maier, K. N. Jayaprakash, M. Jayaraman, K.G. Rajeev, M. Manoharan, V. Kotliansky, I. Röhl, E.S. Leshchiner, R. Langer, D.G. Anderson, Development of lipidoid-siRNA formulations for systemic delivery to the liver, *Mol. Ther. J. Am. Soc. Gene Ther.* 17 (5) (2009) 872–879.
- [11] J. Kim, A. Jozic, G. Sahay, Naturally Derived Membrane Lipids Impact Nanoparticle-Based Messenger RNA Delivery, *Cell. Mol. Bioeng.* 13 (2020) 463–474.
- [12] S. Patel, et al., Naturally-occurring cholesterol analogues in lipid nanoparticles induce polymorphic shape and enhance intracellular delivery of mRNA, *Nat. Commun.* 11 (2020) 1–13.
- [13] J.A. Kulkarni, et al., Design of lipid nanoparticles for in vitro and in vivo delivery of plasmid DNA, *Nanomed. Nanotechnol. Biol. Med.* 13 (2017) 1377–1387.
- [14] X. Cheng, R.J. Lee, The role of helper lipids in lipid nanoparticles (LNPs) designed for oligonucleotide delivery, *Adv. Drug Deliv. Rev.* 99 (2016) 129–137.
- [15] Q. Cheng, et al., Selective organ targeting (SORT) nanoparticles for tissue-specific mRNA delivery and CRISPR-Cas gene editing, *Nat. Nanotechnol.* 15 (2020) 313–320.
- [16] P.T. Ivanova, et al., Lipid composition of viral envelope of three strains of influenza virus – not all viruses are created equal, *ACS Infect. Dis.* 1 (2015) 399–452.
- [17] K. Morizono, I.S.Y. Chen, Role of Phosphatidylserine Receptors in Enveloped Virus Infection, *J. Virol.* 88 (2014) 4275–4290.
- [18] J. Wang, L. Qiao, Z. Hou, G. Luo, J.-H. Ou, TIM-1 Promotes Hepatitis C Virus Cell Attachment and Infection, *J. Virol.* 91 (2) (2017), <https://doi.org/10.1128/JVI.01583-16>.
- [19] B. Brunton, et al., TIM-1 serves as a receptor for Ebola virus in vivo, enhancing viremia and pathogenesis, *PLoS Negl. Trop. Dis.* 13 (2019).
- [20] L.-W. Chu, C.-J. Yang, K.-J. Peng, P.-L. Chen, S.-J. Wang, Y.-H. Ping, TIM-1 As a Signal Receptor Triggers Dengue Virus-Induced Autophagy, *Int. J. Mol. Sci.* 20 (19) (2019) 4893, <https://doi.org/10.3390/ijms20194893>.
- [21] A. Amara, J. Mercer, Viral apoptotic mimicry, *Nat. Rev. Microbiol.* 13 (8) (2015) 461–469.
- [22] A.C. Doran, A. Yurdagül, I. Tabas, Efferocytosis in health and disease, *Nat. Rev. Immunol.* 20 (4) (2020) 254–267, <https://doi.org/10.1038/s41577-019-0240-6>.
- [23] E. Boada-Romero, J. Martinez, B.L. Heckmann, D.R. Green, The clearance of dead cells by efferocytosis, *Nat. Rev. Mol. Cell Biol.* 21 (7) (2020) 398–414.
- [24] S.P. Davies, G.M. Reynolds, Z. Stamatiki, Clearance of Apoptotic Cells by Tissue Epithelia: A Putative Role for Hepatocytes in Liver Efferocytosis, *Front. Immunol.* 9 (2018).
- [25] J.C. Seeberg, et al., Non-professional phagocytosis: a general feature of normal tissue cells, *Sci. Rep.* 9 (2019) 11875.
- [26] M.B. Naeni, V. Bianconi, M. Pirro, A. Sahebkar, The role of phosphatidylserine recognition receptors in multiple biological functions, *Cell. Mol. Biol. Lett.* 25 (1) (2020), <https://doi.org/10.1186/s11658-020-00214-z>.
- [27] J.L.M. Wanderley, R.A. DaMatta, M.A. Barcinski, Apoptotic mimicry as a strategy for the establishment of parasitic infections: parasite- and host-derived phosphatidylserine as key molecule, *Cell Commun. Signal.* 18 (2020) 10.
- [28] A. Matsumoto, et al., Role of Phosphatidylserine-Derived Negative Surface Charges in the Recognition and Uptake of Intravenously Injected B16BL6-Derived Exosomes by Macrophages, *J. Pharm. Sci.* 106 (2017) 168–175.
- [29] X. Wei, et al., Surface Phosphatidylserine Is Responsible for the Internalization of Microvesicles Derived from Hypoxia-Induced Human Bone Marrow Mesenchymal Stem Cells into Human Endothelial Cells, *PLOS ONE* 11 (2016) e0147360.
- [30] Z. Yao, Y. Qiao, X. Li, J. Chen, J. Ding, L.u. Bai, F. Shen, B. Shi, J. Liu, L.u. Peng, J. Li, Z. Yuan, R.M. Sandri-Goldin, Exosomes Exploit the Virus Entry Machinery and Pathway To Transmit Alpha Interferon-Induced Antiviral Activity, *J. Virol.* 92 (24) (2018), <https://doi.org/10.1128/JVI.01578-18>.
- [31] S. Pollock, et al., Uptake and trafficking of liposomes to the endoplasmic reticulum, *FASEB J. Off. Publ. Fed. Am. Soc. Exp. Biol.* 24 (2010) 1866–1878.
- [32] J. Buck, D. Mueller, U. Mettall, M. Ackermann, H.M. Grisch-Chan, B. Thöny, A. Zumbuehl, J. Huwyler, D. Witzigmann, Improvement of DNA Vector Delivery of DOTAP Lipoplexes by Short-Chain Aminolipids, *ACS Omega* 5 (38) (2020) 24724–24732.
- [33] S. Sieber, P. Grossen, P. Detampel, S. Siegfried, D. Witzigmann, J. Huwyler, Zebrafish as an early stage screening tool to study the systemic circulation of nanoparticulate drug delivery systems in vivo, *J. Control. Release* 264 (2017) 180–191.
- [34] J.S. Bolten, A. Pratsinis, C.L. Alter, G. Fricker, J. Huwyler, Zebrafish (*Danio rerio*) larva as an in vivo vertebrate model to study renal function, *Am. J. Physiol.-Ren. Physiol.* (2022), <https://doi.org/10.1152/ajprenal.00375.2021>.
- [35] A.L. Bailey, P.R. Cullis, Membrane Fusion with Cationic Liposomes: Effects of Target Membrane Lipid Composition ¹, *Biochemistry* 36 (1997) 1628–1634.
- [36] F.C. Tsui, D.M. Ojcius, W.L. Hubbell, The intrinsic pKa values for phosphatidylserine and phosphatidylethanolamine in phosphatidylcholine host bilayers, *Biophys. J.* 49 (1986) 459–468.
- [37] L. Li, S.A. Pabit, S.P. Meisburger, L. Pollack, Double-stranded RNA resists condensation, *Phys. Rev. Lett.* 106 (2011), 108101.

3.4. PART IV: APPLICATION OF THE ZEBRAFISH MODEL

Claudia Lotter et al.

European Journal of Pharmaceutics and Biopharmaceutics 172 (2022) 134–143

- [38] H. Kettiger, A. Schipanski, P. Wick, J. Huwyler, Engineered nanomaterial uptake and tissue distribution: from cell to organism, *Int. J. Nanomedicine* 8 (2013) 3255–3269.
- [39] F. Braet, E. Wisse, Structural and functional aspects of liver sinusoidal endothelial cell fenestrae: a review, *Comp. Hepatol.* 1 (2002) 1.
- [40] V. Francia, R.M. Schiffelers, P.R. Cullis, D. Witzigmann, The Biomolecular Corona of Lipid Nanoparticles for Gene Therapy, *Bioconjug. Chem.* 31 (2020) 2046–2059.
- [41] M.J. Mitchell, et al., Engineering precision nanoparticles for drug delivery, *Nat. Rev. Drug Discov.* 20 (2021) 101–124.
- [42] S. Martins, et al., Solid lipid nanoparticles as intracellular drug transporters: An investigation of the uptake mechanism and pathway, *Int. J. Pharm.* 430 (2012) 216–227.
- [43] L. Meertens, X. Carnec, M. Lecoïn, R. Ramdasi, F. Guivel-Benhassine, E. Lew, G. Lemke, O. Schwartz, A. Amara, The TIM and TAM Families of Phosphatidylserine Receptors Mediate Dengue Virus Entry, *Cell Host Microbe* 12 (4) (2012) 544–557.
- [44] A.S. Kondratowicz, et al., T-cell immunoglobulin and mucin domain 1 (TIM-1) is a receptor for Zaire Ebolavirus and Lake Victoria Marburgvirus, *Proc. Natl. Acad. Sci.* 108 (2011) 8426–8431.
- [45] A.K.K. Leung, Y.Y.C. Tam, P.R. Cullis, Lipid Nanoparticles for Short Interfering RNA Delivery, *Adv. Genet.* 88 (2014) 71–110.
- [46] V.A. Fadok, et al., Exposure of phosphatidylserine on the surface of apoptotic lymphocytes triggers specific recognition and removal by macrophages, *J. Immunol.* 148 (1992) 2207–2216.
- [47] G.V. Limmon, et al., Scavenger receptor class-A is a novel cell surface receptor for double-stranded RNA, *FASEB J. Off. Publ. Fed. Am. Soc. Exp. Biol.* 22 (2008) 159–167.
- [48] A. Kakigi, et al., Actin filaments and microtubules regulate endocytosis in marginal cells of the stria vascularis, *Acta Otolaryngol. (Stockh.)* 128 (2008) 856–860.
- [49] E. Pandey, A.S. Nour, E.N. Harris, Prominent Receptors of Liver Sinusoidal Endothelial Cells in Liver Homeostasis and Disease, *Front. Physiol.* 11 (2020) 873.
- [50] S. Sieber, P. Grossen, J. Bussmann, F. Campbell, A. Kros, D. Witzigmann, J. Huwyler, Zebrafish as a preclinical in vivo screening model for nanomedicines, *Adv. Drug Deliv. Rev.* 151–152 (2019) 152–168, <https://doi.org/10.1016/j.addr.2019.01.001>.
- [51] P.L. Turecek, M.J. Bossard, F. Schoetens, I.A. Ivens, PEGylation of Biopharmaceuticals: A Review of Chemistry and Nonclinical Safety Information of Approved Drugs, *J. Pharm. Sci.* 105 (2016) 460–475.
- [52] M. Sedighi, et al., Rapid optimization of liposome characteristics using a combined microfluidics and design-of-experiment approach, *Drug Deliv. Transl. Res.* 9 (2019) 404–413.
- [53] F. Campbell, F.L. Bos, S. Sieber, G. Arias-Alpizar, B.E. Koch, J. Huwyler, A. Kros, J. Bussmann, Directing Nanoparticle Biodistribution through Evasion and Exploitation of Stab2-Dependent Nanoparticle Uptake, *ACS Nano* 12 (3) (2018) 2138–2150.
- [54] F.J. Verweij, C. Revenu, G. Arras, F. Dingli, D. Loew, D.M. Pegtel, G. Follain, G. Allio, J.G. Goetz, P. Zimmermann, P. Herbomel, F. Del Bene, G. Raposo, G. van Niel, Live Tracking of Inter-organ Communication by Endogenous Exosomes In Vivo, *Dev. Cell* 48 (4) (2019) 573–589.e4.
- [55] M. Darabi, A. Kontush, Phosphatidylserine in atherosclerosis, *Curr. Opin. Lipidol.* 27 (4) (2016) 414–420.

3.4.4 Publication 4

***In vivo* acoustic manipulation of microparticles in zebrafish embryos**

Viktor Manuel Jooss, **Jan Stephan Bolten**, Jörg Huwyler, Daniel Ahmed

Sci Adv. 2022 Mar 25;8(12):eabm2785.

doi: 10.1126/sciadv.abm2785.

Personal contribution:

My contribution to this research article includes zebrafish larvae experiments to assess pharmacokinetic aspects. I was involved in the designing, planning, and executing *in vivo* studies. Thus, I wrote parts of the method, results, and discussion sections and proofread the manuscript.

ENGINEERING

In vivo acoustic manipulation of microparticles in zebrafish embryos

Viktor Manuel Jooss¹, Jan Stephan Bolten², Jörg Huwlyer², Daniel Ahmed^{1*}

In vivo micromanipulation using ultrasound is an exciting technology with promises for cancer research, brain research, vasculature biology, diseases, and treatment development. In the present work, we demonstrate in vivo manipulation of gas-filled microparticles using zebrafish embryos as a vertebrate model system. Micromanipulation methods often are conducted in vitro, and they do not fully reflect the complex environment associated in vivo. Four piezoelectric actuators were positioned orthogonally to each other around an off-centered fluidic channel that allowed for two-dimensional manipulation of intravenously injected microbubbles. Selective manipulation of microbubbles inside a blood vessel with micrometer precision was achieved without interfering with circulating blood cells. Last, we studied the viability of zebrafish embryos subjected to the acoustic field. This successful high-precision, in vivo acoustic manipulation of intravenously injected microbubbles offers potentially promising therapeutic options.

INTRODUCTION

Micromanipulation methods, which include optical (1), optoelectronic (2), acoustic (3–20), or magnetic (21–24), are commonly used to elucidate biological processes at the cellular level. However, studies involving micromanipulation are often conducted in vitro, which does not fully reflect the complexity of in vivo cellular environments. Successful transition of micromanipulation methods to in vivo use will have particularly substantial impacts in the fields of cancer research, brain research, and vasculature biology.

Recently, researchers have used optical tweezers to trap and manipulate particles and cells in small animal models, for example, within the vasculatures of zebrafish embryos (ZFEs) (25) and in the almost-transparent blood vessels in the ears of mice (26). In addition, optical tweezers have been used to manipulate otoliths to control vestibular behaviors in larval zebrafish (27, 28). Notably, although the high spatial resolution of optical tweezers makes them attractive for use in small model organisms, optical methods are restricted to transparent samples. Other drawbacks of optical methods are their association with bulky, complex, and expensive setups that may be difficult and expensive to miniaturize and their high power. Optical methods can cause physiological damage due to laser-induced heating and multiphoton absorption in biological materials (29). It is also worth noting that optical tweezers have limited penetration depth, on the scale of millimeters, which is not sufficient for manipulation tasks in larger animals.

Magnetic systems have the potential to open up manipulation to nontransparent samples and larger penetration depths. For example, injection of magnetic microparticles into zebrafish and mouse embryos has been used to enable three-dimensional (3D) rotational manipulation for microscopy (30). Magnetically responsive ferrofluid microdroplets have been used to quantify anisotropic stress in a mouse embryo (31). Magnetic micro- and nanoparticles have also been used for in vivo drug delivery in mice, and more recently, magnetic microrobots and swarms have been successfully navigated

inside mice (32). However, magnetism-based methods have the fundamental drawback of depending on particles that have been doped with magnetic materials. In addition, when in the animal body, the particles are cleared through iron metabolism, which can take months from the time of administration (33, 34).

Acoustic methods for in vivo micromanipulation represent an exciting technology that has potential to bypass the above-mentioned problems. In general, the radiation forces associated with acoustic systems are large, typically in the micro- to nanonewtons (35). A recent study demonstrated the use of an ultrasound beam consisting of 256 piezo elements to trap a 3-mm glass bead inside the urinary bladder of a pig (36). Another used four piezo elements to develop an acoustic vortex generator and manipulate microparticles within rodent vasculatures (37). In the context of small model organisms such as *Caenorhabditis elegans* and zebrafish, acoustic manipulation technology has been widely used for organism-level manipulation and levitation, but no work to date has been conducted on controlling foreign particles inside small-organism vasculatures (3, 38–41). In vivo manipulation inside a zebrafish requires sufficient force to overcome drag, selective trapping of a microparticle of interest, and high-precision manipulation on account of vasculature micrometer dimensions. Here, we report the development of an in vivo acoustic manipulation method that addresses these fundamental challenges. Manipulation of injected microparticles to a spatially targeted location in ZFEs could open up new approaches for targeted drug therapies and tightly controlled toxicity studies.

Zebrafish are small aquatic vertebrates widely used as a standard animal model in research on account of their small size, transparent bodies, rapid embryonic development process, and relatively simple genetic manipulation. Numerous genetic zebrafish disease models have been used to study clinically relevant disorders including heart disease, anemias, cancer, and diseases of the nervous system (42). The ZFE model thus serves as an alternative, high-throughput, cost-effective method for drug screening and is frequently used to identify cures. However, current drug screening methodologies cannot avoid exposing the entire fish to the drug of interest. More accurate effects and conclusions could be realized by specifically delivering a drug to the tissue or site where its effect is desired; for example,

Copyright © 2022
The Authors, some
rights reserved;
exclusive licensee
American Association
for the Advancement
of Science. No claim to
original U.S. Government
Works. Distributed
under a Creative
Commons Attribution
License 4.0 (CC BY).

¹Acoustics Robotics Systems Lab (ARSL), ETH-Zürich, Rüschlikon CH-8803, Switzerland.

²Department of Pharmaceutical Sciences, Division of Pharmaceutical Technology, University of Basel, Basel CH-4056, Switzerland.

*Corresponding author. Email: dahmed@ethz.ch

delivering a heart disease medication directly to the heart would enable precise observation of its metabolism, toxicologic effects, and elimination in that tissue. Furthermore, selective delivery by means of micromanipulation can aid in decreasing off-target effects and increasing therapeutic efficacy.

Here, we present an *in vivo* acoustic manipulation device and demonstrate microparticle manipulation under blood flow in the vasculatures of ZFEs. In particular, we show acoustic manipulation of gas-filled microbubbles with micrometer precision along with 2D spatial control of a microbubble. We achieved this by designing the zebrafish chamber to be off-center and applying frequency modulation control of the acoustic field. We also demonstrate reversible manipulation, i.e., controlled back and forth motion, of microbubbles in the intersegmental vessels (ISVs) and the cerebral blood vessels of ZFEs. Last, we confirmed the viability of ZFEs in the presence of the acoustic field.

RESULTS

Experimental setup

Our *in vivo* acoustic manipulation device was composed of four identical piezoelectric actuators and a polydimethylsiloxane (PDMS)-based transparent polymer chamber accommodating a circular channel in which the ZFE was arranged (see also fig. S1). The piezoelectric actuators, with thickness-mode resonance frequency of 4.25 MHz, were positioned orthogonally to each other; see Fig. 1A. The zebrafish sample holder was positioned 2 mm off-center with respect to the orthogonally positioned transducer pairs, thus enabling a wider manipulation range of ~ 100 μm . PDMS was selected as the material for the acoustic manipulation chamber due to being optically and acoustically transparent and chemically inert (43). Since the ZFE is also optically transparent, the combination with PDMS is ideally suited for use on inverted microscopes. For the experiment, clinically used ultrasound imaging agents “SonoVue” were carefully injected into the vasculature of ZFE at 72 hours postfertilization (hpf) by a high-precision pneumatic pico-pump. The microbubbles contained sulfur hexafluoride enclosed by a thin lipid-monolayer membrane, thus extending the stability of the microbubbles up to 6 hours (44, 45). The embryo was carefully positioned in the circular channel and subsequently immobilized using an agar gel to ensure that it could not swim away or be made to drift by the presence of an acoustic field (see Materials and Methods). A pair of electronic function generators connected to the piezoelectric transducers were used to maneuver the microbubble *in vivo*. The excitation ultrasound frequencies were modulated from 4.0 to 4.25 MHz, and an applied peak-to-peak voltage (V_{pp}) between 1 and 17.5 V_{pp} was used. The whole setup was positioned on an inverted microscope with phase imaging capabilities to visualize and track the microbubbles inside the vasculature. Last, experimental images and videos were captured using high-sensitivity and high-speed cameras.

Here, we have developed an *in vivo* acoustic manipulation system using clinically approved, commercially available, biocompatible gas-filled polymeric-shelled microbubbles. The intravenously injected microbubbles circulated freely within the vasculature of the ZFE. They drifted through the heart down the dorsal aorta (DA) toward the tail end of the embryo and then recirculated back into the heart through the posterior cardinal vein (PCV).

When acoustic waves propagate through ZFE sample holder, the incident acoustic energy is transmitted and reflected first at the

PDMS/agar and then at the agar/ZFE interface according to the acoustic impedance mismatches (see also Fig. 1C and fig. S2). The acoustic impedance, Z , of a material can be computed as $Z = \rho c$, where ρ and c are the density of the material and the speed of sound in that material, respectively. We assume that the embryo has properties similar to that of other soft biological samples as listed in table S1 (43, 46, 47). The transmission is expressed by the intensity transmission coefficient, T . At the interface between the embryo and the agar gel, the transmission can be calculated as $T = 1 - \left[\frac{Z_{ZFE} - Z_{agar}}{Z_{ZFE} + Z_{agar}} \right]^2$, where Z_{agar} is the impedance of the agar solution, while Z_{ZFE} is the impedance of the ZFE. Since the acoustic impedance of PDMS, agar, and ZFEs is similar to each other (see also table S1), the acoustic wave intensity is transmitted 96.1% at the PDMS/agar interface and 99.9% at the agar/ZFE interface. The transmission through the soft materials is more than 90%. Thus, the size or geometry of ZFEs should not affect acoustic trapping.

As a pair of oppositely positioned horizontal piezoelectric transducers are activated at a similar frequency and amplitude, a 1D standing acoustic wavefield develops (48). The wavefield comprises of a series of pressure nodal and antinodal lines, which are separated by quarter wavelengths (see also Fig. 1E). This distance $d = \frac{c}{4f}$ depends on the speed of sound of the material and actuation frequency. Similarly, if a second set of piezo transducers in the x direction is actuated, then they produce a standing wavefield propagating in the x direction. The two sets of wavefields interfere, and their superposition produces a 2D standing acoustic wavefield with nodal and antinodal points (48). The distance between each nodal point was measured to be 182 ± 17 μm at 4.2 MHz when actuated with 5 V_{pp} . The 1D and 2D lattice-like acoustic pattern produced inside a circular channel is shown in Fig. 1 (D and E) (see also movies S1 and S2).

When acoustic waves travel through a liquid containing microparticles, they induce a time-average acoustic radiation force on the particles (49). This force, which results from the scattering of incident waves, is composed of primary and secondary radiation forces. The primary radiation force arises due to interactions of particles with the standing wavefield. The primary radiation force, $F_R(x) = 4\pi\Phi(\tilde{\kappa}, \tilde{\rho}) k_x a^3 E_a \sin(2k_x x)$, on a small spherical compressible particle at position x in an acoustic pressure field can be estimated from the time-averaged gradient of the Gor'kov potential (49, 50). The radius a of the particle in this case is much smaller than the acoustic wavelength λ in a 1D standing wavefield of wave number k_x . E_a denotes the acoustic energy density. The acoustophoretic contrast factor $\Phi = \frac{1}{3} \left[\frac{5\tilde{\rho} - 2}{2\tilde{\rho} + 1} - \tilde{\kappa} \right]$ determines the directionality of

the radiation force; $\tilde{\rho} = \frac{\rho_s}{\rho_0}$, where ρ_0 and ρ_s respectively denote the density of the liquid and of the particle; $\tilde{\kappa} = \frac{\kappa_s}{\kappa_0}$, where κ_0 and κ_s respectively denote the compressibility of the liquid and the particle. The acoustophoretic contrast factor Φ for polystyrene particles is +0.24 in water, suggesting that they will move to the nodal pressure lines. In contrast, the behavior of the shelled microbubbles in an acoustic field is size dependent. Depending on size, the resonance frequency ranges between 1 and 9 MHz, as indicated by the manufacturer (44, 51, 52). Microbubbles that have resonance frequencies larger than the excitation frequency move to the pressure antinodes, while those having a resonance frequency smaller than the excitation frequency move to the pressure nodes (51, 52). To clarify the trapping locations of the microbubbles, we filled a microchannel with SonoVue microbubbles. Under excitation frequencies between

AQ6

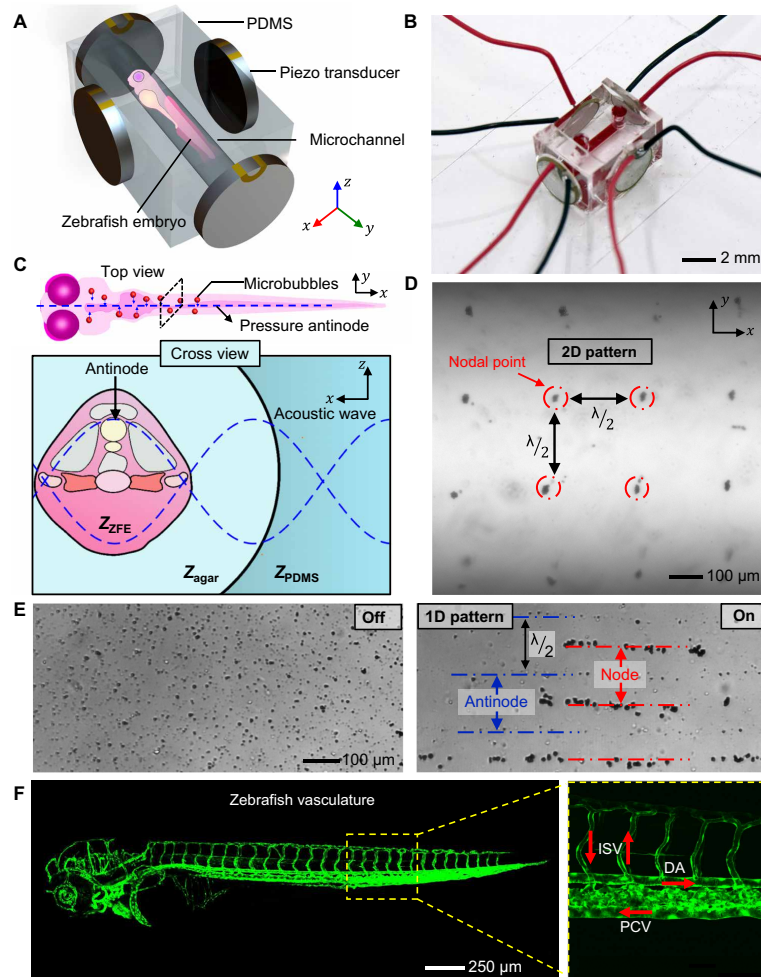


Fig. 1. Experimental design and concept of the in vivo acoustic manipulation system. (A) Schematic of the in vivo acoustofluidic device, which comprises a transparent PDMS chamber for the ZFE and four identical piezo transducers. (B) Micrograph of the in vivo acoustic manipulation chamber. Red dye was infused to highlight the channel. (C) Schematic of an acoustic wave penetrating a ZFE. A standing acoustic wave is established across a ZFE that is fixed in agar gel. When the acoustic wave encounters the PDMS/agar and agar/ZFE interfaces, its energy is partially reflected and partially transmitted (see also table S1). (D) The 2D lattice-like acoustic pattern is produced inside the microchannel by the acoustic system. (E) The 1D patterning demonstrates microbubbles that have resonance frequencies larger than the excitation frequency positioned at the pressure antinodes, while microbubbles having smaller resonance frequency than the excitation frequency are trapped at the nodes. An ultrasound induced 1D patterning of gas-filled microbubbles. The images illustrate the distribution of microbubbles before and after applying ultrasound. In the 1D pattern, microbubbles with resonance frequencies higher than the excitation frequency are shown positioned at the pressure antinodes, while microbubbles with resonance frequencies lower than the excitation frequency are seen trapped at the nodes. (F) Fluorescence image of a *tg(kdrl:eGFP)* ZFE, expressing green fluorescent protein (GFP) in endothelial cells, highlighting its vasculature network. Red arrows indicate direction of blood flow, e.g., dorsal artery (DA), intersegmental vessels (ISV), and posterior cardinal vein (PCV).

4.0 and 4.25 MHz, bubbles smaller than 4 μm move to the antinode, while those larger than 4 μm move to the node (shown in Fig. 1E). A wide range of microbubbles and clusters of microbubbles (~6 to 14 μm) were detected in the in vitro experiments. The microbubbles used in the ZFE therefore move toward the pressure node (see also fig. S3 and movie S2).

In vivo microbubble trapping

In this section, we focus on trapping a freely recirculating gas-filled microbubble in the vasculature of a ZFE. In Fig. 2 (A and C), a microbubble circulates from right to left in the DA until the acoustic field is turned on at 2.3 s. The consequent primary acoustic radiation force, F_R , moves the bubble into the nearest acoustic trap (node),

SCIENCE ADVANCES | RESEARCH ARTICLE

which is located to the right, against the flow (see also movie S5). Figure 2 (B and D) depicts an equivalent experiment in which the head of the fish is oriented in the opposite direction; thus, the flow direction is from left to right. As in the previous experiment, a microbubble inside the DA drifts downstream until the acoustic field is turned on at 0.7 s, upon which the microbubble travels toward the nearest acoustic trap, in this case, upstream to the left (movie S6). A ZFE fixed in agar may occasionally drift slightly when subjected to ultrasound over a period of a few seconds.

In addition to the primary acoustic radiation force, F_R , the bubble experiences “Stokes” drag force, F_D (49). The influence of inertia forces in this experiment is characterized by the Reynolds number. The Reynolds number, $Re = \frac{\rho a \Delta v}{\mu}$, of a microbubble circulating inside the vasculature is measured to be 3.23×10^{-6} , where $\rho = 1010 \text{ kg m}^{-3}$ is the density of human blood plasma, $a = 6 \text{ }\mu\text{m}$ is the diameter of the microbubble, $\mu = 1.5 \text{ cP}$ is the dynamic viscosity of the blood plasma, and $\Delta v \sim 0.8 \text{ }\mu\text{m s}^{-1}$ is the velocity difference between bubble and medium (53, 54). There is no literature on the density of ZFE blood plasma. The physical properties of human blood and ZFE blood are similar (55). We therefore approximate the ZFE blood plasma density as the one of human blood plasma. The velocity of the bubble’s

transit upstream is determined empirically from an image sequence, and the velocity of the blood flow is approximated as the drifting speed of the bubble in the absence of acoustic force. Since the calculated Reynolds number is low ($Re \ll 1$), inertia effects become negligible; thus, the acoustic radiation force is balanced by the Stokes drag, i.e., $F_R = F_D$. Therefore, we can estimate the maximum acoustic radiation force acting on the microbubble as $F_R = F_D = 6\pi\eta a \Delta v$, which is in the order of piconewtons (see also Supplementary Text).

In contrast to microbubbles, we observed that the red blood cells (RBCs) in the vasculature were hardly affected in the presence of ultrasound. Microbubbles and cluster of microbubbles detected in the ZFE had a diameter of $\sim 6 \text{ }\mu\text{m}$, while the observed RBCs had a diameter of $\sim 6 \text{ }\mu\text{m}$. The Stokes drag acting onto the microbubbles is therefore similar in magnitude compared to the RBCs. Microbubbles ($0.004 \times 10^6 \frac{\text{kg}}{\text{m}^2 \text{ s}}$) have a larger acoustic impedance mismatch with the surrounding blood plasma ($1.57 \times 10^6 \frac{\text{kg}}{\text{m}^2 \text{ s}}$) than RBCs ($1.6 \times 10^6 \frac{\text{kg}}{\text{m}^2 \text{ s}}$) (41). The acoustic pressure wave scatters more at the microbubbles, which results in a higher acoustic radiation force acting on the microbubbles. As a result of much larger acoustic radiation force, the microbubbles are selectively manipulated by the acoustic field.

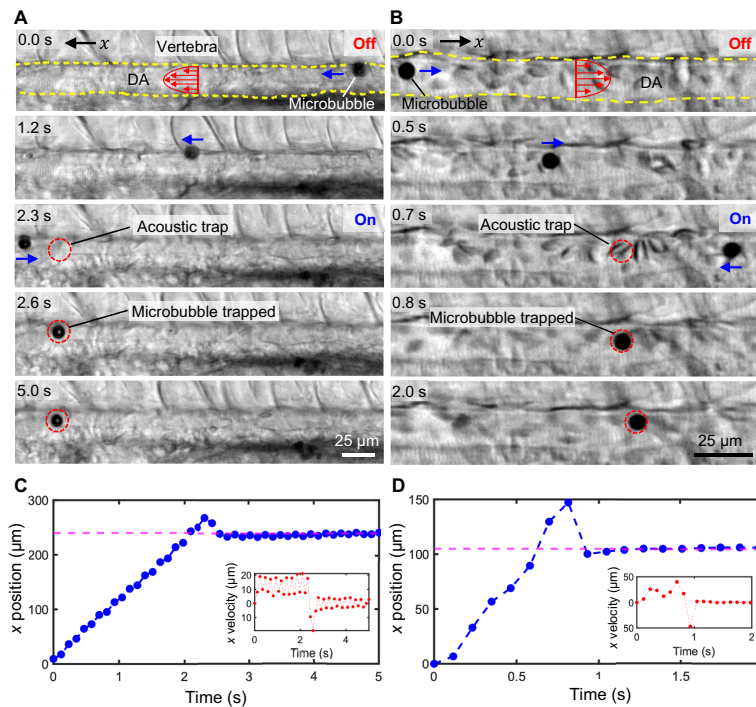


Fig. 2. Microbubble manipulation inside the DA of ZFEs. (A) Image sequences demonstrating a gas-filled microbubble migrating under right-to-left flow that became trapped in the DA when ultrasound was activated (at ~ 2.3 s). The microbubble traveled against flow to reach the antinode, indicated by the dotted red circle. (B) A microbubble traveling under left-to-right flow in the DA of another fish similarly became trapped. Note that the microbubbles are traveling much faster upstream than downstream, which can be attributed to acoustic radiation force. The ZFE was observed to drift vertically $7.6 \text{ }\mu\text{m}$ (smaller than the wavelength of $365 \text{ }\mu\text{m}$). (C) The plots illustrating the location and speed (inset) of a microbubble tracked for the image sequence in (A). A magenta dotted line indicates the location of the pressure node. (D) Plots of the x position and the x velocity (inset) of the microbubble in (B). The pressure nodal position is indicated by magenta dotted lines.

In vivo microbubble manipulation

Next, we demonstrate controlled dynamic manipulation of trapped microbubbles inside a ZFE. Trapped microbubbles can be made to translate by changing the nodal positions of a standing wavefield, i.e., by tuning the excitation frequency emitted by the piezo transducer. A change in frequency Δf results in a change in wavelength $\Delta\lambda$. Since the microbubbles are trapped at the nodes, they move with the node shift; however, the effective range of this manipulation is extremely small (see also movie S3). The piezoelectric transducers mounted to the setup have a quality factor Q of 26 to 93 and achieve maximum oscillation when activated at their resonance frequency of 4.05 to 4.17 MHz (see also figs. S6 and S7). Driving the transducers off-resonance decreases the mechanical output amplitude, thus limiting effective translation of the microbubbles. Within the frequency window of 4.0 to 4.25 MHz, the difference in wavelength in water is approximately $\Delta\lambda = \lambda_1 - \lambda_2 \approx 23 \mu\text{m}$.

To increase the range of motion, we positioned the fish chamber 2 mm off-center relative to the wavefield, shown schematically in Fig. 3A. In a standing wavefield, each node location is sited half a wavelength ($\lambda/2$) away from its adjacent antinodes. A change in frequency Δf results in a change in wavelength $\Delta\lambda$; the node positions therefore shift when the excitation frequency is modulated, with only the node at the center of the wavefield remaining stationary. The displacement of each node increases proportionally with its distance from the center (3); that is, when we change the wavelength by $\Delta\lambda$, the innermost antinodes, which are half a wavelength ($\lambda/2$) from the central node, will move by $\Delta\lambda/2$; the next tier out, which is one wavelength (λ) from the center, moves by $\Delta\lambda$; the ones that are two wavelengths (2λ) from the center move by $2\Delta\lambda$; and so forth. Siting the chamber five wavelengths ($5\lambda = 2 \text{ mm}$) off-center made the node translations five times larger than the shift in wavelength ($\Delta\lambda = 23 \mu\text{m}$), producing a net translation of $5 \times 23 = 115 \mu\text{m}$ (see also figs. S6 and S7 and movie S4).

The piezo transducers arranged to the left and right of the ZFE control the x position of the microbubble, while those above and below control its y position (Fig. 3A). Figure 3B shows a superimposed time-lapse image of a microbubble that was manipulated right to left by increasing the frequency of the x -axis piezo transducers from 4.0 to 4.25 MHz at $15 V_{pp}$, while the y -axis piezo is kept constant at 4.1 MHz and $12.5 V_{pp}$. The microbubble traveled $106 \mu\text{m}$ upstream in the PCV, i.e., against blood flow, over the course of 13 s (movie S7). This movement of $106 \mu\text{m}$ is 92% of the maximal net translation of the device. Likewise, Fig. 3C illustrates a microbubble maneuver in the y direction within the 16- μm -wide DA as the y -axis piezo transducers were switched from 4.0 to 4.25 and back to 4.0 MHz at $12.5 V_{pp}$, causing the microbubble to move orthogonally to the flow (movie S9). During this process, the x -oriented transducers were maintained constant at a frequency of 4.1 MHz and amplitude of $12.5 V_{pp}$ sufficient to counter the blood flow, thus holding the microbubble in the x direction. The microbubble does not move further than $16 \mu\text{m}$, as it is blocked by the vessel walls of the DA. Such complete 2D control of a microrobot inside a vasculature under flow would allow the navigation of injected carriers through the body to a target location. Therefore, this approach could provide a foundation for future locally targeted drug delivery or spatially selective drug screening.

Manipulation of microbubbles in different regions

We demonstrated manipulation of microbubbles in the DA and the PCV, which are the two largest vessels in the ZFE exhibiting the highest flow rates (56). Subsequent experiments investigate whether this acoustic-directed movement is repeatable and reversible throughout the body in different regions. With this control, a microbubble could be injected near the heart and manipulated to an arbitrary location in the vasculature. In Fig. 4A, a constant frequency was applied in the y direction such that the bubble was fixed in the middle of the DA. Meanwhile, switching the frequency between 4.1 and 4.15 MHz

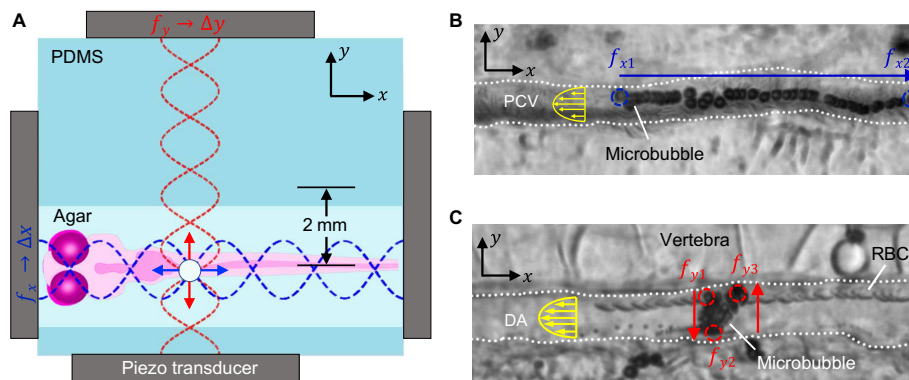


Fig. 3. 2D control of a microbubble using frequency modulation control. (A) A schematic demonstrates the zebrafish chamber positioned 2 mm off-center with respect to the orthogonally positioned transducer pairs enabling a wider manipulation range. (B) A microbubble is made to move in the x direction against the flow as the transducers placed in line with the fish have their frequencies changed from $f_{x1} = 4.0 \text{ MHz}$ to $f_{x2} = 4.25 \text{ MHz}$, $15 V_{pp}$, while $f_y = 4.1 \text{ MHz}$ is kept constant at $12.5 V_{pp}$. (C) Equivalently, altering the excitation frequency of the piezo transducers alongside the ZFE from $f_{y1} = 4.0 \text{ MHz}$ to $f_{y2} = 4.25 \text{ MHz}$ at $12.5 V_{pp}$ and back to $f_{y3} = 4.1 \text{ MHz}$ at $12.5 V_{pp}$ thus results in movement of the microbubble in the y direction, i.e., perpendicular to the blood flow. In the process, the particle remains stable in the x direction as $f_x = 4.1 \text{ MHz}$ is kept constant.

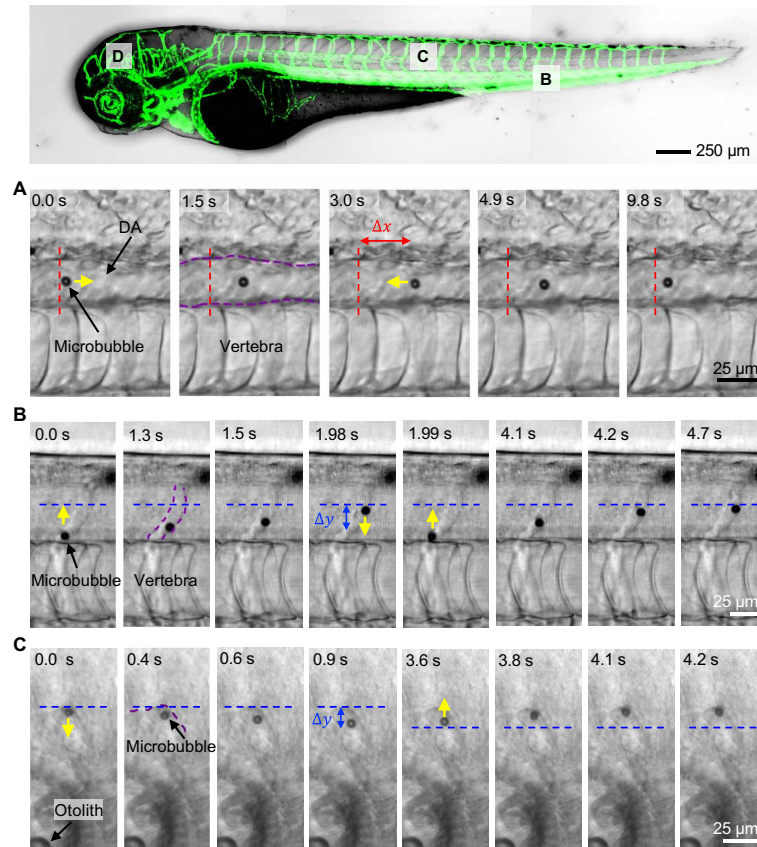


Fig. 4. Acoustic manipulation in vivo at different locations within the zebrafish vasculature. To demonstrate full directional control, a bubble was directed along the vasculature and back to its initial position multiple times by shifting the frequency. **(A)** The microbubble was reversibly moved horizontally $22\ \mu\text{m}$ left and right in the $21\text{-}\mu\text{m}$ -wide DA by varying the frequency controlling the horizontal position f_x between 4.1 and 4.15 MHz at a constant amplitude of $10\ V_{pp}$. **(B)** The bubble likewise traveled and returned $29.85\ \mu\text{m}$ in the y direction without stiction in the ISV, which has a diameter close to that of contrast agents and passing RBCs by varying the frequency controlling the vertical position f_y between 4.15 and 4.25 MHz at a constant amplitude of $12.5\ V_{pp}$. **(C)** Last, the same reversible behavior was demonstrated with a traveled distance of $9\ \mu\text{m}$ in a cerebral blood vessel, close to the otoliths by varying the frequency controlling the vertical position f_y between 4.1 and 4.25 MHz at a constant amplitude of $10\ V_{pp}$.

at a constant amplitude of $12.5\ V_{pp}$ of the x -direction actuators manipulated the bubble upstream by $26\ \mu\text{m}$. Afterward, reversal of that actuation frequency caused the bubble to travel back to its initial position. The final location of the bubble deviated from its initial position by $5\ \mu\text{m}$ (movie S11). Relative to the DA, other segments of the vasculature with smaller diameters experience lower flow rates. Figure 4B shows repeated up and down movement inside the ISV over a distance of $21\ \mu\text{m}$. This motion is caused by the actuators located above and below the ZFE with varying frequency between 4.15 and 4.25 MHz at a constant amplitude of $12.5\ V_{pp}$ (movie S12). Last, we demonstrated tweezing of microbubbles at sites other than in the fish's tail, specifically inside the cerebral vasculature (Fig. 4C). In this case, the bubble was moved away from the vasculature wall by $9\ \mu\text{m}$ and then back to its original position at the wall by varying

the frequency controlling the vertical between 4.1 and 4.25 MHz at a constant amplitude of $10\ V_{pp}$ (movie S13). This reversible back and forth movement throughout the body supports this system as a possible conceptual foundation for localized applications.

Viability study of ZFEs

A ZFE at 72 hpf has a total length of $\sim 3.5\ \text{mm}$, and its whole body experiences acoustic radiation force. We expect that imposing this force on tissue and RBCs puts stress on the cardiovascular system. The ZFEs in our experiments experience an acoustic field in pulses of $30\ \text{s}$ with a subsequent recovery time of $1\ \text{min}$. We observe a voltage-dependent reaction in heart rate and pumping at voltages above $10\ V_{pp}$ (see Fig. 5). The acoustic radiation force scales with the square of the actuation voltage. We observed that voltages between

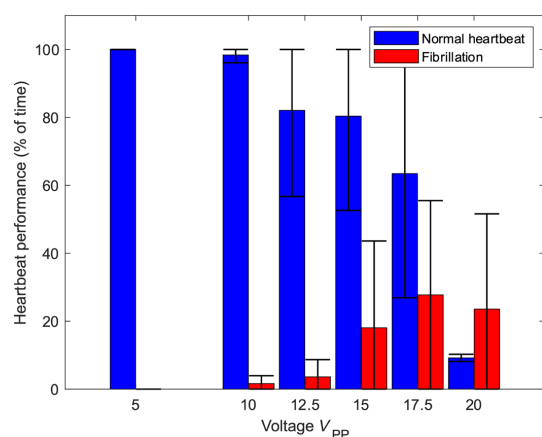


Fig. 5. Viability of ZFE in the presence of ultrasound. To demonstrate the viability of the acoustic actuation on cardiac function, untreated ZFEs were placed into the acoustic channel and exposed to acoustic excitation across a range of voltages in pulses of 30 s with a subsequent recovery time of 1 min. Up to a voltage of 17.5 V_{pp} , fibrillation was reversible and did not impair ZFE viability. The error bar represents the SD for a minimum of five data points.

12.5 and 15 V_{pp} applied to the piezo transducer can lead to fibrillation (temporary erratic behavior of the heart) and can stop the heart for a limited amount of time (~30 s); however, after the application of acoustics has ceased, the heart recovers back to its initial movement within 1 min (see also movies S14 and S15). In contrast, a voltage of 17.5 V_{pp} stops the heartbeat within 30 s. After ceasing such excitation, the stopped heart in some specimens starts fibrillating within 30 s and may fully recover in minutes. At a still-higher excitation voltage of 20 V_{pp} , permanent deformation can result, i.e., buckling along the long axis of the zebrafish body. We therefore conclude that an excitation voltage of no more than 12.5 V_{pp} or limited excitation time at values of up to 17.5 V_{pp} will ensure the continuing viability of a ZFE. Last, we investigated whether the electric field produced by the piezo transducers has any effect on the cardiac function of the ZFE. A similar viability study was conducted with an acoustically isolated 1-mm air gap between the transducer and the PDMS chamber, and no changes in heart rate were detected (see also movie S16). For higher animal models, the standing wavefield is smaller than the body size; thus, the acoustic field does not completely excite the animal's entire body. The cardiovascular effect of the acoustic field in mice or humans is therefore presumably less intense, increasing the viability of acoustic manipulation.

DISCUSSION

Here, we demonstrate microparticle manipulation inside ZFEs using ultrasound. Ultrasound is attractive for its ability to penetrate deep into tissue, for being unaffected by tissue opacity, and for generating a broad range of directed forces. We used ultrasound to manipulate microbubbles with micrometer precision inside the DA of zebrafish. The setup demonstrates controlled up-, down-, and cross-stream manipulation throughout the vasculature by controlling the acoustic actuation frequency. We further realized controlled

manipulation of microbubbles in ISVs and cerebral blood vessels. Last, we investigated the viability of ZFEs subjected to the acoustic field.

After injection the microbubbles circulate freely inside the fish for up to 15 min in the absence of any acoustic fields. As an acoustic field excites the bubbles, they clump together into groups due to secondary “Bjerknes” forces (57) as they move into an acoustic trap. The enlarged cluster of bubbles can reduce circulation time in the fish depending on the number of injected bubbles. The bubbles remain in clusters after the acoustic field has been turned off for around 30 s. However, stiction of single or groups of bubbles inside the zebrafish vasculature has not been observed to be fatal. A control over the number of injected bubbles may result in less agglomeration of bubbles throughout the vasculature.

Our system shows reliable trapping of bubbles and patterning of particles in water of a 1.5-mm-wide channel. A subsequent change in actuation frequency moves the position of the trap and thereby the trapped bubble. During *in vivo* experiments, the acoustic node may be located within the ZFE tissue but outside the 5- to 25- μ m-wide vasculature walls. As a result, the position of trapped injected microbubbles may differ from the actual node location. Without the visual feedback of the precise node position, the execution of a desired frequency shift to precisely move a trapped microbubble is challenging. Furthermore, we observed a deviation between the output signal of the piezo transducer and the excitation signal applied to the function generator at the resonance frequency of the transducers (see also fig. S4). A more sophisticated frequency control with, for example, a displacement transfer function or autoalignment might simplify path planning of bubbles inside the fish.

As acoustic waves penetrate different biological tissue, they get scattered, transmitted, and attenuated. We have not observed bulk acoustic streaming in the zebrafish vasculature under the experimental conditions used in this study. Therefore, bulk streaming in the form of “Rayleigh” or “Eckart” streaming should not compromise the performance of acoustic trapping. Our results show that transmission is sufficiently large to acoustically manipulate particles under flow in ZFE throughout the whole body of the ZFE, independent of tissue type, flow conditions, vessel diameter, or incident angle. Larger animal models have a longer distance between actuator and circulating microbubble. A resulting increased attenuation might limit location-dependent acoustic *in vivo* manipulation.

Microbubbles in combination with ultrasound have already been shown to trigger drug release (58). Here, we now present controlled *in vivo* manipulation of microbubbles in the vasculature of a ZFE. We believe that spatial control of drug-loaded microparticles can be exploited for targeted drug delivery. Additional studies are needed to demonstrate that the observed effects in ZFE can be extrapolated to higher vertebrate including humans.

MATERIALS AND METHODS

Experimental setup

The acoustic chamber into which a microbubble-injected ZFE was embedded was transferred to a Zeiss AxioVert 200M (Carl Zeiss, Germany) inverted optical microscope equipped with 2.5 \times , 5 \times , and 10 \times objectives. During experiments, the voltage signals driving the piezo actuators were produced by a Tektronix AFG 3011C function generator (Tektronix, USA) and a GW Instek AFG-2005 function generator (GW Instek, Taiwan). The conductance and impedance of four nonmounted and four mounted piezoelectric transducers were

SCIENCE ADVANCES | RESEARCH ARTICLE

measured using an impedance analyzer (16777K, SinePhase, USA) (see also fig. S5 and table S2). Input power was assessed by measuring the voltage across the transducer and current at the transducer. A “TBS2000” oscilloscope by “Tektronix” was used to measure the voltage across the piezo transducer and a “TCP202” current probe by Tektronix to measure the current to the piezo transducer. By multiplying the root mean square (RMS) voltage and RMS current at the piezo, we computed the apparent input power to the piezo. Images were taken with a Coolsnap HQ2 charge-coupled device camera (Photometrics, USA) at a frame rate of 8.6 fps and processed with PVCamTest software (Photometrics, USA). Subsequent image analysis was performed with FIJI, a package based on ImageJ (imagej.net, USA). For the visualization of the ZFE vasculature in Fig. 1, confocal images of tg(kdrl:eGFP) embryos were acquired using an Olympus FV3000 confocal laser scanning microscope (Olympus, Tokyo, Japan) equipped with a UPlabSApo 20× objective having a numerical aperture of 0.75 (Olympus, Japan). Image acquisition was carried out using a sequential line scan, an excitation wavelength of 488 nm, and an emission wavelength of 500 to 540 nm.

ZFE husbandry

In accordance with the Swiss animal welfare regulations, eggs from *Danio rerio* AB/TU wild-type and kdrl:eGFP [green fluorescent protein (GFP) expressed by endothelial cells] were maintained. They were kept in zebrafish culture media at 28°C, to which 1-phenyl 2-thiourea (30 µg/ml; PTU) was added to prevent the formation of pigment cells. At 3 days after fertilization, ZFEs were anesthetized with 0.01% tricaine, dechlorinated, and embedded in 0.3% agarose containing tricaine and PTU.

ZFE injection

A volume of 2 to 3 nl of SonoVue microbubble solution (Bracco, Italy) was injected into the duct of Cuvier of embedded ZFEs using a micromanipulator (Wagner Instrumentenbau, Schöffengrund, Germany), a pneumatic Pico Pump PV830 (World Precision Instruments, USA), and a Leica SAPO microscope (Leica, Germany). After injection, the ZFEs were manually cut out of the agar, transferred into the acoustic chamber, and re-embedded using low-melting agar.

SUPPLEMENTARY MATERIALS

Supplementary material for this article is available at <https://science.org/doi/10.1126/sciadv.abm2785>

REFERENCES AND NOTES

- Ashkin, J. M. Dziedzic, J. E. Bjorkholm, S. Chu, Observation of a single-beam gradient force optical trap for dielectric particles. *Opt. Lett.* **11**, 288–290 (1986).
- M. C. Wu, Optoelectronic tweezers. *Nat. Photonics* **5**, 322–324 (2011).
- X. Ding, S. C. S. Lin, B. Kiraly, H. Yue, S. Li, I. K. Chiang, J. Shi, S. J. Benkovic, T. J. Huang, On-chip manipulation of single microparticles, cells, and organisms using surface acoustic waves. *Proc. Natl. Acad. Sci. U.S.A.* **109**, 11105–11109 (2012).
- A. Ozcelik, J. Rufo, F. Guo, Y. Gu, P. Li, J. Lata, T. J. Huang, Acoustic tweezers for the life sciences. *Nat. Methods* **15**, 1021–1028 (2018).
- N. Zhang, A. Horesch, J. Friend, Manipulation and mixing of 200 femtoliter droplets in nanofluidic channels using MHz-order surface acoustic waves. *Adv. Sci.* **8**, 2100408 (2021).
- U. S. Jonnalagadda, M. Hill, W. Messaoudi, R. B. Cook, R. O. C. Oreffo, P. Glynne-Jones, R. S. Tare, Acoustically modulated biomechanical stimulation for human cartilage tissue engineering. *Lab Chip* **18**, 473–485 (2018).
- L. Cox, K. Melde, A. Croxford, P. Fischer, B. W. Drinkwater, Acoustic hologram enhanced phased arrays for ultrasonic particle manipulation. *Phys. Rev. Appl.* **12**, 064055 (2019).
- A. Marzo, T. Fushimi, T. Hill, B. W. Drinkwater, Holographic acoustic tweezers: Future applications in medicine and acoustophoretic display. *Intl. Soc. Opt. Phot.* **11083**, 1108304 (2019).
- G. T. Silva, J. H. Lopes, J. P. Leão-Neto, M. K. Nichols, B. W. Drinkwater, Particle patterning by ultrasonic standing waves in a rectangular cavity. *Phys. Rev. Appl.* **11**, 054044 (2019).
- J. Shi, D. Ahmed, X. Mao, S. C. S. Lin, A. Lawit, T. J. Huang, Acoustic tweezers: Patterning cells and microparticles using standing surface acoustic waves (SSAW). *Lab Chip* **9**, 2890–2895 (2009).
- D. J. Collins, B. Morahan, J. Garcia-Bustos, C. Doerig, M. Plebanski, A. Neild, Two-dimensional single-cell patterning with one cell per well driven by surface acoustic waves. *Nat. Commun.* **6**, 8686 (2015).
- J. W. Ng, A. Neild, Multiple outcome particle manipulation using cascaded surface acoustic waves (CSAW). *Microfluid. Nanofluid.* **25**, 10.1007/s10404-020-02417-4, (2021).
- A. Neild, Motion controlled by sound. *Nature* **537**, 493–494 (2016).
- L. Ren, N. Nama, J. M. McNeill, F. Soto, Z. Yan, W. Liu, W. Wang, J. Wang, T. E. Mallouk, 3D steerable, acoustically powered microswimmers for single-particle manipulation. *Sci. Adv.* **5**, eaax3084 (2019).
- D. Ahmed, M. Lu, A. Nourhani, P. E. Lammert, Z. Stratton, H. S. Muddana, V. H. Crespi, T. J. Huang, Selectively manipulable acoustic-powered microswimmers. *Sci. Rep.* **5**, 9744 (2015).
- D. Ahmed, T. Baasch, B. Jang, S. Pane, J. Dual, B. J. Nelson, Artificial swimmers propelled by acoustically activated flagella. *Nano Lett.* **16**, 4968–4974 (2016).
- D. Ahmed, T. Baasch, N. Blondel, N. Läubli, J. Dual, B. J. Nelson, Neutrophil-inspired propulsion in a combined acoustic and magnetic field. *Nat. Commun.* **8**, 770 (2017).
- D. Ahmed, C. Dillinger, A. Hong, B. J. Nelson, Artificial acousto-magnetic soft microswimmers. *Adv. Mater. Technol.* **2**, 1700050 (2017).
- D. Ahmed, A. Sukhov, D. Hauri, D. Rodrigue, G. Maranta, J. Harting, B. J. Nelson, Bioinspired acousto-magnetic microswarm robots with upstream motility. *Nat. Mach. Intell.* **3**, 116–124 (2021).
- C. Dillinger, N. Nama, D. Ahmed, Ultrasound-activated ciliary bands for microrobotic systems inspired by starfish. *Nat. Commun.* **12**, 6455 (2021).
- A. Snezhko, I. S. Aranson, Magnetic manipulation of self-assembled colloidal asters. *Nat. Mater.* **10**, 698–703 (2011).
- X. Wang, C. Ho, Y. Tsatskis, J. Law, Z. Zhang, M. Zhu, C. Dai, F. Wang, M. Tan, S. Hopyan, H. McNeill, Y. Sun, Nanorobots: Intracellular manipulation and measurement with multipole magnetic tweezers. *Sci. Robot.* **4**, eaav6180 (2019).
- Z. Wu, L. Li, Y. Yang, P. Hu, Y. Li, S. Y. Yang, L. V. Wang, W. Gao, A microrobotic system guided by photoacoustic computed tomography for targeted navigation in intestines in vivo. *Sci. Robot.* **4**, eaax0613 (2019).
- M. Zhu, K. Zhang, H. Tao, S. Hopyan, Y. Sun, Magnetic micromanipulation for in vivo measurement of stiffness heterogeneity and anisotropy in the mouse mandibular arch. *Research* **2020**, 7914074 (2020).
- P. L. Johansen, F. Fenaroli, L. Evensen, G. Griffiths, G. Koster, Optical micromanipulation of nanoparticles and cells inside living zebrafish. *Nat. Commun.* **7**, 10974 (2016).
- M.-C. Zhong, X.-B. Wei, J. H. Zhou, Z. Q. Wang, Y. M. Li, Trapping red blood cells in living animals using optical tweezers. *Nat. Commun.* **4**, 1768 (2013).
- I. A. Favre-Bulle, A. B. Stilgoe, H. Rubinsztein-Dunlop, E. K. Scott, Optical trapping of otoliths drives vestibular behaviours in larval zebrafish. *Nat. Commun.* **8**, 630 (2017).
- I. A. Favre-Bulle, M. A. Taylor, E. Marquez-Legorreta, G. Vanwallieghem, R. E. Poulsen, H. Rubinsztein-Dunlop, E. K. Scott, Sound generation in zebrafish with bio-opto-acoustics. *Nat. Commun.* **11**, 6120 (2020).
- M. B. Rasmussen, L. B. Oddershede, H. Siegmundfeldt, Optical tweezers cause physiological damage to *Escherichia coli* and *Listeria* bacteria. *Appl. Environ. Microbiol.* **74**, 2441–2446 (2008).
- F. Berndt, G. Shah, R. M. Power, J. Brugués, J. Huisken, Dynamic and non-contact 3D sample rotation for microscopy. *Nat. Commun.* **9**, 5025 (2018).
- O. Campàs, T. Mammoto, S. Hasso, R. A. Sperling, D. O’Connell, A. G. Bischof, R. Maas, D. A. Weitz, L. Mahadevan, D. E. Ingber, Quantifying cell-generated mechanical forces within living embryonic tissues. *Nat. Methods* **11**, 183–189 (2014).
- J. Yu, D. Jin, K. F. Chan, Q. Wang, K. Yuan, L. Zhang, Active generation and magnetic actuation of microrobotic swarms in bio-fluids. *Nat. Commun.* **10**, 5631 (2019).
- A. Albanese, P. S. Tang, W. C. W. Chan, The effect of nanoparticle size, shape, and surface chemistry on biological systems. *Annu. Rev. Biomed. Eng.* **14**, 1–16 (2012).
- B. Ballou, B. C. Lagerholm, L. A. Ernst, M. P. Bruchez, A. S. Waggoner, Noninvasive imaging of quantum dots in mice. *Bioconjug. Chem.* **15**, 79–86 (2004).
- K. Dholakia, B. W. Drinkwater, M. Ritsch-Marte, Comparing acoustic and optical forces for biomedical research. *Nat. Rev. Phys.* **2**, 480–491 (2020).
- M. A. Ghanem, A. D. Maxwell, Y. N. Wang, B. W. Cunitz, V. A. Khokhlova, O. A. Sapozhnikov, M. R. Bailey, Noninvasive acoustic manipulation of objects in a living body. *Proc. Natl. Acad. Sci. U.S.A.* **117**, 16848–16855 (2020).

37. W. C. Lo, C. H. Fan, Y. J. Ho, C. W. Lin, C. K. Yeh, Tornado-inspired acoustic vortex tweezer for trapping and manipulating microbubbles. *Proc. Natl. Acad. Sci. U.S.A.* **118**, e2023188118 (2021).
38. N. F. Läubli, J. T. Burri, J. Marquard, H. Vogler, G. Mosca, N. Vertti-Quintero, N. Shamsudhin, A. DeMello, U. Grossniklaus, D. Ahmed, B. J. Nelson, 3D mechanical characterization of single cells and small organisms using acoustic manipulation and force microscopy. *Nat. Commun.* **12**, 2583 (2021).
39. D. Ahmed, A. Ozcelik, N. Bojanala, N. Nama, A. Upadhyay, Y. Chen, W. Hanna-Rose, T. J. Huang, Rotational manipulation of single cells and organisms using acoustic waves. *Nat. Commun.* **7**, 11085 (2016).
40. C. Chen, Y. Gu, J. Philippe, P. Zhang, H. Bachman, J. Zhang, J. Mai, J. Rufo, J. F. Rawls, E. E. Davis, N. Katsanis, T. J. Huang, Acoustofluidic rotational tweezing enables high-speed contactless morphological phenotyping of zebrafish larvae. *Nat. Commun.* **12**, 1118 (2021).
41. M. Sundvik, H. J. Nieminen, A. Salmi, P. Panula, E. Hægström, Effects of acoustic levitation on the development of zebrafish, *Danio rerio*, embryos. *Sci. Rep.* **5**, 13596 (2015).
42. L. I. Zon, R. T. Peterson, In vivo drug discovery in the zebrafish. *Nat. Rev. Drug Discov.* **4**, 35–44 (2005).
43. I. Leibacher, S. Schatzer, J. Dual, Impedance matched channel walls in acoustofluidic systems. *Lab Chip* **14**, 463–470 (2014).
44. C. Greis, Technology overview: SonoVue (Bracco, Milan). *Eur. Radiol.* **14**, P11–P15 (2004).
45. Bracco Imaging srl, Annex I Summary of Product Characteristics SonoVue (European Medicines Agency, 2013); www.ema.europa.eu/en/medicines/human/EPAR/sonovue#product-information-section.
46. Y. Lin, L. Lin, M. Cheng, L. Jin, L. Du, T. Han, L. Xu, A. C. H. Yu, P. Qin, Effect of acoustic parameters on the cavitation behavior of SonoVue microbubbles induced by pulsed ultrasound. *Ultrason. Sonochem.* **35**, 176–184 (2017).
47. A. Cafarelli, A. Verbeni, A. Poliziani, P. Dario, A. Menciaci, L. Ricotti, Tuning acoustic and mechanical properties of materials for ultrasound phantoms and smart substrates for cell cultures. *Acta Biomater.* **49**, 368–378 (2017).
48. Z. Hou, Z. Zhou, P. Liu, Y. Pei, Deformable oscillation of particles patterning by parametric bulk acoustic waves. *Extreme Mech. Lett.* **37**, 100716 (2020).
49. H. Bruus, Acoustofluidics 7: The acoustic radiation force on small particles. *Lab Chip* **12**, 1014–1021 (2012).
50. H. Bruus, Acoustofluidics 10: Scaling laws in acoustophoresis. *Lab Chip* **12**, 1578–1586 (2012).
51. A. Doinikov, Acoustic radiation forces: Classical theory and recent advances. *Recent Res. Dev. Acoust.* **1**, 39–67 (2003).
52. A. Doinikov, Bubble and particle dynamics in acoustic fields: Modern trends and applications: 2005. *Res. Signpost.* **661**, 338 (2006).
53. S. H. Wang, L. P. Lee, J. S. Lee, A linear relation between the compressibility and density of blood. *J. Acoust. Soc. Am.* **109**, 390–396 (2001).
54. J. Lee, T. C. Chou, D. Kang, H. Kang, J. Chen, K. I. Baek, W. Wang, Y. Ding, D. Di Carlo, Y. C. Tai, T. K. Hsiai, A rapid capillary-pressure driven micro-channel to demonstrate newtonian fluid behavior of zebrafish blood at high shear rates. *Sci. Rep.* **7**, 1980 (2017).
55. J. Lee, M. E. Moghadam, E. Kung, H. Cao, T. Beebe, Y. Miller, B. L. Roman, C. L. Lien, N. C. Chi, A. L. Marsden, T. K. Hsiai, Moving domain computational fluid dynamics to interface with an embryonic model of cardiac morphogenesis. *PLOS ONE* **8**, e72924 (2013).
56. F. Santoso, B. P. Sampurna, Y. H. Lai, S. T. Liang, E. Hao, J. R. Chen, C. Der Hsiao, Development of a simple imagej-based method for dynamic blood flow tracking in zebrafish embryos and its application in drug toxicity evaluation. *Inventions* **4**, 65 (2019).
57. A. A. Doinikov, Bjerknes forces between two bubbles in a viscous fluid. *J. Acoust. Soc. Am.* **106**, 3305–3312 (1999).
58. C. Van Ballegoie, A. Man, M. Win, D. T. Yapp, Spatially specific liposomal cancer therapy triggered by clinical external sources of energy. *Pharmaceutics* **11**, 125 (2019).

Acknowledgments

Funding: This project has received funding from the European Research Council (ERC) under the European Union's Horizon 2020 Research and Innovation Programme grant agreement no. 853309 (SONOBOTS). **Author contributions:** V.M.J. performed all the experiments and performed data analysis with feedback from D.A. The ZFEs and guidance for the zebrafish experiments were provided by J.S.B. and J.H. All authors contributed to the experimental design, scientific presentation, and discussion and wrote the manuscript. D.A. initiated, provided overall guidance, and supervised the project. **Competing interests:** The authors declare that they have no competing interests. **Data and materials availability:** All data needed to evaluate the conclusions in the paper are present in the paper and/or the Supplementary Materials.

Submitted 19 September 2021

Accepted 2 February 2022

Published 25 March 2022

10.1126/sciadv.abm2785

DISCUSSION & OUTLOOK

In the research presented in this PhD thesis, zebrafish larvae were established as a vertebrate model to study renal function, nephrotoxicity, and the pharmacokinetics of intravenously injected nanoparticles. This thesis is structured into four chapters. First, key renal functions were investigated. Next, macroscopic structural changes in renal organs induced by gentamicin treatment were analyzed using different imaging methods. Third, zebrafish larvae were used to verify drug-induced mitochondrial toxicity in proximal tubules. Fourth, as a reliable and predictive vertebrate model, the zebrafish larva was applied to investigate the pharmacokinetics of nanoparticles.

The following section summarizes all projects that comprised this PhD thesis and places them within a bigger context. The benefits, applications, and limitations of zebrafish larvae as a vertebrate model are discussed.

4.1 The use of zebrafish larvae as a vertebrate model to study renal function

Our studies verified that the zebrafish larva is a powerful vertebrate model: adult zebrafish lay hundreds of eggs that can be raised in a standardized environment, thus allowing for highly reproducible experiments. Since zebrafish have a yolk, they can feed themselves up to five days post-fertilization, which reduces maintenance work. In addition, they are not considered animals up to 120 hours post-fertilization, and therefore their use before this time is not restricted by guidelines [102]. Since they are transparent, *in vivo* functions can be observed with the naked eye or confocal microscopy using intravenously injected fluorophores. Zebrafish have a fully sequenced genome, high genetic similarities to human beings, a short generation time, and rapid embryogenesis [97]. Results can be reliably translated from *in vitro* to *in vivo* (vertebrates) to reduce, replace and refine animal experiments (3R principles). Our model allowed mechanistic studies to understand the (visual) observation. For the administration of compounds, intravenous injection into the bloodstream enables a defined application of a substance of interest [15]. This strategy favors the use of zebrafish in many disciplines such as vertebrate development research, behavioral studies, toxicology, pharmacology, and pharmacokinetics [97]. Therefore, zebrafish facilities are widely available and can be shared among research groups.

In conclusion, the use of zebrafish as a model organism is associated with a large number of offspring generated every ten days, high accessibility, standardization, and fewer ethical and legal aspects compared to animal models. In view of these benefits, zebrafish fulfill the rationale, serving as a powerful vertebrate model in biomedical disciplines such as nephrology.

With respect to renal elimination, zebrafish larvae share similarities in kidney formation, and anatomy with vertebrates and humans [109, 111]. This is not surprising since transcription factors responsible for patterning in the zebrafish are evolutionarily conserved in mammals [111, 112]. Therefore, in-depth studies on functionality must verify the similarity of the zebrafish to mammalian beings. Examples of functionality include glomerular filtration, active tubular excretion, and reabsorption of various transport systems. In Part 3.1, key renal functions in zebrafish larvae were assessed and confirmed.

First, hydrodynamic size-dependent glomerular filtration of fluorescent macromolecules enables certainty that intravenously injected macromolecules have similar filtration characteristics as those observed in humans. This is especially fundamental for reliable pharmacokinetic studies of nanoparticles and other enzyme-peptide-based formulations (Chapter 3.4.1 - 3.4.4) [113–115].

Second, verified ABC/SLC-mediated renal excretion enables the identification of (non-fluorescent) inhibitors of these transport systems. Thereby, potential nonfluorescent inhibitors are preinjected into zebrafish larvae, followed by the administration of the fluorescent transporter substrate. Changes in signal intensity in blood vessels indicate different renal excretion kinetics and, therefore, allow for identifying transporter-specific inhibition.

In various applications, our kidney model supports other zebrafish studies using intravenously injected drugs that might interfere with these transport systems. Examples are previous preclinical pharmacological studies in our group using ABC-transporter sensitive antibiotic medicines to remove macrophage-accumulated bacteria [116]. Awareness and the substrate-specificity of renal excretion are relevant for injection and plasma concentrations for different time points after injection. Furthermore, our models allow for the identification of inhibitors of ABC/SLC and megalin/cubilin transporters that

can increase the plasma concentration of co-transported drugs and toxins.

Importantly, intravenously administered compounds do not only interfere with the renal system. Its characteristics to interact with non-renal elimination organs, for instance, macrophages, and liver-sinusoidal endothelial cells, such as stab-2, is an exciting readout of the zebrafish model [15, 98, 108]. The pharmacokinetics of fluorescent substances in the entire organism can be analyzed using the distinct visual accumulation patterns indicative of specific elimination processes. Lipophilic compounds with high biodistribution characteristics and reactive compounds change their pharmacokinetic profile when they bind to circulating plasma proteins. We could verify that reactive fluorescent dyes are likely to bind small plasma proteins and to be reabsorbed in proximal tubules by means of megalin/cubilin transport systems [117, 118]. This was visible in the accumulation of fluorescent dye within proximal renal epithelial cells [15]. It should be noted that the cleavage of a fluorescent macromolecule or already impurified samples containing various populations of particles can falsify the readout. For instance, unstable antibodies (molecular weight < 75 kDa) were labeled, and their partial reabsorption in tubular epithelial cells indicated glomerular filtration in preliminary studies (data not shown). When applying the zebrafish glomerular filtration assays to pharmacokinetic studies of nanoparticles and macromolecules, fluorescent correlation spectroscopy as a technique to measure the hydrodynamic diameter and verify the pure labeled sample before *in vivo* experimentation is desired [15].

It is important to mention that the zebrafish model relies on an injection-based administration of compounds that has to be learned. Injection platforms must be purchased (around CHF 15-20k) and be available to the operator. Furthermore, screening with multiple conditions, such as time dependency, concentrations, and various substances, takes more effort and time than transporter studies in killifish models or cell culture experiments by pipetting the drug into the medium.

4.1. THE USE OF ZEBRAFISH LARVAE AS A VERTEBRATE MODEL TO STUDY RENAL FUNCTION

Furthermore, high concentrations of fluorescent substrates are required to be visible in the transparent zebrafish larvae (e.g. injection of 1 nL of a 0.2 μm in an aqueous solution). Solubility enhancers, such as DMSO, can increase the solubility of highly lipophilic substances to a certain extent but are also toxic [15]. Regarding substrate and inhibitor specificity, both teleost models have limitations in the study of very closely related transporter members. This is especially seen for OATs, such as OAT1 (SLC22A6) and OAT4 (SLC22A11) [119]. Both transporters have substrate overlap and can take over in the case of specific inhibition, knockdown, or genetic polymorphism of a transporter [119]. Thus, particular species specificity can limit receptor and transporter recognition of substrates and inhibitors.

Noteworthy, the pronephros of zebrafish is the major organ of hematopoiesis that is equivalent to the bone marrow of mammals [120]. Interestingly, hematopoietic stem and progenitor cells were further found in the caudal hematopoietic tissue by two days, thymus at three days and the kidney at four days post-fertilization [120]. Despite the anatomical distinction, the transcription factors, signaling molecules, and genetic programs controlling hematopoiesis are highly conserved between zebrafish and mammals [120]. They were intensively used in the last decades as an advantageous model to investigate gene regulators for hematopoiesis since their oxygen exchange relies on passive diffusion [120]. Nevertheless, renal damage induced by nephrotoxins can also affect hematopoietic stem and progenitor cells, potentially causing a higher toxic and systemic effect.

In conclusion, zebrafish larvae are, together with *Drosophila*, so far the only *in vivo* vertebrate models that allow for studying the renal functions mentioned in this thesis [121].

4.2 X-ray-based microtomography

Verified key renal functions enable the use of zebrafish larvae in nephrotoxicological studies. Functional reabsorption processes into the renal epithelial cells are considered to be responsible for certain nephrotoxins [23]. Gentamicin is a clinically applied antibiotic agent that causes tubular toxicity and is often used as a model nephrotoxin [51, 122]. Its accumulation in renal epithelial cells is associated with megalin/cubulin-mediated endocytosis and OCT-mediated accumulation [51, 123, 124]. Structural changes that occur in renal organs as a result of gentamicin treatment are observed in vertebrates such as rats and mice [91, 125]. We hypothesized that structural changes in the renal organs of zebrafish larvae, as a valid model, must be similar to vertebrates. Adequate techniques for imaging the renal organs of zebrafish have to be established to promote their application in nephrotoxicity. Here, fluorescence-based laser scanning confocal microscopy and X-ray-based microtomography imaging techniques were compared.

Fluorophore-based imaging methods to investigate renal processes and structural changes in the renal organs of zebrafish larvae are very popular. Intravenous injection of fluorescent substrates of ABC/SLC transporters, polymers with different molecular weights, and fluorescent assays allow for visual observations within defined organs of zebrafish larvae [15]. Real-time imaging and time-dependent studies are advantageous when using laser-scanning confocal microscopy. Furthermore, imaging intact zebrafish organs and structures is possible when transgenic zebrafish lines expressing a fluorescent protein (eGFP) within organs of interest are used [106]. Here, the decay of the signal intensity of eGFP within the glomerulus of the transgenic (wt1b:eGFP) line upon gentamicin injection is indicative of glomerular toxicity. This can be visualized using confocal microscopy because thin optical sections through the fluorescent specimens of up to 100 micrometers or more in thickness are possible [126]. Dedicated quantification protocols in post-processing software, such as Fiji image analysis software (version 2.1.0/1.53c)

or Imaris, allow for three-dimensional signal intensity measurements. Similar scripts have also been adapted to assess the signal intensity of fluorescent ABC/SLC substrates, polymers, and nanoparticles within the blood vessels (e.g., dorsal aorta) of zebrafish larvae. For three-dimensional reconstructions, slices through the organ can be aligned to obtain an artificial rendering that allows for studying volumes. Since confocal microscopes are widely distributed in many laboratories, researchers have easy access that favors fast and easy data acquisition. In this regard, laser-scanning confocal microscopy is a powerful imaging method enabling the imaging of up to 15 zebrafish larvae per hour (depending on the acquisition parameters).

However, rendering multiple slices of confocal laser scanning images through zebrafish larvae (z-stacks) relies on signal intensities with higher or lower pixel-noise ratios depending on the distance from the laser (depth of focus) [127]. This can reveal inaccurate three-dimensional information, especially in deeply located anatomical structures [127]. Unfortunately, the working distance of the laser beam is insufficient to image the entire zebrafish larvae, which is approximately 0.5 mm thick. This is relevant for rendering tiny renal luminal tubules with a diameter of a few micrometers located deep in the tissue. Here, alternative non-fluorescence-based imaging techniques with a good tissue penetration ability, such as X-ray-based microtomography, are more beneficial.

X-ray-based microtomography is a label-free imaging method that relies on absorption contrast (for hard tissue) or phase contrast (for soft tissue) for three-dimensional imaging of postmortem specimens [128]. A synchrotron radiation facility achieves the highest density and spatial resolutions for microanatomical structures of specimen tissues without physical slicing. This facility yields a pixel size of up to 0.65 μm with high optical resolution compared to fluorescent-based imaging techniques [128]. Density-rich structures, such as the eye and nuclei, can be easily distinguished from low-density structures, such as renal luminal spaces and soft tissue. Our study showed that mi-

crotopography images are qualitatively comparable to classical histology. Spatial alterations of the pronephros can be visually observed, segmented, and quantified using image-processing software.

However, this unique instrumentation offers limited beam times based on accepted applications or extra payments [128]. If an application is accepted, beam time is usually provided after half a year for a short defined time. Experiments at a synchrotron facility are time-consuming and highly experienced researchers (often physicists) are needed to run experiments and process the acquired data. In Europe, only a handful of synchrotron radiation facilities are available (e.g., Swiss Light Source at the Paul Scherrer Institute in Switzerland, European Synchrotron Radiation Facility in Grenoble, Deutsches Elektronen-Synchrotron in Hamburg, Soleil in Paris and the Diamond Light Source in the United Kingdom).

In this regard, laboratory-based systems have improved substantially in the last couple of years and have increased the access to X-ray-based microtomography [128]. In our study, we compared older laboratory-based systems, such as SkyScan 1275 and nanotom m available at the Core Facility of the University of Basel, with the user-friendly third-generation scanners. With the latter, excellent pixel resolution for micrometer specimens and biological tissue comparable to synchrotron radiation facilities was obtained [128, 129]. It should be noted that acquisition time at laboratory-based systems is longer (hours) compared to synchrotron radiation facilities (minutes). We do not believe that prolonged acquisition time limits the use of laboratory-based systems in biomedical and clinical sciences. We hypothesize that automated intelligence tissue recognition, analysis, and technological advantages will evolve extensively in the coming years and enable various X-ray-based microtomography applications in biomedical sciences.

It is important to mention that our study contributed to funding a new-generation laboratory-based system at the University of Basel that will run by the end of 2023.

Combined with our analysis of structural aberrations in the renal organs of zebrafish larvae and murine biopsies following gentamicin treatment, we substantially contributed to attracting attention to and confirming the possibilities of using X-ray-based microtomography for diagnostic purposes. We believe that combining the fluorescent-based imaging method (fast and high throughput) with X-ray-based microtomography (high resolution and label-free) enables the in-depth study of structural changes in renal organs induced by various nephrotoxins in the zebrafish larvae model, with translational relevance to mammals.

4.3 Mechanistic toxicity studies

Zebrafish larvae and mice show similar structural aberrations of the glomerulus and the proximal tubules after gentamicin treatment. Methodologies for assessing mechanistic toxicological studies were established for the use of zebrafish larvae as a translational *in vivo* vertebrate model. We showed that zebrafish larvae offer advantages for extrapolating cellular toxicological studies from cell-based assays to living organisms.

The toxic damage caused to mitochondria by tubular nephrotoxins was investigated with the help of teleost models. We used iopamidol, a contrast agent known to be toxic for proximal tubules, but its damage to mitochondria is not fully verified [130–132]. Studies were compared with the toxic insult of two model nephrotoxins affecting mitochondria, cadmium chloride and gentamicin [23]. We confirmed the proximal tubular toxicity of iopamidol in HEK293T cells and isolated proximal tubules of killifish and in the pronephros of zebrafish larvae. Although both teleost models are more beneficial than *in vitro* cell-based assays, zebrafish larvae offer various advantages as an *in vivo* model. This is explained with the following lines of evidence.

First, the zebrafish larva is an easy-to-handle laboratory vertebrate model, as explained under the heading 4.1 "The use of zebrafish larvae as a vertebrate model to study renal function."

Second, the toxicological assessment of nephrotoxin in a living organism respects the interaction of several organs such as the heart and kidney, as well as energy metabolism in organisms. Occasionally, renal damage is associated with cardiac edema formation that significantly affects the pathogenesis of congestive heart failure [133, 134], which was also observed in our studies. Third, zebrafish larvae have fully functional pronephros regarding excretion, reabsorption transporters, and glomerular filtration. Nephrotoxicity mediated by specific reabsorption transporters tends to reflect the mammalian mode of action. For instance, reabsorption from the luminal space into the renal epithelial cells

is the mode of toxicity for a broad class of drugs such as aminoglycosides [117, 118]. Thus, zebrafish larvae also allow for the study of toxicity in the glomerulus. Fourth, using dedicated imaging techniques, visual changes in morphology can be assessed in distinct parts such as Bowman's capsule, proximal tubules, and distal tubules with relevance to mammals. Furthermore, isolating renal epithelial cells (or other fluorescent cells depending on the transgenic zebrafish line used) allows for in-depth studies, for example, specific cell organelles or transcriptional levels of biomarkers [135].

Fifth, interaction studies of macrophages, plasma proteins, and stabilin-mediated scavenging respect more mammalian-like conditions about the pharmacokinetics and interactions of nephrotoxins. This is relevant for nephrotoxins with high plasma protein binding characteristics such as digitoxin [136].

Sixth, the use of mitochondria-specific assays, as shown, can be additionally applied to other organs. Examples are single-cell analysis of cells of the glomerulus using the transgenic (wt1b:eGFP) line or assessing the toxic impact of a stabilin knockdown on renal epithelial cells upon intoxication with a nephrotoxin using a special-engineered zebrafish line (*stab2^{ibl2}*) [107, 108].

4.4 Application of zebrafish for pharmacokinetic studies of nanoparticles

A functional kidney in zebrafish larvae allows the use of the model for broader application. In view of the usefulness and high predictability of the zebrafish model, it was applied to study the pharmacokinetics of nanoparticles. Based on fundamental work done in our research group [98, 106, 108], we carried out more applied studies benefiting from methodologies established by the kidney projects.

A human-similar size-dependent glomerular filtration is elemental for comparing the pharmacokinetics of intravenously injected nanoparticles in zebrafish larvae with vertebrates. We could show that the glomerular filtration threshold depends more on the hydrodynamic volume than molecular weight [15]. This result confirms that nanoparticles with (usually) hydrodynamic volumes of more than 100 nm are not filtered. Importantly, size-dependent glomerular filtration was verified at 96 hours post-fertilization. Pharmacokinetic studies were done using 48 to 96-hour post-fertilized zebrafish larvae. Notably, the glomerular filtration barrier unit appeared to be well developed 72 hours post-fertilization, but slit diaphragms between foot processes are rarely observed [137]. We conclude that fine size-dependent glomerular filtration studies are not possible before 96 hours post-fertilization. But, based on our results, bigger nanoparticles (> 100 nm) cannot penetrate the filtration barrier at 48 to 72 hours post-fertilization.

Since no glomerular filtration of intravenously injected nanoparticles and therapeutic peptides (> 100 nm diameter and > 8 nm, respectively) were observed, the pharmacokinetics are mainly determined by their physicochemical properties and interaction with non-renal scavenging mechanisms. Similar imaging protocols, as in the kidney project, were applied to investigate the stabilin-mediated clearance of therapeutic peptides using dextran sulfate as a competitive stabilin inhibitor and macrophage clearance with

comparable imaging strategies [115]. The following paragraphs give insights into the pharmacokinetics of nanoparticles using the zebrafish model.

Lipid nanoparticles are stable because they are spherical and made up of ionizable lipids, helper lipids, and polyethylene glycol that all together enclose genetic material or drugs [114]. The pharmacokinetic stability is mainly determined by the choice of polyethylene glycol. Its dissociation from the particle after a particular period causes immediate scavenging by macrophages, stabilin receptors, or nanoparticles eaten up by endothelial cells via endocytosis [113, 114]. When nanoparticles are fluorescently labeled, their circulation behavior and scavenging can be studied in real-time. Compared to previous studies assessing aspects of pharmacokinetics in zebrafish larvae, we focused our analysis on the fate of the enclosed drug or genetic material such as DNA or mRNA. For instance, the pharmacokinetic profile of modified light-sensitive doxorubicin-loaded nanoparticles was studied in zebrafish larvae [113]. Upon the application of a specific light trigger, aggregated nanoparticles within endothelial cells and macrophages significantly released more doxorubicin than non-photoactivatable nanoparticles [113]. Since doxorubicin is a weak fluorescent drug, the nanoparticle shell circulating in the blood hindered the detection of the fluorescent signal of doxorubicin because of quenching effects [113]. But upon its release and accumulation in the tissue, doxorubicin was detected. Of note, doxorubicin is likely rapidly cleared through the *mdr1*-orthologue renal transport system [138].

Similar findings were observed using non-viral lipid nanoparticle pDNA/mRNA constructs modified with phosphatidylserine to enhance their uptake [114]. These were around 120-140 nm in diameter and were intravenously injected into zebrafish. As soon as the polyethylene glycol linkers dissociated from the core of the nanoparticle, they were eaten up via clathrin-mediated endocytosis [114]. The transfection of the GFP-coding genes was assessed in the endothelial cells and macrophages of zebrafish owing

to their translation into the fluorescent GFP protein [114]. In these transfection experiments, zebrafish larvae are beneficial for investigating the pharmacokinetics at an early stage before animal experiments are done.

In our studies, the uptake of the different nanoparticles in the endothelial cells of zebrafish larvae is based on general endocytosis without any targeting strategies. Active targeting is an important goal in the design of novel nanoparticles to treat specific organs. Such approaches were initially inspired by Paul Ehrlich (1907), who introduced the visionary concept of the magic bullet for targeted drug delivery [139]. Active targeting can be achieved by using specific ligands on the nanoparticle shell or a defined lipid composition [115, 140]. A novel active targeting strategy was assessed in zebrafish using acoustic manipulation of microparticles [141]. The rationale for using ultrasound is the manipulation of intravenously administered gas-filled microparticles in x- and y- directions from the outside. Many systems have been established to assess acoustic-mediated manipulation, but none has been done in a vertebrate-replacing *in vivo* system. Along or against the bloodstream of zebrafish larvae, circulating microparticles (> 1 μm diameter) were manipulated by four piezoelectric actuators [141]. We highlight the possibility of using zebrafish larvae as an *in vivo* test model to design and test microbubbles for acoustic manipulation under live biological conditions. Future steps rely on the manufacturing of (fluorescent) drug-loaded and gas-filled particles that can be manipulated in the blood vessel to a place of interest. A defined and sharp increase in voltage would burst the particle and cause local drug administration. Such approaches can reduce toxic side effects and enhance treatment success. As an example, this is relevant for the initiation of thrombolysis in a clogged blood vessel [142]. or to improve the penetration of the blood-brain barrier through the oscillation of intravenously administered microbubbles [143, 144]. Using zebrafish larvae, such strategies can be assessed early in the developmental steps in alignment with the 3R principles.

4.5 Future perspectives of the zebrafish model

Despite the many advantages of the zebrafish larvae kidney model, it has some limitations compared to *ex vivo* studies, such as the killifish and *in vivo* animal models. The following aspects are limitations that need to be considered or further developed when using zebrafish as a vertebrate model to study renal function and toxicology.

First, not all previously introduced drug-induced renal toxicities (Chapter 1.2 and Table 1.1) can be studied in the presented teleost models. We verified that acute drug-induced toxicity (administered with a bolus injection or incubation) affecting the mitochondria of renal tubules is possible. Chronic exposure (more than two days) that often causes autoimmune-mediated renal toxicities can not be studied in teleost models because they can only be used for a short time, as previously explained in Chapter 4.1. Such studies needed to be carried out under valid animal experimentation permissions. Acute glomerular-related and interstitial toxicities could be studied more in detail if fluorescent transgenic lines expressing GFP in these cell types were available using our established protocols.

Second, urine cannot be collected because zebrafish have an open renal system and lack a urinary bladder. Strategies used to measure the concentration of cleared (fluorescent) substances in the incubation media are challenging owing to the low concentration. Consequently, highly sensitive analytical methods need to be established to measure the content of cleared substances in the incubation media. Similar counts for blood and urine biochemical analysis. This standard method is established in animal studies and enables the analysis of changes in urinary and blood biomarkers, and immune cells [145].

Third, there are limitations in studying the signaling pathways of drug transporters in zebrafish larvae. Usually, studies on how nephrotoxins interact with ABC transporters are important to understand the pharmacokinetics involved. Such studies were substan-

tially investigated in, for example, isolated proximal tubules of killifish [146]. Proteins involved in the signaling cascade of ABC transporters were determined using specific inhibitors [147]. For instance, the effect of nephrotoxins (gentamicin) on Mrp2 transport and the mechanism involved were confirmed in isolated proximal tubules of killifish [89]. Such studies are based on the use of various, often lipophilic, inhibitors of the transport signaling cascade and spiked into the incubation media of isolated renal tubules. Similar studies in zebrafish larvae are complex since many lipophilic inhibitors cannot be administered in the required concentration to observe an effect. Here an in-depth study and evaluation of water-soluble inhibitors of the signal cascades need to be established. Fourth, the zebrafish does not have a functional liver before five days post-fertilization [148, 149]. Therefore, alternative clearance mechanisms with respect to the liver-induced metabolism of xenobiotics are not considered to be present in zebrafish larvae. However, studies investigating metabolism via P450 cytochromes are very controversial. Reports have revealed that P450 cytochromes are partially present but do not contribute significantly to the outcome of pharmacological or toxicological safety studies [150]. Others have verified CYP3A4, 2D6, and 2C functional activities of a test compound in two- to three-day-old zebrafish, although others have not [151]. Therefore, metabolism in zebrafish larvae cannot be neglected and should be carefully considered during experimentation. This differs significantly from vertebrate *in vivo* studies with functional liver metabolism. This limits the screening of transporter involvement and toxicity studies of, in particular, prodrug and cytochrome-caused metabolites in zebrafish larvae [152]. Fifth, the exact blood volume of zebrafish during different stages of embryogenesis changes rapidly and is not yet fully known. We hypothesized that blood volume ranges from 60 nL (two days old) to 120 nL (four days old) [15]. This information is essential for plasma concentration calculations with respect to extrapolation to mammals. Sixth, a comparative quantitative analysis of plasma concentration of intravenously in-

jected nanoparticles or other fluorescent substances using fluorescent correlation spectroscopy would finally verify the applicability of the zebrafish model as a vertebrate model.

CONCLUSION

During this PhD research study, four major work packages were created to elaborate on the use of zebrafish larvae to study renal function, nephrotoxicity, and early-stage *in vivo* pharmacokinetic studies.

First, the zebrafish has demonstrated a fully functional kidney. Key renal features, such as glomerular filtration, proximal tubular excretion, and reabsorption, were found to be similar to those observed in mammals. Imaging and treatment protocols were established, and detailed non-renal clearance mechanisms were described. These features allow for the use of zebrafish larvae for renal elimination studies by applying the experimental setup (**Part I**).

Second, a functional kidney is fundamental for the use of zebrafish larvae for nephrotoxicity studies. Morphological aberrations of the pronephros and the glomerulus upon administering a nephrotoxin were studied using dedicated imaging techniques. We compared confocal microscopy and X-ray-based microtomography to visualize gentamicin-induced kidney damage and compared the observed damage with kidney biopsies of mice. Comparable resolution of microtomography data from a synchrotron radiation

facility compared with laboratory-based microtomography apparatuses offer future in-house applications in biomedical sciences with respect to diagnostics **(Part II)**.

Third, macroscopic changes in renal organs that are similar to mammals highlight the translatability of zebrafish larvae. A mechanistic study of renal tubular damage was done using iopamidol, a frequently used iodinated contrast agent associated with renal impairment. The toxicity of iopamidol on mitochondria of proximal renal epithelial cells in zebrafish larvae was assessed using fluorescent-based toxicological assays. Results were confirmed using isolated proximal tubules of killifish and were compared with gentamicin sulfate and cadmium chloride, two well-known tubular toxicants **(Part III)**.

Fourth, since the zebrafish is an excellent translational vertebrate model, it was applied for the pharmacokinetic development and early-stage *in vivo* assessment of nanoparticle. The biodistribution, drug release, non-renal elimination processes, transfection of pDNA/mRNA genetic information encapsulated in nanoparticles, and acoustic manipulation of gas-filled particles were tested in zebrafish larvae. These findings successfully demonstrated the benefits of the zebrafish model under dynamic biological conditions **(Part IV)**.

Conclusively, the findings of this PhD research show the usefulness and possibilities of using zebrafish larvae for renal physiological and nephrotoxicological applications. The renal and non-renal elimination processes reflect more mammalian similar characteristics than *in vitro* cell culture experiments. Zebrafish larvae can also be applied in several aspects for pharmacokinetic studies of intravenously injected nanoparticles.

BIBLIOGRAPHY

- [1] Zaher A. Radi. Kidney Pathophysiology, Toxicology, and Drug-Induced Injury in Drug Development. *International Journal of Toxicology*, 38(3):215–227, May 2019. Publisher: SAGE Publications Inc.
- [2] Wanda M. Haschek, Colin G. Rousseaux, Matthew A. Wallig, Brad Bolon, and Ricardo Ochoa. *Haschek and Rousseaux's Handbook of Toxicologic Pathology*. Academic Press, May 2013. Google-Books-ID: RXsdAAAAQBAJ.
- [3] Thomas Benzing and David Salant. Insights into Glomerular Filtration and Albuminuria. *New England Journal of Medicine*, 384(15):1437–1446, April 2021. Publisher: Massachusetts Medical Society.
- [4] Miriam A. Wallace. Anatomy and Physiology of the Kidney. *AORN Journal*, 68(5):799–820, 1998. [_eprint: https://onlinelibrary.wiley.com/doi/pdf/10.1016/S0001-2092%2806%2962377-6](https://onlinelibrary.wiley.com/doi/pdf/10.1016/S0001-2092%2806%2962377-6).
- [5] Hidetake Kurihara and Tatsuo Sakai. Cell biology of mesangial cells: the third cell that maintains the glomerular capillary. *Anatomical Science International*, 92(2):173–186, March 2017.
- [6] Madhav C. Menon, Peter Y. Chuang, and Cijiang John He. The Glomerular Filtration Barrier: Components and Crosstalk. *International Journal of Nephrology*, 2012:749010, 2012.
- [7] Kerstin Ebefors, Emelie Lassén, Nanditha Anandakrishnan, Evren U. Azeloglu, and Ilse S. Daehn. Modeling the Glomerular Filtration Barrier and Intercellular Crosstalk. *Frontiers in Physiology*, 12:689083, June 2021.
- [8] Ilse S. Daehn and Jeremy S. Duffield. The glomerular filtration barrier: a structural target for novel kidney therapies. *Nature Reviews. Drug Discovery*, 20(10):770–788, 2021.
- [9] Börje Haraldsson and Marie Jeansson. Glomerular filtration barrier. *Current Opinion in Nephrology and Hypertension*, 18(4):331–335, July 2009.
- [10] Norman P. Curthoys and Orson W. Moe. Proximal Tubule Function and Response to Acidosis. *Clinical Journal of the American Society of Nephrology : CJASN*, 9(9):1627–1638, September 2014.
- [11] Amanda N. Marra, Yue Li, and Rebecca A. Wingert. Antennas of organ morphogenesis: the roles of cilia in vertebrate kidney development. *Genesis (New York, N.y. : 2000)*, 54(9):457–469, September 2016.
- [12] Rikke Nielsen, Erik Ilsø Christensen, and Henrik Birn. Megalin and cubilin in proximal tubule protein reabsorption: from experimental models to human disease. *Kidney International*, 89(1):58–67, January 2016.
- [13] Xiaodong Liu. ABC Family Transporters. In Xiaodong Liu and Guoyu Pan, editors, *Drug Transporters in Drug Disposition, Effects and Toxicity*, Advances in Experimental Medicine and Biology, pages 13–100. Springer, Singapore, 2019.

BIBLIOGRAPHY

- [14] Hideyuki Motohashi and Ken-ichi Inui. Organic Cation Transporter OCTs (SLC22) and MATEs (SLC47) in the Human Kidney. *The AAPS Journal*, 15(2):581–588, February 2013.
- [15] Jan Stephan Bolten, Anna Pratsinis, Claudio Luca Alter, Gert Fricker, and Jörg Huwyler. Zebrafish (*Danio rerio*) larva as an in vivo vertebrate model to study renal function. *American Journal of Physiology-Renal Physiology*, 322(3):F280–F294, March 2022. Publisher: American Physiological Society.
- [16] Miriam Zacchia, Giovanna Capolongo, Luca Rinaldi, and Giovambattista Capasso. The importance of the thick ascending limb of Henles loop in renal physiology and pathophysiology. *International Journal of Nephrology and Renovascular Disease*, 11:81–92, February 2018.
- [17] David B. Mount. Thick Ascending Limb of the Loop of Henle. *Clinical Journal of the American Society of Nephrology : CJASN*, 9(11):1974–1986, November 2014.
- [18] R. Todd Alexander and Henrik Dimke. Effect of diuretics on renal tubular transport of calcium and magnesium. *American Journal of Physiology-Renal Physiology*, 312(6):F998–F1015, June 2017. Publisher: American Physiological Society.
- [19] Lawrence G. Palmer and Jürgen Schnermann. Integrated Control of Na Transport along the Nephron. *Clinical Journal of the American Society of Nephrology : CJASN*, 10(4):676–687, April 2015.
- [20] Muhammad F. Hashmi, Onecia Benjamin, and Sarah L. Lappin. End-Stage Renal Disease. In *StatPearls*. StatPearls Publishing, Treasure Island (FL), 2022.
- [21] João Faria, Sabbir Ahmed, Karin G. F. Gerritsen, Silvia M. Mihaila, and Rosalinde Masereeuw. Kidney-based in vitro models for drug-induced toxicity testing. *Archives of Toxicology*, 93(12):3397–3418, December 2019. Company: Springer Distributor: Springer Institution: Springer Label: Springer Number: 12 Publisher: Springer Berlin Heidelberg.
- [22] J. Kaufman, M. Dhakal, B. Patel, and R. Hamburger. Community-acquired acute renal failure. *American Journal of Kidney Diseases: The Official Journal of the National Kidney Foundation*, 17(2):191–198, February 1991.
- [23] Cynthia A. Naughton. Drug-Induced Nephrotoxicity. *American Family Physician*, 78(6):743–750, September 2008.
- [24] Hardik Mody, Vidya Ramakrishnan, Maher Chaar, Jovin Lezeau, Adrian Rump, Kareem Taha, Lawrence Lesko, and Sihem Ait-Oudhia. A Review on Drug-Induced Nephrotoxicity: Pathophysiological Mechanisms, Drug Classes, Clinical Management, and Recent Advances in Mathematical Modeling and Simulation Approaches. *Clinical Pharmacology in Drug Development*, 9(8):896–909, 2020. _eprint: <https://onlinelibrary.wiley.com/doi/pdf/10.1002/cpdd.879>.
- [25] Marina Vivarelli, Laura Massella, Barbara Ruggiero, and Francesco Emma. Minimal Change Disease. *Clinical journal of the American Society of Nephrology: CJASN*, 12(2):332–345, February 2017.
- [26] Emmanuel Letavernier, Patrick Bruneval, Chantal Mandet, Jean-Paul Duong Van Huyen, Marie-Noëlle Péraldi, Imed Helal, Laure-Hélène Noël, and Christophe Legendre. High sirolimus levels may induce focal segmental glomerulosclerosis de novo. *Clinical journal of the American Society of Nephrology: CJASN*, 2(2):326–333, March 2007.
- [27] Kimberly Reidy and Frederick J. Kaskel. Pathophysiology of focal segmental glomerulosclerosis. *Pediatric Nephrology (Berlin, Germany)*, 22(3):350–354, 2007.

- [28] Mark A Perazella and Randy L Luciano. Review of select causes of drug-induced AKI. *Expert Review of Clinical Pharmacology*, 8(4):367–371, July 2015. Publisher: Taylor & Francis _eprint: <https://doi.org/10.1586/17512433.2015.1045489>.
- [29] Alwin HL Loh and Arthur H Cohen. Drug-induced Kidney Disease Pathology and Current Concepts. *Annals of the Academy of Medicine, Singapore*, 38(3):240–250, March 2009.
- [30] Jai Radhakrishnan and Mark A. Perazella. Drug-Induced Glomerular Disease: Attention Required! *Clinical Journal of the American Society of Nephrology*, 10(7):1287, July 2015.
- [31] Ramy M. Hanna, Marina Barsoum, Farid Arman, Umut Selamet, Huma Hasnain, and Ira Kurtz. Nephrotoxicity induced by intravitreal vascular endothelial growth factor inhibitors: emerging evidence. *Kidney International*, 96(3):572–580, September 2019.
- [32] Ramy M Hanna, Eduardo A Lopez, Huma Hasnain, Umut Selamet, James Wilson, Peter N Youssef, Nermeen Akladeous, Suphamai Bunnapradist, and Michael B Gorin. Three patients with injection of intravitreal vascular endothelial growth factor inhibitors and subsequent exacerbation of chronic proteinuria and hypertension. *Clinical Kidney Journal*, 12(1):92–100, February 2019.
- [33] Michael Shye, Ramy M Hanna, Sapna S Patel, Ngoc Tram-Tran, Jean Hou, Collin Mccannel, Maham Khalid, Mina Hanna, Lama Abdelnour, and Ira Kurtz. Worsening proteinuria and renal function after intravitreal vascular endothelial growth factor blockade for diabetic proliferative retinopathy. *Clinical Kidney Journal*, 13(6):969–980, December 2020.
- [34] Mark A. Perazella. Renal Vulnerability to Drug Toxicity. *Clinical Journal of the American Society of Nephrology*, 4(7):1275, July 2009.
- [35] Glen S. Markowitz and Mark A. Perazella. Drug-induced renal failure: a focus on tubulointerstitial disease. *Clinica Chimica Acta*, 351(1):31–47, January 2005.
- [36] Mark A. Perazella. Crystal-induced acute renal failure. *The American Journal of Medicine*, 106(4):459–465, April 1999.
- [37] Hassane Izzedine, Vincent Launay-Vacher, and Gilbert Deray. Antiviral Drug-Induced Nephrotoxicity. *American Journal of Kidney Diseases*, 45(5):804–817, May 2005.
- [38] Randy L. Luciano and Mark A. Perazella. Crystalline-induced kidney disease: a case for urine microscopy. *Clinical Kidney Journal*, 8(2):131–136, April 2015.
- [39] Hassane Izzedine, François Xavier Lescure, and Fabrice Bonnet. HIV medication-based urolithiasis. *Clinical Kidney Journal*, 7(2):121–126, April 2014.
- [40] S. Swaminathan, S. Pollett, R. Loblay, and C. Macleod. Sulfonamide crystals and acute renal failure. *Internal Medicine Journal*, 36(6):399–400, 2006. _eprint: <https://onlinelibrary.wiley.com/doi/pdf/10.1111/j.1445-5994.2006.01080.x>.
- [41] Samih H. Nasr, Dawn S. Milliner, Thomas D. Wooldridge, and Sanjeev Sethi. Triamterene Crystalline Nephropathy. *American Journal of Kidney Diseases*, 63(1):148–152, January 2014.
- [42] George Sunny Pazhayattil and Anushree C Shirali. Drug-induced impairment of renal function. *International Journal of Nephrology and Renovascular Disease*, 7:457–468, December 2014.
- [43] Charles M Kodner. Diagnosis and Management of Acute Interstitial Nephritis. 67(12), 2003.
- [44] Fatemeh Ghane Shahrbaaf and Farahnak Assadi. Drug-induced renal disorders. *Journal of Renal Injury Prevention*, 4(3):57–60, September 2015.

BIBLIOGRAPHY

- [45] Mark A. Perazella. Pharmacology behind Common Drug Nephrotoxicities. *Clinical Journal of the American Society of Nephrology*, 13(12):1897, December 2018.
- [46] Thomas D. Nolin and Jonathan Himmelfarb. Mechanisms of Drug-Induced Nephrotoxicity. In Jack Uetrecht, editor, *Adverse Drug Reactions*, Handbook of Experimental Pharmacology, pages 111–130. Springer, Berlin, Heidelberg, 2010.
- [47] M. P. Mingeot-Leclercq and P. M. Tulkens. Aminoglycosides: nephrotoxicity. *Antimicrobial Agents and Chemotherapy*, 43(5):1003–1012, May 1999.
- [48] Pitchai Balakumar, Ankur Rohilla, and Arunachalam Thangathirupathi. Gentamicin-induced nephrotoxicity: Do we have a promising therapeutic approach to blunt it? *Pharmacological Research*, 62(3):179–186, September 2010.
- [49] Nicholas J Lowe, Joshua M Wieder, Alan Rosenbach, Kent Johnson, Robin Kunkel, Carol Bainbridge, Teresa Bourget, Ivailo Dimov, Karen Simpson, Edwin Glass, and Morris T Grabie. Long-term low-dose cyclosporine therapy for severe psoriasis: Effects on renal function and structure. *Journal of the American Academy of Dermatology*, 35(5, Part 1):710–719, November 1996.
- [50] Shigeo Takebayashi, Shiro Jimi, Masaru Segawa, and Yasuhiro Kiyoshi. Cadmium induces osteomalacia mediated by proximal tubular atrophy and disturbances of phosphate reabsorption. A study of 11 autopsies. *Pathology - Research and Practice*, 196(9):653–663, January 2000.
- [51] Juan Carlos Jado, Blanca Humanes, María Ángeles González-Nicolás, Sonia Camaño, José Manuel Lara, Beatriz López, Emilia Cercenado, Julio García-Bordas, Alberto Tejedor, and Alberto Lázaro. Nephroprotective Effect of Cilastatin against Gentamicin-Induced Renal Injury In Vitro and In Vivo without Altering Its Bactericidal Efficiency. *Antioxidants*, 9(9), September 2020.
- [52] Andrew M. Hall, Francesco Trepiccione, and Robert J. Unwin. Drug toxicity in the proximal tubule: new models, methods and mechanisms. *Pediatric Nephrology*, 37(5):973–982, May 2022.
- [53] Mark A. Perazella. Drug-induced acute kidney injury: diverse mechanisms of tubular injury. *Current Opinion in Critical Care*, 25(6):550–557, December 2019.
- [54] G B Fogazzi. CrystaUria: a neglected aspect of urinary sediment analysis.
- [55] Joanne Y.-C. Soo, Jitske Jansen, Rosalinde Masereeuw, and Melissa H. Little. Advances in predictive in vitro models of drug-induced nephrotoxicity. *Nature reviews. Nephrology*, 14(6):378–393, June 2018.
- [56] Johnny X Huang, Mark A Blaskovich, and Matthew A Cooper. Cell- and biomarker-based assays for predicting nephrotoxicity. *Expert Opinion on Drug Metabolism & Toxicology*, 10(12):1621–1635, December 2014. Publisher: Taylor & Francis _eprint: <https://doi.org/10.1517/17425255.2014.967681>.
- [57] M. J. Ryan, G. Johnson, J. Kirk, S. M. Fuerstenberg, R. A. Zager, and B. Torok-Storb. HK-2: an immortalized proximal tubule epithelial cell line from normal adult human kidney. *Kidney International*, 45(1):48–57, January 1994.
- [58] Matthias Wieser, Guido Stadler, Paul Jennings, Berthold Streubel, Walter Pfaller, Peter Ambros, Claus Riedl, Hermann Katinger, Johannes Grillari, and Regina Grillari-Voglauer. hTERT alone immortalizes epithelial cells of renal proximal tubules without changing their functional characteristics. *American Journal of Physiology. Renal Physiology*, 295(5):F1365–1375, November 2008.
- [59] Martijn J. Wilmer, Moin A. Saleem, Rosalinde Masereeuw, Lan Ni, Thea J. van der Velden, Frans G. Russel, Peter W. Mathieson, Leo A. Monnens, Lambertus P. van den Heuvel, and Elena N. Levchenko. Novel conditionally immortalized human proximal tubule cell line expressing functional influx and efflux transporters. *Cell and Tissue Research*, 339(2):449–457, February 2010.

- [60] Lorraine C. Racusen, C. Monteil, Anita Sgrignoli, Margit Lucskay, S. Marouillat, John G. S. Rhim, and Jean-paul Morin. Cell lines with extended in vitro growth potential from human renal proximal tubule: Characterization, response to inducers, and comparison with established cell lines. *Journal of Laboratory and Clinical Medicine*, 129(3):318–329, March 1997.
- [61] J. P. Morin, S. Marouillat, C. Lendormi, and C. Monteil. Comparative impact of cephaloridine on glutathione and related enzymes in LLC-PK1, LLC-RK1, and primary cultures of rat and rabbit proximal tubule cells. *Cell Biology and Toxicology*, 12(4-6):275–282, December 1996.
- [62] R. Nielsen, H. Birn, S. K. Moestrup, M. Nielsen, P. Verroust, and E. I. Christensen. Characterization of a kidney proximal tubule cell line, LLC-PK1, expressing endocytotic active megalin. *Journal of the American Society of Nephrology: JASN*, 9(10):1767–1776, October 1998.
- [63] Dieter Steinmassl, Walter Pfaller, Gerhard Gstraunthaler, and Wolfgang Hoffmann. LLC-PK1 epithelia as a model for in vitro assessment of proximal tubular nephrotoxicity. *In Vitro Cellular & Developmental Biology - Animal*, 31(2):94–106, February 1995.
- [64] J. J. H. Chu and M. L. Ng. Infection of polarized epithelial cells with flavivirus West Nile: polarized entry and egress of virus occur through the apical surface. *Journal of General Virology*, 83(10):2427–2435, 2002. Publisher: Microbiology Society,.
- [65] Bruce A. McClane and Ganes Chakrabarti. New insights into the cytotoxic mechanisms of Clostridium perfringens enterotoxin. *Anaerobe*, 10(2):107–114, April 2004.
- [66] Walter C. Prozialeck, Joshua R. Edwards, Peter C. Lamar, and Conor S. Smith. Epithelial barrier characteristics and expression of cell adhesion molecules in proximal tubule-derived cell lines commonly used for in vitro toxicity studies. *Toxicology in Vitro*, 20(6):942–953, September 2006.
- [67] Pilar Carranza-Rosales, Salvador Said-Fernández, Julio Sepúlveda-Saavedra, Delia E. Cruz-Vega, and A. Jay Gandolfi. Morphologic and functional alterations induced by low doses of mercuric chloride in the kidney OK cell line: ultrastructural evidence for an apoptotic mechanism of damage. *Toxicology*, 210(2):111–121, June 2005.
- [68] Elizabeth McNeil, Christopher T. Capaldo, and Ian G. Macara. Zonula Occludens-1 Function in the Assembly of Tight Junctions in Madin-Darby Canine Kidney Epithelial Cells. *Molecular Biology of the Cell*, 17(4):1922–1932, April 2006.
- [69] Kyoko Hayashi. Role of tight junctions of polarized epithelial MDCK cells in the replication of herpes simplex virus type 1. *Journal of Medical Virology*, 47(4):323–329, 1995. _eprint: <https://onlinelibrary.wiley.com/doi/pdf/10.1002/jmv.1890470406>.
- [70] Daniel Schiwiek, Nicole Endlich, Lawrence Holzman, Harry Holthöfer, Wilhelm Kriz, and Karlhans Endlich. Stable expression of nephrin and localization to cell-cell contacts in novel murine podocyte cell lines. *Kidney International*, 66(1):91–101, July 2004.
- [71] Sarah E. Jenkinson, Git W. Chung, Ellen van Loon, Nur S. Bakar, Abigail M. Dalzell, and Colin D. A. Brown. The limitations of renal epithelial cell line HK-2 as a model of drug transporter expression and function in the proximal tubule. *Pflügers Archiv - European Journal of Physiology*, 464(6):601–611, December 2012.
- [72] Paul A. Glynn. Primary Culture of Human Proximal Renal Tubular Epithelial Cells. In Thomas J. Evans, editor, *Septic Shock Methods and Protocols*, Methods in Molecular Medicine, pages 197–205. Humana Press, Totowa, NJ, 2000.
- [73] Walter C. Prozialeck and Joshua R. Edwards. Cell Adhesion Molecules in Chemically-Induced Renal Injury. *Pharmacology & therapeutics*, 114(1):74–93, April 2007.

BIBLIOGRAPHY

- [74] Jianwen Hu, Jizhong Han, Haoran Li, Xian Zhang, Lan Lan Liu, Fei Chen, and Bin Zeng. Human Embryonic Kidney 293 Cells: A Vehicle for Biopharmaceutical Manufacturing, Structural Biology, and Electrophysiology. *Cells, Tissues, Organs*, 205(1):1–8, 2018.
- [75] Lydia Aschauer, Giada Carta, Nadine Vogelsang, Eberhard Schlatter, and Paul Jennings. Expression of xenobiotic transporters in the human renal proximal tubule cell line RPTEC/TERT1. *Toxicology in Vitro*, 30(1, Part A):95–105, December 2015.
- [76] Jing Xu, Munehiro Kitada, Yoshio Ogura, Haijie Liu, and Daisuke Koya. Dapagliflozin Restores Impaired Autophagy and Suppresses Inflammation in High Glucose-Treated HK-2 Cells. *Cells*, 10(6):1457, June 2021.
- [77] Sunita J. Shukla, Ruili Huang, Christopher P. Austin, and Menghang Xia. The future of toxicity testing: a focus on in vitro methods using a quantitative high-throughput screening platform. *Drug Discovery Today*, 15(23-24):997–1007, December 2010.
- [78] Steffen Baltes, Alexandra M. Gastens, Maren Fedrowitz, Heidrun Potschka, Volkhard Kaefer, and Wolfgang Löscher. Differences in the transport of the antiepileptic drugs phenytoin, levetiracetam and carbamazepine by human and mouse P-glycoprotein. *Neuropharmacology*, 52(2):333–346, February 2007.
- [79] P. Limtrakul, S. Siwanon, S. Yodkeeree, and C. Duangrat. Effect of *Stemona curtisii* root extract on P-glycoprotein and MRP-1 function in multidrug-resistant cancer cells. *Phytomedicine*, 14(6):381–389, June 2007.
- [80] Lianne J. Stevens, Joanne M. Donkers, Jeroen Dubbeld, Wouter H. J. Vaes, Catherijne A. J. Knibbe, Ian P. J. Alwayn, and Evita van de Steeg. Towards human ex vivo organ perfusion models to elucidate drug pharmacokinetics in health and disease. *Drug Metabolism Reviews*, 52(3):438–454, July 2020. Publisher: Taylor & Francis _eprint: <https://doi.org/10.1080/03602532.2020.1772280>.
- [81] Vijaya L. Damaraju, Carol E. Cass, and Michael B. Sawyer. Chapter 6 Renal Conservation of Folates: Role of Folate Transport Proteins. In *Vitamins & Hormones*, volume 79 of *Folic Acid and Folates*, pages 185–202. Academic Press, January 2008.
- [82] R. Hori, N. Okamura, T. Aiba, and Y. Tanigawara. Role of P-glycoprotein in renal tubular secretion of digoxin in the isolated perfused rat kidney. *Journal of Pharmacology and Experimental Therapeutics*, 266(3):1620–1625, September 1993. Publisher: American Society for Pharmacology and Experimental Therapeutics.
- [83] J. M. Nishiitsutsuji-Uwo, B. D. Ross, and H. A. Krebs. Metabolic activities of the isolated perfused rat kidney. *Biochemical Journal*, 103(3):852–862, June 1967.
- [84] J. T. Van Crugten, B. C. Sallustio, R. L. Nation, and A. A. Somogyi. Renal tubular transport of morphine, morphine-6-glucuronide, and morphine-3-glucuronide in the isolated perfused rat kidney. *Drug Metabolism and Disposition*, 19(6):1087–1092, November 1991. Publisher: American Society for Pharmacology and Experimental Therapeutics.
- [85] Gert Fricker, Heike Gutmann, Agathe Droulle, Juergen Drewe, and David Miller. Epithelial Transport of Anthelmintic Ivermectin in a Novel Model of Isolated Proximal Kidney Tubules. *Pharmaceutical research*, 16:1570–5, November 1999.
- [86] Carsten H. Baehr, Gert Fricker, and David S. Miller. Fluorescein-methotrexate transport in dogfish shark (*Squalus acanthias*) choroid plexus. *American Journal of Physiology-Regulatory, Integrative and Comparative Physiology*, 291(2):R464–R472, August 2006.

- [87] Rosalinde Masereeuw, Sylvie A. Terlouw, Rémon A. M. H. van Aubel, Frans G. M. Russel, and David S. Miller. Endothelin B Receptor-Mediated Regulation of ATP-Driven Drug Secretion in Renal Proximal Tubule. *Molecular Pharmacology*, 57(1):59–67, January 2000. Publisher: American Society for Pharmacology and Experimental Therapeutics Section: Article.
- [88] D. S. Miller. Protein kinase C regulation of organic anion transport in renal proximal tubule. *The American Journal of Physiology*, 274(1):F156–164, January 1998.
- [89] Sylvia Notenboom, David S. Miller, Leon H. Kuik, Paul Smits, Frans G. M. Russel, and Rosalinde Masereeuw. Short-Term Exposure of Renal Proximal Tubules to Gentamicin Increases Long-Term Multidrug Resistance Protein 2 (Abcc2) Transport Function and Reduces Nephrotoxicant Sensitivity. *Journal of Pharmacology and Experimental Therapeutics*, 315(2):912–920, November 2005. Publisher: American Society for Pharmacology and Experimental Therapeutics Section: GASTROINTESTINAL, HEPATIC, PULMONARY, AND RENAL.
- [90] Sylvia Notenboom, David S. Miller, Paul Smits, Frans G. M. Russel, and Rosalinde Masereeuw. Role of NO in endothelin-regulated drug transport in the renal proximal tubule. *American Journal of Physiology-Renal Physiology*, 282(3):F458–F464, March 2002.
- [91] Krit Jaikumkao, Anchalee Pongchaidecha, La-ongdao Thongnak, Keerati Wanchai, Phatchawan Arjinajarn, Varanuj Chatsudhipong, Nipon Chattipakorn, and Anusorn Lungkaphin. Amelioration of Renal Inflammation, Endoplasmic Reticulum Stress and Apoptosis Underlies the Protective Effect of Low Dosage of Atorvastatin in Gentamicin-Induced Nephrotoxicity. *PLOS ONE*, 11(10):e0164528, November 2016. Publisher: Public Library of Science.
- [92] Akram Jamshidzadeh, Reza Heidari, Soliman MohammadiSamani, Negar Azarpira, Asma Najbi, Parisa Jahani, and Narges Abdoli. A Comparison between the Nephrotoxic Profile of Gentamicin and Gentamicin Nanoparticles in Mice. *Journal of Biochemical and Molecular Toxicology*, 29(2):57–62, 2015. _eprint: <https://onlinelibrary.wiley.com/doi/pdf/10.1002/jbt.21667>.
- [93] Mohamed A. Nassan, Mohamed M. Soliman, Adil Aldhahrani, Fayez Althobaiti, and Adel Q. Alkhedaide. Ameliorative impacts of Glycyrrhiza glabra root extract against nephrotoxicity induced by gentamicin in mice. *Food Science & Nutrition*, 9(7):3405–3413, May 2021.
- [94] Cokun Silan, Ozge Uzun, Nil Ustünda Comunolu, Sanem Gokçen, Selma Bedirhan, and Müjgan Cengiz. Gentamicin-induced nephrotoxicity in rats ameliorated and healing effects of resveratrol. *Biological & Pharmaceutical Bulletin*, 30(1):79–83, January 2007.
- [95] Bárbara Tavares and Susana Santos Lopes. The importance of Zebrafish in biomedical research. *Acta Medica Portuguesa*, 26(5):583–592, 2013.
- [96] Charles B. Kimmel, William W. Ballard, Seth R. Kimmel, Bonnie Ullmann, and Thomas F. Schilling. Stages of embryonic development of the zebrafish. *Developmental Dynamics*, 203(3):253–310, 1995. _eprint: <https://onlinelibrary.wiley.com/doi/pdf/10.1002/aja.1002030302>.
- [97] Tsegay Teame, Zhen Zhang, Chao Ran, Hongling Zhang, Yalin Yang, Qianwen Ding, Minxu Xie, Chenchen Gao, Yongan Ye, Ming Duan, and Zhigang Zhou. The use of zebrafish (*Danio rerio*) as biomedical models. *Animal Frontiers*, 9(3):68–77, June 2019.
- [98] Sandro Sieber, Philip Grossen, Pascal Detampel, Salome Siegfried, Dominik Witzigmann, and Jörg Huwyler. Zebrafish as an early stage screening tool to study the systemic circulation of nanoparticulate drug delivery systems in vivo. *Journal of Controlled Release*, 264:180–191, October 2017.

BIBLIOGRAPHY

- [99] Uwe Strähle, Stefan Scholz, Robert Geisler, Petra Greiner, Henner Hollert, Sepand Rastegar, Axel Schumacher, Ingrid Selderslaghs, Carsten Weiss, Hilda Witters, and Thomas Braunbeck. Zebrafish embryos as an alternative to animal experiments—a commentary on the definition of the onset of protected life stages in animal welfare regulations. *Reproductive Toxicology (Elmsford, N.Y.)*, 33(2):128–132, April 2012.
- [100] Tae-Young Choi, Tae-Ik Choi, Yu-Ri Lee, Seong-Kyu Choe, and Cheol-Hee Kim. Zebrafish as an animal model for biomedical research. *Experimental & Molecular Medicine*, 53(3):310–317, March 2021.
- [101] Vandana S. Nikam, Deeksha Singh, Rohan Takawale, and Minal R. Ghante. Zebrafish: An emerging whole-organism screening tool in safety pharmacology. *Indian Journal of Pharmacology*, 52(6):505–513, 2020.
- [102] Rodrigo Zanandrea, Carla D. Bonan, and Maria M. Campos. Zebrafish as a model for inflammation and drug discovery. *Drug Discovery Today*, 25(12):2201–2211, December 2020.
- [103] Ling-Ling Jiang, Kang Li, Dong-Lin Yan, Mi-Fang Yang, Lan Ma, and Li-Zhe Xie. Toxicity Assessment of 4 Azo Dyes in Zebrafish Embryos. *International Journal of Toxicology*, 39(2):115–123, March 2020. Publisher: SAGE Publications Inc.
- [104] Xiaopan Luo, Long Chen, Yunlong Zhang, Jintao Liu, and Hong Xie. Developmental and cardiac toxicities of propofol in zebrafish larvae. *Comparative Biochemistry and Physiology Part C: Toxicology & Pharmacology*, 237:108838, November 2020.
- [105] Carmine Merola, Tyrone LuconXiccato, Cristiano Bertolucci, and Monia Perugini. Behavioural effects of early-life exposure to parabens in zebrafish larvae. *Journal of Applied Toxicology*, n/a(n/a). _eprint: <https://analyticalsciencejournals.onlinelibrary.wiley.com/doi/pdf/10.1002/jat.4171>.
- [106] Sandro Sieber, Philip Grossen, Jeroen Bussmann, Frederick Campbell, Alexander Kros, Dominik Witzigmann, and Jörg Huwyler. Zebrafish as a preclinical in vivo screening model for nanomedicines. *Advanced Drug Delivery Reviews*, 151-152:152–168, 2019.
- [107] Frederick Campbell, Frank L. Bos, Sandro Sieber, Gabriela Arias-Alpizar, Bjørn E. Koch, Jörg Huwyler, Alexander Kros, and Jeroen Bussmann. Directing Nanoparticle Biodistribution through Evasion and Exploitation of Stab2-Dependent Nanoparticle Uptake. *ACS Nano*, 12(3):2138–2150, March 2018.
- [108] Sandro Sieber, Philip Grossen, Philipp Uhl, Pascal Detampel, Walter Mier, Dominik Witzigmann, and Jörg Huwyler. Zebrafish as a predictive screening model to assess macrophage clearance of liposomes in vivo. *Nanomedicine: Nanotechnology, Biology and Medicine*, 17:82–93, April 2019.
- [109] Iain Drummond. Making a zebrafish kidney: a tale of two tubes. *Trends in Cell Biology*, 13(7):357–365, July 2003.
- [110] Iain A. Drummond and Alan J. Davidson. Chapter 9 - Zebrafish Kidney Development. In H. William Detrich, Monte Westerfield, and Leonard I. Zon, editors, *Methods in Cell Biology*, volume 100 of *The Zebrafish: Cellular and Developmental Biology, Part A*, pages 233–260. Academic Press, January 2010.
- [111] R. A. Wingert and A. J. Davidson. The zebrafish pronephros: A model to study nephron segmentation. *Kidney International*, 73(10):1120–1127, May 2008.
- [112] Richard W. Naylor, Sarah S. Qubisi, and Alan J. Davidson. Zebrafish Pronephros Development. In Rachel K. Miller, editor, *Kidney Development and Disease*, pages 27–53. Springer International Publishing, Cham, 2017.

- [113] Nisha Chander, Johannes Morstein, Jan S. Bolten, Andrej Shemet, Pieter R. Cullis, Dirk Trauner, and Dominik Witzigmann. Optimized Photoactivatable Lipid Nanoparticles Enable Red Light Triggered Drug Release. *Small*, n/a(n/a):2008198. [_eprint: https://onlinelibrary.wiley.com/doi/pdf/10.1002/sml.202008198](https://onlinelibrary.wiley.com/doi/pdf/10.1002/sml.202008198).
- [114] Claudia. Lotter, Claudio. Luca. Alter, Jan. Stephan. Bolten, Pascal. Detampel, Cornelia. G. Palivan, Toma. Einfalt, and Jörg. Huwylar. Incorporation of phosphatidylserine improves efficiency of lipid based gene delivery systems. *European Journal of Pharmaceutics and Biopharmaceutics*, page S0939641122000285, February 2022.
- [115] Anna Pratsinis, Philipp Uhl, Jan Stephan Bolten, Patrick Hauswirth, Susanne Heidi Schenk, Stephan Urban, Walter Mier, Dominik Witzigmann, and Jörg Huwylar. Virus-Derived Peptides for Hepatic Enzyme Delivery. *Molecular Pharmaceutics*, 18(5):2004–2014, May 2021.
- [116] Y. A. Nikolaev, A. V. Tutelyan, N. G. Loiko, J. Buck, S. V. Sidorenko, I. Lazareva, V. Gostev, O. Y. Manzenyuk, I. G. Shemyakin, R. A. Abramovich, J. Huwylar, and G. I. El-Registan. The use of 4-Hexylresorcinol as antibiotic adjuvant. *PLOS ONE*, 15(9):e0239147, September 2020. Publisher: Public Library of Science.
- [117] Uwe Anzenberger, Nana Bit-Avragim, Stefan Rohr, Franziska Rudolph, Bastian Dehmel, Thomas E. Willnow, and Salim Abdelilah-Seyfried. Elucidation of megalin/LRP2-dependent endocytic transport processes in the larval zebrafish pronephros. *Journal of Cell Science*, 119(10):2127–2137, May 2006.
- [118] Jia Sun, Kjell Hultenby, Jonas Axelsson, Johan Nordström, Bing He, Annika Wernerson, and Karin Lindström. Proximal Tubular Expression Patterns of Megalin and Cubilin in Proteinuric Nephropathies. *Kidney International Reports*, 2(4):721–732, March 2017.
- [119] Sanjay K. Nigam, Kevin T. Bush, Gleb Martovetsky, Sun-Young Ahn, Henry C. Liu, Erin Richard, Vibha Bhatnagar, and Wei Wu. The Organic Anion Transporter (OAT) Family: A Systems Biology Perspective. *Physiological Reviews*, 95(1):83–123, January 2015. Publisher: American Physiological Society.
- [120] Aniket V. Gore, Laura M. Pillay, Marina Venero Galanternik, and Brant M. Weinstein. The Zebrafish: A Fantastic Model for Hematopoietic Development and Disease. *Wiley interdisciplinary reviews. Developmental biology*, 7(3):e312, May 2018.
- [121] Cassandra Millet-Boureima, Jessica Porras Marroquin, and Chiara Gamberi. Modeling Renal Disease On the Fly. *BioMed Research International*, 2018:5697436, May 2018.
- [122] Pavle Randjelovic, Slavimir Veljkovic, Nenad Stojiljkovic, Duan Sokolovic, and Ivan Ilic. Gentamicin nephrotoxicity in animals: Current knowledge and future perspectives. *EXCLI Journal*, 16:388–399, March 2017.
- [123] Zhibo Gai, Michele Visentin, Christian Hiller, Evelin Krajnc, Tongzhou Li, Junhui Zhen, and Gerd A. Kullak-Ublick. Organic Cation Transporter 2 Overexpression May Confer an Increased Risk of Gentamicin-Induced Nephrotoxicity. *Antimicrobial Agents and Chemotherapy*, 60(9):5573–5580, August 2016.
- [124] Yaremi Quiros, Laura Vicente-Vicente, Ana I. Morales, José M. López-Novoa, and Francisco J. López-Hernández. An Integrative Overview on the Mechanisms Underlying the Renal Tubular Cytotoxicity of Gentamicin. *Toxicological Sciences*, 119(2):245–256, February 2011.

BIBLIOGRAPHY

- [125] Naglaa A. Bayomy, Reda H. Elbakary, Marwa A. A. Ibrahim, and Eman Z. Abdelaziz. Effect of Lycopene and Rosmarinic Acid on Gentamicin Induced Renal Cortical Oxidative Stress, Apoptosis, and Autophagy in Adult Male Albino Rat. *The Anatomical Record*, 300(6):1137–1149, 2017. _eprint: <https://onlinelibrary.wiley.com/doi/pdf/10.1002/ar.23525>.
- [126] David R. Sandison and Watt W. Webb. Background rejection and signal-to-noise optimization in confocal and alternative fluorescence microscopes. *Applied Optics*, 33(4):603–615, February 1994. Publisher: Optica Publishing Group.
- [127] Amicia D. Elliott. Confocal Microscopy: Principles and Modern Practices. *Current Protocols in Cytometry*, 92(1):e68, March 2020.
- [128] Alexandra Migga, Georg Schulz, Griffin Rodgers, Melissa Osterwalder, Christine Tanner, Holger Blank, Iwan Jerjen, Phil Salmon, William Twengström, Mario Scheel, Timm Weitkamp, Christian M. Schlepütz, Jan S. Bolten, Jörg Huwyler, Gerhard Hotz, Srinivas Madduri, and Bert Müller. Comparative hard x-ray tomography for virtual histology of zebrafish larva, human tooth cementum, and porcine nerve. *Journal of Medical Imaging*, 9(3):031507, March 2022. Publisher: SPIE.
- [129] Emre Cörek, Griffin Rodgers, Stefan Siegrist, Tomaz Einfalt, Pascal Detampel, Christian M. Schlepütz, Sandro Sieber, Pascal Fluder, Georg Schulz, Harald Unterweger, Christoph Alexiou, Bert Müller, Maxim Puchkov, and Jörg Huwyler. Metal-Based Nanoparticles: Shedding Light on Metal-Based Nanoparticles in Zebrafish by Computed Tomography with Micrometer Resolution (Small 31/2020). *Small*, 16(31):2070170, 2020. _eprint: <https://onlinelibrary.wiley.com/doi/pdf/10.1002/smll.202070170>.
- [130] J. E. Bird, M. R. Giancarli, J. R. Megill, and S. K. Durham. Effects of endothelin in radiocontrast-induced nephropathy in rats are mediated through endothelin-A receptors. *Journal of the American Society of Nephrology*, 7(8):1153–1157, August 1996. Publisher: American Society of Nephrology.
- [131] Kathy Hardiek, Richard E. Katholi, Vickram Ramkumar, and Cynthia Deitrick. Proximal tubule cell response to radiographic contrast media. *American Journal of Physiology-Renal Physiology*, 280(1):F61–F70, January 2001. Publisher: American Physiological Society.
- [132] Takahiro Sugiura, Yasushi Hirasawa, Tohru Toyoshi, and Yasuo Matsumura. Effects of Agmatine on Contrast-Induced Nephropathy in Rats and Rabbits. *Biological and Pharmaceutical Bulletin*, 43(10):1556–1561, October 2020.
- [133] Paul J. Cannon. The Kidney in Heart Failure. *New England Journal of Medicine*, 296(1):26–32, January 1977. Publisher: Massachusetts Medical Society.
- [134] Joerg C. Schefold, Gerasimos Filippatos, Gerd Hasenfuss, Stefan D. Anker, and Stephan von Haehling. Heart failure and kidney dysfunction: epidemiology, mechanisms and management. *Nature Reviews Nephrology*, 12(10):610–623, October 2016. Number: 10 Publisher: Nature Publishing Group.
- [135] Jianqing She, Zuyi Yuan, Yue Wu, Junfang Chen, and Jens Kroll. Targeting erythropoietin protects against proteinuria in type 2 diabetic patients and in zebrafish. *Molecular Metabolism*, 8:189–202, November 2017.
- [136] Joseph J. H. M. Lohman and Frans W. H. M. Merkus. Plasma protein binding of digitoxin and some other drugs in renal disease. *Pharmaceutisch Weekblad*, 9(2):75–78, April 1987.
- [137] Albrecht G. Kramer-Zucker, Stephanie Wiessner, Abbie M. Jensen, and Iain A. Drummond. Organization of the pronephric filtration apparatus in zebrafish requires Nephrin, Podocin and the FERM domain protein Mosaic eyes. *Developmental Biology*, 285(2):316–329, September 2005.

- [138] Erica L. Woodahl, Matthew H. Crouthamel, Tot Bui, Danny D. Shen, and Rodney J. Y. Ho. MDR1 (ABCB1) G1199A (Ser400Asn) polymorphism alters transepithelial permeability and sensitivity to anticancer agents. *Cancer Chemotherapy and Pharmacology*, 64(1):183–188, June 2009.
- [139] Bernhard Witkop. Paul Ehrlich and His Magic Bullets, Revisited. *Proceedings of the American Philosophical Society*, 143(4):540–557, 1999. Publisher: American Philosophical Society.
- [140] Roy Pattipeiluhu, Gabriela Arias-Alpizar, Genc Basha, Karen Y. T. Chan, Jeroen Bussmann, Thomas H. Sharp, Mohammad-Amin Moradi, Nico Sommerdijk, Edward N. Harris, Pieter R. Cullis, Alexander Kros, Dominik Witzigmann, and Frederick Campbell. Anionic Lipid Nanoparticles Preferentially Deliver mRNA to the Hepatic Reticuloendothelial System. *Advanced materials (Deerfield Beach, Fla.)*, 34(16):e2201095, April 2022.
- [141] Viktor Manuel Jooss, Jan Stephan Bolten, Jörg Huwyler, and Daniel Ahmed. In vivo acoustic manipulation of microparticles in zebrafish embryos. *Science Advances*, 8(12):eabm2785, March 2022.
- [142] Siyu Wang, Xixi Guo, Weijun Xiu, Yang Liu, Lili Ren, Huaxin Xiao, Fang Yang, Yu Gao, Chenjie Xu, and Lianhui Wang. Accelerating thrombolysis using a precision and clot-penetrating drug delivery strategy by nanoparticle-shelled microbubbles. *Science Advances*, 6(31):eaz8204, July 2020.
- [143] Hong Chen and Elisa E Konofagou. The size of bloodbrain barrier opening induced by focused ultrasound is dictated by the acoustic pressure. *Journal of Cerebral Blood Flow & Metabolism*, 34(7):1197–1204, July 2014.
- [144] Ying Meng, Kullervo Hynynen, and Nir Lipsman. Applications of focused ultrasound in the brain: from thermoablation to drug delivery. *Nature Reviews Neurology*, 17(1):7–22, January 2021. Number: 1 Publisher: Nature Publishing Group.
- [145] Ana I. Morales, Dominique Detaille, Marta Prieto, Angel Puente, Elsa Briones, Miguel Arévalo, Xavier Lerverve, José M. López-Novoa, and Mohamad-Yehia El-Mir. Metformin prevents experimental gentamicin-induced nephropathy by a mitochondria-dependent pathway. *Kidney International*, 77(10):861–869, May 2010.
- [146] Goetze Oezen, Eva-Maria Schentarra, Jan Stephan Bolten, Joerg Huwyler, and Gert Fricker. Sodium arsenite but not aluminum chloride stimulates ABC transporter activity in renal proximal tubules of killifish (*Fundulus heteroclitus*). *Aquatic Toxicology (Amsterdam, Netherlands)*, 252:106314, November 2022.
- [147] Sylvia Notenboom, David S. Miller, P. Smits, Frans G. M. Russel, and Rosalinde Masereeuw. Involvement of guanylyl cyclase and cGMP in the regulation of Mrp2-mediated transport in the proximal tubule. *American Journal of Physiology-Renal Physiology*, 287(1):F33–F38, July 2004.
- [148] Jaime Chu and Kirsten C. Sadler. A New School in Liver Development: Lessons from Zebrafish. *Hepatology (Baltimore, Md.)*, 50(5):1656–1663, November 2009.
- [149] Deanna L. Howarth, Mike Passeri, and Kirsten C. Sadler. Drinks like a fish: Using zebrafish to understand alcoholic liver disease. *Alcoholism, clinical and experimental research*, 35(5):826–829, May 2011.
- [150] W. Alderton, S. Berghmans, P. Butler, H. Chassaing, A. Fleming, Z. Golder, F. Richards, and I. Gardner. Accumulation and metabolism of drugs and CYP probe substrates in zebrafish larvae. *Xenobiotica*, 40(8):547–557, August 2010. Publisher: Taylor & Francis _eprint: <https://doi.org/10.3109/00498254.2010.493960>.

BIBLIOGRAPHY

- [151] Carina de Souza Anselmo, Vinicius Figueiredo Sardela, Valeria Pereira de Sousa, and Henrique Marcelo Gualberto Pereira. Zebrafish (*Danio rerio*): A valuable tool for predicting the metabolism of xenobiotics in humans? *Comparative Biochemistry and Physiology Part C: Toxicology & Pharmacology*, 212:34–46, October 2018.
- [152] Kuei-Meng Wu. A New Classification of Prodrugs: Regulatory Perspectives. *Pharmaceuticals*, 2(3):77–81, October 2009.

ABBREVIATIONS

Abbreviation	Definition
ABC	ATP-binding cassette
AIN	acute interstitial nephritis
BCRP	breast cancer resistance protein
CIN	chronic interstitial nephritis
eGFP	enhanced green fluorescent protein
FSGS	focal segmental glomerulosclerosis
GBM	glomerular filtration barrier
HEK293	human embryonic kidney cell
HK-2	human kidney 2
MATE	multidrug and toxin extrusion protein
MCD	minimal change disease
MDIBL	Mount Desert Island Biological Laboratory
MDR	multidrug resistance protein
MRP	multidrug resistance-associated protein
NSAIDs	non-steroidal anti-inflammatory drugs
OAT	organic anionic transporter
OCT	organic cationic transporter
OCTN	organic cationic and carnitine transporter
SLC	solute carrier
TERT	telomerase reverse transcriptase

ACKNOWLEDGMENT

I want to thank my supervisor and mentor, **Prof. Dr. Jörg Huwyler**, for giving me the opportunity to work in his research group. His motivational, fascinating, and supportive attitude helped me to tackle various scientific questions. I appreciated working with him and pursuing so many scientific projects but also exploring unknown territory. I am very grateful that I had the opportunity to participate in research stays in Maine. Thank you very much, Jörg.

For his co-supervision and expert opinion in collaborative scientific projects, I would like to thank **Prof. Dr. Alex Odermatt**. I also want to thank **Prof. Dr. Andrea Huwiler** for being the external expert in my doctoral committee and **Prof. Dr. Christoph Meier** for being the chair.

It was also a great experience to work with my colleagues of the **Pharmaceutical Technology group** in the lab, exchange scientific discussions, and spend time together. A big thank goes to **Dr. Anna Pratsinis**, **Dr. Noëmi Roos**, and **Dr. Riccardo Mancuso** for our collaborative work during my time at the Pharmacenter. I learned a lot from all of you and appreciated your constant support.

I want to thank **Dr. Susanne Schenk** and **Dr. Sandro Sieber**, who both introduced me at the beginning to sciences and showed me various methods. I also thank **Dr. Susanne Schenk** for her constant scientific support during my PhD.

Furthermore, I thank all my collaborators for working with me. In particular, I want to thank **Prof. Dr. Gert Fricker** for our formative time in Maine. You nicely introduced

ACKNOWLEDGMENT

me to the killifish model and everybody working on the campus. Thus, we had a nice time in Maine together and enjoyed very much exploring the island in our free time.

I also thank my colleagues from the **Biomaterial Science Center**. We had an excellent collaboration, and I could learn a lot in the field of X-ray-based microtomography and had the opportunity to visit the synchrotron facility Soleil in France with you.

A big thank goes to **Dr. Soledad Levano** for her help regarding mice experiments.

Furthermore, I would like to thank the research group of **Prof. Dr. Markus Affolter** and **PD. Dr. Heinz-Georg (Henry) Belting** for sharing their zebrafish facility with us and for collaborative maintenance work. A great thank goes to **Katrin Gundel** for her outstanding support and help with zebrafish maintenance and experiments. Further, I thank **Alexa Barnby** for proofreading the manuscript.

I also want to thank **my colleagues** I met during my PhD at the Pharmacenter of the University of Basel. I appreciated the social activities together.

Furthermore, I want to thank **all my friends** who have always been here for me and helped me in challenging times. This meant a lot to me and allowed me to pursue scientific work.

I also want to thank my **tennis colleagues** for having adventurous and funny sports events with a lot of good times, sportive success, and a lot of training sessions.

Finally, I want to thank my entire family, especially **Dr. Roger Bolten** and **Nicole Bolten**, for their support during my PhD. They have always supported me and given me valuable advice. I also thank my sister and brother, **Monique Bolten** and **Timon Bolten**, for their patience and emotional support. It was always entertaining to tell them funny lab stories and give them insights into the world of academic sciences.

Lastly, I thank my dear girlfriend, **Aleksandra (Lexi) Blagojevic**, for her endless (emotional) support and for being by my side. I appreciate the support we give each other. With you at my side, this time flew by.